Ministry of Education and Science of the Russian Federation
Saint Petersburg National Research University of Information
Technologies, Mechanics, and Optics

NANOSYSTEMS:

PHYSICS, CHEMISTRY, MATHEMATICS

2013, volume 4(6)

Наносистемы: физика, химия, математика

2013, том 4, № 6

NANOSYSTEMS:

PHYSICS, CHEMISTRY, MATHEMATICS

ADVISORY BOARD MEMBERS

Chairman: V.N. Vasiliev *(St. Petersburg, Russia)*,
V.M. Ievlev *(Voronezh)*, P.S. Kop'ev*(St. Petersburg, Russia)*,
V.N. Parmon *(Novosibirsk)*, A.I. Rusanov *(St. Petersburg, Russia)*.

EDITORIAL BOARD

Editor-in-Chief: N.F. Morozov *(St. Petersburg, Russia)*
Deputy Editor-in-Chief: I.Yu. Popov *(St. Petersburg, Russia)*

Section Co-Editors:
Physics – V.M. Uzdin *(St. Petersburg, Russia)*,
Chemistry, material science –V.V. Gusarov *(St. Petersburg, Russia)*,
Mechanics – A.K. Belyaev *(St. Petersburg, Russia)*,
Mathematics – I.Yu. Popov *(St. Petersburg, Russia)*.

Editorial Board Members:
V.M. Adamyan *(Odessa, Ukraine)*; O.V. Al'myasheva *(St. Petersburg, Russia)*; S. Bechta *(Stockholm, Sweden)*; V.G. Bespalov *(St. Petersburg, Russia)*; A. Chatterjee (*Hyderabad, India)*; S.A. Chivilikhin *(St. Petersburg, Russia)*; A.V. Chizhov *(Dubna, Russia)*; P.P. Fedorov *(Moscow, Russia)*; E.A. Gudilin *(Moscow, Russia)*; D.A. Indeitsev *(St. Petersburg, Russia)*; A.L. Ivanovskii *(Ekaterinburg, Russia)*; H. Jónsson *(Reykjavik, Iceland)*; A.A. Kiselev *(Madison, USA)*; Yu.S. Kivshar *(Canberra, Australia)*; S.A. Kozlov *(St. Petersburg, Russia)*; Yu.B. Kudasov *(Sarov, Russia)*; S.E. Kul'kova *(Tomsk, Russia)*; P.A. Kurasov *(Stockholm, Sweden)*; A.V. Lukashin *(Moscow, Russia)*; V.A. Margulis *(Saransk, Russia)*; I.V. Melikhov *(Moscow, Russia)*; G.P. Miroshnichenko *(St. Petersburg, Russia)*; H. Neidhardt *(Berlin, Germany)*; K. Pankrashkin *(Orsay, France)*; B.S. Pavlov *(Auckland, New Zealand)*; A.V. Ragulya *(Kiev, Ukraine)*; V. Rajendran *(Tamil Nadu, India)*; V.P. Romanov *(St. Petersburg, Russia)*; V.Ya. Rudyak *(Novosibirsk, Russia)*; V.M. Talanov *(Novocherkassk, Russia)*; A.Ya. Vul' *(St. Petersburg, Russia)*.

Editors:
I.V. Blinova; A.I. Popov; M.A. Skryabin; A.I. Trifanov; E.S. Trifanova *(St. Petersburg, Russia)*, R. Simoneaux *(USA)*.

Address: University ITMO, Kronverkskiy pr., 49, St. Petersburg 197101, Russia.
Phone: +7(812)232-67-65, **Journal site:** http://nanojournal.ifmo.ru/,
E-mail: popov1955@gmail.com

AIM AND SCOPE

The scope of the journal includes all areas of nano-sciences. Papers devoted to basic problems of physics, chemistry, material science and mathematics inspired by nanosystems investigations are welcomed. Both theoretical and experimental works concerning the properties and behavior of nanosystems, problems of its creation and application, mathematical methods of nanosystem studies are considered.

The journal publishes scientific reviews (up to 30 journal pages), research papers (up to 15 pages) and letters (up to 5 pages). All manuscripts are peer-reviewed. Authors are informed about the referee opinion and the Editorial decision.

Content

MATHEMATICS

PHYSICS

CHEMISTRY AND MATERIAL SCIENCE

NANOSYSTEMS: PHYSICS, CHEMISTRY, MATHEMATICS, 2013, 4 (6), P. 725–746

SEMICLASSICAL ANALYSIS OF TUNNELING THROUGH A SMOOTH POTENTIAL BARRIER AND LOCALIZED STATES IN GRAPHENE MONOLAYER WITH MASS GAP

[1]V. V. Zalipaev, [2]C. M. Linton

[1] Krylov State Research Institute, St. Petersburg, Russia
[2] Loughborough University, Loughborough, UK
v.zalipaev@lboro.ac.uk, c.m.linton@lboro.ac.uk

PACS 03.65.-w, 03.65.Sq, 04.20Ha, 04.30Db

We present a semiclassical analysis of Dirac electron tunnelling in a graphene monolayer with mass gap through a smooth potential barrier in the ballistic regime. This 1D scattering problem is formulated in terms of a transfer matrix and treated in the WKB approximation. For a skew electron incidence this WKB approximation deals, in general, with four turning points. Between the first and the second, and the third and the fourth, turning points two tunnelling domains are observed. Scattering through a smooth barrier in graphene resembles scattering through a double barrier for the 1D Schrödinger operator, i.e. a Fabry-Perot resonator. The main results of the paper are WKB formulas for the entries of the barrier transfer matrix which explain the mechanism of total transmission through the barrier in a graphene monolayer with mass gap for some resonance values of energy of a skew incident electron. Moreover, we show the existence of modes localized within the barrier and exponentially decaying away from it and its behaviour depending on mass gap. There are two sets of energy eigenlevels, complex with small imaginary part and real, determined by a Bohr-Sommerfeld quantization condition, above and below the cut-off energy. It is shown that total transmission through the barrier takes place when the energy of the incident electron coincides with the real part of one of the complex energy eigenlevels. These facts were confirmed by numerical simulations performed using the finite element method (COMSOL).

Keywords: Graphene monolayer with mass gap, high-energy eigenstates, semiclassical approximation, generalized Bohr-Sommerfeld quantization condition.

1. Introduction

In this paper we study 2D electron transport in a graphene monolayer with mass gap with a smooth potential barrier. The general description of graphene electron transport may be found in the following reviews and publications [1-9]. Theory and experiments on electron transport in graphene and the related phenomenon of Klein tunnelling were described in many reviews and papers, for example, in [3], [10], [11], [12], [13], [14], [15]. It is worth mentioning the papers [16], [17], where analysis of electron-holes conductance oscillation in transport through barriers in graphene nano-ribbons was presented similar to 2D electron gas transport in semiconductors ([18], [19], [20]).

Graphene, a sheet of single carbon atom honeycomb lattice, is well-known for its unique electron ballistic transport properties. It is regarded as an ideal medium for many applications such as graphene-based electronic devices [1]. However, graphene is a zero-bandgap semiconductor and exhibits semimetallic behaviour. Without bandgap opening it cannot be applied directly to semiconductors devices such as field-effect transistors which cannot operate in the absence of a bandgap in the material [21]. Thus, creating tunable bandgap gives an opportunity of enormous applications of graphene in digital electronics. In the quest of creating the tunable bandgap, several physical and chemical approaches have been proposed and implemented successfully. This privides the motivation to study electron ballistic transport in graphene in the presence of a tunable bandgap. Generating the tunable bandgap for graphene in studies of electron ballistic transport means an appearance of a mass term in the Dirac system describing electron-hole quasi particle transport dynamics.

In the paper we present a semiclassical analysis of Dirac electron-hole tunnelling in a graphene monolayer with mass gap through a smooth barrier representing electrostatic potential in the ballistic regime. This 1D scattering problem is formulated in terms of transfer matrix and treated in the WKB (adiabatic) approximation for the Dirac system. For a skew electron incidence this WKB approximation deals with four turning points $x_i,\ i = 1, 2, 3, 4$. For this scattering problem we assume that incident electron energy belongs to the middle part of the segment $[0, U_0]$, where U_0 is the height of the barrier. Thus, between x_1 and x_2, and x_3 and x_4 we observe two tunnelling strips of total internal reflection similar to the well-known case in electromagnetic optics where the solution exponentially decay and grow. Between the asymptotically small neighbourhoods of $x_i,\ i = 1, 2, 3, 4$ (boundary layers), we have five domains with WKB type asymptotic solutions, three domains with oscillatory behaviour and two with exponentially decaying and growing asymptotics. A gluing procedure between these five solutions is based on the matched asymptotic techniques (see [22], [23]) applied to so-called effective Schrödinger equation that is equivalent to the initial Dirac system (see [24], [25]). This gluing procedure leads to WKB formulas for the entries of the barrier transfer matrix that give all the transmission and reflection coefficients in this scattering problems.

It is worth mentioning that the scattering through a smooth barrier in graphene resembles scattering through a double barrier for 1D Schrödinger operator, i.e. a 1D Fabry-Perot resonator. From the point of view of physics of graphene, for positive energies close to one-half of the potential height $U_0 > 0$ we observe incident, reflected and transmitted electronic states outside the barrier, whereas under the barrier we have a hole state (n-p-n junction). For negative energies close to one-half of the potential height $U_0 < 0$ we observe incident, reflected and transmitted hole states outside the barrier, whereas under the barrier we have electronic states (p-n-p junction). It was Silvestrov and Efetov [17] who first demonstrated that in graphene a single parabolic barrier is similar to the double barrier potential well in GaAs/AlGaAs. They have shown that for the Dirac chiral relativistic electrons or holes there exist quasibound states. Parts of the left and right slopes of the parabolic potential barrier are acting like tunnelling barriers.

It is important to note that there is a strong difference between rectangular and smooth potential barriers. The presence of stable bound states for a rectangular barrier was first demonstrated by Pereira et al [26]. However in this case the double barrier structure does not arise and therefore the bound states are associated with a trapping into a potential well. Here we show that similar bound states can exist in a more generic situation when there is a single 1D smooth potential barrier formed in a graphene monolayer by some external electrostatic potential.

The main results of the paper are WKB formulas for the entries of the barrier transfer matrix which explain the mechanism of total transmission through an arbitrary smooth barrier in a graphene monolayer with mass gap for some resonance values of the energy of a skew incident electron. Crucially we show the existence of modes localized within the barrier and exponentially decaying away from it. There are two sets of energy eigenlevels, complex (quasibound states with small imaginary part i.e. long lifetime) and real (bound states), determined by a Bohr-Sommerfeld quantization condition, above and below the cut-off energy, respectively. This differs from previous results. It is shown that the total transmission through the barrier takes place when the energy of an incident electron, which is above the cut-off energy, coincides with the real part of a complex energy eigenlevel of the first set of modes localized within the barrier. These facts were confirmed by numerical simulations for the reflection and transmission coefficients performed using the finite element method (COMSOL).

It is worth noting that the Dirac electron scattering by an arbitrary smooth barrier in a graphene monolayer but with zero mass gap in semiclassical approximation was briefly described in [27] stating only the main results. Here we present a more detailed general semiclassical analysis of Dirac electron tunnelling in a graphene monolayer with mass gap through a smooth potential barrier in the ballistic regime.

The paper is organized as follows. First, in section 2, we give a general details of the WKB description of tunnelling through a smooth barrier in a graphene monolayer with mass gap. In the next section we discuss WKB asymptotic solutions for the Dirac system with mass gap. In section, a 4 WKB asymptotic solution uniform with respect to p_γ for tunnelling through a smooth steps, left and right, is constructed. Building the total barrier transfer matrix is described in section 5. Analysis of quasi-bound and real bound states localized within the barrier is given in section 6. The results of numerical analysis are presented in section 7.

2. Tunnelling through a smooth barrier in graphene monolayer with mass gap

The procedure for deriving a theory describing elementary electronic properties of single layer graphene (see, for example, [9] and [4], section 2) works for electrons whose energy is close to Fermi level when their momenta are close to the Dirac points K and K' of the Brillouin zone. It uses the representation in the tight-binding 2D lattice Hamiltonian and expanding the operators up to a linear order with respect to momentum within a neighbourhood of the Dirac points, and thus, leading to the effective Hamiltonian with Dirac operator in the first approximation.

Consider a scattering problem for the Dirac operator describing an electron-hole in the presence of a scalar potential representing a smooth localized barrier with the height $U_0 > 0$ (see Fig.1) The problem can be described by the following 2D Dirac system (see, for example, [4])

$$[v_F(\bar{\sigma} \cdot \frac{\hbar}{i}\nabla) + mv_F^2\sigma_3 + U(\mathbf{x})]\psi(\mathbf{x}) = E\psi(\mathbf{x}),\ \psi(\mathbf{x}) = \begin{pmatrix} u \\ v \end{pmatrix}, \tag{1}$$

where $\mathbf{x} = (x, y)$. Here u, v are the components of the spinor wave function describing electron density distribution localized on sites of sublattice A or B of the honeycomb graphene structure (see [9]), v_F is the Fermi velocity, $m = const$ is the electron effective mass, $\hbar$ is the Planck constant, and $\bar{\sigma} = (\sigma_x, \sigma_y)$ with Pauli matrices

$$\sigma_x = \begin{pmatrix} 0 & 1 \\ 1 & 0 \end{pmatrix},\ \sigma_y = \begin{pmatrix} 0 & -i \\ i & 0 \end{pmatrix},\ \sigma_z = \begin{pmatrix} 1 & 0 \\ 0 & -1 \end{pmatrix}.$$

If we assume that the potential representing the smooth barrier does not depend on y, i.e. $U = U(x)$, then we can look for a solution in the form

$$\psi(\mathbf{x}) = e^{i\frac{p_y}{\hbar}y} \begin{pmatrix} u(x) \\ v(x) \end{pmatrix},$$

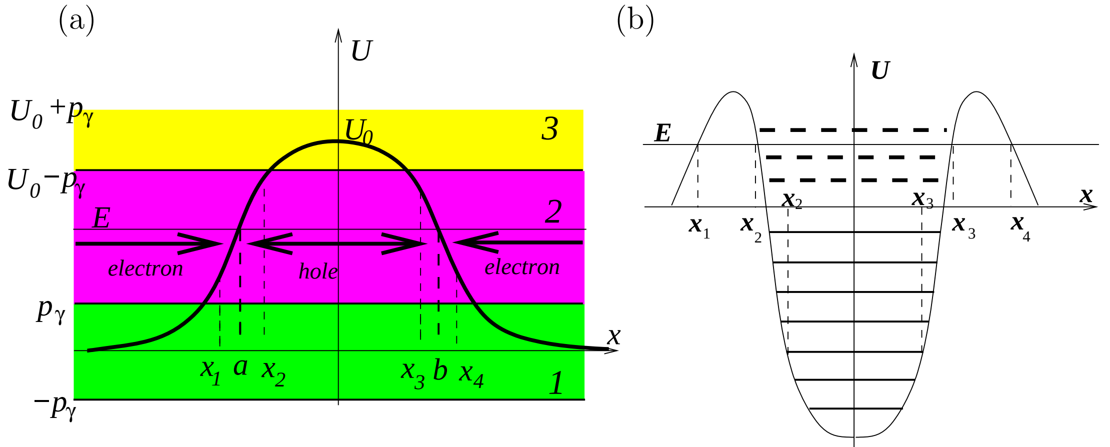

FIG. 1. The three energy zones, shown in green - 1, pink - 2 and yellow - 3 colours are associated with the diverse character of scattering and localization for potential behaviour. The schematic shape of the two barrier potential for 1D Schrödinger, which is equivalent to the smooth potential barrier in graphene presented in the Fig.1(a) when the energy of quasi-particles belongs to 1 and 2 zones, i.e. $-p_\gamma < E < U_0 - p_\gamma$.

where p_y means value of the transverse momentum component describing the angle of incidence. Then, we obtain the Dirac system of two first order ODEs

$$\begin{pmatrix} U(x) - E + mv_F^2 & v_F[-i\hbar\partial_x - ip_y] \\ v_F[-i\hbar\partial_x + ip_y] & U(x) - E - mv_F^2 \end{pmatrix} \begin{pmatrix} u \\ v \end{pmatrix} = \begin{pmatrix} 0 \\ 0 \end{pmatrix}. \tag{2}$$

We assume that the potential $U(x)$ has just one maximum and vanishes exponentially as $x \to \pm\infty$. Thus, $U(x)$ is being localized within a strip directed along Y axis.

It is more convenient to use the dimensionless system

$$\begin{pmatrix} U(x) - E + \gamma & -ih\partial_x - ip_y \\ -ih\partial_x + ip_y & U(x) - E - \gamma \end{pmatrix} \begin{pmatrix} u \\ v \end{pmatrix} = \begin{pmatrix} 0 \\ 0 \end{pmatrix}, \tag{3}$$

with the dimensionless rescaled variables that we shall be using below, that is, $x/D \to x$ with D being a characteristic length scale for the external potential, $E/E_0 \to E$ with E_0 being a characteristic energy scale. Then, we have $v_F p_y/E_0 \to p_y$, and $U(x/D)/E_0 \to U(x)$. Then the mass term is given by

$$\gamma = \frac{mv_F^2}{E_0} = const \geqslant 0. \tag{4}$$

The WKB solution may be constructed if the dimensionless parameter

$$h = \frac{\hbar v_F}{E_0 D}$$

is small ($h \ll 1$). Typical values of E_0 and D are in the ranges 10-100 meV and 100-500 nm. For example, for $E_0 = 100\,meV$, $D = 66\,nm$, we have $h = 0.1$.

Let $p_\gamma = \sqrt{p_y^2 + \gamma^2} \geqslant 0$. In Fig. 1(a), 3 zones are shown that illustrate different scattering regimes for the smooth barrier scattering problem. These zones are exactly the same as for the rectangular barrier with the height U_0. Below zone 1, $E < -p_\gamma$, we have total transmission and exponentially small reflection, asymptotic solutions are of oscillatory type everywhere. In zone 1 (green), $-p_\gamma < E < p_\gamma$ ($E = \pm p_\gamma$ are the cut-off energy values), there is no propagation outside the barrier, however there are oscillatory solutions within the barrier. In the zone 2 (pink), $p_\gamma < E < U_0 - p_\gamma$, there are oscillatory solutions outside and within the barrier (zone of resonance tunnelling). In zone 3 (yellow), $U_0 - p_\gamma < E < U_0 + p_\gamma$, there is no propagation through the barrier, we have total reflection and exponentially small transmission. Above zone 3 $E > U_0 + p_\gamma$, we have total transmission and exponentially small reflection, asymptotic solutions are of oscillatory type everywhere.

In the paper, we study the scattering problem for zone 2 and localized states in zone 1. In the first case, there are 5 domains with different WKB asymptotic solutions:

$$\Omega_1 = \{x : -\infty < x < x_1\},$$

$$\Omega_2 = \{x : x_1 < x < x_2\},$$

$$\Omega_3 = \{x : x_2 < x < x_3\},$$

$$\Omega_4 = \{x : x_3 < x < x_4\},$$

$$\Omega_5 = \{x : x_4 < x < +\infty\},$$

where the turning points x_i with $i = 1, 2, 3, 4$, are the roots of the equation

$$(E - U(x))^2 - p_\gamma^2 = 0.$$

The regions Ω_1, Ω_3 and Ω_5, in which

$$(E - U(x))^2 - p_\gamma^2 > 0,$$

will be referred to as classically allowed domains, whereas Ω_2 and Ω_4, in which

$$(E - U(x))^2 - p_\gamma^2 < 0$$

are classically forbidden domains. Note that as $p_\gamma \to 0$ for fixed value of E, the turning points coalesce.

These three energy zones are associated with diverse character of scattering through this potential barrier. The Dirac electron and hole bound states arise in a process of resonance tunnelling through this smooth potential. The quasi-bound states are to be found in the pink zone 2, confined by two tunnelling strips between the turning points x_1, x_2 and x_3, x_4, whereas the real bound states are located in zone 1 between x_2 and x_3. The schematic shape of the two barrier potential for 1D Schrödinger shown in Fig. 1(b) is equivalent to the smooth potential in graphene presented in the Fig.1(a) when the energy of quasi particles belongs to zones 1 and 2, i.e. $-p_\gamma < E < U_0 - p_\gamma$. Quasi-bound states shown in Fig. 1(a) by dashed lines are confined by two tunnelling strips between x_1, x_2 and x_3, x_4.

It is worth remarking that when p_γ is fixed, and if E moves down from zone 2 to zone 1, the turning points x_1 and x_4 disappear ($x_1 \to -\infty$, $x_4 \to +\infty$) such that inside zone 1 we have only x_2 and x_3. When we move down within zone 1, the turning points x_2 and x_3 get more separated. When E moves up from zone 2 to zone 3, the turning points x_2 and x_3 coalesce and disappear such that inside zone 3 we have only x_1 and x_4. When we move up from zone 3, the turning points x_1 and x_4 coalesce and disappear, and we obtain total transmission. In the paper we assume that $U_0 > 2p_\gamma$. Thus, zone 2 should not disappear from the diagram in Fig.1(a).

3. WKB asymptotic solutions for Dirac system

It is convenient to introduce

$$W=\frac{u+v}{2},\ V=\frac{u-v}{2}. \tag{5}$$

Then, the system (3) reads

$$\begin{aligned}(U-E)W+(\gamma+ip_y)V-ihW'=0,\\ (U-E)V+(\gamma-ip_y)W+ihV'=0.\end{aligned} \tag{6}$$

Eliminating V,

$$V=\frac{ihW'+(E-U)W}{\gamma+ip_y}, \tag{7}$$

we obtain the so-called effective Schrödinger equation with complex coefficient

$$h^2W''+(\xi^2-p_\gamma^2+ihU')W=0, \tag{8}$$

where $\xi=U(x)-E$. The WKB oscillatory asymptotic solution to (8) in the classically allowed domains is to be sought in the form (see [23]) with real $S(x)$

$$W=e^{\frac{i}{h}S(x)}\sum_{j=0}^{+\infty}(-ih)^jW_j(x). \tag{9}$$

To the leading order we obtain

$$S=\pm S_p(x,x_n)=\pm\int_{x_n}^{x}p_xdx,\ p_x=\sqrt{\xi^2-p_\gamma^2}>0,\ n=1,2,3,4, \tag{10}$$

and up to a constant multiplier w_0, for a wave traveling to the right we have

$$W=w_0\frac{e^{\frac{i}{h}S_p(x,x_n)}}{\sqrt{p_x}}\sqrt{\frac{\mp p_\gamma}{\xi+p_x}}(1+O(h)), \tag{11}$$

while for a wave traveling to the left we have

$$W=w_0\frac{e^{-\frac{i}{h}S_p(x,x_n)}}{\sqrt{p_x}}\sqrt{\frac{\xi+p_x}{\mp p_\gamma}}(1+O(h)). \tag{12}$$

Here $-p_\gamma$ corresponds to solutions referred to $x_{1,4}$ as $U(x_{1,4})-E=-p_\gamma$, whereas $+p_\gamma$ corresponds to $x_{2,3}$ as $U(x_{2,3})-E=p_\gamma$.

We seek the WKB exponentially decaying or growing asymptotic solution to (8) in the classically forbidden domains in the form (see [23]) with real $S(x)$

$$W=e^{\frac{1}{h}S(x)}\sum_{j=0}^{+\infty}h^jW_j(x). \tag{13}$$

To leading order we obtain

$$S=\pm S_q(x,x_n)=\pm\int_{x_n}^{x}q_xdx,\ q_x=\sqrt{p_\gamma^2-\xi^2}>0, \tag{14}$$

and up to a constant multiplier w_0, we have

$$W=w_0\frac{e^{\frac{1}{h}S_q(x,x_n)}}{\sqrt{q_x}}e^{-\frac{i}{2}(\arcsin\frac{\xi}{p_\gamma}\pm\frac{\pi}{2})}(1+O(h)), \tag{15}$$

or

$$W = w_0 \frac{e^{-\frac{1}{h}S_q(x,x_n)}}{\sqrt{q_x}} e^{\frac{i}{2}(\arcsin\frac{\xi}{p_\gamma}\pm\frac{\pi}{2})}(1+O(h)), \tag{16}$$

and again $+\pi/2$ corresponds to solutions referred to $x_{1,4}$, whereas $-\pi/2$ corresponds to $x_{2,3}$. All these asymptotic solutions break down at the turning points $\xi = -p_\gamma$ for x_1 and x_4, and $\xi = p_\gamma$ for x_2 and x_3.

4. WKB asymptotic solution for tunnelling through a smooth step (uniform asymptotics w.r.t. p_γ)

Consider the scattering problem for the smooth barrier under the assumption that $p_\gamma < E < U_0 - p_\gamma$, $U_0 > 0$ and all four turning points are present. From the point of view of scattering through the barrier we observe incident, reflected and transmitted electronic states at $x < -a$ and $x > a$, whereas under the barrier $-a < x < a$ we have a hole state (n-p-n junction, see Fig. 1). The transfer matrix for the left slope is defined as follows

$$d = Ta,\ T_L = \begin{pmatrix} T_{11}^L & T_{12}^L \\ T_{21}^L & T_{22}^L \end{pmatrix},\ d = \begin{pmatrix} d_1 \\ d_2 \end{pmatrix},\ a = \begin{pmatrix} a_1 \\ a_2 \end{pmatrix}, \tag{17}$$

where we assume that $U(-\infty) = 0$, and $U(+\infty) = U_0 = \mathit{const}$. This means that the potential $U(x)$ behaves like a smooth monotone step. The connection coefficients a and d are defined in the asymptotic expansion of the solution at $\mp\infty$. Namely, as $x \to -\infty$, we have

$$\psi = \frac{1}{\sqrt{2\rho^- \cos\theta^-}}\left(a_1 e^{\frac{i}{h}p_x^- x + i\Phi_0}\begin{pmatrix} e^{-i\theta^-/2} \\ \rho^- e^{i\theta^-/2}\end{pmatrix} + a_2 e^{-\frac{i}{h}p_x^- x - i\Phi_0}\begin{pmatrix} e^{i\theta^-/2} \\ -\rho^- e^{-i\theta^-/2}\end{pmatrix}\right) =$$

$$= a_1 e^{\frac{i}{h}p_x^- x} e_1^- + a_2 e^{-\frac{i}{h}p_x^- x} e_2^-, \tag{18}$$

$$p_x^- = \sqrt{E^2 - p_\gamma^2},\ \rho^- = \frac{\sqrt{(p_x^-)^2 + p_y^2}}{E+\gamma},$$

and Φ_0 is a constant phase factor. As $x \to +\infty$, then

$$\psi = \frac{1}{\sqrt{2\rho^+ \cos\theta^+}}\left(d_1 e^{\frac{i}{h}p_x^+ x + i\Phi_0}\begin{pmatrix} e^{-i\frac{\theta^+}{2}} \\ -\rho^+ e^{i\frac{\theta^+}{2}}\end{pmatrix} + d_2 e^{-\frac{i}{h}p_x^+ x - i\Phi_0}\begin{pmatrix} e^{i\frac{\theta^+}{2}} \\ \rho^+ e^{-i\frac{\theta^+}{2}}\end{pmatrix}\right)$$

$$= d_1 e^{\frac{i}{h}p_x^+ x} e_1^+ + a_2 e^{-\frac{i}{h}p_x^+ x} e_2^+, \tag{19}$$

and

$$p_x^+ = \sqrt{(E-U_0)^2 - p_\gamma^2},\ \rho^+ = \frac{\sqrt{(p_x^+)^2 + p_y^2}}{U_0 - E - \gamma},$$

and $\theta^\pm = \arg(p_x^\pm + ip_y)$. This asymptotic behaviour at $\mp\infty$ is very important as the corresponding transfer matrix satisfies canonical properties presented in Appendix A. This normalization leads to the conservation of the probability current (see (74)) written as

$$|a_1|^2 - |a_2|^2 = |d_2|^2 - |d_1|^2. \tag{20}$$

Then, the WKB asymptotic solution valid for $x < x_1$ that matches (18) has to be written as follows

$$\psi = \frac{1}{\sqrt{p_x}}\left(a_1 e^{\frac{i}{h}S_p(x,x_1) - i\Phi_1}\sqrt{\frac{-p_\gamma}{p_x+\xi}}\begin{pmatrix} 1 - \frac{p_x+\xi}{ip_y+\gamma} \\ 1 + \frac{p_x+\xi}{ip_y+\gamma}\end{pmatrix} + \right.$$

$$ia_2 e^{-\frac{i}{h}S_p(x,x_1)-i\Phi_2}\sqrt{\frac{p_x+\xi}{-p_\gamma}}\begin{pmatrix}1+\frac{p_x-\xi}{ip_y+\gamma}\\ 1+\frac{\xi-p_x}{ip_y+\gamma}\end{pmatrix}\Big), \tag{21}$$

where

$$\Phi_1 = \arg\big\{e^{i\frac{\theta^-}{2}}(1-\frac{p_x^- - E}{ip_y+\gamma})\sqrt{\frac{-p_\gamma}{p_x^-(p_x^- - E)}}\big\},$$

$$\Phi_2 = \arg\big\{ie^{-i\frac{\theta^-}{2}}(1+\frac{p_x^- + E}{ip_y+\gamma})\sqrt{\frac{p_x^- - E}{-p_\gamma p_x^-}}\big\}. \tag{22}$$

The WKB asymptotic solution valid for $x > x_2$ which corresponds to (19) has to be written as follows

$$\psi = \frac{1}{\sqrt{p_x}}\Big(-id_1 e^{\frac{i}{h}S_p(x,x_2)-i\Phi_2}\sqrt{\frac{p_\gamma}{p_x+\xi}}\begin{pmatrix}1-\frac{p_x+\xi}{ip_y+\gamma}\\ 1+\frac{p_x+\xi}{ip_y+\gamma}\end{pmatrix}+$$

$$d_2 e^{-\frac{i}{h}S_p(x,x_2)-i\Phi_1}\sqrt{\frac{p_x+\xi}{p_\gamma}}\begin{pmatrix}1+\frac{p_x-\xi}{ip_y+\gamma}\\ 1+\frac{\xi-p_x}{ip_y+\gamma}\end{pmatrix}\Big). \tag{23}$$

Thus, taking into account (5), for the WKB solution to the effective Schrödinger equation (8) we obtain

$$W = \frac{1}{\sqrt{p_x}}\big(a_1 e^{\frac{i}{h}S_p(x,x_1)-i\Phi_1}\sqrt{\frac{-p_\gamma}{\xi+p_x}}+ia_2 e^{\frac{-i}{h}S_p(x,x_1)-i\Phi_2}\sqrt{\frac{\xi+p_x}{-p_\gamma}}\big)(1+O(h)), \tag{24}$$

for $x < x_1$ ($\xi < -p_\gamma$), then,

$$W = \frac{1}{\sqrt{p_x}}\big(-id_1 e^{\frac{i}{h}S_p(x,x_2)-i\Phi_2}\sqrt{\frac{p_\gamma}{\xi+p_x}}+d_2 e^{\frac{-i}{h}S_p(x,x_2)-i\Phi_1}\sqrt{\frac{\xi+p_x}{p_\gamma}}\big)(1+O(h)), \tag{25}$$

for $x > x_2$ ($\xi > p_\gamma$). All these asymptotic expansions break down at the turning points $x_{1,2}$.

According to [22], [23], we construct an asymptotic solution to (8), uniform with respect to p_γ by means of the comparison equation

$$h^2 y_{zz} + (h(\nu+\frac{1}{2}) - \frac{z^2}{4})y = 0. \tag{26}$$

By gluing this solution with (24) and (25), we derive the slope transfer matrix connecting $a_{1,2}$ and $d_{1,2}$. Thus, we seek a uniform asymptotic solution to (8) in the form

$$W = \sqrt{2}h^{\nu/2}\Big(\frac{\frac{z^2}{4}-a^2)}{q(x)}\Big)^{1/4}\Big(b_1 D_\nu(h^{-1/2}z) + b_2 D_{-\nu-1}(ih^{-1/2}z)\Big)(1+O(h)), \tag{27}$$

where solutions to (26)

$$y_{1,2}(z) = D_\nu(h^{-1/2}z),\ D_{-\nu-1}(ih^{-1/2}z)$$

are parabolic cylinder functions. According to the comparison equation method, after substitution of (27) into (8), we find that the function $z(x)$ is to be determined from the equation

$$z'^2(a^2 - \frac{z^2}{4}) = q(x), \tag{28}$$

where

$$a^2 = h(\nu+\frac{1}{2}),\ q(x) = \xi^2 - p_\gamma^2 + ihU' = q_0(x) + ihU', \tag{29}$$

and a or ν are to be determined later. From (28) for $x > x_2$ ($\xi > p_\gamma$) we have

$$i\int_{\bar{x}_2}^{x} \sqrt{q(t)}dt = \int_{2a}^{z} \sqrt{\frac{z^2}{4} - a^2}dz,$$

whereas for $x < x_1$ ($\xi < -p_\gamma$),

$$i\int_{x}^{\bar{x}_1} \sqrt{q(t)}dt = \int_{z}^{-2a} \sqrt{\frac{z^2}{4} - a^2}dz,$$

where $\bar{x}_{1,2}$ are complex roots of $q(x) = 0$. The branches of the complex functions $\sqrt{q(x)}$ and $\sqrt{z}$ are fixed by the following asymptotic expansions for $x >> x_2$ ($|z| \to \infty$)

$$\frac{i}{h}\int_{\bar{x}_2}^{x} \sqrt{q(t)}dt \sim \frac{z^2}{4h} - \frac{a^2}{h}\log z - \frac{a^2}{2h}(1 - \log a^2), \tag{30}$$

and $x << x_1$

$$\frac{i}{h}\int_{x}^{\bar{x}_1} \sqrt{q(t)}dt \sim \frac{z^2}{4h} - \frac{a^2}{h}\log(-z) - \frac{a^2}{2h}(1 - \log a^2). \tag{31}$$

From (28) we obtain

$$i\int_{\bar{x}_1}^{\bar{x}_2} \sqrt{-q(x)}dx = \int_{-2a}^{2a} \sqrt{a^2 - \frac{z^2}{4}}dz = \pi a^2. \tag{32}$$

On the other side, using the estimate

$$\frac{1}{h}\int_{\bar{x}_1}^{\bar{x}_2} \sqrt{-q(t)}dt = \frac{1}{h}\int_{x_1}^{x_2} \sqrt{-q_0(t)}dt - \frac{i\pi}{2} + O(h),$$

we have

$$\pi a^2 = \pi h(\frac{1}{2} + \nu) = i\int_{x_1}^{x_2} \sqrt{-q_0(x)}dx + \frac{\pi h}{2}. \tag{33}$$

Hence, ν is given by

$$\nu = \frac{iQ_1}{\pi h}, \tag{34}$$

where

$$Q_1 = \int_{x_1}^{x_2} \sqrt{-q_0(x)}dx. \tag{35}$$

The following estimates are very important when we glue the solution (27) with asymptotics (24) and (25). For $x >> x_2$ we have

$$\frac{i}{h}\int_{\bar{x}_2}^{x} \sqrt{q(t)}dt \sim \frac{i}{h}\int_{x_2}^{x} \sqrt{q_0(t)}dt - \frac{1}{2}\log\frac{2\xi}{p_\gamma} - \frac{1}{4} + \frac{1}{2}(1+\nu)\log\frac{\nu+1}{\nu}, \tag{36}$$

and for $x << x_1$

$$\frac{i}{h}\int\limits_{x}^{\bar{x}_1}\sqrt{q(t)}dt \sim \frac{i}{h}\int\limits_{x}^{x_1}\sqrt{q_0(t)}dt - \frac{1}{2}\log\frac{2\xi}{-p_\gamma} - \frac{1}{4} + \frac{1}{2}(1+\nu)\log\frac{\nu+1}{\nu}. \tag{37}$$

Then, after taking into account (30) and (31), it follows that for $x >> x_2$ ($|z| >> |a|$)

$$\frac{z^2}{4h} - \frac{a^2}{h}\log z \sim \frac{i}{h}\int\limits_{x_2}^{x}\sqrt{q_0(t)}dt - \frac{1}{2}\log\frac{2\xi}{p_\gamma} + \zeta, \tag{38}$$

and for $x << x_1$

$$\frac{z^2}{4h} - \frac{a^2}{h}\log(-z) \sim \frac{i}{h}\int\limits_{x}^{x_1}\sqrt{q_0(t)}dt - \frac{1}{2}\log\frac{2\xi}{-p_\gamma} + \zeta. \tag{39}$$

where

$$\zeta = \frac{a^2}{2h}(1-\log a^2) + \frac{1}{2}(\nu+\frac{1}{2})\log\frac{\nu+\frac{1}{2}}{\nu} - \frac{1}{4} = \frac{1}{2}(\nu+\frac{1}{2})(1-\log(h\nu)) - \frac{1}{4}.$$

In a case of linear potential with constant U' we may use the substitute

$$z = \sqrt{2U'}e^{i\pi/4}(x-a), \tag{40}$$

(see [25]). In this case equation (8) transforms exactly into (26). For a more general case of $U(x)$, considered as a perturbation of the case of linear potential, our z belongs to a finite neighbourhood of the complex plane based on the line (40), where $U' = U'(a)$ ($E = U(a)$). Thus, we assume that for large $|z|$ the asymptotic expansions of the parabolic cylinder functions in (27) is applied in a way similar to the case of the linear potential.

Using the asymptotic expansions of the parabolic cylinder functions for large argument (see the appendix C), we obtain for $x >> x_2$

$$W \sim \frac{z^{1/2}}{(\xi^2-p_y^2)^{1/4}}\Bigg(b_1 e^{-z^2/4h}z^\nu h^{-\nu/2} + \tag{41}$$

$$b_2[e^{z^2/4h-i\frac{\pi}{2}(\nu+1)}z^{-\nu-1}h^{\nu/2+1/2} + e^{-z^2/4h-i\pi\nu/2}z^\nu h^{-\nu/2}\frac{\sqrt{2\pi}}{\Gamma(\nu+1)}]\Bigg).$$

for $x << x_1$

$$W \sim \frac{(-z)^{1/2}}{(\xi^2-p_y^2)^{1/4}}\Bigg(b_1[e^{-z^2/4h}z^\nu h^{-\nu/2} - e^{z^2/4h-i\pi\nu}z^{-\nu-1}h^{\nu/2+1/2}\frac{\sqrt{2\pi}}{\Gamma(-\nu)}] + \tag{42}$$

$$b_2 e^{z^2/4h-i\frac{\pi}{2}(\nu+1)}z^{-\nu-1}h^{\nu/2+1/2}\Bigg),$$

where $\Gamma(z)$ is the Gamma function. Matching these two asymptotic expansions with the WKB asymptotics (24), (25), correspondingly, and using (38) and (39), leads to the following system

$$\left\{\begin{array}{rcl} a_1 e^{-i\Phi_1} & = & b_1(-1)^\nu e^{-\zeta}, \\ ia_2 e^{-i\Phi_2} & = & (-b_1 e^{-i\pi\nu}\frac{\sqrt{2\pi}}{\Gamma(-\nu)} + b_2 e^{-i\frac{\pi}{2}(\nu+1)})h^{\nu+1/2}(-1)^{-\nu-1}e^\zeta, \\ -id_1 e^{-i\Phi_2} & = & b_2 e^{\zeta-i\frac{\pi}{2}(\nu+1)}h^{\nu+1/2}, \\ d_2 e^{-i\Phi_1} & = & (b_1 + b_2 e^{-i\frac{\pi}{2}\nu}\frac{\sqrt{2\pi}}{\Gamma(\nu+1)})e^{-\zeta}. \end{array}\right. \tag{43}$$

Let us introduce new notation:

$$\mu_0 = -(-1)^{-\nu} = -e^{i\pi\nu} = -e^{-\frac{Q_1}{h}}, \tag{44}$$

$$\mu_1 = ie^{i\pi\nu+2\zeta}\frac{\sqrt{2\pi}}{\Gamma(-\nu)}h^{\nu+1/2},\ \mu_2 = -e^{-2\zeta}\frac{\sqrt{2\pi}}{\Gamma(1+\nu)}h^{-\nu-1/2}. \tag{45}$$

Then, the system (43) reads

$$\left\{\begin{array}{rcl} a_1e^{-i\Phi_1} & = & -b_1\frac{e^{-\zeta}}{\mu_0}, \\ ia_2e^{-i\Phi_2} & = & b_1\frac{i\mu_1}{\mu_0}e^{-\zeta} - ib_2e^{\zeta-i\frac{\pi}{2}\nu}h^{\nu+1/2}\mu_0, \\ -id_1e^{-i\Phi_2} & = & -ib_2e^{\zeta-i\frac{\pi}{2}\nu}h^{\nu+1/2}, \\ d_2e^{-i\Phi_1} & = & b_1e^{-\zeta} + b_2e^{\zeta+i\frac{\pi}{2}\nu}h^{\nu+1/2}\frac{\mu_2}{\mu_0}. \end{array}\right. \tag{46}$$

Now eliminating b_1 and b_2 from the system (46), we obtain the relations determining the transfer matrix T^L

$$\left\{\begin{array}{rcl} d_1 & = & -a_1e^{i\alpha}\frac{\mu_1}{\mu_0} - a_2\frac{1}{\mu_0}, \\ d_2 & = & -a_1(\mu_0 - \frac{\mu_1\mu_2}{\mu_0}) + e^{-i\alpha}a_2\frac{\mu_2}{\mu_0}, \end{array}\right. \tag{47}$$

that is

$$T^L_{11} = -e^{i\alpha}\frac{\mu_1}{\mu_0},\ T^L_{12} = -\frac{1}{\mu_0},\ T^L_{21} = -\mu_0 + \frac{\mu_1\mu_2}{\mu_0} = -\frac{1}{\mu_0},\ T^L_{22} = e^{-i\alpha}\frac{\mu_2}{\mu_0}, \tag{48}$$

where $\alpha = \Phi_2 - \Phi_1$. The expressions for μ_1 can be simplified as follows

$$\mu_1 = -i\nu\exp\big(i\pi\nu + (\nu+\frac{1}{2})(1-\log(h\nu)) - \frac{1}{2}\big)\frac{\sqrt{2\pi}}{\Gamma(1-\nu)}h^{\nu+1/2}$$

$$= -i\nu\exp\big(-\frac{Q_1}{2h} + i\frac{Q_1}{\pi h}(1-\log(\frac{Q_1}{\pi h})) - \frac{1}{2}\log\nu\big)\frac{\sqrt{2\pi}}{\Gamma(1-\nu)}.$$

Using the properties of the Gamma function (see [29])

$$|\Gamma(1\mp\nu)| = \sqrt{\frac{\pi\nu}{\sin(\pi\nu)}} = \sqrt{\frac{2Q_1}{h(e^{Q_1/h} - e^{-Q_1/h})}},$$

we derive

$$\mu_1 = e^{i\theta_1}\sqrt{1-e^{-2Q_1/h}}, \tag{49}$$

where

$$\theta_1 = \theta(Q_1) = \frac{Q_1}{\pi h}(1-\log(\frac{Q_1}{\pi h})) - \frac{\pi}{4} - \arg\Gamma(1-i\frac{Q_1}{\pi h}). \tag{50}$$

Similarly, taking into account that

$$\arg\Gamma(1+\nu) = -\arg\Gamma(1-\nu),$$

we obtain

$$\mu_2 = -e^{-i\theta_1}\sqrt{1-e^{-2Q_1/h}}. \tag{51}$$

Hence, the left slope transfer matrix reads

$$T^L(\alpha, Q_1) = \begin{pmatrix} -\frac{r_1}{t} & \frac{1}{t} \\ \frac{1}{t} & \frac{r_2}{t} \end{pmatrix} =$$

$$\begin{pmatrix} e^{i(\theta_1+\alpha)+Q_1/h}\sqrt{1-e^{-2Q_1/h}} & e^{\frac{Q_1}{h}} \\ e^{\frac{Q_1}{h}} & e^{-i(\theta_1+\alpha)+Q_1/h}\sqrt{1-e^{-2Q_1/h}} \end{pmatrix}. \tag{52}$$

It is clear that the transfer matrix for the left slope satisfies all the properties in Appendix A, namely

$$T^L_{22} = (T^L_{11})^*,\ T^L_{12} = (T^L_{21})^*,\ \det T_L = -1.$$

One can easily understand that the quantities $r_{1,2}$ mean the corresponding reflection coefficients, and t is the transmission coefficient.

It is worth remarking that due to the asymptotics as $x \to +\infty$

$$Im \log\left(\Gamma(-ix)\right) = \frac{\pi}{4} + x(1-\log x) + O(\frac{1}{x}),$$

if $\frac{Q_1}{h} \to +\infty$ (the turning points $\xi = \pm p_\gamma$ do not coalesce), we observe that

$$\arg\Gamma(1-i\frac{Q_1}{h\pi}) = \arg(-i\frac{Q_1}{h\pi}) + \arg\Gamma(-i\frac{Q_1}{h\pi}) = -\frac{\pi}{4} + \frac{Q_1}{h\pi}(1-\log\frac{Q_1}{h\pi}),$$

and, consequently from (50), we obtain that $\theta_1 \to 0$. Thus, up to small exponential errors the transfer matrix (52) coincides with the corresponding non-uniform (wrt p_γ) asymptotic representation (121) obtained in the Appendix D.

For the right slope, uniform asymptotics for the entries of the transfer matrix may be obtained similarly to the derivation of the non-uniform asymptotic result (124) in the Appendix D, namely,

$$T^R(\alpha, Q_2) = \begin{pmatrix} e^{i(\theta_2-\alpha)+Q_2/h}\sqrt{1-e^{-2Q_2/h}} & e^{\frac{Q_2}{h}} \\ e^{\frac{Q_2}{h}} & e^{-i(\theta_2-\alpha)+Q_2/h}\sqrt{1-e^{-2Q_2/h}} \end{pmatrix}. \tag{53}$$

5. WKB asymptotic solution for scattering through a smooth barrier

Consider a problem of scattering through the smooth barrier (see Fig. 1(a)) under assumption that $p_\gamma < E < U_0 - p_\gamma$ and all four turning points $x_i,\ i = 1,2,3,4$ are separated. In this case we have again 5 domains $\Omega_i,\ i = 1,2,...,5$ to describe 5 WKB forms of solution to leading order. From the point of view of physics of graphene, we observe incident, reflected and transmitted electronic states at $x < a$ and $x > b$, whereas under the barrier $a < x < b$ we have a hole state (n-p-n junction, see Fig. 1(a)).

We formulate the problem for scattering through the barrier for the transfer matrix T, connecting the coefficients $a_{1,2}$ of the asymptotics

$$\psi = e^{\frac{i}{h}S_p(x,x_1)}a_1e_1 + e^{-\frac{i}{h}S_p(x,x_1)}a_2e_2, \tag{54}$$

for $x < x_1$, and $d_{1,2}$ of the asymptotics

$$\psi = e^{\frac{i}{h}S_p(x,x_4)}d_1e_1 + e^{-\frac{i}{h}S_p(x,x_4)}d_2e_2, \tag{55}$$

for $x > x_4$, such that $d = Ta$, where $e_{1,2}$ are corresponding eigenvectors (see (21)). Taking into account the transfer matrices obtained for scattering through the left and right slopes of the barrier (T^L and T^R in (52), (53)), the total transfer matrix T may be obtained as the product

$$T = T^R\begin{pmatrix} e^{\frac{i}{h}P} & 0 \\ 0 & e^{-\frac{i}{h}P} \end{pmatrix}T^L, \tag{56}$$

where

$$P = \int\limits_{x_2}^{x_3} \sqrt{\left(U(x)-E\right)^2 - p_\gamma^2}dx.$$

Then, the entries of the matrix T read

$$T_{11}=e^{\frac{Q_1}{h}+\frac{Q_2}{h}}[s_1s_2e^{i(\theta_1+\theta_2+\frac{P}{h})}+e^{-i\frac{P}{h}}], \tag{57}$$

$$T_{22}=e^{\frac{Q_1}{h}+\frac{Q_2}{h}}[s_1s_2e^{-i(\theta_1+\theta_2+\frac{P}{h})}+e^{i\frac{P}{h}}], \tag{58}$$

$$T_{12}=e^{-i\alpha+\frac{Q_1}{h}+\frac{Q_2}{h}}[s_2e^{i(\theta_2+\frac{P}{h})}+s_1e^{-i(\theta_1+\frac{P}{h})}], \tag{59}$$

$$T_{21}=e^{i\alpha+\frac{Q_1}{h}+\frac{Q_2}{h}}[s_2e^{-i(\theta_2+\frac{P}{h})}+s_1e^{i(\theta_1+\frac{P}{h})}], \tag{60}$$

where

$$s_i=\sqrt{1-e^{-2Q_i/h}},\ i=1,2.$$

They satisfy the classical properties of a transfer matrix (see Appendix B)

$$T_{22}=T_{11}^*,\ T_{21}=T_{12}^*,\ \det T=1.$$

If $a_1=1,\ a_2=r_1,\ d_1=t_1,\ d_2=0$, then

$$t_1=\frac{1}{T_{22}},\ r_1=-\frac{T_{21}}{T_{22}},\ |t_1|^2+|r_1|^2=1.$$

If $a_1=0,\ a_2=t_2,\ d_1=r_2,\ d_2=1$, then

$$t_2=t_1=t,\ r_2=\frac{T_{12}}{T_{22}},\ |t_2|^2+|r_2|^2=1.$$

Correspondingly, the unitary scattering matrix, defined as

$$\begin{pmatrix} a_2\\ d_1\end{pmatrix}=\hat{S}\begin{pmatrix} a_1\\ d_2\end{pmatrix},$$

may be written as follows

$$\hat{S}=\begin{pmatrix} r_1 & t\\ t & r_2\end{pmatrix}.$$

The transmission coefficient is given by

$$t=\frac{1}{T_{22}}.$$

Total transmission takes place only for symmetric barrier when $Q_2=Q_1=Q$ $(\theta_2=\theta_1=\theta)$. Then, we have

$$t=e^{i\theta}\left(\cos{(\frac{P}{h}+\theta)}(2e^{\frac{2Q}{h}}-1)+i\sin{(\frac{P}{h}+\theta)}\right)^{-1}, \tag{61}$$

$$r_1=\frac{2\cos{(\frac{P}{h}+\theta)}e^{\frac{2Q}{h}+i(\theta+\alpha)}\sqrt{1-e^{-2Q/h}}}{\cos{(\frac{P}{h}+\theta)}(2e^{\frac{2Q}{h}}-1)+i\sin{(\frac{P}{h}+\theta)}}. \tag{62}$$

It is clear that if

$$P(E)+h\theta=h\pi(n+\frac{1}{2}),\ n=0,1,2,\dots, \tag{63}$$

than we have total transmission $|t|=1$.

It is worth noting that the formula for the transmission coefficient (61) was first obtained in [25] for a single layer of graphene without gap.

6. WKB asymptotic solution for complex resonant and real bound states localized within the smooth barrier

Consider a problem of resonant states localized within the smooth barrier (see Fig. 1). For the sake of simplicity consider the case of symmetric barrier, that is, $Q_1 = Q_2 = Q$, $\theta_1 = \theta_2 = \theta$. Now, let the turning points be $-x_2, -x_1, x_1, x_2$, and $0 < x_1 < x_2$. Again, when the energy of electron-hole is greater than the cut-off energy ($E > E_c = p_\gamma$), we have 5 domains $\Omega_i,\ i = 1, 2, ..., 5$ and 5 WKB forms of solution to leading order. To determine the correct radiation conditions as $x \to \pm\infty$ that are necessary for the localization, we present WKB solutions in the domains 1 and 5 in the form

$$\psi = e^{-\frac{i}{h}S_p(x,-x_2)}a_2 e_2,\ \ \psi = e^{\frac{i}{h}S_p(x,x_2)}d_1 e_1, \tag{64}$$

respectively, where $e_{1,2}$ are the corresponding eigenvectors (see (18) in section 4). If $a_1 = 0,\ d_2 = 0,\ a_2 \neq 0$, then

$$T_{22}(E) = 0, \tag{65}$$

and as a result we obtain a Bohr-Sommerfeld quantization condition for complex energy eigenlevels

$$h^{-1}P(E) + \theta + \frac{i}{2}\log\left(1 - e^{\frac{-2Q}{h}}\right) = \pi\left(n + \frac{1}{2}\right),\ \ n = 0, 1, 2, ..., N_1 \tag{66}$$

for $p_\gamma < E < U_0$. Solutions to this equation are complex resonances $E_n = Re(E_n) - i\Gamma_n$, where Γ_n^{-1} is the lifetime of the localized resonance. What is important is that the real part of these complex positive resonances decrease with n, thus showing off the anti-particle hole-like character of the localized modes. For these resonances we have $\Gamma_n > 0$. From (66), we obtain the important estimate

$$\Gamma_n = \frac{hw}{2\Delta t},\ \ w = -\log\left(1 - e^{-2Q/h}\right),\ \ \Delta t = -\left.\frac{dP}{dE}\right|_{E=E_n}. \tag{67}$$

This is the equivalent of the formula (14) in [17]. Namely, w is the transmission probability through the tunnelling strip, and Δt is the time interval between the turning points $-x_1$ and x_1. If $p_\gamma \to 0$, then $Q \to 0$, and $\Gamma_n \to +\infty$, that is opposite to [17] (to be exact, the estimate for Γ_n in [17] works only for linear potential when p_γ is not small).

For the second set for the bound states, when the energy of electron-hole is smaller than the cut-off energy ($E < p_\gamma$), we have 2 turning points $-x_1$ and x_1. Between them we have got oscillatory WKB solutions

$$\psi = e^{\frac{i}{h}S_p(x,-x_1)}\bar{d}_1 e_1 + e^{-\frac{i}{h}S_p(x,-x_1)}\bar{d}_2 e_2, \tag{68}$$

or

$$\psi = e^{\frac{i}{h}S_p(x,x_1)}\bar{a}_1 e_1 + e^{-\frac{i}{h}S_p(x,x_1)}\bar{a}_2 e_2, \tag{69}$$

and outside decaying

$$\psi = e^{\frac{1}{h}S_q(x,-x_1)}\bar{c}_2 l_2,\ \ x < -x_1,\ \ \psi = e^{-\frac{1}{h}S_q(x,x_1)}\bar{c}_1 l_1,\ \ x > x_1, \tag{70}$$

where $l_{1,2}$ are corresponding eigenvectors

$$l_{1,2} = \frac{\pm\frac{i}{2}\left(\arcsin\frac{\xi}{p_\gamma} - \frac{\pi}{2}\right)}{\sqrt{q_x}}\begin{pmatrix} 1 \mp \frac{iq_x \pm \xi}{\gamma + ip_y} \\ 1 \pm \frac{iq_x \pm \xi}{\gamma + ip_y} \end{pmatrix}.$$

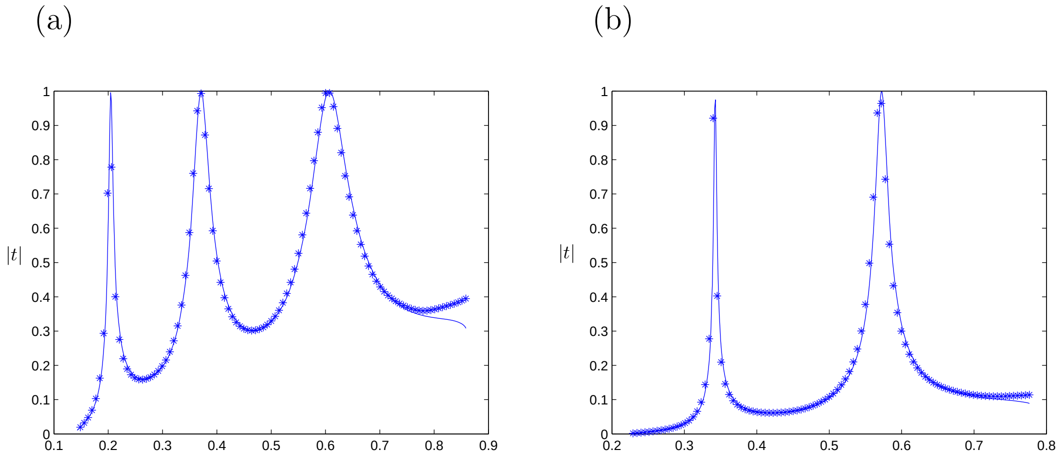

FIG. 2. The dependences of $|t(E)|$ are shown for $p_y = 0.1$ - a and $p_y = 0.2$ - b for the potential $U = 1/\cosh 2x$, and the other parameters are $h = 0.1$, $\gamma = 0.1$.

By gluing these WKB solutions through the two boundary layers near $-x_1$ and x_1 and using the techniques described in the Appendix D, we eliminate $\bar{a}_{1,2}$ and $\bar{d}_{1,2}$ and come to the homogeneous system

$$i\bar{c}_1 + \bar{c}_2 e^{\frac{i}{h}P} = 0,$$

$$i\bar{c}_1 - \bar{c}_2 e^{-\frac{i}{h}P} = 0.$$

Thus, we derive the Bohr-Sommerfeld quantization condition for real energy eigenlevels (bound states) inside the cut-off energy strip for $0 < E < p_\gamma$.

$$P(E) = h\pi(n + \frac{1}{2}), \;\; n = N_1 + 1, ...N_2. \tag{71}$$

7. Numerical results

In this section we illustrate the effectiveness of the semiclassical formulae for the transmission coefficients (61) and the energy spectrum obtained from Bohr-Sommerfeld quantization conditions (66) by comparing their data with the results obtained by means of the finite element method (COMSOL). All the computations were done for the symmetric barrier

$$U = \frac{1}{\cosh 2x}. \tag{72}$$

The other dimensionless parameters are $h = 0.1$, $\gamma = 0.1$. In Fig. 2a and 2b the dependences of $|t(E)|$ are shown for $p_y = 0.1$ and $p_y = 0.2$. One can see a very good agreement between semiclassical results and the data obtained by means of finite element method. In Fig. 2a there are 3 resonances of total transmission ($|t(E)| = 1$) that take place for $E = Re(E_{1,2,3})$ where $E_{1,2,3}$ are obtained from (66) and $E_1 = 0.607 - i0.035$, $E_2 = 0.371 - i0.016$, $E_3 = 0.205 - i0.0044$. In Fig. 2b there are only 2 resonances that take place for $E = Re(E_{1,2})$ and $E_1 = 0.572 - i0.01$, $E_2 = 0.343 - i0.002$. Note that $\Gamma_n = Im(E_n)$ decrease with n what is in complete agreement with the thickness of the resonances shown in Fig. 2a and 2b.

In Fig. 3 the real parts of E_n for the first seven eigenvalues of quasibound (shown in the triangular domain only) and the next six E_n for the bound states are computed

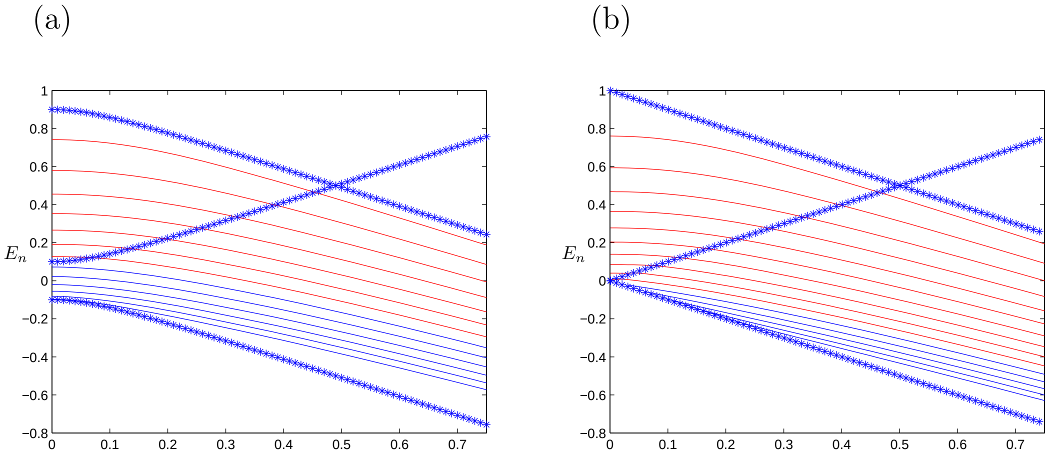

FIG. 3. The real parts of E_n for the first seven eigenvalues of quasibound (shown in the triangular domain only) and the next six E_n for the bound states are computed semiclassically with respect to p_y using Bohr-Sommerfeld quantization conditions (66) and (71) with mass gap $\gamma = 0.1$ - a and $\gamma = 0.0$ - b. The lines depicted with stars represent $E = \pm p_\gamma$ and $E = U_0 - p_\gamma$.

semiclassically for the symmetric barrier

$$U = \frac{1}{\cosh x} \tag{73}$$

with respect to p_y using Bohr-Sommerfeld quantization conditions (66) and (71) with mass gap $\gamma = 0.1$ and $\gamma = 0.0$. The structure of the energy eigenlevels has been deformed due to the presence of the mass gap. It is clearly seen that in the case of normal incidence $p_y = 0$ there are six bound states within the gap opposite to the gapless monolayer.

8. Appendix A. Transfer and scattering matrix properties for a smooth step

Let us come back to the scattering problem in terms of transfer matrix T (see [28]) for the left slope of the entire barrier formulated in (17). Taking into account the conservation of the x-component of the probability density current (see equation (8) in [24] or (18) in [25])

$$J_x = \bar{v}u + \bar{u}v, \tag{74}$$

we obtain that

$$|a_1|^2 - |a_2|^2 = |d_2|^2 - |d_1|^2. \tag{75}$$

Thus, for the slope transfer matrix T it holds that

$$\bar{T}_{21}T_{22} - \bar{T}_{11}T_{12} = 0,\ |T_{21}|^2 - |T_{11}|^2 = 1,\ |T_{22}|^2 - |T_{12}|^2 = -1, \tag{76}$$

or

$$T^{+}\begin{pmatrix} -1 & 0 \\ 0 & 1 \end{pmatrix} T = \begin{pmatrix} 1 & 0 \\ 0 & -1 \end{pmatrix}. \tag{77}$$

As a result we have $|T_{11}| = |T_{22}|$, $|T_{12}| = |T_{21}|$, $|det(T)| = 1$. For the scattering matrix

$$S = \begin{pmatrix} S_{11} & S_{12} \\ S_{21} & S_{22} \end{pmatrix} \tag{78}$$

we have

$$S\begin{pmatrix} a_1 \\ d_1 \end{pmatrix} = \begin{pmatrix} a_2 \\ d_2 \end{pmatrix}, \tag{79}$$

and

$$|a_1|^2 + |d_1|^2 = |a_2|^2 + |d_2|^2. \tag{80}$$

From (80) we obtain that

$$S^+ S = S S^+ = I, \tag{81}$$

thus, the scattering matrix is unitary. If entries of S are known, than,

$$T = \begin{pmatrix} -S_{11}/S_{12} & 1/S_{12} \\ S_{21} - S_{11}S_{22}/S_{12} & S_{22}/S_{12} \end{pmatrix}, \ det(T) = -S_{21}/S_{12}. \tag{82}$$

Time-reversal symmetry in scattering through the graphene barrier would mean that

$$(\sigma_3 \psi)^* = e^{-\frac{i}{h} p_x^- x} a_1^* e_2^- + e^{\frac{i}{h} p_x^-} a_2^* e_1^-, \ x \in \Omega_1, \tag{83}$$

$$(\sigma_3 \psi)^* = e^{-\frac{i}{h} p_x^+} d_1^* e_2^+ + e^{\frac{i}{h} p_x^+} d_2^* e_1^+, \ x \in \Omega_3, \tag{84}$$

where

$$\sigma_3 = \begin{pmatrix} 1 & 0 \\ 0 & -1 \end{pmatrix},$$

are both asymptotic solutions to the Dirac system. Thus, we have

$$S \begin{pmatrix} a_2^* \\ d_2^* \end{pmatrix} = \begin{pmatrix} a_1^* \\ d_1^* \end{pmatrix}, \tag{85}$$

$$T \begin{pmatrix} a_2^* \\ a_1^* \end{pmatrix} = \begin{pmatrix} d_2^* \\ d_1^* \end{pmatrix}. \tag{86}$$

In what follows that

$$S = S^T, \ \begin{pmatrix} 0 & 1 \\ 1 & 0 \end{pmatrix} T \begin{pmatrix} 0 & 1 \\ 1 & 0 \end{pmatrix} = T^*. \tag{87}$$

Thus, $S_{12} = S_{21}$,

$$detT = -1, \tag{88}$$

and

$$T = \begin{pmatrix} T_{11} & T_{12} \\ T_{12}^* & T_{11}^* \end{pmatrix}. \tag{89}$$

If $a_1 = 1, \ a_2 = r_1, \ d_1 = 0, \ d_2 = t_1$, then

$$t_1 = \frac{1}{T_{12}^L}, \ r_1 = -\frac{T_{11}^L}{T_{12}^L}, \ |r_1|^2 + |t_1|^2 = 1. \tag{90}$$

If $a_1 = 0, \ a_2 = t_2, \ d_1 = 1, \ d_2 = r_2$, then

$$t_2 = \frac{1}{T_{12}^L}, \ r_2 = \frac{T_{22}^L}{T_{12}^L}, \ |r_2|^2 + |t_2|^2 = 1. \tag{91}$$

9. Appendix B. Transfer and scattering matrix properties for a smooth barrier

Let us formulate this scattering problem in terms of transfer matrix T for the entire barrier (see (54), (55), $Ta = d$). However, for the barrier we have

$$|a_1|^2 - |a_2|^2 = |d_1|^2 - |d_2|^2, \tag{92}$$

and

$$T^+ \begin{pmatrix} 1 & 0 \\ 0 & -1 \end{pmatrix} T = \begin{pmatrix} 1 & 0 \\ 0 & -1 \end{pmatrix}. \tag{93}$$

For the scattering matrix S we have

$$S \begin{pmatrix} a_1 \\ d_2 \end{pmatrix} = \begin{pmatrix} a_2 \\ d_1 \end{pmatrix}, \tag{94}$$

and

$$|a_1|^2 + |d_2|^2 = |a_2|^2 + |d_1|^2. \tag{95}$$

From (95) we obtain that

$$S^+ S = S S^+ = I. \tag{96}$$

If entries of S are known, than,

$$T = \begin{pmatrix} S_{21} - S_{11} S_{22}/S_{12} & S_{22}/S_{12} \\ -S_{11}/S_{12} & 1/S_{12} \end{pmatrix}, \; det(T) = S_{21}/S_{12}. \tag{97}$$

Taking into account the time-reversal symmetry in scattering through the graphene barrier, we obtain $S = S^T$, and

$$T = \begin{pmatrix} T_{11} & T_{12} \\ T_{12}^* & T_{11}^* \end{pmatrix}, \; det T = 1. \tag{98}$$

10. Appendix C

For the equation (8) (effective Schrödinger equation)

$$h^2 W'' + (\xi^2 - p_\gamma^2 + ihU')W = 0, \tag{99}$$

we shall have

$$W = \frac{1}{\sqrt{p_x}} \big(a_1 e^{\frac{i}{h} S_p(x,x_1) - i\Phi_1} \sqrt{\frac{-p_\gamma}{\xi + p_x}} + i a_2 e^{\frac{-i}{h} S_p(x,x_1) - i\Phi_2} \sqrt{\frac{\xi + p_x}{-p_\gamma}} \big)(1 + O(h)), \tag{100}$$

for $x < x_1$ ($\xi < -p_\gamma$), then,

$$W = \frac{1}{\sqrt{q_x}} \big(c_1 e^{-\frac{1}{h} S_q(x,x_1)} e^{\frac{i}{2}(\arcsin\frac{\xi}{p_\gamma} + \frac{\pi}{2})} + c_2 e^{\frac{1}{h} S_q(x,x_1)} e^{-\frac{i}{2}(\arcsin\frac{\xi}{p_\gamma} + \frac{\pi}{2})} \big)(1 + O(h)), \tag{101}$$

for $x_1 < x < x_2$ ($-p_\gamma < \xi < p_\gamma$), and

$$\frac{1}{\sqrt{p_x}} \big(- i d_1 e^{\frac{i}{h} S_p(x,x_2) - i\Phi_2} \sqrt{\frac{p_\gamma}{\xi + p_x}} + d_2 e^{\frac{-i}{h} S_p(x,x_2) - i\Phi_1} \sqrt{\frac{\xi + p_x}{p_\gamma}} \big)(1 + O(h)), \tag{102}$$

for $x > x_2$ ($\xi > p_\gamma$).

To leading order, the uniform asymptotic representation within the neighbourhood of x_1 is given by (see ([23], chapter 4, section 3.3))

$$W = h^{-1/6} \sqrt{\frac{\pi}{z'}} \cosh\mu_1 \Big(b_1^{(1)} Ai(h^{-2/3} z) + b_2^{(1)} Bi(h^{-2/3} z) \Big) + \tag{103}$$

$$+ih^{1/6}\sqrt{\frac{\pi}{-zz'}}\sinh\mu_1\Big(b_1^{(1)}Ai'(h^{-2/3}z)+b_2^{(1)}Bi'(h^{-2/3}z)\Big),$$

for $x \leqslant x_1$ ($\xi \leqslant -p_\gamma$), and

$$W = h^{-1/6}\sqrt{\frac{\pi}{z'}}\cos\nu_1\Big(b_1^{(1)}Ai(h^{-2/3}z)+b_2^{(1)}Bi(h^{-2/3}z)\Big)+ \tag{104}$$

$$-ih^{1/6}\sqrt{\frac{\pi}{zz'}}\sin\nu_1\Big(b_1^{(1)}Ai'(h^{-2/3}z)+b_2^{(1)}Bi'(h^{-2/3}z)\Big),$$

for $x \geqslant x_1$ ($\xi \geqslant -p_\gamma$). Here we have introduced

$$z = -\Big(\frac{3}{2}\int_x^{x_1} p_x dx'\Big)^{2/3} < 0,\ x \leqslant x_1\ (\xi \leqslant -p_\gamma), \tag{105}$$

$$z = \Big(\frac{3}{2}\int_{x_1}^{x} p_x dx'\Big)^{2/3} > 0,\ x \geqslant x_1\ (\xi \geqslant -p_\gamma), \tag{106}$$

$$\mu_1 = \log\sqrt{\frac{\xi+p_x}{-p_\gamma}},\ \nu_1 = \frac{1}{2}(\arcsin\frac{\xi}{p_\gamma}+\frac{\pi}{2}). \tag{107}$$

Note that for this neighbourhood $z'(x) > 0$. According to ([23], chapter 4, section 3.3), the functions $A_0 = \cosh\mu_1$, $B_0 = -\sinh\mu_1$ are the solutions to the following systems for $x \leqslant x_1$ ($\xi \leqslant -p_\gamma$),

$$\begin{aligned}&2z'\sqrt{-z}B_0' + A_0 = 0,\\&2z'\sqrt{-z}A_0' + B_0 = 0,\end{aligned} \tag{108}$$

where

$$z'\sqrt{-z} = p_x.$$

For $x \geqslant x_1$ ($\xi \geqslant -p_\gamma$), $A_0 = \cos\nu_1$, $B_0 = -i\sin\nu_1$ are the solutions to

$$\begin{aligned}&2z'\sqrt{z}B_0' + iA_0 = 0,\\&2z'\sqrt{z}A_0' + iB_0 = 0,\end{aligned} \tag{109}$$

where

$$z'\sqrt{z} = q_x.$$

To leading order, the uniform asymptotic representation within the neighbourhood of x_2 is similarly given by

$$W = h^{-1/6}\sqrt{\frac{\pi}{|z'|}}\cosh\mu_2\Big(b_1^{(2)}Ai(h^{-2/3}z)+b_2^{(2)}Bi(h^{-2/3}z)\Big)+ \tag{110}$$

$$-ih^{1/6}\sqrt{\frac{\pi}{-z|z'|}}\sinh\mu_2\Big(b_1^{(2)}Ai'(h^{-2/3}z)+b_2^{(2)}Bi'(h^{-2/3}z)\Big),$$

for $x \geqslant x_2$ ($\xi \geqslant p_\gamma$), and

$$W = h^{-1/6}\sqrt{\frac{\pi}{|z'|}}\cos\nu_2\Big(b_1^{(2)}Ai(h^{-2/3}z)+b_2^{(2)}Bi(h^{-2/3}z)\Big)+ \tag{111}$$

$$ih^{1/6}\sqrt{\frac{\pi}{z|z'|}}\sin\nu_2\Big(b_1^{(2)}Ai'(h^{-2/3}z)+b_2^{(2)}Bi'(h^{-2/3}z)\Big),$$

for $x \leqslant x_2$ $(\xi \leqslant p_\gamma)$. Here we have introduced

$$z = -\left(\frac{3}{2}\int\limits_{x_2}^{x} p_x dx'\right)^{2/3} < 0, \; x \geqslant x_2 \; (\xi \geqslant p_\gamma), \tag{112}$$

$$z = \left(\frac{3}{2}\int\limits_{x}^{x_1} p_x dx'\right)^{2/3} > 0, \; x \leqslant x_2 \; (\xi \leqslant p_\gamma), \tag{113}$$

$$\mu_2 = \log\sqrt{\frac{\xi + p_x}{p_\gamma}}, \; \nu_2 = \frac{1}{2}(\arcsin\frac{\xi}{p_\gamma} - \frac{\pi}{2}). \tag{114}$$

Note that for this neighbourhood $z'(x) < 0$. According to ([23], chapter 4, section 3.3), the functions $A_0 = \cosh\mu_2$, $B_0 = \sinh\mu_1$ are the solutions to the systems (108) for $x \geqslant x_2$ $(\xi \geqslant p_\gamma)$, where

$$-z'\sqrt{-z} = p_x.$$

For $x \leqslant x_2$ $(\xi \leqslant p_\gamma)$, $A_0 = \cos\nu_2$, $B_0 = i\sin\nu_2$ are the solutions to (109) with

$$-z'\sqrt{z} = q_x.$$

Now, using the asymptotic expansions of the Airy functions $Ai(x)$ and $Bi(x)$ (see Appendix C) and matching the uniform asymptotic expansions (103) and (104) within the neighbourhood of x_1 with WKB asymptotics (100) for $x \ll x_1$, we obtain

$$a_1 e^{-i\Phi_1} = \frac{1}{2}(b_1^{(1)} e^{i\pi/4} + b_2^{(1)} e^{-i\pi/4}), \tag{115}$$

$$ia_2 e^{-i\Phi_2} = \frac{1}{2}(b_1^{(1)} e^{-i\pi/4} + b_2^{(1)} e^{i\pi/4}). \tag{116}$$

Matching the uniform asymptotic expansions (103) and (104) within the neighbourhood of x_1 with WKB asymptotics (101) for $x \gg x_1$, we obtain

$$e^{i\pi/4} c_1 = \frac{1}{2} b_1^{(1)} e^{i\pi/4}, \; e^{-i\pi/4} c_2 = \frac{1}{2} b_2^{(1)} e^{-i\pi/4}. \tag{117}$$

Matching the uniform asymptotic expansions (110) and (111) within the neighbourhood of x_2 with WKB asymptotics (101) for $x \ll x_2$, we obtain

$$e^{-Q_1/h + i\pi/2} c_1 = b_2^{(2)}, \; 2e^{Q_1/h - i\pi/2} c_2 = b_1^{(2)}, \tag{118}$$

where

$$Q_1 = \int\limits_{x_1}^{x_2} q_x(x) dx.$$

Matching the uniform asymptotic expansions (110) and (111) within the neighbourhood of x_2 with WKB asymptotics (102) for $x \gg x_2$, we obtain

$$-id_1 e^{-i\Phi_3} = \frac{1}{2}(b_1^{(2)} e^{-i\pi/4} + b_2^{(2)} e^{i\pi/4}), \tag{119}$$

$$d_2 e^{-i\Phi_4} = \frac{1}{2}(b_1^{(2)} e^{i\pi/4} + b_2^{(2)} e^{-i\pi/4}). \tag{120}$$

Now we derive the entries of the transfer matrix T^L connecting d and a

$$T^L(\alpha, Q_1) = \begin{pmatrix} e^{i\alpha}(e^{\frac{Q_1}{h}} - \frac{e^{-\frac{Q_1}{h}}}{4}) & e^{\frac{Q_1}{h}} + \frac{e^{-\frac{Q_1}{h}}}{4} \\ e^{\frac{Q_1}{h}} + \frac{e^{-\frac{Q_1}{h}}}{4} & e^{-i\alpha}(e^{\frac{Q_1}{h}} - \frac{e^{-\frac{Q_1}{h}}}{4}) \end{pmatrix}, \tag{121}$$

where $\alpha = \Phi_2 - \Phi_1$. It is clear that the transfer matrix for the left slope satisfies all the properties (75)-(91).

For the right slope we have the following scattering problem

$$W = \frac{1}{\sqrt{p_x}}\big(-ia_1 e^{\frac{i}{h}S_p(x,x_3)-i\Phi_2}\sqrt{\frac{p_\gamma}{\xi+p_x}} + a_2 e^{\frac{-i}{h}S_p(x,x_3)-i\Phi_1}\sqrt{\frac{\xi+p_x}{p_\gamma}}\,\big)(1+O(h)), \qquad (122)$$

for $x < x_3$ ($\xi > p_\gamma$), and

$$W = \frac{1}{\sqrt{p_x}}\big(d_1 e^{\frac{i}{h}S_p(x,x_4)-i\Phi_1}\sqrt{\frac{-p_\gamma}{\xi+p_x}} + id_2 e^{\frac{-i}{h}S_p(x,x_2)-i\Phi_2}\sqrt{\frac{\xi+p_x}{-p_\gamma}}\,\big)(1+O(h)), \qquad (123)$$

for $x > x_4$ ($\xi < -p_\gamma$). By performing complex conjugation for (122), (123), and using (24), (25) and (121), derived for the left slope, we obtain

$$\begin{pmatrix} -a_1^* e^{i\Phi_2} \\ a_2^* e^{i\Phi_1} \end{pmatrix} = T^L(\alpha, Q_2) \begin{pmatrix} d_1^* e^{i\Phi_1} \\ -d_2^* e^{i\Phi_2} \end{pmatrix},$$

and thus, we have $d = T^R a$ with

$$T^R(\alpha, Q_2) = \begin{pmatrix} e^{-i\alpha}(e^{\frac{Q_2}{h}} - \frac{e^{-\frac{Q_2}{h}}}{4}) & e^{\frac{Q_2}{h}} + \frac{e^{-\frac{Q_2}{h}}}{4} \\ e^{\frac{Q_2}{h}} + \frac{e^{-\frac{Q_2}{h}}}{4} & e^{i\alpha}(e^{\frac{Q_2}{h}} - \frac{e^{-\frac{Q_2}{h}}}{4}) \end{pmatrix}, \qquad (124)$$

where

$$Q_2 = \int_{x_3}^{x_4} q_x(x)dx.$$

11. Conclusion

Semiclassical analysis of Dirac electron with mass gap tunnelling through a smooth Gaussian shape barrier representing an electrostatic potential in the ballistic regime has been presented. The corresponding 1D scattering problem is formulated in terms of a transfer matrix and treated in the WKB (adiabatic) approximation. For skew electron incidence the WKB approximation deals with the asymptotic analysis of matched asymptotic techniques and boundary layers for four turning points. Scattering through a smooth barrier in graphene resembles scattering through a double barrier for 1D Schrödinger operator, i.e. a 1D Fabry-Perot resonator. The main results of the paper are WKB formulas for the entries of the transfer matrix. They explain the mechanism of total transmission of a Dirac electron in graphene with mass gap through a smooth barrier for some resonance values of the energy of skew incident electrons. Moreover, we have showed the existence of modes localized within the barrier and exponentially decaying away from it for two discrete complex and real sets of energy eigenlevels determined by a Bohr-Sommerfeld quantization condition. It has been shown that total transmission through the barrier takes place when the energy of the incident electron coincides with the real part of one of the complex energy eigenlevels. These facts have been confirmed by numerical simulations performed using the finite element method (COMSOL). It is necessary to note that some of the details of the comparison equation method of WKB analysis used in the paper require more rigorous treatment. These part of the work along with further detailed discussion on other scattering regimes through the barrier will be carried on in future publications.

Acknowledgments

The authors would like to thank Prof S.Yu. Dobrokhotov, Prof J. Ferapontov, Prof F. Kusmartsev, Dr D. Maksimov and Dr A.Vagov for constructive discussions and valuable remarks.

References

[1] A. K. Geim and K. S. Novoselov. The rise of graphene. Nature Mater. **6**, 183, 2007.

[2] M. I. Katsnelson. Graphene: carbon in two dimensions. Mater. Today, 10:20, 2007.

[3] M. I. Katsnelson, K. S. Novoselov, and A. K. Geim. Chiral tunnelling and the Klein paradox in graphene. Nature Physics, **2**, 620, 2006.

[4] Castro Neto, A.H., Guinea, F., Peres, N.M.R., Geim, A.K., and Novoselov, K.S. The electronic properties of graphene. Rev. Mod. Phys. **81**, Jan-March, 109-162, 2009.

[5] C. W. J. Beenakker. Colloquium: Andreev reflection and Klein tunnelling in graphene. Rev. Mod. Phys, 80:1337, 2008.

[6] A. K. Geim. Graphene: Status and prospects. Science, 324:1530, 2009.

[7] N. M. R. Peres. Colloquium: The transport properties of graphene: An introduction. Rev. Mod. Phys, 82:2673, 2010.

[8] M. A. H. Vozmediano, M. I. Katsnelson, and F. Guinea. Gauge fields in graphene. Phys. Rep., 496:109, 2010.

[9] Semenoff G.W. Condensed-matter simulation of the three-dimensional anomaly. PRL **53**, 26 (1984).

[10] O. Klein. Die Reflexion von Elektronen an einem Potentialsprung nach der relativistischen Dynamik von Dirac. Z. Phys, 53:157-165, 1929.

[11] A. Calogeracos and N. Dombey. History and physics of the Klein paradox. Contemp. Phys., 40:313, 1999.

[12] N. Dombey and A. Calogeracos. Seventy years of the Klein paradox. Phys. Rep., 315:41, 1999.

[13] S. V. Vonsovsky and M. S. Svirsky. The Klein paradox and the Zitterbewegung of an electron in a field with a constant scalar potential. Uspekhi Fiz. Nauk, 163(5):115, 1993.

[14] R.-K. Su, G. G. Siu, and X. Chou. Barrier penetration and Klein paradox. J. Phys. A, 26:1001, 1993.

[15] Cheianov, V.V., Fal'ko, V.I. Selective transmission of Dirac electrons and ballistic magnetoresistance of n-p junctions in graphene. Phys.Rev. B. **74**, 041403(R), 2006.

[16] Fistul, M.V., Efetov, K.B. Electromagnetic-Field-Induced Suppression of Transport through n-p Junctions in Graphene. PRL **98**, 256803, 2007.

[17] Silvestrov, P.G., Efetov, K.B. Quantum dots in graphene. PRL **98**, 016802, 2007.

[18] Datta, S., 1995 *Electronic transport in mesoscopic systems*, Cambridge University Press, Cambridge.

[19] Mello, P. A., Kumar, N., 2004 *Quantum Transport in Mesoscopic systems*, Oxford University Press, New York.

[20] Stockmann, H. J., 2000, *Quantum Chaos. An Introduction*, Cambridge University Press, Cambridge.

[21] K. S. Novoselov *et al.*. Electric Field Effect in Atomically Thin Carbon Films. Science. **306**, 666, 2004.

[22] F. W. J. Olver. *Asymptotics and Special Functions*, Academic Press, 1974.

[23] M. V. Fedoryuk. *Asymptotic Analysis: Linear Ordinary Differential Equations.* Springer, 1993.

[24] Sonin, E.B. Effect of Klein tunneling on conductance and shot noise in ballistic graphene. Phys.Rev. B. **79**, 195438, 2009.

[25] Tudorovskiy, T., Reijnders, K.J.A., Katsnelson, M.I. Chiral tunneling in single-layer and bilayer graphene. Phys. Scr. **T146**, 014010, 17pp, 2012.

[26] Pereira, J.M., Mlinar, Jr.V., Peeters, F.M., Vasilopoulos, P. Confined states and direction-dependent transmission in graphene quantum wells. Phys.Rev. B. **74**, 045424, 2006.

[27] V. Zalipaev, D.Maximov, C.M.Linton and F.V.Kusmartsev. Quantum states localized in a smooth potential barrier on single layer graphene. Phys. Let. A, **377**, 216-221, 2012.

[28] P. Markos and C Soukoulis. Wave Propagation. From electrons to photonic crystals and left-handed materials. Priceton University Press, 2008.

[29] M. Abramowitz and I. Stegun, editors. *Handbook on Mathematical Functions with Formulas, Graphs, and Mathematical Tables.* Dover, New York, 1965. Chapter 19 on parabolic cylinder functions.

[30] The Wolfram special functions site: http://functions.wolfram.com/Hypergeometrical Functions/Parabolic CylinderD/.

NANOSYSTEMS: PHYSICS, CHEMISTRY, MATHEMATICS, 2013, 4 (6), P. 747–759

WEYL FUNCTION FOR SUM OF OPERATORS TENSOR PRODUCTS

A. A. Boitsev[1], H. Neidhardt[2], I. Yu. Popov[1]

[1]Saint Petersburg National Research University of Information Technologies, Mechanics and Optics, 49 Kronverkskiy, Saint Petersburg, 197101, Russia

[2]Weierstrass Institute for Applied Analysis and Stochastic, Berlin, Germany

boitsevanton@gmail.com, hagen.neidhardt@wias-berlin.de, popov1955@gmail.com

PACS 03.65 Nk

The boundary triplets approach is applied to the construction of self-adjoint extensions of the operator having the form $S = A \otimes I_T + I_A \otimes T$ where the operator A is symmetric and the operator T is bounded and self-adjoint. The formula for the γ-field and the Weyl function corresponding the the boundary triplet Π_S is obtained in terms of the γ-field and the Weyl function corresponding to the boundary triplet Π_A.

Keywords: operator extension, Weyl function, boundary triplet.

1. Introduction

The spectral theory of differential operators is very important for mathematics and has many applications in quantum physics (see, e.g., [1]. The theory of self-adjoint operators and especially of self-adjoint extensions of symmetric operators occupies a special place in the operator theory [2]. In many interesting problems of quantum physics (like the interaction of photons with electrons) the operators take on the form of the sum of tensor products [3], [4]. From general position, the extensions are usually described in terms of so-called boundary triplets [5]. Up to now, there is no boundary triplets method for obtaining all self-adjoint extensions of such an operator.

In particular, we consider a closed densely defined symmetric operator

$$S = A \otimes I_T + I_A \otimes T \tag{1.1}$$

where A is a closed densely defined symmetric operator on the separable Hilbert space $\mathfrak{H}_A$ and T is a bounded self-adjoint operator acting on the separable infinite dimensional Hilbert space $\mathfrak{H}_T$. Notice that the deficiency indices of S are infinite even if A has finite deficiency indices.

Our aim is to describe all self-adjoint extensions of S using the boundary triplet approach. More precisely, assuming that $\Pi_A = \{\mathcal{H}_A, \Gamma_0^A, \Gamma_1^A\}$ is a boundary triplet for A^* we construct a boundary triplet $\Pi_S = \{\mathcal{H}_S, \Gamma_0^S, \Gamma_1^S\}$ for S^*. In addition, using the γ-field $\gamma_A(\cdot)$ and the Weyl function $M_A(\cdot)$ of the boundary triplet Π_A we express the γ-field $\gamma_S(\cdot)$ and Weyl function $M_S(\cdot)$ of Π_S.

The present note generalizes results of [6]. In [6] on the Hilbert space $\mathfrak{H} = L^2(\mathbb{R}_+, \mathcal{H})$ the operator

$$\begin{gathered}(Sf)(x) = -\frac{d^2}{dt^2} f(t) + Tf(t),\\ f \in \mathrm{dom}\,(S) := \{f \in W^{2,2}(\mathbb{R}_+, \mathcal{H}) : f(0) = f'(0) = 0\}.\end{gathered} \tag{1.2}$$

was considered where T is a bounded self-adjoint operator. One easily checks that the operator (1.2) has the form (1.1) where A acts on $L^2(\mathbb{R}_+)$ and is given by

$$(Af)(t) = -\frac{d^2}{dt^2}f(t), \quad f \in \mathrm{dom}\,(A) := \{W^{2,2}(\mathbb{R}_+) : f(0) = f'(0) = 0\}.$$

In [6] it was verified that $\Pi_S = \{\mathcal{H}, \Gamma_0, \Gamma_1\}$

$$\Gamma_0 f := f(0), \quad \Gamma_1 f = f'(0), \quad f \in \mathrm{dom}\,(S^*) = W^{2,2}(\mathbb{R}_+, \mathcal{H}).$$

defines a boundary triplet for S^*. The corresponding Weyl function is given by $M_S(z) = i\sqrt{z - T}$, $z \in \mathbb{C}_\pm$.

Notation. Let $\mathfrak{H}$ and $\mathcal{H}$ be separable Hilbert spaces. The set of bounded linear operators from $\mathfrak{H}_1$ to $\mathfrak{H}_2$ is denoted by $[\mathfrak{H}_1, \mathfrak{H}_2]$; $[\mathfrak{H}] := [\mathfrak{H}, \mathfrak{H}]$. By $\mathfrak{S}_p(\mathfrak{H})$, $p \in (0, \infty]$, we denote the Schatten-v.Neumann ideals of compact operators on $\mathfrak{H}$; in particular, $\mathfrak{S}_\infty(\mathfrak{H})$ denotes the ideal of compact operators in $\mathfrak{H}$.

By $\mathrm{dom}\,(T)$, $\mathrm{ran}\,(T)$ and $\sigma(T)$ we denote the domain, range and spectrum of the operator T, respectively. The symbols $\sigma_p(\cdot)$, $\sigma_c(\cdot)$ and $\sigma_r(\cdot)$ stand for the point, continuous and residual spectrum of a linear operator. Recall that $z \in \sigma_c(H)$ if $\ker\,(H - z) = \{0\}$ and $\mathrm{ran}\,(H - z) \neq \overline{\mathrm{ran}\,(H - z)} = \mathfrak{H}$; $z \in \sigma_r(H)$ if $\ker\,(H - z) = \{0\}$ and $\overline{\mathrm{ran}\,(H - z)} \neq \mathfrak{H}$.

2. Preliminaries

2.1. Linear relations

A linear relation Θ in $\mathcal{H}$ is a closed linear subspace of $\mathcal{H} \oplus \mathcal{H}$. The set of all linear relations in $\mathcal{H}$ is denoted by $\widetilde{\mathcal{C}}(\mathcal{H})$. Denote also by $\mathcal{C}(\mathcal{H})$ the set of all closed linear (not necessarily densely defined) operators in $\mathcal{H}$. Identifying each operator $T \in \mathcal{C}(\mathcal{H})$ with its graph $\mathrm{gr}\,(T)$ we regard $\mathcal{C}(\mathcal{H})$ as a subset of $\widetilde{\mathcal{C}}(\mathcal{H})$.

The role of the set $\widetilde{\mathcal{C}}(\mathcal{H})$ in extension theory becomes clear from Proposition 2.3. However, its role in the operator theory is substantially motivated by the following circumstances: in contrast to $\mathcal{C}(\mathcal{H})$, the set $\widetilde{\mathcal{C}}(\mathcal{H})$ is closed with respect to taking inverse and adjoint relations Θ^{-1} and Θ^*. The latter are given by: $\Theta^{-1} = \{\{g, f\} : \{f, g\} \in \Theta\}$ and

$$\Theta^* = \left\{ \begin{pmatrix} k \\ k' \end{pmatrix} : (h', k) = (h, k') \text{ for all } \begin{pmatrix} h \\ h' \end{pmatrix} \in \Theta \right\}.$$

A linear relation Θ is called symmetric if $\Theta \subset \Theta^*$ and self-adjoint if $\Theta = \Theta^*$.

2.2. Boundary triplets and proper extensions

Let us briefly recall some basic facts regarding boundary triplets. Let S be a densely defined closed symmetric operator with equal deficiency indices $n_\pm(S) := \dim(\mathfrak{N}_{\pm\mathrm{i}})$, $\mathfrak{N}_z := \ker\,(S^* - z)$, $z \in \mathbb{C}_\pm$, acting on some separable Hilbert space $\mathfrak{H}$.

Definition 2.1.
(i) *A closed extension $\widetilde{S}$ of S is called proper if* $\mathrm{dom}\,(S) \subset \mathrm{dom}\,(\widetilde{S}) \subset \mathrm{dom}\,(S^*)$.
(ii) *Two proper extensions $\widetilde{S}'$, $\widetilde{S}$ are called disjoint if* $\mathrm{dom}\,(\widetilde{S}') \cap \mathrm{dom}\,(\widetilde{S}) = \mathrm{dom}\,(S)$ *and transversal if in addition* $\mathrm{dom}\,(\widetilde{S}') + \mathrm{dom}\,(\widetilde{S}) = \mathrm{dom}\,(S^*)$.

We denote by Ext_S the set of all proper extensions of S completed by the non-proper extensions S and S^* is denoted. Any self-adjoint or maximal dissipative (accumulative) extension is proper.

Definition 2.2 ([7]). A triplet $\Pi = \{\mathcal{H}, \Gamma_0, \Gamma_1\}$, where $\mathcal{H}$ is an auxiliary Hilbert space and $\Gamma_0, \Gamma_1 : \mathrm{dom}\,(S^*) \to \mathcal{H}$ are linear mappings, is called a boundary triplet for S^* if the "abstract Green's identity"

$$(S^*f, g) - (f, S^*g) = (\Gamma_1 f, \Gamma_0 g) - (\Gamma_0 f, \Gamma_1 g), \quad f, g \in \mathrm{dom}\,(S^*). \tag{2.1}$$

is satisfied and the mapping $\Gamma := (\Gamma_0, \Gamma_1)^\top : \mathrm{dom}\,(S^*) \to \mathcal{H} \oplus \mathcal{H}$ is surjective, i.e. $\mathrm{ran}\,(\Gamma) = \mathcal{H} \oplus \mathcal{H}$. $\Diamond$

A boundary triplet $\Pi = \{\mathcal{H}, \Gamma_0, \Gamma_1\}$ for S^* always exists whenever $n_+(S) = n_-(S)$. Note also that $n_\pm(S) = \dim(\mathcal{H})$ and $\ker\,(\Gamma_0) \cap \ker\,(\Gamma_1) = \mathrm{dom}\,(S)$.

In general, the linear maps $\Gamma_j : \mathfrak{H} \longrightarrow \mathcal{H}$, $j = 0, 1$, are neither bounded nor closed. However, equipping the domain $\mathrm{dom}\,(S^*)$ with the graph norm

$$\|f\|^2_{S^*} := \|S^*\|^2 + \|f\|^2, \qquad f \in \mathrm{dom}\,(S^*), \tag{2.2}$$

one gets a Hilbert space, which is denoted by $\mathfrak{H}_+(S^*)$, and regarding the maps $\Gamma_j : \mathfrak{H} \longrightarrow \mathcal{H}$, $j = 0, 1$, as acting from $\mathfrak{H}_+(S^*)$ into $\mathcal{H}$ it turns out that that the operators $\Gamma_j : \mathfrak{H}_+(S^*) \longrightarrow \mathcal{H}$, $j = 0, 1$, are bounded. In the following work we denote the operator $\Gamma_j : \mathfrak{H}_+(S^*) \longrightarrow \mathcal{H}$ by $\widehat{\Gamma}_j : \mathfrak{H}_+(S^*) \longrightarrow \mathcal{H}$, $j = 0, 1$. From surjectivity it follows that $\mathrm{ran}\,(\widehat{\Gamma}) = \mathcal{H} \oplus \mathcal{H}$, where $\widehat{\Gamma} := (\widehat{\Gamma}_1, \widehat{\Gamma}_1)$. Notice that the abstract Green's identity (2.1) can be written as

$$(\widehat{S}^* f, g) - (f, \widehat{S}^* g) = (\widehat{\Gamma}_1 f, \widehat{\Gamma}_0 g) - (\widehat{\Gamma}_0 f, \widehat{\Gamma}_1 g), \quad f, g \in \mathrm{dom}\,(S^*). \tag{2.3}$$

where $\widehat{S}^*$ denotes the operator S^* regarded as acting from $\mathfrak{H}_+(S^*)$ into $\mathfrak{H}$.

With any boundary triplet Π one associates two canonical self-adjoint extensions $S_j := S^* \upharpoonright \ker\,(\Gamma_j)$, $j \in \{0, 1\}$. Conversely, for any extension $S_0 = S_0^* \in \mathrm{Ext}_S$ there exists a (non-unique) boundary triplet $\Pi = \{\mathcal{H}, \Gamma_0, \Gamma_1\}$ for S^* such that $S_0 := S^* \upharpoonright \ker\,(\Gamma_0)$.

Using the concept of boundary triplets one can parameterize all proper extensions of A in the following way.

Proposition 2.3 ([8, 9]). *Let* $\Pi = \{\mathcal{H}, \Gamma_0, \Gamma_1\}$ *be a boundary triplet for* S^*. *Then the mapping*

$$\mathrm{Ext_S} \ni \widetilde{\mathrm{S}} \to \Gamma \mathrm{dom}\,(\widetilde{\mathrm{S}}) = (\Gamma_0 \mathrm{f}, \Gamma_1 \mathrm{f})^\top : \ \mathrm{f} \in \mathrm{dom}\,(\widetilde{\mathrm{S}})\} =: \Theta \in \widetilde{\mathcal{C}}(\mathcal{H}) \tag{2.4}$$

establishes a bijective correspondence between the sets $\mathrm{Ext_S}$ *and* $\widetilde{\mathcal{C}}(\mathcal{H})$. *We write* $\widetilde{S} = S_\Theta$ *if* $\widetilde{S}$ *corresponds to* Θ *by* (2.4). *Moreover, the following holds:*

(i) $S^*_\Theta = S_{\Theta^*}$, *in particular,* $S^*_\Theta = S_\Theta$ *if and only if* $\Theta^* = \Theta$.

(ii) S_Θ *is symmetric (self-adjoint) if and only if* Θ *is symmetric (self-adjoint).*

(iii) *The extensions* S_Θ *and* S_0 *are disjoint (transversal) if and only if there is a closed (bounded) operator* B *such that* $\Theta = \mathrm{gr}\,(B)$. *In this case* (2.4) *takes the form*

$$S_\Theta := S_{\mathrm{gr}\,(B)} = S^* \upharpoonright \ker\,(\Gamma_1 - B\Gamma_0). \tag{2.5}$$

In particular, $S_j := S^* \upharpoonright \ker\,(\Gamma_j) = S_{\Theta_j}$, $j \in \{0, 1\}$, where $\Theta_0 := \{0\} \times \mathcal{H}$ and $\Theta_1 := \mathcal{H} \times \{0\} = \mathrm{gr}\,(\mathbb{O})$ where $\mathbb{O}$ denotes the zero operator in $\mathcal{H}$. Note also that $\widetilde{\mathcal{C}}(\mathcal{H})$ contains the trivial linear relations $\{0\} \times \{0\}$ and $\mathcal{H} \times \mathcal{H}$ parameterizing the extensions S and S^*, respectively, for any boundary triplet Π.

2.3. γ-field and Weyl function

It is well known that Weyl functions are important tools in the direct and inverse spectral theory of Sturm-Liouville operators. In [8, 11] the concept of Weyl function was generalized to the case of an arbitrary symmetric operator S with $n_+(S) = n_-(S) \leqslant \infty$. Following [8], we briefly recall basic facts on Weyl functions and γ-fields associated with a boundary triplet Π.

Definition 2.4 ([8, 11]). Let $\Pi = \{\mathcal{H}, \Gamma_0, \Gamma_1\}$ be a boundary triplet for S^* and $S_0 = S^* \upharpoonright \ker(\Gamma_0)$. The operator valued functions $\gamma(\cdot) : \rho(S_0) \to [\mathcal{H}, \mathcal{H}]$ and $M(\cdot) : \ \rho(S_0) \to [\mathcal{H}]$ defined by

$$\gamma(z) := \left(\Gamma_0 \upharpoonright \mathfrak{N}_z\right)^{-1} \qquad \text{and} \qquad M(z) := \Gamma_1 \gamma(z), \quad z \in \rho(S_0), \tag{2.6}$$

are called the γ-field and the Weyl function, respectively, corresponding to the boundary triplet Π.

Clearly, the Weyl function can equivalently be defined by

$$M(z)\Gamma_0 f_z = \Gamma_1 f_z, \qquad f_z \in \mathfrak{N}_z, \quad z \in \rho(S_0).$$

The γ-field $\gamma(\cdot)$ and the Weyl function $M(\cdot)$ in (2.6) are well defined. Moreover, both $\gamma(\cdot)$ and $M(\cdot)$ are holomorphic on $\rho(S_0)$ and the following relations

$$\gamma(z) = \left(I + (z - \zeta)(S_0 - z)^{-1}\right)\gamma(\zeta), \qquad z, \zeta \in \rho(S_0), \tag{2.7}$$

and

$$M(z) - M(\zeta)^* = (z - \overline{\zeta})\gamma(\zeta)^*\gamma(z), \qquad z, \zeta \in \rho(S_0), \tag{2.8}$$

hold. Identity (2.8) yields that $M(\cdot)$ is $[\mathcal{H}]$-valued Nevanlinna function ($M(\cdot) \in R[\mathcal{H}]$), i.e. $M(\cdot)$ is $[\mathcal{H}]$-valued holomorphic function on $\mathbb{C}_\pm$ satisfying

$$M(z) = M(\overline{z})^* \qquad \text{and} \qquad \frac{\mathrm{Im(M(z))}}{\mathrm{Im(z)}} \geqslant 0, \qquad z \in \mathbb{C}_+ \cup \mathbb{C}_-.$$

It also follows from (2.8) that $0 \in \rho(\mathrm{Im(M(z))})$ for all $z \in \mathbb{C}_\pm$.

2.4. Krein-type formula for resolvents

Let $\Pi = \{\mathcal{H}, \Gamma_0, \Gamma_1\}$ be a boundary triplet for S^*, $M(\cdot)$ and $\gamma(\cdot)$ the corresponding Weyl function and γ-field, respectively. For any proper (not necessarily self-adjoint) extension $\widetilde{S}_\Theta \in \mathrm{Ext_S}$ with non-empty resolvent set $\rho(\widetilde{S}_\Theta)$ the following Krein-type formula holds (cf. [8, 11, 12])

$$(S_\Theta - z)^{-1} - (S_0 - z)^{-1} = \gamma(z)(\Theta - M(z))^{-1}\gamma^*(\overline{z}), \quad z \in \rho(S_0) \cap \rho(S_\Theta). \tag{2.9}$$

Formula (2.9) extends the known Krein formula for canonical resolvents to the case of any $S_\Theta \in \mathrm{Ext_S}$ with $\rho(S_\Theta) \neq \emptyset$. Moreover, due to relations (2.4), (2.5) and (2.6) formula (2.9) is connected with the boundary triplet Π. We emphasize, that this connection makes it possible to apply the Krein-type formula (2.9) to boundary value problems.

2.5. Operator spectral integrals

Let us recall some useful facts regarding operator spectral integrals. We follow in essentially [10, Section I.5.1].

Definition 2.5. Let $E(\cdot)$ be a spectral measure defined on the Borel sets $\mathcal{B}$ of the real axis $\mathbb{R}$. Let us assume that the support $\operatorname{supp}(E)$ is a bounded set, i.e. $\operatorname{supp}(E) \subset [a,b)$, $-\infty < a < b < \infty$. Further, let $G(\cdot) : [a,b) \longrightarrow \mathcal{B}(\mathfrak{H})$ be a Borel measurable function. Let $\mathfrak{Z}$ be a partition of the interval $[a,b)$ of the form $[a,b) = [\lambda_0, \lambda_1) \cup [\lambda_1, \lambda_2) \cup \cdots \cup [\lambda_{n-1}, \lambda_n)$ where $\lambda_0 = a$ and $\lambda_n = b$, and put $\Delta_m := [\lambda_{m-1}, \lambda_m)$, $m = 1, \ldots, n$. Thus $[a,b) = \bigcup_{m=1}^n \Delta_m$ and the intervals Δ_m are pairwise disjoint. Let $|\mathfrak{Z}| := \max_m |\Delta_m|$ and let

$$F_{\mathfrak{Z}}(G) := \sum_{m=1}^{n} G(x_m) E(\Delta_m), \qquad x_m \in \Delta_m.$$

If there is an operator $F_0 \in \mathcal{B}(\mathfrak{H})$ such that $\lim_{|\mathfrak{Z}| \to 0} \|F_{\mathfrak{Z}}(G) - F_0\| = 0$ independent of $\mathfrak{Z}$ and $\{x_m\}$, then F_0 is called the operator spectral integral of $G(\cdot)$ with respect to $E(\cdot)$ and is denoted by

$$F_0 = \int_a^b G(\lambda) dE(\lambda).$$

Remark 2.6. Similarly the operator spectral integral $\int_a^b dE(\lambda) G(\lambda)$ can be defined as above.

If $f(\cdot) : [a,b) \longrightarrow \mathfrak{H}$ is a Borel measurable function, then the vector spectral integral $\int_a^b dE(\lambda) f(\lambda)$ can be defined similarly.

Let us indicate some properties of the operator spectral integral.

(i) If $G(\lambda) := g(\lambda) I$ where $g(\cdot) \in C([a,b])$, then $\int_a^b G(\lambda) dE(\lambda)$ exists and coincides with scalar spectral integral $\int_a^b g(\lambda) dE(\lambda)$.

(ii) If $\int_a^b G(\lambda) dE(\lambda)$ exists and $h(\cdot) \in C([a,b])$, then also $\int_a^b h(\lambda) G(\lambda) dE(\lambda)$ exists and one has

$$\int_a^b h(\lambda) G(\lambda) dE(\lambda) = \int_a^b G(\lambda) dE(\lambda) \int_a^b h(\lambda) dE(\lambda).$$

Proposition 2.7 (Proposition I.5.1.2 of [10]). *Let $G(\cdot)$ be defined on $[a,b)$ and assume the existence of the derivative $G'(\lambda)$ with respect to the operator norm on $[a,b)$. Further, let $G'(\cdot)$ be Bochner integrable on $[a,b)$ and assume that $A(\lambda) = A(a) + \int_a^\lambda G'(x) dx$. Then $\int_a^b G(\lambda) dE(\lambda)$ exists and the estimate*

$$\left\| \int_a^b G(\lambda) dE(\lambda) \right\| \leqslant \|G(a)\| + \int_a^b \|G'(\lambda)\| d\lambda$$

is valid.

Similar existence theorems can be proven for the other types of spectral integrals. For instance the vector spectral integral exists if $f(\cdot)$ is strongly continuous, strongly differentiable on $[a,b]$ and if $f'(\cdot)$ is also strongly continuous. In particular, the operator and vector spectral integrals exist if the integrands $G(\cdot)$ and $f(\cdot)$ are holomorphic.

3. Main results

Let A be a closed symmetric operator with equal deficiency indices acting in the separable Hilbert space $\mathfrak{H}_A$ and let T be a bounded self-adjoint operator acting in the separable Hilbert space $\mathcal{H}_T$. We consider the operator $S = A \otimes I_T + I_A \otimes T$. To define the operator S we first consider the operator $A \otimes I_T$. The operator $A \otimes I_T$ is defined as the closure of the operator $A \odot I_I$ defined by

$$\mathrm{dom}\,(A \odot I_T) := \left\{ f = \sum_{k=1}^{r} g_k \otimes h_k : g_k \in \mathrm{dom}\,(A), \quad h_k \in \mathcal{H}_T, \quad r \in \mathbb{N} \right\}$$

and

$$(A \odot I_T)f = \sum_{k=1}^{r} A g_k \otimes h_k, \quad f \in \mathrm{dom}\,(A \odot I_T).$$

One can easily check that $A \odot I_T$ is a densely defined symmetric operator which yields that $A \otimes I_T$ is a densely defined closed symmetric operator. By $\mathfrak{H}_+(A)$ we denote Hilbert space which is obtained equipping the domain $\mathrm{dom}\,(A)$ with the graph norm of A, cf. (2.2). $\mathrm{dom}\,(A \otimes I_T) = \mathfrak{H}_+(A) \otimes \mathcal{H}_T$. By Proposition 7.26 of [2] we have $(A \otimes I_T)^* = A^* \otimes I_T$. Its domain is given by $\mathrm{dom}\,(A^* \otimes I_T) = \mathfrak{H}_+(A^*) \otimes \mathcal{H}_T$.

Similarly, the operator $I_A \otimes T$ can be defined. $I_A \otimes T$ is found to be a bounded self-adjoint operator with norm $\|T\|$. The operator $S := A \otimes I_T + I_A \otimes T$ is a well-defined closed symmetric operator with domain $\mathrm{dom}\,(A \otimes I_T)$. Notice that

$$S = \overline{A \odot I_T + I_A \odot T} = \overline{A \odot I_T} + I_A \otimes T.$$

Its adjoint is given $S^* = A^* \otimes I_T + I_A \otimes T$.

Let $\widehat{\Gamma}_j := \widehat{\Gamma}^A_j \otimes I_T : \mathfrak{H}_+(A^*) \otimes \mathcal{H}_T \longrightarrow \mathcal{H}_A \otimes \mathcal{H}_T$, $j = 0, 1$. Since $\mathrm{ran}\,(\widehat{\Gamma}^A) = \mathcal{H}_A \oplus \mathcal{H}_A$ we have $\mathrm{ran}\,(\widehat{\Gamma}) = (\mathcal{H}_A \otimes \mathcal{H}_T) \oplus (\mathcal{H}_A \otimes \mathcal{H}_T)$ where $\widehat{\Gamma} := (\widehat{\Gamma}_0, \widehat{\Gamma}_1)$. Let us consider the embedding operator $J : \mathfrak{H}_+(A^*) \otimes \mathcal{H}_T \longrightarrow \mathcal{H}_A \otimes \mathcal{H}_T$. We introduce the operator $\Gamma_j : \mathrm{dom}\,(A^* \otimes I_T) \longrightarrow \mathcal{H}_A \otimes \mathcal{H}_T$ by setting

$$\Gamma_j J \widehat{f} := \widehat{\Gamma}_j \widehat{f}, \quad \widehat{f} \in \mathfrak{H}_+(A^*) \otimes \mathcal{H}_T, \quad j = 0, 1. \tag{3.1}$$

Notice that $\mathrm{ran}\,(J) = \mathrm{dom}\,(A^* \otimes I_T)$. Since $\mathrm{ran}\,(\widehat{\Gamma}) = (\mathcal{H}_A \otimes \mathcal{H}_T) \oplus (\mathcal{H}_A \otimes \mathcal{H}_T)$ we get $\mathrm{ran}\,(\Gamma) = (\mathcal{H}_A \otimes \mathcal{H}_T) \oplus (\mathcal{H}_A \otimes \mathcal{H}_T)$ where $\Gamma = (\Gamma_0, \Gamma_1)$. Let us introduce the triplet $\Pi = \{\mathcal{H}, \Gamma_0, \Gamma_1\}$ where $\mathcal{H} := \mathcal{H}_A \otimes \mathcal{H}_T$ and Γ_j are given by (3.1).

Proposition 3.1. *If* $\Pi_A = \{\mathcal{H}_A, \Gamma^A_0, \Gamma^A_1\}$ *is a boundary triplet for* A^*, *then* $\Pi = \{\mathcal{H}, \Gamma_0, \Gamma_1\}$ *is a boundary triplet for* S^*

Proof. First, we are going to show that Π is a boundary triplet for $(A \otimes I_I)^* = A^* \otimes I_T$. The surjectivity of $\Gamma = (\Gamma_0, \Gamma_1)$ was already shown above. Next, we check that the "Green's identity" holds Let $g_k, g'_k \in \mathfrak{H}_+(A^*)$, $h_k, h'_k \in \mathcal{H}_T$ so that $f = \sum\limits_{k=1}^{N} g_k \otimes h_k$ and $f' = \sum\limits_{j=1}^{M} g'_j \otimes h'_j$. We have

$$\Big((A^* \otimes I_T) J \sum_{k=1}^{N} g_k \otimes h_k, J \sum_{j=1}^{M} g'_j \otimes h'_j\Big) - \Big(J \sum_{k=1}^{N} g_k \otimes h_k, J(A^* \otimes I_T) \sum_{j=1}^{M} g'_j \otimes h'_j\Big)$$
$$= \sum_{k=1}^{N} \sum_{j=1}^{M} (h_k, h'_j) \left[(A^* J_{A^*} g_k, J_{A^*} g'_j) - (J_{A^*} g_k, A^* J_{A^*} g'_j)\right]$$
$$= \sum_{k=1}^{N} \sum_{j=1}^{M} (h_k, h'_j) \left[(\Gamma^A_1 J_{A^*} g_k, \Gamma^A_0 J_{A^*} g'_j) - (\Gamma^A_0 J_{A^*} g_k, \Gamma^A_1 J_{A^*} g'_j)\right]$$

where $J_{A^*} : \mathfrak{H}_+(A^*) \longrightarrow \mathfrak{H}_A$ is the embeding operator. Similarly we get

$$\Big(\Gamma_1 J \sum_{k=1}^{N} g_k \otimes h_k, \Gamma_0 J \sum_{j=1}^{M} g'_j \otimes h'_j\Big) - \Big(\Gamma_0 J \sum_{k=1}^{N} g_k \otimes h_k, \Gamma_1 J \sum_{j=1}^{M} g'_j \otimes h'_j\Big)$$
$$= \sum_{k=1}^{N}\sum_{j=1}^{M} (h_k, h'_j) \left[(\Gamma_1^A J_{A^*} g_k, \Gamma_0^A J_{A^*} g'_j) - (\Gamma_0^A J_{A^*} g_k, \Gamma_1^A J_{A^*} g'_j)\right].$$

Hence we get

$$\Big((A^* \otimes I_T) J \sum_{k=1}^{N} g_k \otimes h_k, J \sum_{j=1}^{M} g'_j \otimes h'_j\Big) - \Big(J \sum_{k=1}^{N} g_k \otimes h_k, J (A^* \otimes I_T) \sum_{j=1}^{M} g'_j \otimes h'_j\Big)$$
$$= \Big(\Gamma_1 J \sum_{k=1}^{N} g_k \otimes h_k, \Gamma_0 J \sum_{j=1}^{M} g'_j \otimes h'_j\Big) - \Big(\Gamma_0 J \sum_{k=1}^{N} g_k \otimes h_k, \Gamma_1 J \sum_{j=1}^{M} g'_j \otimes h'_j\Big)$$

which yields

$$\Big((A^* \otimes I_T) J \sum_{k=1}^{N} g_k \otimes h_k, J \sum_{j=1}^{M} g'_j \otimes h'_j\Big) - \Big(J \sum_{k=1}^{N} g_k \otimes h_k, (A^* \otimes I_T) J \sum_{j=1}^{M} g'_j \otimes h'_j\Big)$$
$$= \Big(\widehat{\Gamma}_1 \sum_{k=1}^{N} g_k \otimes h_k, \widehat{\Gamma}_0 \sum_{j=1}^{M} g'_j \otimes h'_j\Big) - \Big(\widehat{\Gamma}_0 \sum_{k=1}^{N} g_k \otimes h_k, \widehat{\Gamma}_1 \sum_{j=1}^{M} g'_j \otimes h'_j\Big)$$

Since elements of the form $f = \sum_{k=1}^{N} g_k \otimes h_k$ and $f' = \sum_{j=1}^{M} g'_j \otimes h'_j$ are dense in $\mathfrak{H}_+(A^*)$ the equality can be closed which gives

$$\Big((A^* \otimes I_T) J f, J f'\Big) - \Big(J f, (A^* \otimes I_T) J f'\Big) = \Big(\widehat{\Gamma}_1 f, \widehat{\Gamma}_0 f'\Big) - \Big(\widehat{\Gamma}_0 f, \widehat{\Gamma}_1 f'\Big)$$

for $f, f' \in \mathfrak{H}_+(A^*) \otimes \mathcal{H}_T$ which immediately yields the abstract Green's identity for $A^* \otimes I_T$. Hence Π is a boundary triplet $A^* \otimes I_T$. Since $T_A \otimes T$ is a bounded self-adjoint operator one proves that Π is a boundary for S^*. Indeed, since $\mathrm{dom}\,(A^* \otimes I_T) = \mathrm{dom}\,(S^*)$ one immediately verifies the abstract Green's identity and $\Gamma \mathrm{dom}\,(A^* \otimes I_T) = \Gamma \mathrm{dom}\,(S^*)$ shows the surjectivity. ☐

Let us also mention that $S_0 := S^* \upharpoonright \ker(\Gamma_0^S)$ admits the representation

$$S_0 = A_0 \otimes I_{\mathcal{H}_T} + I_{\mathcal{H}_A} \otimes T. \tag{3.2}$$

Let $E_T(\lambda)$, $\lambda \in \mathbb{R}$, be the spectral measure of the self-adjoint operator T. Obviously,

$$\widehat{E}_T(\lambda) := I_A \otimes E_T(\lambda), \quad \lambda \in \mathbb{R},$$

defines a spectral measure on $\mathcal{H}_A \otimes \mathcal{H}_T$.

Proposition 3.2. *Let Π_A be a boundary triplet for A^* with γ-field $\gamma_A(z)$. If Π_S is the boundary triplet of Proposition 3.1 of S^*, then the γ-field $\gamma_S(\cdot)$ of Π_S admits the representation*

$$\gamma_S(z) = \int_a^b d\widehat{E}_T(\lambda)\, \gamma_A(z - \lambda) \otimes I_{\mathcal{H}_T} = \int_a^b \gamma_A(z - \lambda) \otimes I_{\mathcal{H}_T}\, d\widehat{E}_T(\lambda) \tag{3.3}$$

$z \in \mathbb{C}_\pm$ where $\sigma(T) \subset [a, b)$.

Proof. We set $G(\lambda) := \gamma_A(z-\lambda) \otimes I_T$, $\lambda \in [a,b)$. From (2.7) we get

$$G'(\lambda) = (A_0 - \zeta)(A_0 - z + \lambda)^{-2}\gamma_A(\zeta) \otimes I_T, \qquad \lambda \in \mathbb{R}.$$

Since $\int_a^b \|G'(\lambda)\|\, d\lambda < \infty$ the operator spectral integral

$$D(z) := \int_{\mathbb{R}} \gamma_A(z-\lambda) \otimes I_{\mathcal{H}_T}\, d\widehat{E}_T(\lambda) \tag{3.4}$$

exists by Proposition 2.7. We will show that $\operatorname{ran}(D(z)) \subseteq \mathfrak{H}_+(S^* - z)$. Let $\mathfrak{Z}$ be a partition of $[a,b)$ and let us consider the Riemann sum

$$D_{\mathfrak{Z}}(z) := \sum_{k=1}^{n} \gamma_A(z-\lambda_k) \otimes I_T\, \widehat{E}_T(\Delta_k), \qquad \lambda_k \in \Delta_k. \tag{3.5}$$

For every $z \in \mathbb{C}_\pm$ one has $\lim_{|\mathfrak{Z}|\to 0} \|D_{\mathfrak{Z}}(z) - D(z)\| = 0$. Obviously, for each $\mathfrak{Z}$ we have $D_{\mathfrak{Z}} f \in \mathfrak{H}_+(S^*)$, $f \in \mathfrak{H}$. Let us estimate the operator norm of $(\gamma_A(z-\lambda_k) \otimes I_T)\, \widehat{E}_T(\Delta_k)$ with respect to the Hilbert space $\mathfrak{H}_+(S^* - z)$. Obviously we have

$$\begin{aligned}&(S^* - z)(\gamma_A(z-\lambda_k) \otimes I_T)\, \widehat{E}_T(\Delta_k)\\ &\quad = (A^* - z)\gamma_A(z-\lambda_k) \otimes E_T(\Delta_k) + \gamma_A(z-\lambda_k) \otimes TE_T(\Delta_k).\end{aligned}$$

which yields

$$(S^* - z)(\gamma_A(z-\lambda_k) \otimes I_T)\, \widehat{E}_T(\Delta_k) = \gamma_A(z-\lambda_k) \otimes (TE_T(\Delta_k) - \lambda_k E_T(\Delta_k))$$

Hence we find

$$\|(S^* - z)(\gamma_A(z-\lambda_k) \otimes I_T)\, \widehat{E}_T(\Delta_k)\| \leqslant \|\gamma_A(z-\lambda_k)\|\, \|TE_T(\Delta_k) - \lambda_k E_T(\Delta_k)\|.$$

Since $\|TE_T(\Delta_k) - \lambda_k E_T(\Delta_k)\| \leqslant |\Delta_k|$, where $|\cdot|$ is the Lebesgue measure of the set Δ_k, we find

$$\|(S^* - z)(\gamma_A(z-\lambda_k) \otimes I_T)\, \widehat{E}_T(\Delta_k)\| \leqslant \|\gamma_A(z-\lambda_k)\|\, |\Delta_k|.$$

Using that $C_{\gamma_A}(z) := \sup_{\lambda\in[a,b)} \|\gamma_A(z-\lambda)\| < \infty$ we immediately get the estimate

$$\|(S^* - z)D_{\mathfrak{Z}}(z)\| \leqslant C_{\gamma_A}(z)(b-a), \qquad z \in \mathbb{C}_\pm. \tag{3.6}$$

In particular we get $\|(S^* - z)D(z)\| \leqslant C_{\gamma_A}(z)(b-a)$, $z \in \mathbb{C}_\pm$. Let us show that the integral $D(z)$ also exists in the strong sense in $\mathfrak{H}_+(S^* - z)$.

$$\begin{aligned}(S^* - z)D_{\mathfrak{Z}}(z) g \otimes h &= ((A^* - z) \otimes I_T)D_{\mathfrak{Z}}(z) g \otimes h + (I_A \otimes T)D_{\mathfrak{Z}}(z) g \otimes h\\
&= ((A^* - z) \otimes I_T)\sum_{k=1}^{n} \gamma_A(z-\lambda_k) g \otimes E_T(\Delta_k) h + (I_A \otimes T)\sum_{k=1}^{n} \gamma_A(z-\lambda_k) g \otimes E_T(\Delta_k) h\\
&= \sum_{k=1}^{n} -\lambda_k \gamma_A(z-\lambda_k) g \otimes E_T(\Delta_k) h + \sum_{k=1}^{n} \gamma_A(z-\lambda_k) g \otimes TE_T(\Delta_k) h\\
&= \sum_{k=1}^{n} \gamma_A(z-\lambda_k) g \otimes (TE_T(\Delta_k) - \lambda_k E_T(\Delta_k)) h\\
&= \Bigl(\sum_{k=1}^{n} \gamma_A(z-\lambda_k) g \otimes (TE_T(\Delta_k) - \lambda_k E_T(\Delta_k)) h\Bigr).\end{aligned}$$

Hence

$$\|(S^* - z)D_{\mathfrak{Z}}(z) g \otimes h\| = \sum_{k=1}^{n} \|\gamma_A(z-\lambda_k) g \otimes (TE_T(\Delta_k) - \lambda_k E_T(\Delta_k)) h\|,$$

we have

$$\|(S^* - z)D_{\mathfrak{Z}}(z)g \otimes h\| \leqslant \sum_{k=1}^{n} \|\gamma_A(z-\lambda_k)g\| \, \|(TE_T(\Delta_k) - \lambda_k E_T(\Delta_k))h\|. \tag{3.7}$$

Finally we obtain

$$\|(S^* - z)D_{\mathfrak{Z}}(z)g \otimes h\| \leqslant \|h\| \sum_{k=1}^{n} \|\gamma_A(z-\lambda_k)g\| \, |\Delta_k| \, . \tag{3.8}$$

Let $\mathfrak{Z}'$ be a refinement of $\mathfrak{Z}$, that $\mathfrak{Z}' = \{\Delta'_{k'}\}_{k'=1}^{n'}$ where for each k' there is always a k such that $\Delta'_{k'} \subseteq \Delta_k$. This yields the estimate

$$\|(S^* - z)(D_{\mathfrak{Z}}(z) - D_{\mathfrak{Z}'}(z))g \otimes h\| \leqslant \|h\| \sum_{k'=1}^{n'} \|(\gamma_A(z-\lambda'_{k'}) - \gamma_A(z-\lambda_k))g\| \, |\Delta'_{k'}| \, . \tag{3.9}$$

where $\lambda'_{k'} \in \Delta_{k'} \subseteq \Delta_k \ni \lambda_k$. Hence $|\lambda'_{k'} - \lambda_k| \leqslant |\Delta_k| \leqslant |\mathfrak{Z}|$. Using (2.7) we find

$$\|\gamma_A(z-\lambda'_{k'})g - \gamma_A(z-\lambda_k)\| \leqslant \frac{1}{\mathrm{Im(z)}} \sup_{\lambda \in [a,b)} \left\| \frac{S_0 - \zeta}{S_0 - z + \lambda} \right\| \, \|\gamma_A(\zeta)\| \, |\mathfrak{Z}|$$

which yields the estimate

$$\|(S^* - z)(D_{\mathfrak{Z}}(z) - D_{\mathfrak{Z}'}(z))g \otimes h\| \leqslant (b-a)\|h\| \, \|g\| \frac{1}{\mathrm{Im(z)}} \sup_{\lambda \in [a,b)} \left\| \frac{S_0 - \zeta}{S_0 - z + \lambda} \right\| \, \|\gamma_A(\zeta)\| \, |\mathfrak{Z}| \, . \tag{3.10}$$

Hence the Riemann sums $D_{\mathfrak{Z}}(z)$ converge strongly in $\mathfrak{H}_+(S^* - z)$ as $|\mathfrak{Z}| \to 0$. Since the Hilbert spaces $\mathfrak{H}_+(S^*)$ and $\mathfrak{H}_+(S^* - z)$, $z \in \mathbb{C}_\pm$, are isomorph the Riemann sums converge strongly in $\mathfrak{H}_+(S^*)$.

It remains to show that $(S^* - z)D(z) = 0$. Recall that

$$\begin{aligned}(S^* - z)D_{\mathfrak{Z}}(z)g \otimes h &= \sum_{k=1}^{n}((A^* - z)\gamma_A(z-\lambda_k)g \otimes E_T(\Delta_k)h + \gamma_A(z-\lambda_k)g \otimes TE_T(\Delta_k)h) \\ &= \sum_{k=1}^{n} \gamma_A(z-\lambda_k)g \otimes (TE_T(\Delta_k) - \lambda_k E_T(\Delta_k))h.\end{aligned}$$

For instance,

$$\|(S^* - z)D_{\mathfrak{Z}}(z)g \otimes h\| = \sum_{k=1}^{n} \|\gamma_A(z-\lambda_k)g \otimes (TE_T(\Delta_k) - \lambda_k E_T(\Delta_k))h\| \leqslant$$
$$\sum_{k=1}^{n} \|\gamma_A(z-\lambda_k)g\| \|(T - \lambda_k)E_T(\Delta_k)h\|$$

To the degree that $\|\gamma_A(z-\lambda_k)\|$ is bounded, we have $\|(S^* - z)D_{\mathfrak{Z}}(z)g \otimes h\| \to 0$ as $|\mathfrak{Z}| \to 0$ for any $g \otimes h$. For the element of the form $f = \sum\limits_{k=1}^{n} g_k \otimes h_k$ obviously the same result holds. Then, we use that the set of $f = \sum\limits_{k=1}^{n} g_k \otimes h_k$ is dense in $\mathfrak{H}_+(S^*)$ □

Proposition 3.3. *Let* Π_A *be a boundary triplet for* A^* *with Weyl function* $M_A(\cdot)$. *If* Π_S *is the boundary triplet of Proposition 3.1 of* S^*, *then the Weyl function* $M_S(\cdot)$ *of* Π_S *admits the representation*

$$\begin{aligned} M_S(z) &= \int_a^b d\widehat{E}_T(\lambda)\; M_A(z-\lambda)\otimes I_{\mathcal{H}_T} \\ &= \int_a^b M_A(z-\lambda)\otimes I_{\mathcal{H}_T}\; d\widehat{E}_T(\lambda), \end{aligned} \tag{3.11}$$

$z \in \mathbb{C}_\pm$ *where* $\sigma(T) \subset [a,b)$. *In particular, if* $n_\pm(A) = 1$, *then* $M_A(\cdot)$ *is scalar,* $\mathcal{H}_S = \mathcal{H}_T$ *and*

$$M_S(z) = M_A(z - T), \qquad z \in \mathbb{C}_\pm. \tag{3.12}$$

Proof. We set $G(\lambda) := M_A(z-\lambda)\otimes I_T$, $\lambda \in [a,b)$. From (2.7), (2.8) we get

$$G'(\lambda) = -\gamma_A(\zeta)^*\gamma_A(z-\lambda) + (z-\lambda-\overline{\zeta})\gamma_A(\zeta)^*(A_0-\zeta)(A_0-z+\lambda)^{-2}\gamma_A(\zeta)\otimes I_T, \qquad \lambda\in\mathbb{R}. \tag{3.13}$$

Since $\int_a^b \|G'(\lambda)\|\, d\lambda < \infty$ the operator spectral integral

$$D(z) := \int_{\mathbb{R}} \gamma_A(z-\lambda)\otimes I_{\mathcal{H}_T}\; d\widehat{E}_T(\lambda) \tag{3.14}$$

exists by Proposition 2.7.

Analogously to Proposition 3.2, we can prove that the integral exists in the strong sense in $\mathfrak{H}_+(S^* - z)$ and in $\mathfrak{H}_+(S^*)$, as the spaces are isomorph.

Let us note $D_3(z) = \sum\limits_{k=1}^{n} \gamma_A(z-\lambda_k)\otimes I_T\widehat{E}_T(\Delta_k)$. Then,

$$\Gamma_1^S D_3(z) = \Gamma_1^S \sum_{k=1}^{n} \gamma_A(z-\lambda_k)\otimes I_T\widehat{E}_T(\Delta_k) =$$

$$\sum_{k=1}^{n} \Gamma_1^A\gamma_A(z-\lambda_k)\otimes E_T(\Delta_k) = \sum_{k=1}^{n} M_A(z-\lambda_k)\otimes E_T(\Delta_k) = L_3(z)$$

As far as $L_3(z)$ and $D_3(z)$ converge in a strong sense in $\mathfrak{H}_+(S^*)$ and Γ_0^S is bounded in $\mathfrak{H}_+(S^*)$, we get the estimate. ☐

Note: In case T has pure point spectrum, the formula (3.11) becomes simpler

$$M_S(z) = \sum_{\lambda} M_A(z-\lambda)\otimes\xi_\lambda, \tag{3.15}$$

where ξ_λ is an eigenvector of T, corresponding to λ

4. Example 1

In this section we will describe a simple example. Let's consider the symmetric operator $A = -\frac{d^2}{dx^2}$ with the domain

$$\operatorname{dom}(A) = \{f \in W_2^2(0;+\infty) : f(0) = f'(0) = 0\}$$

in the Hilbert space $L^2(\mathbb{R})$. Notice that $n_\pm(A) = 1$. Let's consider the following bounded self-adjoint operator

$$T = \begin{pmatrix} 1 & 0 \\ 0 & -1 \end{pmatrix}$$

acting on $\mathcal{H}_T = \mathbb{C}^2$. We introduce the operator $S = A\otimes I_T + I_A\otimes T$ defined in $\mathcal{H}_A \otimes H_T$. Our goal is to get the γ-field and the Weyl function corresponding to H in terms of γ-field and the Weyl function, corresponding to A, using the results described above.

Obviously, operator A^* has the deficiency indices $(1;1)$, so it's deficiency subspace is one-dimensional. Let us calculate the boundary form of the operator A^*. Integrating by parts, we get:

$$(A^*f,g)-(f,A^*g)=-\int\limits_0^{+\infty} f''\bar{g}dx=-f'\bar{g}|_0^{+\infty}+f\bar{g}'|_0^{+\infty}-\int\limits_0^{+\infty} f\bar{g}''dx.$$

So,

$$(A^*f,g)-(f,A^*g)=-f'\bar{g}|_0^{+\infty}+f\bar{g}'|_0^{+\infty}.$$

Recall that an element f from the domain of the adjoint operator also satisfies the condition $f(+\infty), f'(+\infty)=0$. Hence, we have:

$$(A^*f,g)-(f,A^*g)=-f(0)\bar{g}'(0)+f'(0)\bar{g}(0).$$

Now we can obtain the boundary operators, corresponding to A^*:

$$\Gamma_0^A f=f(0),\qquad \Gamma_1^A f=f'(0)$$

Recalling the result of Proposition 3.1, we introduce the boundary operators for H^*:

$$\Gamma_0^S f=f(0)\otimes I, \Gamma_1^S f=f'(0)\otimes I.$$

Let us calculate the γ-field, corresponding to A^*. The deficiency element of the operator A^*, corresponding to the point z, has the form: $e^{i\sqrt{z}x}$ (we choose the branch of the square root in such a way that $\Im\sqrt{z}>0$). Applying Γ_0^A, we have:

$$\Gamma_0^A e^{i\sqrt{z}x}=1$$

so that

$$\gamma_A(z)=1.$$

Let us describe the γ-field, corresponding to S^*. As far as T is self-adjoint, the spectral decomposition holds:

$$T=P_1-P_2,$$

where P_1 and P_2 are the projectors onto the invariant subspaces of the operator T, corresponding to the eigenvalues 1 and -1, respectively. The projectors have the following forms:

$$P_1=\begin{pmatrix} 1 & 0 \\ 0 & 0 \end{pmatrix},\quad P_2=\begin{pmatrix} 0 & 0 \\ 0 & 1 \end{pmatrix}.$$

Using the result of Proposition (3.2), we have:

$$\gamma_S(z)=\gamma_A(z-1)\otimes P_1+\gamma_A(z+1)\otimes P_2=\begin{pmatrix} 1 & 0 \\ 0 & 1 \end{pmatrix}.$$

The corresponding Weyl function is obviously as follows:

$$M_A(z)=\Gamma_1^A\gamma_A(z)=i\sqrt{z}.$$

Using the result of Proposition (3.3), we have:

$$M_S(z)=M_A(z-1)\otimes P_1+M_A(z+1)\otimes P_2=\begin{pmatrix} i\sqrt{z-1} & 0 \\ 0 & i\sqrt{z+1} \end{pmatrix}.$$

5. Example 2

In this example we consider an operator $S = A \otimes I_T + I_A \otimes B$ defined in $\mathcal{H}_A \otimes \mathcal{H}_T$, $\mathcal{H}_A = L_2(a,b), \mathcal{H}_T = \mathbb{C}^2$. Let us take the symmetric operator A as negative Laplacian $A = -\frac{d^2}{dx^2}$ with the domain $\mathrm{dom}\,(A) = \{\phi \in W^{2,2}[a;b] | \phi(a) = \phi(b) = \phi'(a) = \phi'(b) = 0\}$ and a self-adjoint operator T be the same as in previous example. Let us obtain the γ-field for S.

The boundary operators for A^* are:

$$\widehat{\Gamma}_0 f = \begin{pmatrix} f'(b) \\ f(a) \end{pmatrix}, \quad \widehat{\Gamma}_1 f = \begin{pmatrix} f(b) \\ f'(a) \end{pmatrix}$$

Then, the boundary operators for the operator S^* are:

$$\Gamma_0 f = \begin{pmatrix} f'(b) \\ f(a) \end{pmatrix} \otimes I, \quad \Gamma_1 f = \begin{pmatrix} f(b) \\ f'(a) \end{pmatrix} \otimes I \tag{5.1}$$

Due to the fact that the deficiency elements of A corresponding to the point z are

$$e^{i\sqrt{z}x}, e^{-i\sqrt{z}x}, \tag{5.2}$$

we obtain the γ-field $\gamma_A(z)$ for A^* in the form

$$\gamma_A(z) = \frac{-i}{2\sqrt{z}\cos(\sqrt{z}(b-a))} \begin{pmatrix} e^{-i\sqrt{z}a} & i\sqrt{z}e^{-i\sqrt{z}b} \\ -e^{i\sqrt{z}a} & i\sqrt{z}e^{i\sqrt{z}b} \end{pmatrix} \tag{5.3}$$

So, using the result of **Proposition 3.3.**, we have:

$$\gamma_S(z) = \gamma_A(z-1) \otimes \begin{pmatrix} 1 & 0 \\ 0 & 0 \end{pmatrix} + \gamma_A(z+1) \otimes \begin{pmatrix} 0 & 0 \\ 0 & 1 \end{pmatrix}. \tag{5.4}$$

Direct calculation of the Weyl function for A^* gives us

$$M_A(z) = \frac{1}{\sqrt{z}\cos(\sqrt{z}(b-a))} \cdot \begin{pmatrix} \sin(\sqrt{z}(b-a)) & \sqrt{z} \\ \sqrt{z} & \sqrt{z}\sin\sqrt{z}(b-a) \end{pmatrix}. \tag{5.5}$$

Then,

$$M_S(z) = M_A(z-1) \otimes \begin{pmatrix} 1 & 0 \\ 0 & 0 \end{pmatrix} + M_A(z+1) \otimes \begin{pmatrix} 0 & 0 \\ 0 & 1 \end{pmatrix} \tag{5.6}$$

6. Concluding remarks

In this paper we considered the γ-field and the Weyl function corresponding to the boundary triplet Π_S for the operator $S = A \otimes I_T + I_A \otimes T$ where the operator A is symmetric and the operator T is bounded and self-adjoint. We obtained the formulas in terms of the γ-field and the Weyl function corresponding to the boundary triplet Π_A. The result can be immediately applied to the scattering theory due to the relation between the Weyl function and the scattering matrix (see, e.g., [13]). There is an interesting question about the case when the operator T is unbounded (it is well known that this case has many specific features [14]). We will present the corresponding result in the next paper.

Acknowledgments

Supported by Federal Targeted Program "Scientific and Educational Human Resources for Innovation-Driven Russia" (contract 16.740.11.0030), grant 11-08-00267 of Russian Foundation for Basic Researches and grants of the President of Russia (state contract 14.124.13.2045-MK and grant MK-1493.2013.1), by Program of Development of Leading Russian Universities. A part of this work was made during visits of IYP and AAB to Berlin. We thank WIAS Berlin for kind hospitality.

References

[1] M.S.Birman, M.Z.Solomyak. *Spectral Theory of Selfadjoint Operators in Hilbert Space.* Kluwer, Dordrecht (1987).

[2] Konrad Schmüdgen. *Unbounded self-adjoint operators on Hilbert space*, volume 265 of *Graduate Texts in Mathematics.* Springer, Dordrecht, 2012.

[3] B.S.Pavlov. Operator extensions theory and explicitly solvable models. *Uspekhi Mat. Nauk.* **42** (6). P. 99-131 (1987); English transl in: *Russ. Math. Surv.* **42**, P. 127-168 (1987).

[4] N.Bagraev, G.Martin, B.S.Pavlov, A.Yafyasov. Landau-Zener effect for a quasi-2D periodic sandwich. *Nanosystems: Phys. Chem. Math.* **2** (4), P. 32-50 (2011).

[5] V.Ryzhov. A general boundary value problem and its Weyl function. *Opuscula Math.* **27** (2), P. 305-331.

[6] M. Malamud, H. Neidhardt. Sturm-liouville boundary value problems with operator potentials and unitary equivalence. *J. Differ. Equations*, **252** (11), P. 5875–5922 (2012).

[7] V. I. Gorbachuk, M. L. Gorbachuk. *Boundary value problems for operator differential equations*, volume 48 of *Mathematics and its Applications (Soviet Series).* Kluwer Academic Publishers Group, Dordrecht (1991).

[8] V. A. Derkach and M. M. Malamud. Generalized resolvents and the boundary value problems for Hermitian operators with gaps. *J. Funct. Anal.* **95** (1), P. 1–95 (1991).

[9] M. M. Malamud. Some classes of extensions of a Hermitian operator with lacunae. *Ukraïn. Mat. Zh.* **44** (2), P. 215–233 (1992).

[10] H. Baumgärtel, M. Wollenberg. *Mathematical scattering theory*, volume 59 of *Mathematical Textbooks and Monographs, Part II: Mathematical Monographs.* Akademie-Verlag, Berlin (1983).

[11] V. A. Derkach, M. M. Malamud. On the Weyl function and Hermite operators with lacunae. *Dokl. Akad. Nauk SSSR*, **293** (5), P. 1041–1046 (1987).

[12] V. A. Derkach, M. M. Malamud. The extension theory of Hermitian operators and the moment problem. *J. Math. Sci.* **73** (2), P. 141–242 (1995).

[13] J. Berndt, M. M. Malamud, H. Ntidhardt. Scattering matrices and Weyl functions. *Proc. London Math. Soc.* **97** (3), P. 568–598 (2008).

[14] A. N. Kochubei. On extensions of symmetric operators and symmetric binary relations. *Mat. Zametki.* **17**, P. 41-48 (1975).

NANOSYSTEMS: PHYSICS, CHEMISTRY, MATHEMATICS, 2013, 4 (6), P. 760–771

STUDY OF DYNAMICS OF MICROSTRUCTURAL TRANSFORMATIONS IN CRYSTALLINE YTTRIA NANOPOWDER

R. P. Ermakov, P. P. Fedorov, V. V. Voronov
Prokhorov General Physics Institute, Russian Academy of Sciences, Moscow, Russia
x-ray_diffraction@mail.ru

PACS 61.05.C-

This paper is a continuation of a previously reported study of the microstructure transformations in crystalline yttria nanopowder prepared by soft chemistry via precipitation from aqueous acidic nitrates. We have observed the aforementioned transformations over extended periods of time at 900 °C and 1100 °C (isothermal annealing) with the use of X-ray diffraction analysis (full profile analysis of reflections, etc.).

Keywords: yttrium oxide, optical ceramics, X-ray diffraction phase analysis.

1. Introduction

This paper is a continuation of our previous studies [1] of transformations of the microstructure of crystalline yttria nanopowder at 600 °C and 800 °C during isothermal annealing. Such information is crucial for the preparation of yttria-based optical ceramics, which are more advantageous than single crystals of the same chemical composition [2–4]. Crystalline yttria nanopowders can easily be prepared by annealing yttrium hydroxynitrate, which is incidentally the most inexpensive yttria nanopowder precursor [5–10]. The latter has to satisfy very strict criteria of chemical purity and microstructure, and this is why studying the dynamics of structural transformations in yttria nanopowders under annealing is so important: it allows control over the properties of yttria nanopowder samples. Therefore, the topic of our study was X-ray diffraction analysis (including full profile analysis of reflections) and scanning electron microscopy investigation of domains of coherent scattering (DCS), their morphology and crystallite microdeformations under annealing at 900 °C and 1100 °C for 1–1440 minutes.

2. Experimental

Our experiments included the preparation of the starting yttrium hydroxynitrate by precipitation with aqueous ammonia from aqueous nitrate solutions, followed by conversion to crystalline yttria nanopowder via annealing. We used both 99.99% pure yttria and nitric acid as well as 99.5% pure ammonia as our starting materials. Component additions were controlled with a Hanna Instrument pH-meter (usually, pH values varied within 0.76–9.00 interval). Thermal treatment of the prepared samples was carried out in alumina crucibles in SNOL ovens under air. For detailed protocols of these syntheses please see our previous paper [1].

The phase composition and particle morphology of all synthesized samples were studied by X-ray diffraction analysis, transmission and scanning electron microscopy (TEM and SEM, respectively). We used Bruker D8 Discover A25 DaVinci Design ($\mathrm{Cu}_{K\alpha}$ – radiation, standard Bragg-Brentano assembly) diffractometer for describing specimen microstructure dynamics and for estimating the content of X-ray amorphous phase in synthesized yttria nanopowder. Full profile analysis of the X-ray diffraction patterns was carried out using TOPAS [11, 12] and

FullProf [13] software (Pawley [14], LeBail [15] and modified Rietveld [16] techniques). TEM and SEM images were recorded using a Leo 912 AB Omega and NVision 40 microscopes.

3. Results and Discussion

3.1. Calculation of domains of coherent scattering (DCS) and microdeformations

Full-profile Rietveld analysis of X-ray pattern peak profiles was carried out using Voight function approximation (a bundle of Cauchy and Gaussian functions). In turn, the Voight function was approximated by pseudo-Voight function (sum of Cauchy and Gaussian components) with inclusion Figner's divergence [17]. We assumed that the small size of DCS and microdeformations contributed to the broadening of both Voight function components, but these contributions depended on the scattering angle in a different manner as per Scherrer and Stokes formulas:

$$\beta_{size} = \frac{\lambda}{D\cos(\theta)}, \tag{1}$$

$$\beta_{strain} = 2 \cdot e \cdot \tan(\theta), \tag{2}$$

where β_{size}, β_{strain} – integral broadening caused by size and deformation, respectively; λ – wavelength of monochromatic X-ray irradiation (nm); D – DCS size (nm); e – size of microdeformation. Taking into account equations (1) and (2) as well as the known empirical Cagliotti correlation between peak half-width and its location in the X-ray diffraction pattern, one can suggest the following formulas for Gaussian and Lorentzian half-widths and their dependency from the diffraction angle that were used in FullProf software:

$$\begin{gathered} H_G^2 = (U + (1-\eta)^2 \cdot D_{st}^2(\alpha_D)) \cdot \tan^2(\theta) + V \cdot \tan(\theta) + W + \frac{Ig}{\cos^2(\theta)}, \\ H_L = (X + \eta \cdot D_{st}^2(\alpha_D)) \cdot \tan(\theta) + \frac{Y + F(sz)}{\cos(\theta)}, \end{gathered} \tag{3}$$

where H_G, H_L – contributions of the Gaussian and Lorentzian half-widths to the pseudo-Voight functions, respectively; U, V, W – Cagliotti function parameters refined by cyclic least square technique (LST) for each individual X-ray diffraction pattern; η – weighted contribution of Lorentzian function; $D_{st}(\alpha_D)$, X – microdeformation parameters; Y, $F(sz)$, Ig – DCS parameters. Correct calculation of the DCS and microdeformation values also requires subtraction of the instrument contribution to the observed peak half-widths:

$$\begin{gathered} H^2_{G\_sam} = H^2_{G\_obs} - H^2_{L\_ins}, \\ H_{L\_sam} = H_{L\_obs} - H_{L\_ins}, \end{gathered} \tag{4}$$

where H_{G_sam}, H_{G_obs}, H_{G_ins} – Gaussian half-width of the sample itself, observed half-width and instrumental half-width, respectively; H_{L_sam}, H_{L_obs}, H_{L_ins} – Lorentzian half-width of the sample itself, observed half-width and instrumental half-width, respectively.

Instrument contributions to the peak half-widths were accounted for with the use of alumina specimen (NIST standard) prepared by a technique that excluded broadening lines in its X-ray diffraction pattern associated with DCS and microdeformations. We measured H_{G_ins} and H_{L_ins} for each peak in this alumina standard using profile fitting protocol from FullProf software assuming the following correlations between peak half-width and their reflection angles:

$$H_G^2 = U \cdot \tan^2(\theta) + V \cdot \tan(\theta) + W,$$
$$H_L = X \cdot \tan(\theta) + Y/\cos(\theta) + Z, \tag{5}$$

where U, V, W, X, Y, Z – instrument function parameters, that were determined by LST for each measuring instrument.

We used a very similar approach earlier in analyzing X-ray diffraction patterns [1], but in the present paper we implemented more advanced software that provides better agreement with the experimental data and a better level of refinement for the calculated results.

3.2. Determination of mass content of amorphous phase

The content of the amorphous phase in a sample is the most important factor in powder technology, for it plays a crucial role in determining the mechanism of microstructure changes. There are many methods for evaluating amorphous phase content described in the literature based on the ratio of X-ray diffraction peak area(s) and area(s) of the background. This approach describes quite adequately the dynamics of changing aforementioned amorphous phase content in series of similar samples, but its accuracy is poor (ca. 20% error in determining the actual content of the amorphous phase). In order to remedy the latter drawback, we implemented our own technique of Rietveld-type quantitative phase analysis based on spiking the sample with an alumina standard, mixing it to a pseudo-homogeneous state and recording its X-ray diffraction pattern. If the following ratio:

$$\eta_{st} > \frac{m_{st}}{m_{st} + m_{samp}}, \tag{6}$$

where m_{samp} is a mass of the sample, m_{st} is a mass of spiking standard and η_{st} is a weight part of the standard experimentally determined by Rielveld-type method, is correct, then the sample has an amorphous phase. Content of the latter can be calculated as follows:

$$\eta_{amorphoue} = 1 - (1 - \eta_{samp})\,\frac{m_{samp} + m_{st}}{m_{samp}}, \tag{7}$$

with the relative error not exceeding 1.5%.

3.3. Analysis of basic yttrium hydroxynitrate microstructure

Usually, crystalline yttria nanopowder is prepared by annealing yttrium hydroxynitrate during its chemical synthesis. Prehistory of such yttria samples determines its microstructure and morphology features. For example, one can easily observe anisotropic peak broadening in the typical X-ray diffraction pattern of yttrium hydroxynitrate (Fig. 1).

Most probably, this is caused by anisotropy of the domains of coherent scattering (DCS) and microdeformations. Full-profile Pawley-type analysis of this pattern confirmed the anisotropic character of DCS in this sample (difference between experimental and calculated results in shown in Fig. 1, too). This conclusion was also proven by transmission electron microscopy (TEM) (Fig. 2): sample particles are shaped as ca. 10–13 nm thick platelets with ca. 300 nm diameters.

In other words, the platelet thickness is close to the smallest DCS values presented in Fig. 1. The fact that the other dimension size of the platelets (300 nm) is significantly different from the largest observed DCS value of 44 nm can be explained by differences in the platelets' spatial orientation and corresponding diffraction vector. It is very hard to tell anything about platelet orientation with respect to the crystal lattice axes, but the clear anisotropic broadening of diffraction peaks allows one to assume that all these platelets are somehow ordered, in a

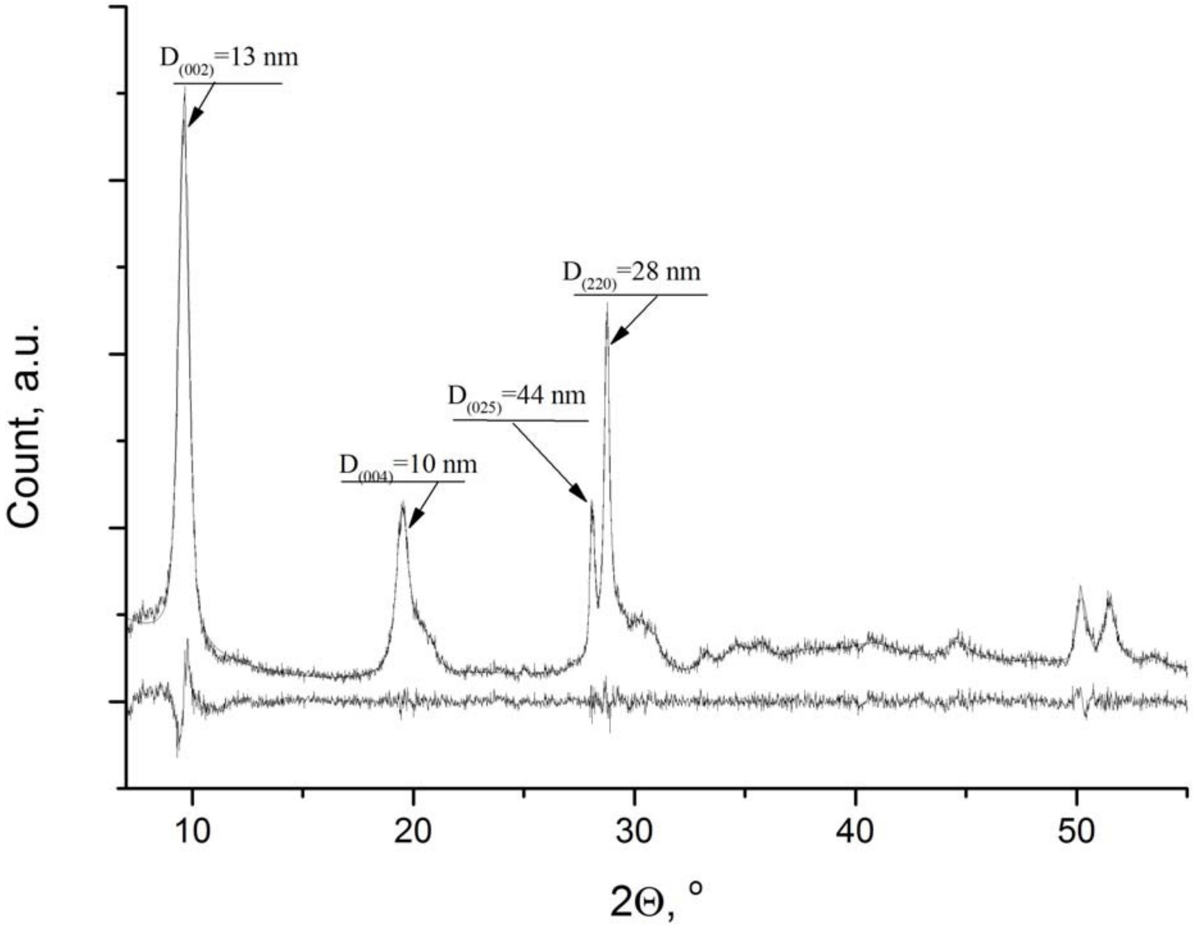

FIG. 1. X-Ray diffraction pattern of yttrium hydroxynitrate

similar spatial arrangement. Another suggestion one can make from the presented experimental data and agreement of the electron microscopy and X-ray diffraction studies results is that all these platelets form an area of coherent scattering (DCS), i.e., the unified crystalline space, not assembly of independent randomly oriented crystallites.

3.4. Dynamics of changes in the microstructure of yttria crystalline nanopowder during isothermal annealing at 900 °C

We studied the effects of isothermal annealing on the changes of yttria crystalline nanopowder microstructure by placing basic yttrium hydroxynitrate samples in a preheated 900 °C oven. Then, after a certain time, samples were retrieved from the heating chamber and studied by X-ray diffraction analysis. The results of this study are presented in Fig. 3.

These data unequivocally demonstrate that 900 °C isothermal annealing caused the formation of yttria in as short as 3 minutes. A further heating resulted only in an increase of the observed diffraction peaks' intensity and a decrease in their half-widths. Additional data, such as changes in a_0 lattice unit cell parameter, DCS, microdeformation values and content of amorphous phase over time are presented in Fig. 4.

They indicate that the content of amorphous phase in these yttria samples drops below 1% after annealing at 900 °C for 5 minutes. Lattice parameters decreased at the beginning of annealing and were stabilized after 300 min of heating. The most reasonable explanation for this fact is that the samples lost volatile components (e.g., water) at the beginning of annealing,

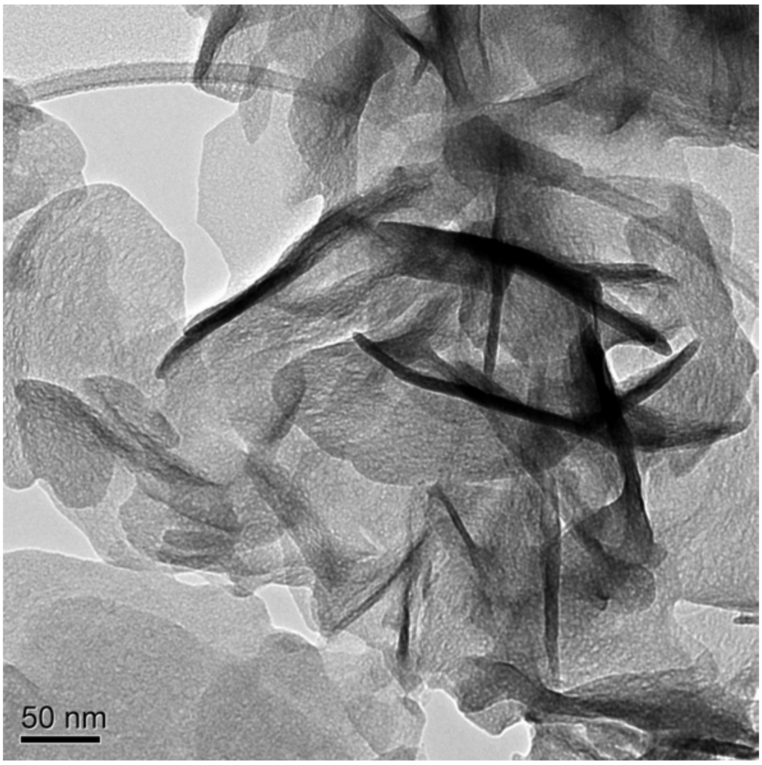

FIG. 2. Transmission electron microscopy (TEM) image of basic yttrium hydroxynitrate

and when there was nothing else to be excluded from the crystalline lattice, its parameter ceased to change. However, the simple presence of such volatiles guaranteed inhomogeneity of the chemical composition of yttria particles, and thus, produced microdeformations. In general, isothermal annealing of yttria leads to an increase of a size of the crystallites, perfecting the crystal order and making crystal composition even over the whole sample (Fig. 4). We have observed these phenomena in our experiments (Fig. 3 and 4). At the same time, it is worth noting that the growth of the DCS and decreasing microdeformation values over time is not steady for DCS (clear stepwise profile) whereas the microdeformations' decrease is relatively smooth.

Changes of the powder samples' microstructure can easily be analyzed with the use of Williamson-Hall charts [18]. If one assumes that the particles scattering X-rays are isotropic, containing evenly distributed microdeformations, then peaks in the diffraction patterns can be described by Lorentzian functions, permitting the use of the following equation:

$$\frac{\beta_{sam}\cos(\theta)}{\lambda} = \frac{1}{D} + \varepsilon\frac{2\sin(\theta)}{\lambda}, \tag{8}$$

where β_{sam} – integral width of diffraction peak, which widening is caused by factors of size and microstructure. This equation can be easily transformed to a linear correlation in the following coordinates: $\frac{\beta_{sam}\cos(\theta)}{\lambda} = f\left(\frac{2\sin(\theta)}{\lambda}\right)$, so the slope of the fitting line is proportional to microdeformations, whereas DCS is inversely proportional to the intercept.

Such charts prepared for 900 °C yttria isothermally annealed crystalline nanopowder (Fig. 5) showed very good linearity of experimental data (R^2 factor was close to 1.0 for all linear fits) and thus justified the use of an isotropic model for the DCS and microdeformation calculations. Lines in the Fig. 5 chart turn clockwise and shift down with an increase in the

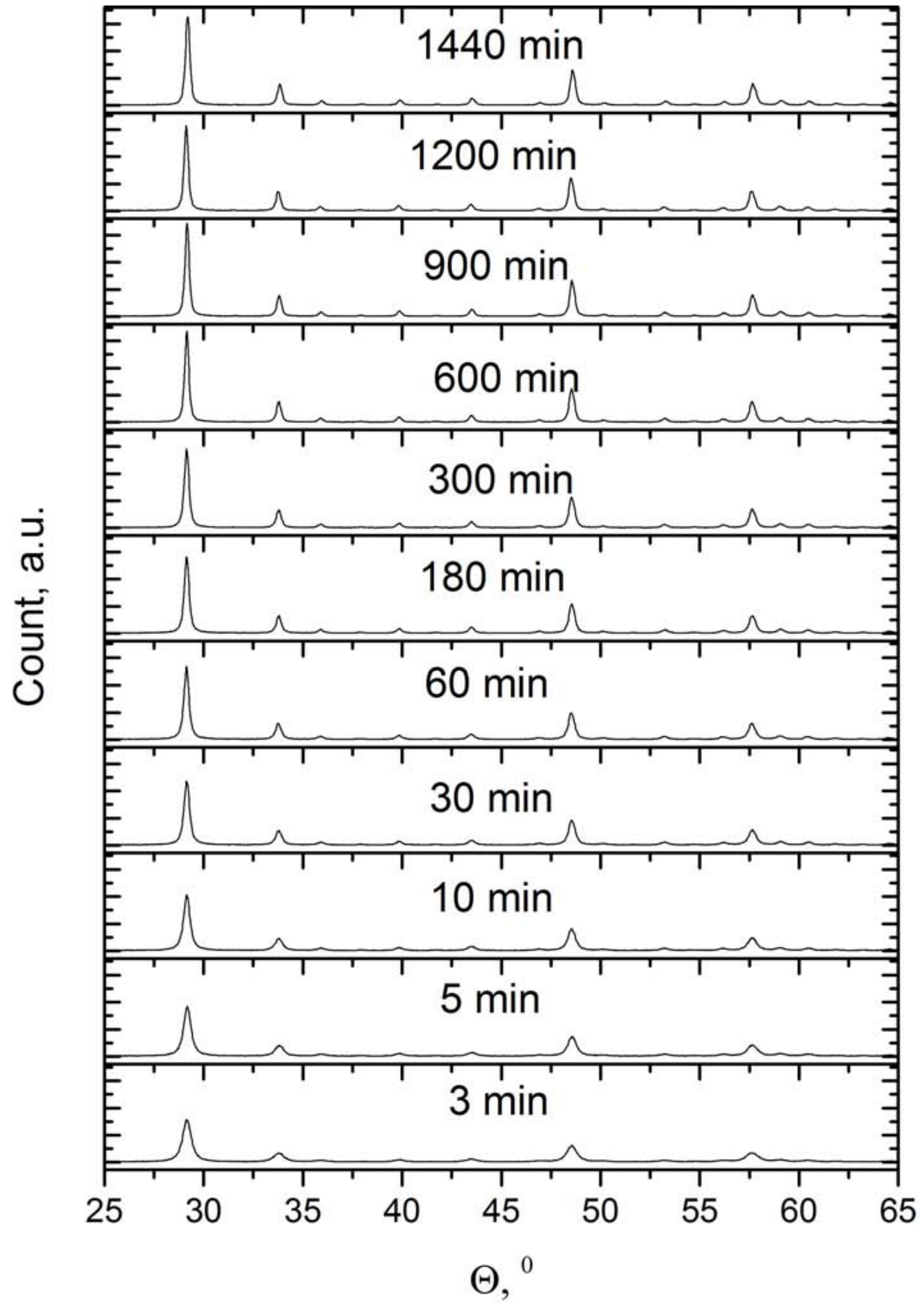

FIG. 3. X-Ray diffraction patterns of yttrium hydroxynitrate samples annealed at 900 °C for different times

annealing time, and these changes occur most notably at the beginning of annealing and after 300 min heating.

3.5. Dynamics of changes in the microstructure of yttria crystalline nanopowder during isothermal annealing at 1100 °C

Results for yttria annealing experiments at 1100 °C are very similar to those obtained at 900 °C (described above). We did not run special experiments to determine the content of the amorphous phase in the samples at the beginning of thermal treatment, for the amorphous phase disappeared at 1100 °C more quickly than the 5 min interval noted for 900 °C experiments, where amorphous components made up less than 1% of the samples after 5 min annealing.

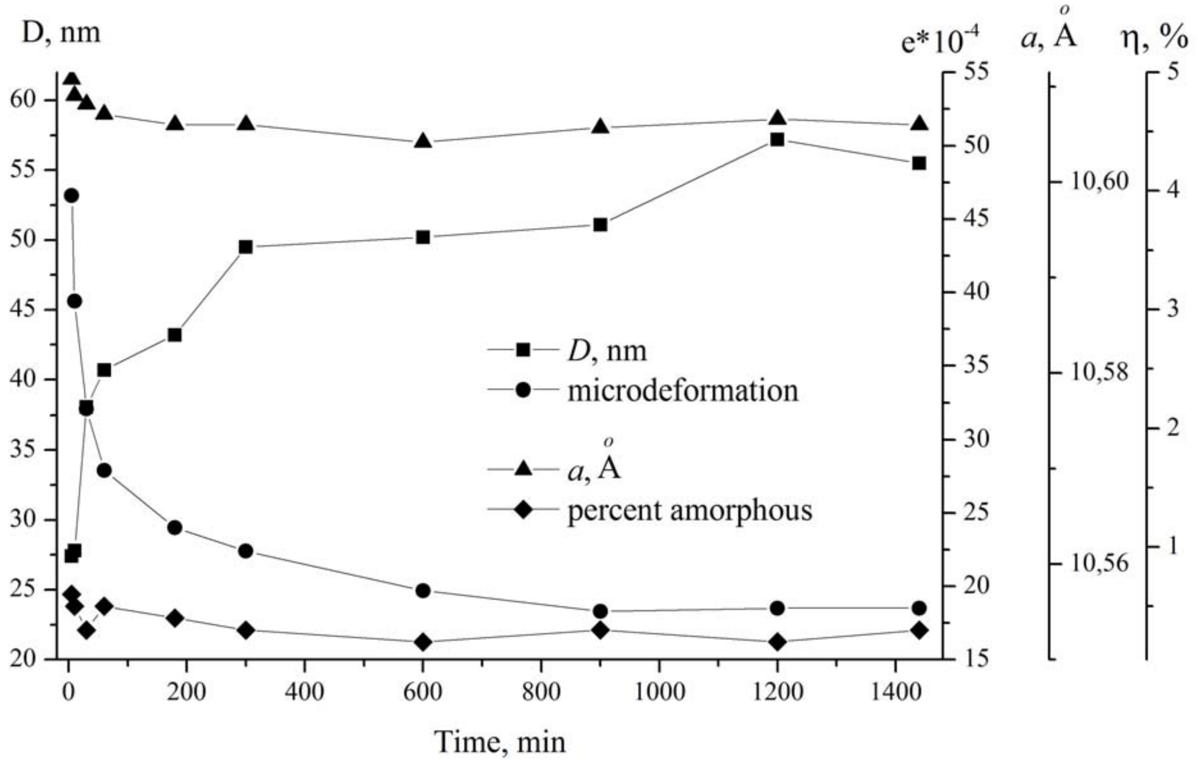

FIG. 4. Microstructure parameters of 900 °C annealed yttria crystalline nanopowder (D is the domains of coherent scattering (DCS), nm; a – cell parameter, Å)

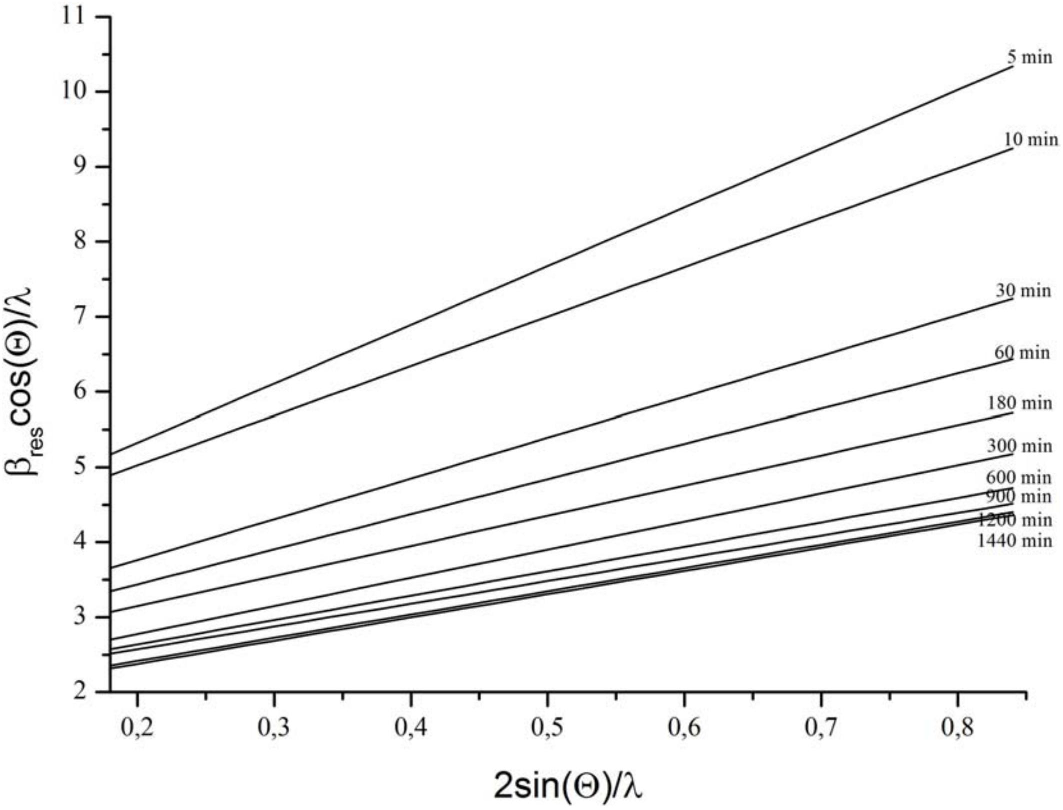

FIG. 5. Williamson-Hall charts for yttria crystalline nanopowder isothermally annealed at 900 °C

At 1100 °C, we observed the same dynamics of peak intensity growth and diminishing half-widths of diffraction lines (Fig. 6), and the most essential observation in these data was that diffraction peak broadening still remained after 420 min annealing.

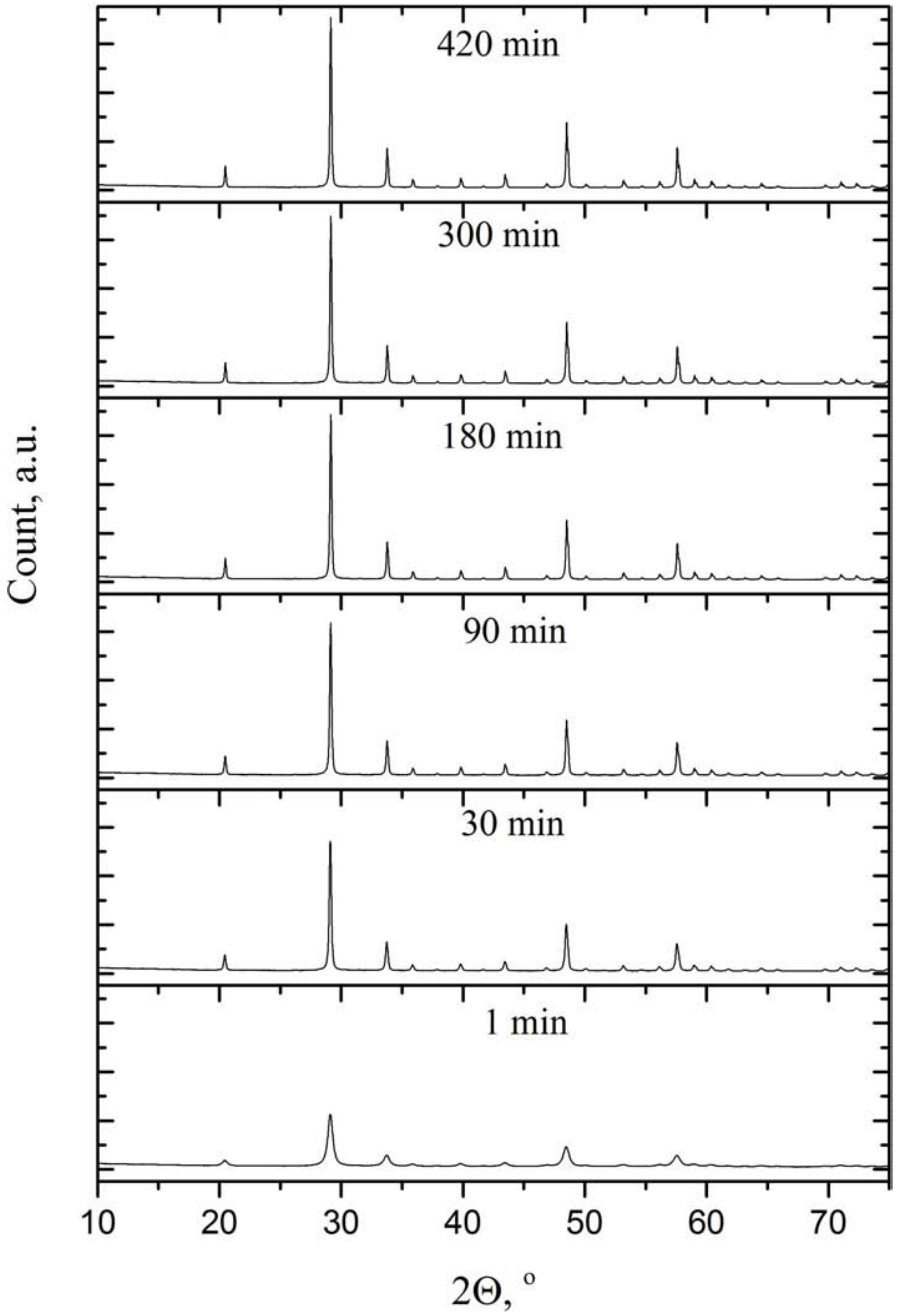

FIG. 6. Yttria nanopowder X-ray diffraction patterns after isothermal annealing at 1100 °C for different times

Scanning electron microscopy (SEM) study of 1100 °C annealed yttria nanoparticles has shown that at the earlier stages of thermal treatment, they possessed platelet shapes (Fig. 7a) – the same shape that existed for yttria precursor, basic yttrium hydroxynitrate. However, if hydroxynitrate demonstrated anisotropic DCS (e.g., see anisotropic diffraction peak broadening for basic yttrium hydroxynitrate in Fig. 1 and its particle images in Fig. 2), the formed yttria

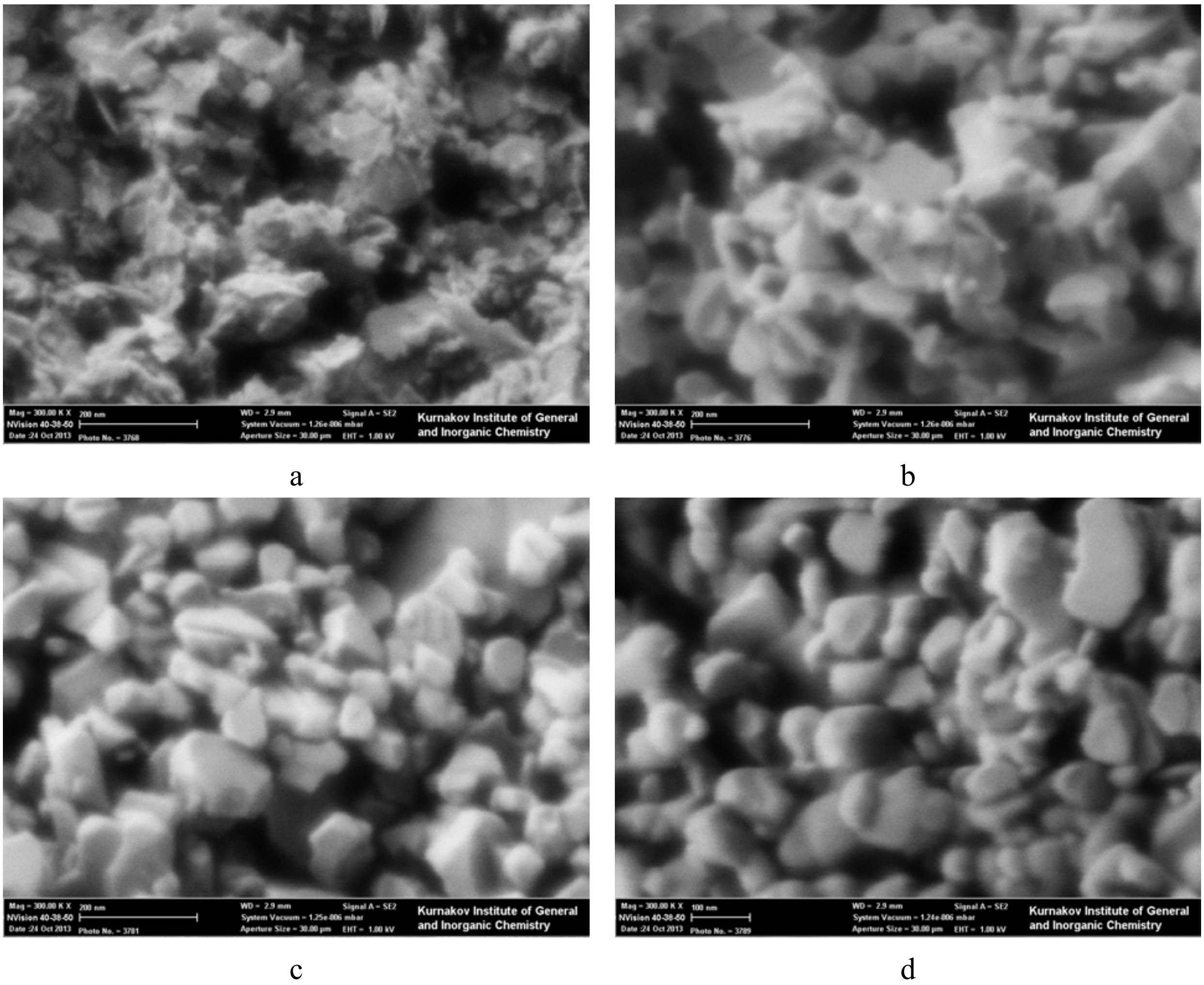

FIG. 7. Scanning electron microscopy (SEM) images of yttria nanoparticles annealed at 1100 °C for 1 min (a), 90 min (b), 300 min (c) and 420 min (d).

nanoparticles did not have such anisotropic character. It is quite probable that at the very early stage of the synthesis, in the course of basic nitrate thermolysis, yttria nanoparticles emerged from their precursor as polycrystalline aggregates made up of independent crystallites. Each platelet formed could have a texture that went undetected by X-ray diffraction method because these platelets were not mutually oriented. Yttria nanoparticles grow in size with increased annealing time, and one can clearly see this in Fig. 7b for the sample heated for 90 min: in addition to increasing the particle size, the deterioration of platelets as well as formation of sphere shaped nanoparticles and – somewhere – even crystal faces are quite visible. Further heating (Fig. 7c and 7d) led to the complete disappearance of the initial platelets and the formation of the larger properly shaped particles with clearly visible faces.

Changes in the microstructure and lattice parameters of 1100 °C annealed yttria nanoparticles are similar to the ones observed in 900 °C experiments (Fig. 8), including step-like changes for DCS values after the same 200 min annealing. Similarly, Williamson-Hall charts for 1100 °C experiments (Fig. 9) showed that the significant qualitative changes in particle microstructure occurred within first 30 min of thermal treatment. All linear fits in Fig. 9 had R^2-factor close to 1.0 thus confirming applicability of isotropic approximation for nanoparticles and their microdeformations.

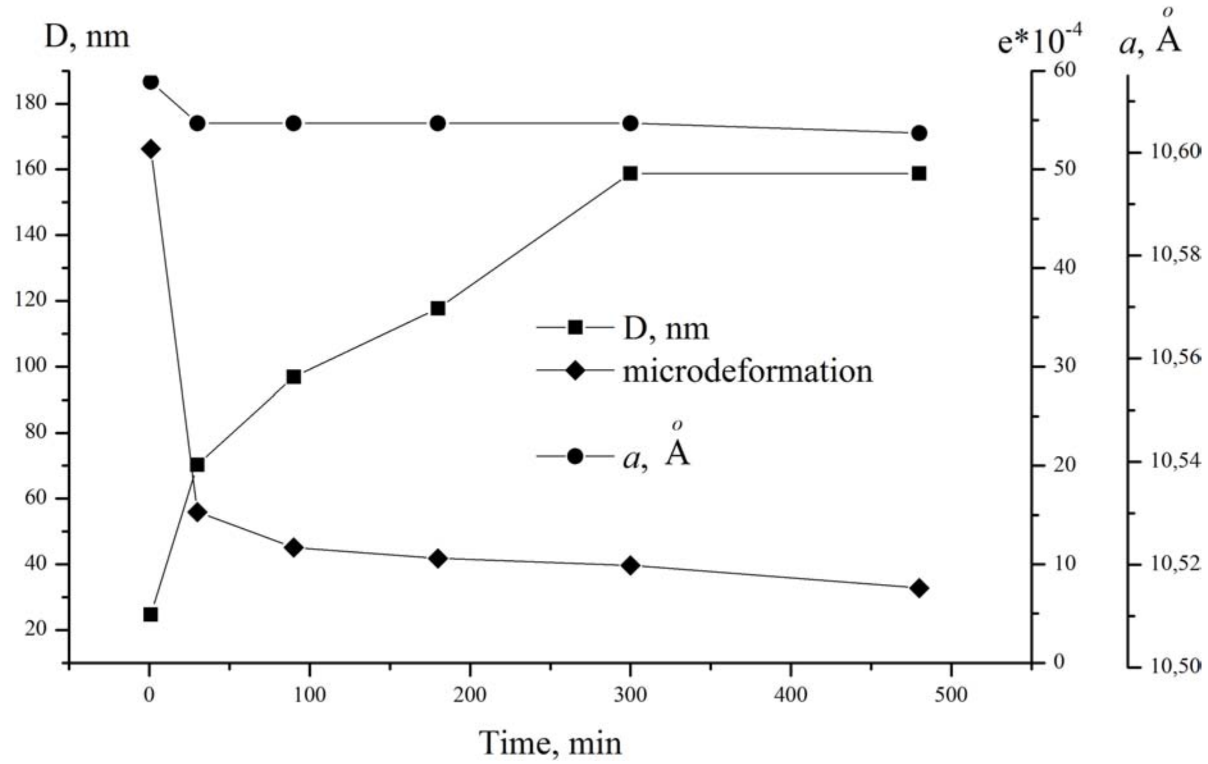

FIG. 8. Microstructure parameters of 1100 °C annealed yttria crystalline nanopowder (D is the domains of coherent scattering (DCS), nm; a – cell parameter, Å)

4. Conclusions

In conclusion, our study has confirmed that the yttria nanopowder precursor, yttrium basic hydroxynitrate, had a platelet morphology which was passed on to the newly-formed yttria nanoparticles during hydroxynitrate thermolysis. The fact that this platelet particle shape was retained at the earlier stages of yttria annealing is in complete agreement with the earlier results of Fedorov et al. [8].

Secondly, our experimental data have proven that the newly formed yttria nanocrystalline platelets were, in fact, polycrystalline aggregates of spherical crystallites incoherently scattering X-ray irradiation (yttria platelets could have had texture, too).

Thirdly, the above experimental data unequivocally indicate that the annealed yttria nanoparticles underwent fast DCS growth and a decline in microdeformations at the beginning of their thermal treatment. Further annealing caused only minor changes in the particle microstructure. This conclusion can be easily supported by the aforementioned Williamson-Hall charts (Figs. 4 and 8). We also suggest that for each annealing temperature, there will be the certain microstructure conditions that would remain unchanged, regardless of the duration of further isothermal annealing. The correlation between the sample's stationary state and its annealing temperature is presented in Fig. 10. However, in order to comment on this correlation and/or explain step-by-step character of DCS changes in the course of annealing, one needs to study the size distribution of the DCS in yttria nanosamples. The latter was outside of the scope of the present work, but will be addressed and discussed in our future publications.

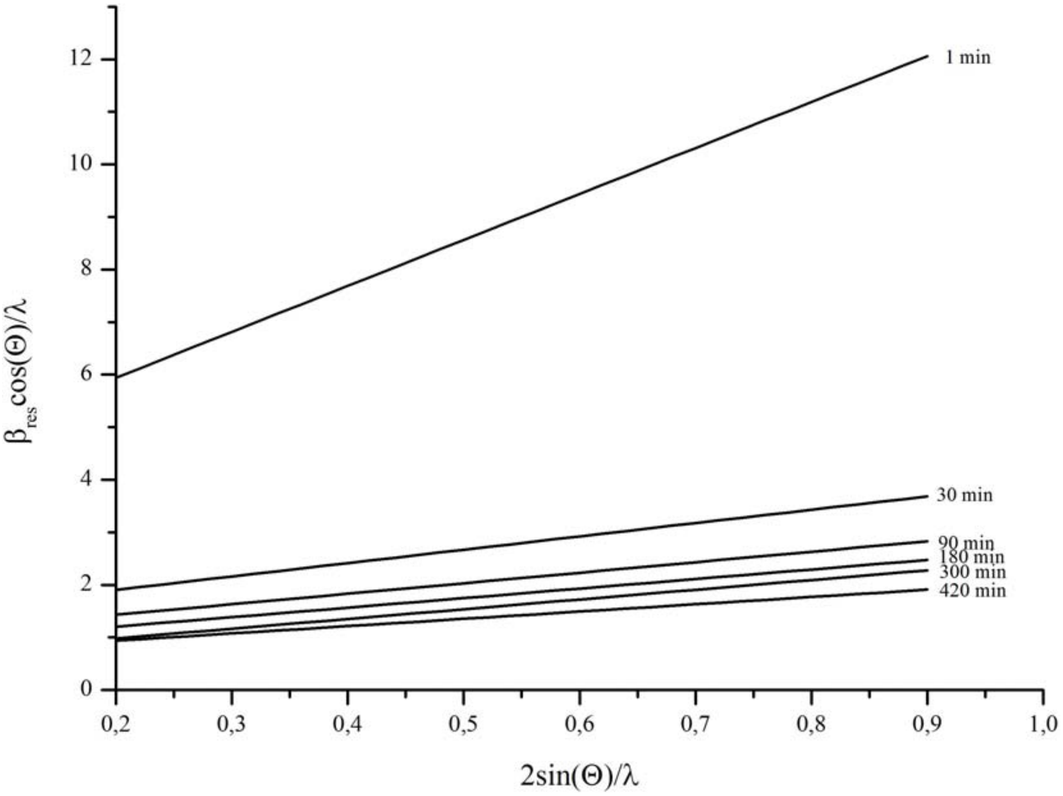

FIG. 9. Williamson-Hall charts for yttria crystalline nanopowder isothermally annealed at 1100 °C

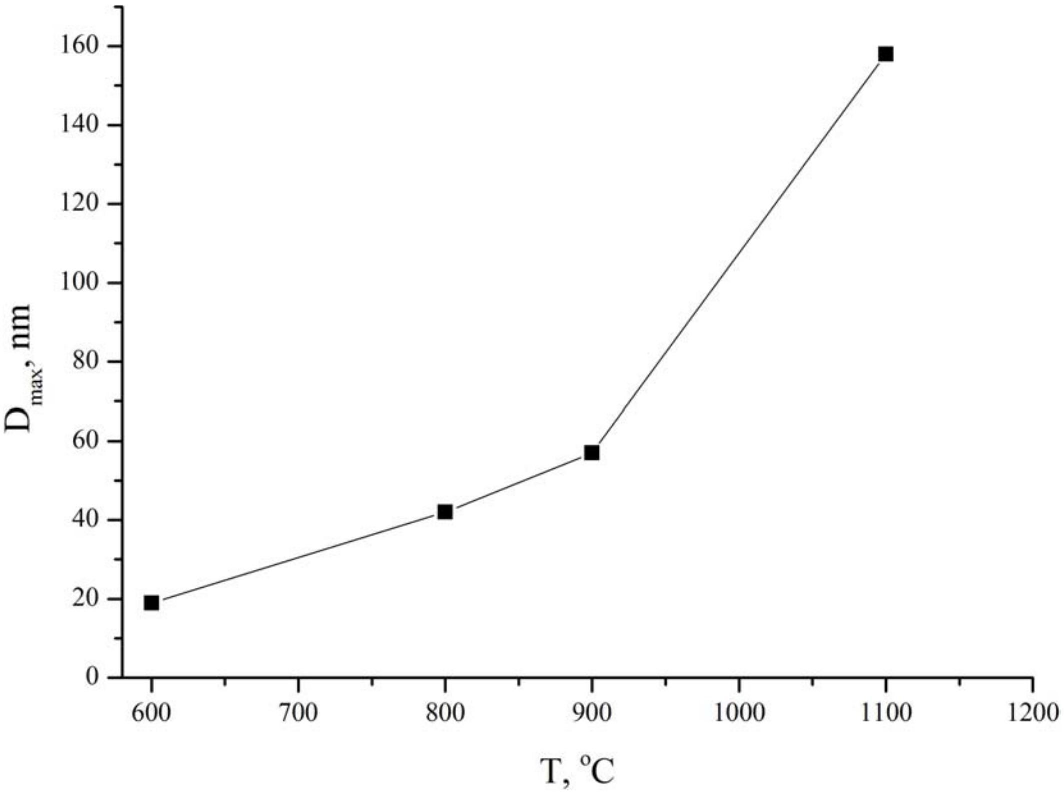

FIG. 10. Maximum DCS value of isothermally annealed yttria particles vs. annealing temperature

References

[1] Ermakov R.P, Fedorov P.P., Voronov V.V. X-ray diffraction study of the phase and morphology changes in yttrium compound nanoparticles. *Nanosystems: physics, chemistry, mathematics*, **4** (2), P. 196–205 (2013).

[2] Sanghera J., Shaw B., Kim W. et al. Ceramic laser materials. *Solid State Lasers XX: Technology and Devices*, Proc. SPIE 7912, 79121Q (2011).

[3] Lupei V., Lupei A., Ikesue A. Single crystal and transparent ceramic Nd-doped oxide laser materials: a comparative spectroscopic investigation. *Journal of Alloys and Compaunds*, **380**, P. 61–70 (2004).

[4] Greskovich ., Chernoch J.P. Polycrystalline ceramic lasers. *J. Appl. Phys.*, **44**, P. 4599–4606 (1973).

[5] Ikegami T., Mori T., Li J., Moriyoshi Y. Fabrication of transparent yttria ceramics by the low-temperature synthesis of yttrium hydroxide. *J. Amer. Ceram. Soc.*, **85**, P. 1725–1729 (2002).

[6] Mouzon J. Synthesis of Yb: Y_2O_3 Nanoparticles and Fabrication of Transparent polycrystalline yttria ceramics. Thesis. Lulea University of Technology. Sweden (2005).

[7] Baranchikov A. E., Ivanov V. K., Dmitriev A. V., et al. Chemical transformations of basic yttrium nitrates during ultrasonic-hydrothermal treatment. *Russian J. Inorg. Chem.*, **51** (11), P. 1689–1695 (2006).

[8] Fedorov P.P., Voronov V.V., et al. Evolution of Yttria nanoparticle ensembles. *Nanotecnologies in Russia*, **5** (9–10), P. 624–634 (2010).

[9] Ivanov V. K., Baranchikov A. E., Vanetsev A. S. et al. Effect of hydrothermal and ultrasonic/hydrothermal treatment on the phase composition and micromorphology of yttrium hydroxocarbonate. *Russian J. Inorg. Chem.*, **52** (9), P. 1321–1327 (2007).

[10] Fedorov P. P., Tkachenko E. A., et al. Yttrium Oxide Nanopowders from Carbonate Precursors. *Russian J. Inorg. Chem.*, **55** (6), P. 883–889 (2010).

[11] Cheary R.W., Coelho A.A. A fundamental parametrs approach to X-ray line-profile fitting. *J. Appl. Cryst.*, **25**, P. 109–121 (1992).

[12] Cheary R.W., Coelho A.A., Cline J.P. Fundamental Parametrs Line Profile Fitting in Laboratory Diffractometrs. *J. Res. Natl. Inst. Standt. Technol.*, **109**, P. 1–25 (2004).

[13] Rodriguez-Carvajal J., Roisnel T. Line broadening analysis using FullProf*: Determination of microstructural properties. *European powder diffraction Epdic*, **443** (4), P. 123–126 (2004).

[14] Pawley G.S. Unit-cell refinement from powder diffraction scans. *J. Appl. Cryst.*, **14**, P. 357–361 (1981).

[15] LeBail A., Duroy H., Fourquet J.L. Abanitio structure determination of LiSbWO4 by X-ray powder diffraction. *Mat. Res. Bull.*, **23**, P. 447–452 (1998).

[16] Rietveld H.M. A profile refinement method for nuclear and magnetic structures. *J. Appl. Cryst.*, **2**, P. 65–71 (1969).

[17] Finger L.W. PROFVAL: functions to calculate powder-pattern peak profiles with axial divergence asymmetry, *J. Appl. Cryst.*, **31**, P. 111 (1998).

[18] Williamson G.K., Hall W.H. X-ray line broadening from filed aluminium and wolfram. *Acta Metallurgica*, **1**, P. 22–31 (1953).

NANOSYSTEMS: PHYSICS, CHEMISTRY, MATHEMATICS, 2013, 4 (6), P. 772–777

INTERFERENCE EFFECTS IN MICROCHIP LASER WITH INTRACAVITY FREQUENCY DOUBLING

[1,2]M. I. Kerobyan,
[1] Institute for physical research, NAS RA, Ashtarak, Armenia
[2] Spectralus CJSC, Yerevan, Armenia
kerobyan.mk@gmail.com

PACS 42.79.Nv, 42.55.Rz

The temperature dependence of output power of microchip laser with intracavity frequency doubling is investigated, where oscillations in the output power are observed. Similar oscillations are observed in the temperature tuning of single pass second harmonic generation in plane parallel nonlinear crystal. It is supposed that in both two cases the oscillations have the same origin. Single pass second harmonic generation is investigated experimentally and theoretically, and it is shown that oscillations are due to multiple beam interference in the nonlinear crystal. Results of the experiments and calculations are presented.

Keywords: Microchip laser, quasi-phase matching, optical second harmonic generation, intracavity frequency doubling.

1. Introduction

Second harmonic generation (SHG) in a nonlinear plane parallel slab has been treated for the first time by Bloembergen and Pershan in 1962 [1], where they took into account the boundary conditions at a plane interface between a linear and nonlinear medium. Since then, interference effects in SHG have been investigated extensively. Several authors report on oscillating behavior of SHG power as a function of wavelength or thickness of the crystal in case of single pass second harmonic generation [2–6]. SHG in plane parallel nonlinear crystal is of interest for us, because it plays important role in the microchip laser with intracavity frequency doubling.

To the best of our knowledge, there are no published papers on the temperature dependence of interference effects in SHG in plane parallel nonlinear crystal. The motivation for this work is the development of green microchip lasers. Microchip laser with intracavity frequency doubling is of great interest, because it is an efficient, powerful and miniature source of green (532nm) light. The cavity of the laser is composed of two planar components: gain crystal is a Nd^{3+}:YVO_4 (YV) and nonlinear crystal is a periodically polled MgO:$LiNbO_3$ (PPLN) [7]. These crystals are optically contacted. Mirrors of the cavity are formed by dielectric coatings directly applied to the crystal surfaces. Input mirror is high reflective (HR) at both fundamental (1064nm) and second harmonic wavelengths (532nm) and anti-reflective (AR) at pump wavelength (808nm). Output mirror is AR at 532nm and HR at 1064nm. Efficiency of pumping depends on the temperature. We use 808nm absorption peak of the YV. Full width at half maximum (FWHM) for π-polarization absorption peak is about 1.8nm. Laser diodes at 808nm are used as a pumping source. The emitting wavelength of these diodes strongly depends on the temperature (typically $d\lambda_{em}/dT \approx 0.3\text{nm}/^{\circ}\text{C}$). Therefore, only 3°C variation of the temperature will halve the peak absorption coefficient. The efficiency of quasi-phase-matched SHG in the nonlinear crystal also strongly depends on the temperature. Thus, investigation of the temperature dependence of microchip laser output power is important in order to improve the energy conversion efficiency and power stability.

2. Temperature dependence of microchip output intensity

To investigate temperature dependence of microchip output, we performed a series of experiments, where the temperature of the laser diode was kept constant with precision of 0.1°C, to avoid fluctuation of the pump wavelength. Temperature of the microchip laser was changed in the range of $20-60$°C and output intensity was registered at different temperatures. The experimental setup is depicted in Fig.1.

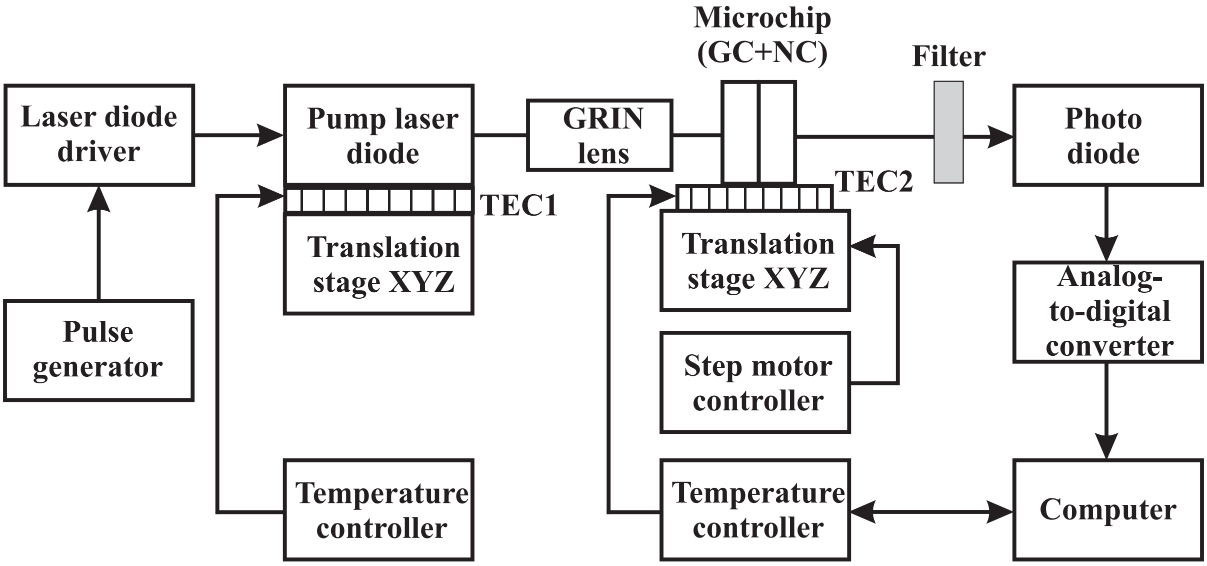

Fig. 1. Experimental setup for measuring temperature dependence of microchip output power

Measurement results are presented in Fig. 2. It can be seen, that there are two kinds of temperature dependence of laser power. The first one (Fig. 2a) is a relatively smooth curve, and two others (Fig. 2b and c) have distinct periodic oscillations. The oscillation period is typically $\tau = (5.4 \pm 0.5)^\circ$ C.

We suppose that oscillations are a result of multiple beam interference in the nonlinear crystal. The most probable reason for the difference in the performance of three microchips shown in Fig. 2 is different residual reflection from the interface between the gain crystal and the nonlinear crystal. For perfect optical contact, the Fresnel reflection from the interface is negligible because the refractive indices of YV and PPLN are nearly equal. The ratio of two refractive indices is 1.032, which gives about 10^{-4}% Fresnel reflection for normal incidence. However, imperfect optical contact (contamination, air bubbles etc.) may lead to higher residual reflection from the interface. We have developed a method for measuring reflection from the interface in high finesse resonator [8], and it was shown that microchips with oscillating behavior have notable reflection from the optically contacted interface, typically higher than 2%. To understand the origin of oscillations observed in the temperature dependence of microchip laser power, we performed theoretical and experimental study of single pass SHG in a plane parallel nonlinear crystal, identical to that used in the microchip laser.

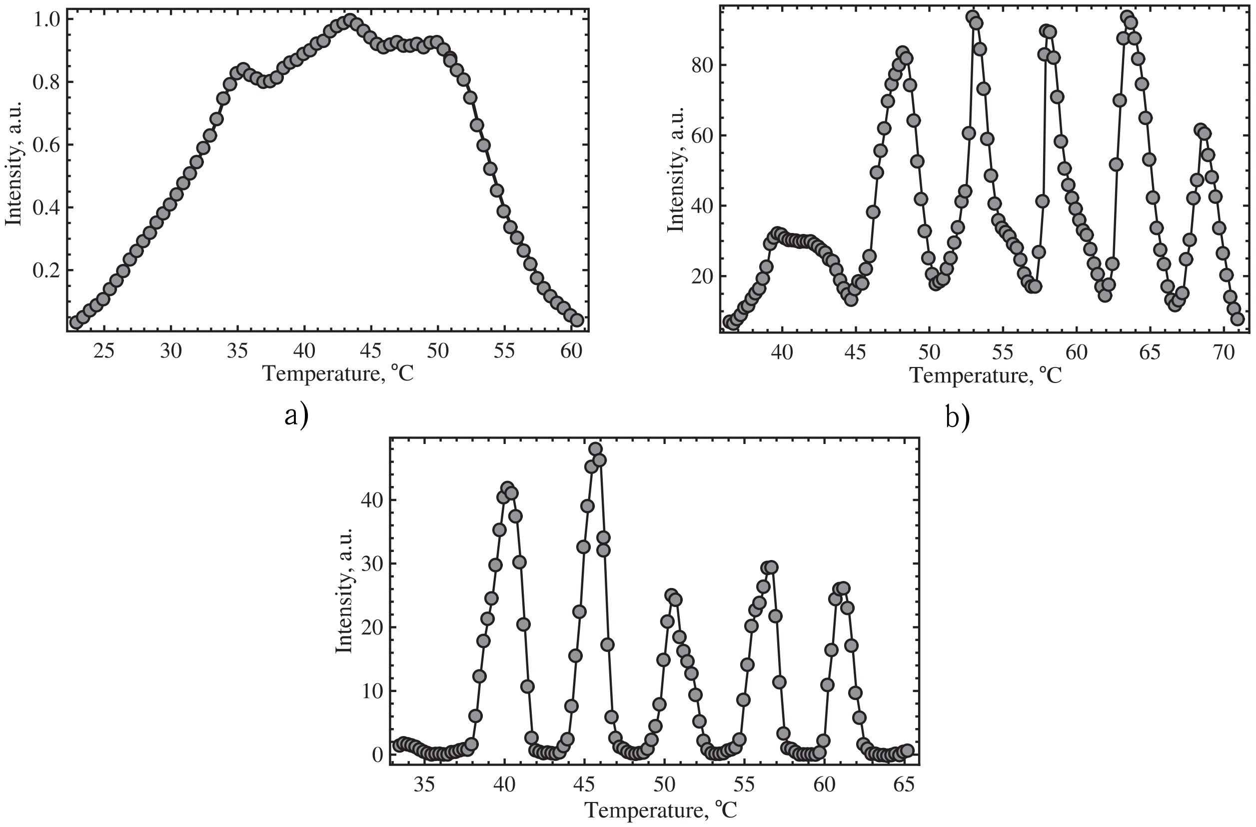

a) b)

c)

Fig. 2. Measurement results of temperature dependence of output power for three different microchips: a) Relatively smooth curve, b,c) Curves with periodic oscillations

3. Single pass SHG

In this section, calculations of the temperature dependence of SHG intensity in a plane-parallel nonlinear crystal are presented and compared to experimental results.

First, the wave equation for second harmonic field is solved [9].

$$\frac{d^2}{dz^2}E_2(z) - \frac{\omega_2^2}{c^2}\varepsilon_2 E_2(z) = \frac{4\pi\omega_2^2}{c^2}P_{NL}(z) \tag{1}$$

where $E_2(z)$ is the electric field of SH wave inside the nonlinear crystal, $P_{NL}(z) = 4d_{eff}E_1^2(z)$ is the nonlinear part of the polarization, d_{eff} is the effective nonlinear susceptibility, $E_1(z)$ is the electric field of the fundamental wave inside the nonlinear crystal, ε_2 is the dielectric susceptibility of the crystal for second harmonic wave, ω_2 is the frequency of the second harmonic wave, c is the speed of light.

Inside the nonlinear crystal, the electric field of the fundamental wave is the sum of multiple reflected waves from the boundaries of the crystal, thus solution of the wave equation is also sought in the form of sum of two waves, propagating in opposite directions $E_2(z) = A_2^+(z)e^{ik_{2\omega}(z)} + A_2^-(z)e^{-ik_{2\omega}(z)}$. To take into account interference between second harmonic waves, we should take into account reflections from the boundaries of the crystal, and write down the appropriate boundary conditions.

$$\begin{cases} A_2^-(l) = r_{2,2\omega} A_2^+(l) e^{2ik_{2\omega}l} \\ A_2^+(0) = r_{1,2\omega} A_2^-(0) \end{cases} \tag{2}$$

where $A_2^+(z)$ and $A_2^-(z)$ are amplitudes of electric field of the second harmonic wave propagating forward and backward in the crystal. $r_{1,2\omega}$ and $r_{2,2\omega}$ are amplitude reflection coefficients of first and second boundaries of the nonlinear crystal for second harmonic wave, l is the length of the crystal. Equation (1) is solved under the following approximations:

1. *Plane wave*. We consider fundamental and second harmonic waves as plane waves.
2. *Undepleted pump*. We consider that fundamental wave amplitude is constant during the propagation through the nonlinear medium, or in other words, second harmonic power is negligible compared to the fundamental power.
3. *Slowly varying amplitude*. We assume that $|d^2A_2/dz^2| \ll |k_2(dA_2/dz)|$. This approximation allows us to reduce the order of differential equation and (2) boundary conditions will be enough to solve it.

Output intensity of the second harmonic wave is equal to

$$I_2 \propto \frac{64\pi^2 {d_{eff}}^2 \omega_2^4}{c^4} l^2 |E_0|^4 \mathrm{sinc}^2\left(\frac{\Delta kl}{2}\right)(FP_\omega)^2 FP_{2\omega} \tag{3}$$

where: $\Delta k = 2k_\omega - k_{2\omega} - 1/\Lambda$ is the phase mismatch, k_ω and $k_{2\omega}$ are wave vectors of the fundamental and second harmonic waves Λ is the domain period of the periodically polled nonlinear crystal, in case of quasi-phase matched second harmonic generation, E_0 is the amplitude of the pump waves electric field, $FP_\omega = (1 + F_\omega \sin(k_\omega l))^{-1}$ and $FP_{2\omega} = (1 + F_{2\omega} \sin(k_{2\omega} l))^{-1}$ are Airy functions describing Fabry-Perot interference for fundamental and second harmonic waves, $F_\omega = 4r_{1,\omega} r_{2,\omega}(1 + r_{1,\omega} r_{2,\omega})^{-2}$ and $F_{2\omega} = 4r_{1,2\omega} r_{2,2\omega}(1 + r_{1,2\omega} r_{2,2\omega})^{-2}$ are finesse of the Airy functions, $r_{1,\omega}$ and $r_{2,\omega}$ are amplitude reflection coefficients of the first and second boundaries of the nonlinear crystal for fundamental wave.

Analyzing formula (3), one can see, that output intensity is the product of 3 functions: sinc function, and two Airy functions describing Fabry-Perot interference. Airy functions in Equation (3) are responsible for the oscillations. They have different oscillating periods: $\tau_\omega = \lambda(n_\omega l(\alpha + \gamma_\omega))^{-1}$ for FP_ω and $\tau_{2\omega} = \lambda(2n_{2\omega} l(\alpha + \gamma_{2\omega}))^{-1}$ for $FP_{2\omega}$, where α is the thermal expansion coefficient of nonlinear crystal for a-axis direction (direction of light propagation). n_ω, γ_ω and $n_{2\omega}, \gamma_{2\omega}$ are extraordinary refractive index and thermo-optic coefficients for fundamental and second harmonic waves, respectively. Polarization of the fundamental and second harmonic waves are parallel to the c-axis of the crystal, and they propagate parallel to the a-axis. The input face of the crystal is polished and its intensity reflection coefficient is about 14% (Fresnel reflection). A dichroic mirror which is antireflective (AR) at 532nm and highly reflective (HR) at 1064nm is applied to the output surface of the crystal.

In Fig. 3 second harmonic intensity versus temperature, calculated with the formula 3 and experimental results are shown with solid line and markers, respectively. The experiment was conducted with a 1.5mm long PPLN plate, identical to the one used in the microchip laser. As a pump source, a CW, 1064nm Nd^{3}+YVO_4 single longitudinal mode laser was used.

Properties of the PPLN used in the calculations are shown in the Table 1.

It can be seen from the Fig. (3) that there is only one oscillation period, so only one Airy function is involved. The reason is the different finesse of the Fabry-Perot

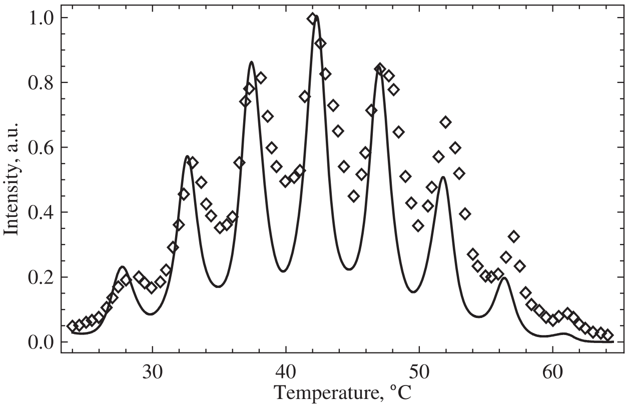

Fig. 3. Calculated and observed temperature dependence of single pass SHG in 1.5mm PPLN

Table 1. Properties of PPLN

Parameter	Value
Length	$l = 1.5mm$
Thermal expansion coefficient	$\alpha = 14.44 * 10^{-6}{}^{\circ}\mathrm{C}^{-1}$
n_e(44°C) at 1064nm	$n_1(44)$=2.148333
n_e(44°C) at 532nm	$n_2(44)$=2.224830
Domain grating period	$\Lambda = 6.94\mu$
Effective nonlinear susceptibility	$d_{eff} = 14pV/m$

interferometer for the fundamental and second harmonic wavelengths. Because of the AR properties of the output mirror, finesse at 532nm is negligible compared to the finesse at 1064nm, so only oscillations caused by multiple beam interference at 1064nm are present. The observed oscillation period for single pass SHG is $\tau_O = (5.1 \pm 0.5)$°C, which is in a good agreement with the calculated value of $\tau_\omega = 4.8$°C.

It can be seen from the Fig. (3) that theoretical calculations clearly predict oscillating behavior of the SHG intensity versus temperature.

4. Conclusion

Investigation of the temperature dependence of microchip output power shows oscillating behavior. Analysis of second harmonic generation in the plane parallel nonlinear crystal shows that oscillations are due to multiple beam interference in the nonlinear crystal. It is supposed that the oscillations in the microchip output power have the same origin. Detailed calculations for interference in the resonator of microchip laser will be conducted in the future.

Acknowledgements

The author is grateful to Dr. Suren Soghomonyan and Anna Gyulasaryan from Spectralus CJSC for valuable discussions and support in the experiments.

References

[1] N. Bloembergen, P. S. Pershan. Light Waves at the Boundary of Nonlinear Media. *Physical Review*, **128**(2), P. 606–622 (1962).

[2] J. P. Van Der Ziel. Effect of Fabry-Perot Interference on Second Harmonic Generation in a GaAs Plate. *IEEE Journal of Quantum Electronics*, **QE-12**(7), P. 407–411 (1976).

[3] R. Morita, T. Kondo, Y. Kaneda, A. Sugihashi, N. Ogasawara, S. Umegaki. Multiple-Reflection Effects in Optical Second-Harmonic Generation. *Japanese Journal of Applied Physics*, **27**(6), P. L1134–L1136 (1988).

[4] W. N. Herman, L. M. Hayden. Maker fringes revisited: second-harmonic generation from birefringent or absorbing materials. *Journal of Optical Society of America B*, **13**(3), P. 416–427 (1995).

[5] G. Buinitskaya, I. Kravetsky, L. Kulyuk, V. Mirovitskii, E. Rusu. Optical second harmonic generation in ZnO Film: multiple-reflection effects, *Moldavian Journal of Physical Science*, **1**(4), P. 77–82 (2002).

[6] G. Telier, C. Boisrobert. Second harmonic generation: Effects of the multiple reflections of the fundamental and the second harmonic waves on the Maker fringes. *Optics Communications*, **279**, P. 183–195 (2007).

[7] S. Essaian, J. Khaydarov, S. Slavov, V. Ter-Mikirtychev, G. Gabrielyan, M. Kerobyan, S. Soghomonyan. Microchip green laser sources: broad range of possibilities. *Proceedings of SPIE*, **8240**, P. 82400I-1–82400I-8 (2000).

[8] M. Kerobyan, A. Gyulasaryan, A. Khachikyan, S. Soghomonyan, G. Gabrielyan, S. Essaian. Measurement of residual reflection at the interface between optically contacted components of microchip laser. *Optics Communications*, **311**(C), P. 38–43 (2013).

[9] W. R. Boyd. Nonlinear Optics (3rd edition). Academic Press, New-York (2008).

NANOSYSTEMS: PHYSICS, CHEMISTRY, MATHEMATICS, 2013, 4 (6), P. 778–794

SPECTRA OF COHERENT TRANSMITTANCE AND REFLECTANCE OF PERIODIC, FIBONACCI, AND THUE-MORSE MULTILAYERS OF DIELECTRIC PARTICLES

A. A. Miskevich, V. A. Loiko

B.I. Stepanov Institute of physics of NAS of Belarus,
68 Nezalezhnastsi ave., Minsk, 220072, Belarus
miskevic@dragon.bas-net.by, loiko@dragon.bas-net.by

PACS 78.67.Pt, 42.70.Qs, 61.44.-n, 68.65.Ac

Coherent transmittance and reflectance of multilayers consisting of one-dimensional Fibonacci, Thue-Morse, and periodic sequences of plane-parallel ordered monolayers of spherical alumina and silica particles are investigated in the 0.3 μm to 2 μm spectral range. Consideration is based on the quasicrystalline approximation for individual monolayers and the transfer matrix method for multilayers. Comparison with sequences of the homogeneous plane-parallel layers is made. It is shown that the Fibonacci and Thue-Morse structures provide more possibilities to control light in comparison with the regular ones. These results can be used for the development of optical filters, solar cells, light emitting diodes, displays, etc.

Keywords: photonic crystal, non-periodic sequence, quasicrystalline approximation, transfer matrix method, coherent transmittance and reflectance.

1. Introduction. Statement of the problem

Currently, ordered structures, such as photonic crystals (PC) and quasicrystals (PQC) are the subject of intense research because they allow one to solve the problems concerning the of control of spectral, temporal and spatial characteristics of light, and thus, to create new types of intensity, phase, and polarization modulators [1-21]. There is a set of natural biological systems which have ordered and quasi-ordered photonic crystal structures [22-24]. Great attention is paid to periodic and non-periodic ordered structures due to the photonic band gap effect [1-3]. Interest in the study of non-periodic ordered structures is caused by the additional possibilities (relative to periodic structures) to control the characteristics of transmitted and reflected light. For example, quasiperiodic PCs can be used to enhance the efficiency of light-emitting diodes [6]. Usually, Fibonacci (quasiperiodic) [10-16] and Thue-Morse (aperiodic) [16-17] sequences of the constituents are considered for such structures. Periodic structures possess the long-range order, while quasiperiodic and aperiodic photonic crystals display long-range and short-range orders.

The one-dimensional (1D) Fibonacci sequence L_n of symbols A and B is built according to the inflation rule $L_n = L_{n-1}L_{n-2}$ (for $n \geqslant 2$, where n is the number of the sequence element), beginning from $L_0 = A$ and $L_1 = AB$: $L_0 = A$, $L_1 = AB$, $L_2 = ABA$, $L_3 = ABAAB$, $L_4 = ABAABABA$,.... The 1D Thue-Morse sequence L_n of symbols A and B is built according to the rule $L_n = L_{n-1}\, \underline{L}_{n-1}$ (for $n \geqslant 1$, where $\underline{L}_{n-1}$ element is “inverted” L_{n-1} element), beginning from $L_0 = A$: $L_0 = A$, $L_1 = AB$, $L_2 = ABBA$, $L_3 = ABBABAAB$, $L_4 = ABBABAABBAABABBA$, ... The A and B symbols indicate sequence constituents with different properties.

Generally, sequences of homogenous layers are considered. The periodic (regular), Fibonacci, and Thue-Morse sequences of the homogeneous layers are schematically presented in Fig. 1. The symbols A and B in this figure indicate different layer types.

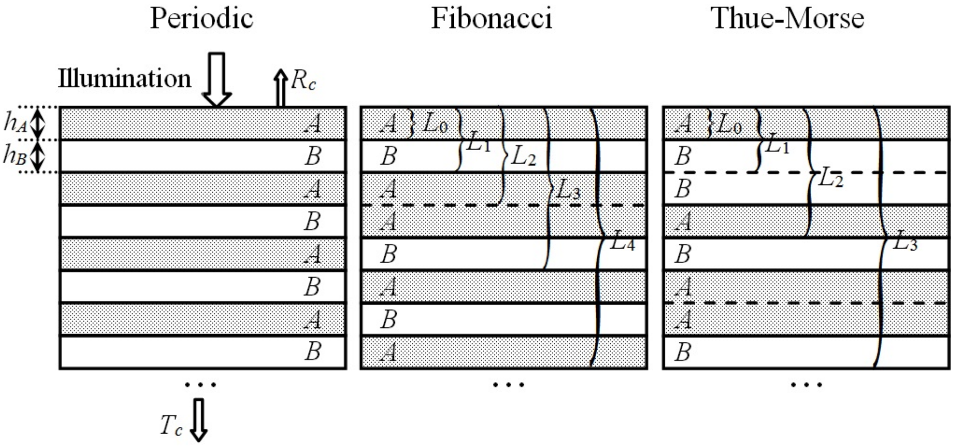

FIG. 1. Schematic representation of layered structures with the periodic (regular), Fibonacci, and Thue-Morse sequences consisting of A and B types of homogeneous layers (side view). With normal illumination, T_c and R_c are the coherent transmission and reflection coefficients, respectively, while h_A and h_B are the thicknesses of the A and B layer types, respectively. The dashed lines denote the "virtual interfaces" between the layers of the same type, and L_n are the sequence elements

The sequences of homogeneous layers are well studied theoretically and experimentally [25–28]. However, structures consisting of non-periodic sequences of particle monolayers have not been sufficiently investigated yet. Such structures provide a new means for photonics applications.

In this work, we investigate theoretical aspects of the spectra of coherent transmission and reflection coefficients of multilayers consisting of periodic, Fibonacci and Thue-Morse sequences of the plane-parallel monolayers of the monodisperse spherical dielectric particles. We consider multilayers consisting of alumina (Al_2O_3) and silica (SiO_2) particles monolayers because these materials are widely used in photonic and optoelectronic devices. The schematic representation of such structures is given in Fig. 2.

It is worth noting that generally, monolayers are mutually independent and can be shifted along the dashed lines depicted in Fig. 2.

The spectral dependences of the real part of the Al_2O_3 and SiO_2 refractive indices $n(\lambda)$ (λ is the wavelength of the incident light) are shown in Fig. 3 [29]. The imaginary parts of the refractive indices in this spectral range for both materials are zero.

2. Coherent transmittance and reflectance of monolayer. Basic equations

We use the quasicrystalline approximation (QCA) [30-34] of the statistical theory of the multiple scattering of waves [30,35-36] to calculate the coherent transmission T_c and reflection R_c coefficients of the monolayer of particles. We write them as follows [31-34]:

$$T_c = |t_c|^2 = \left| 1 - \frac{\eta}{x^2} \sum_{j=1}^{N} (2j+1)(z_j + y_j) \right|^2 , \tag{1}$$

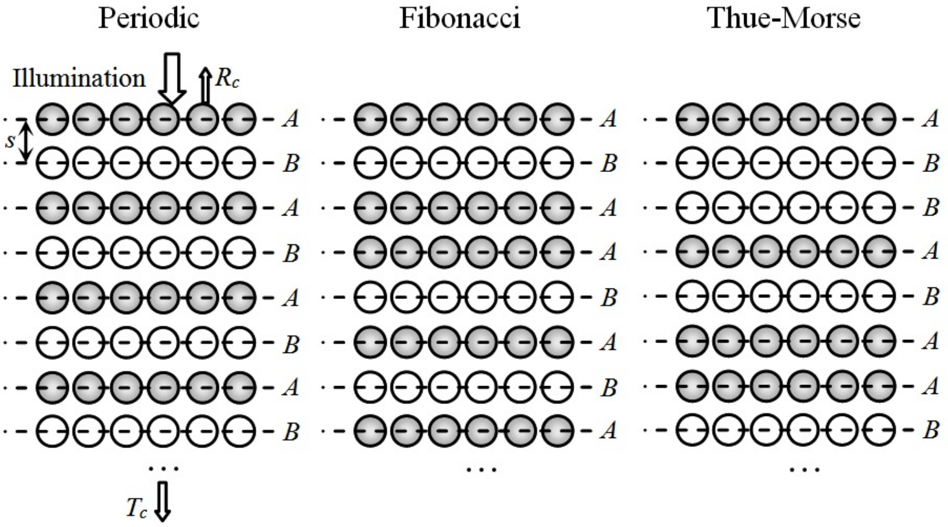

FIG. 2. Schematic representation of the layered structures consisting of the periodic (regular), Fibonacci, and Thue-Morse sequences of particulate monolayers of type A and type B (side view). Illumination is normal to the monolayers planes depicted by the dashed lines. T_c and R_c are the coherent transmission and reflection coefficients, respectively; s is the spacing between the adjacent monolayers

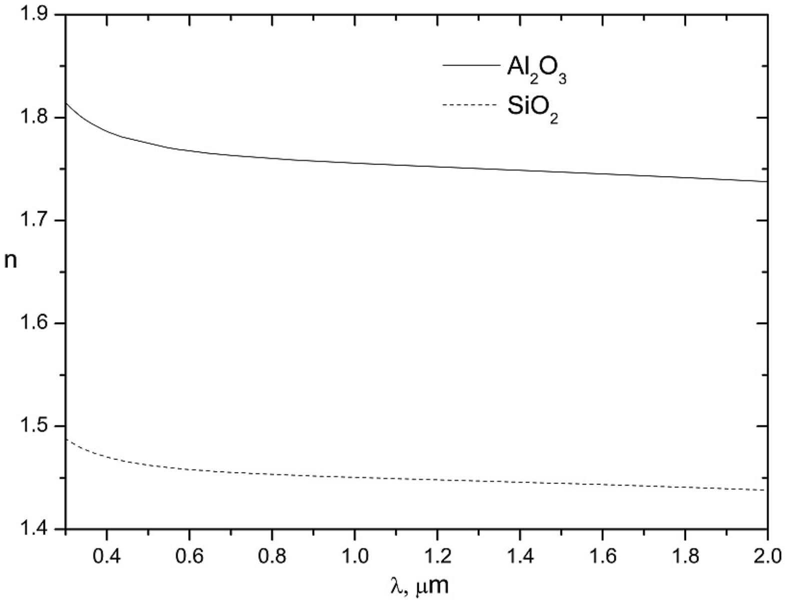

FIG. 3. Spectral dependences of the refractive index n of Al_2O_3 and SiO_2

$$R_c = |r_c|^2 = \left| -\frac{\eta}{x^2} \sum_{j=1}^{N} (-1)^j (2j+1)\,(z_j - y_j) \right|^2 . \tag{2}$$

Here, t_c and r_c are the amplitude coherent transmission and reflection coefficients, respectively, η is the monolayer filling coefficient (the area fraction of the monolayer determined as the ratio of the projection areas of all particles to the area, where they are located), x=πD/λ is the size parameter of particle with diameter of D, λ is the wavelength of the incident light, $N = x$+$4.05x^{1/3}$+2 is the number of terms of the scattering series [37]. The z_j and y_j coefficients are found from the solution of the system of equations:

$$\begin{cases} z_l = b_l + \rho_0 b_l \sum\limits_{j=1}^{N} (A_{lj} z_j + B_{lj} y_j) \\ y_l = a_l + \rho_0 a_l \sum\limits_{j=1}^{N} (A_{lj} y_j + B_{lj} z_j) \end{cases}, \tag{3}$$

where a_l and b_l are the Mie coefficients for the particle size parameter x and complex refractive index $m = n + i\kappa$, ρ_0 is the averaged particle concentration in monolayer. The coefficients A_{lj} and B_{lj} are found from the solution of equations:

$$\begin{gathered} A_{lj} = \tfrac{2j+1}{2} \left[l(l+1) j(j+1) \right]^{-\frac{1}{2}} \times \\ \times \sum_{p=0,2,\ldots}^{N} i^{-p} (2p+1) \left[l(l+1) + j(j+1) - p(p+1) \right] P_p(0) \times \\ \times \begin{pmatrix} l & j & p \\ 0 & 0 & 0 \end{pmatrix} \begin{pmatrix} l & j & p \\ 1 & -1 & 0 \end{pmatrix} H_p, \end{gathered} \tag{4}$$

$$\begin{gathered} B_{lj} = \tfrac{2j+1}{2} \left[l(l+1) j(j+1) \right]^{-\frac{1}{2}} \times \\ \times \sum_{p=0,2,\ldots}^{N} i^{-p} (2p+1) \left[(p+l-j)(p-l+j)(l+j+1+p)(l+j+1-p) \right]^{\frac{1}{2}} P_p(0) \times \\ \times \begin{pmatrix} l & j & p-1 \\ 0 & 0 & 0 \end{pmatrix} \begin{pmatrix} l & j & p \\ 1 & -1 & 0 \end{pmatrix} H_p, \end{gathered} \tag{5}$$

$$H_p = 2\pi \int_D^{\infty} g(R) h_p^{(1)}(kR) R dR. \tag{6}$$

Here, g(R) is the radial distribution function [38-39], $h_p^{(1)}(x)$ is the spherical Hankel function of the first kind and p-th order, $k = 2\pi/\lambda$ is the wavenumber, $\begin{pmatrix} j_1 & j_2 & j_3 \\ m_1 & m_2 & m_3 \end{pmatrix}$ is the Wigner 3j-symbol [40]. To solve Eq. (6), we use the methods described in [31-34].

In the QCA, the coefficients T_c and R_c are determined by the sum of waves scattered by the particles, taking into account their re-illumination and correlation in their spatial locations. The correlation is described by the radial distribution function (RDF), which characterizes the probability of any particle's location in space relative to another one. There is a problem of calculating the RDF at high ordering of particles to make it applicable for the QCA. Recently, we proposed one of the solutions to this problem. We developed a method of calculating the RDF of a near-to-regularly-packed monolayer of spherical particles [33,34]. Such a monolayer represents the planar photonic crystal (PPC) [41-43]. To calculate the RDF of the PPC, we select the center of any particle as the coordinate origin and compute radii of the coordination circles [38,33,34] of the ideal crystal lattice and the number of particle centers for each circle. The distance dependence of the number of particle centers in an ideal lattice is a set of the infinitely narrow peaks at distances equal to the coordination circle radii. Accordingly, the RDF of such a lattice has nonzero values at these distances and zero otherwise. Actual crystals typically have a nonideal lattice with coordination circles “blurred” into the “rings” with the fuzzy edges. Consequently, the peaks of the RDF are blurred as well. We showed [33,34] that the expression for the RDF g(u) of the near-to-regularly-packed monolayer can be written as:

$$g(u) = \rho_0^{-1} \sum_i \frac{N_i}{2\pi R_i} \frac{1}{\sqrt{2\pi}\sigma(u)} \exp\left(-\frac{(u-R_i)^2}{2\sigma^2(u)}\right). \tag{7}$$

Here, $\sigma(u)$ is a blurring function that characterizes the broadening of the peaks with distance u. It is reasonable to use the linear blurring function:

$$\sigma(u) = \sigma_0(au + b). \tag{8}$$

In Eqs. (7) and (8), $u = R/D$ is the dimensionless distance, expressed in particle diameters D ($u \geqslant 1$); R is the distance in a monolayer plane relative to the coordinate origin (see Eq. (6)); ρ_0 is the averaged numerical particle concentration in the monolayer; N_i is the number of particle centers on the coordination circle with radius R_i of an ideal crystal. The ordering degree and the scale of spatial order of the simulated crystals are specified by changing of σ_0, and the a and b coefficients, respectively. Equation (7) takes into account the asymmetry of the RDF’s individual peaks, which are observed experimentally. This allows us to calculate the RDFs of the PCs in a wide range of their ordering degrees. The RDF obtained with Eq. (7) and Eq. (8) is well adapted for utilization in the QCA. The calculation of such a RDF and, consequently, coherent transmission and reflection coefficients of the PPC in the QCA, is fast and requires low amount of computational resources. The RDF of a highly ordered crystal is a sequence of narrow peaks at small $u = R/D$ values (i.e. in the region near to the coordinate origin). With increased u-values, the peaks become wider, the function oscillates and converges to unity. Note that at $\sigma(u)$=const, Eq. (7) transforms into the known expression which describes the Gaussian blurring of peaks [39].

To obtain the RDF of the partially-ordered particle monolayers, we use the solution of the Ornstein-Zernike integral equation [44]. We numerically calculate it in the Percus-Yevick approximation [45] for a system of hard spheres by the iteration method [46]. Note that this function is deduced from the Poisson statistics while taking into account the finite particle size [46,47].

Figure 4 depicts the calculated spectra of the coherent transmission T_c and reflection R_c coefficients and their sum ($T_c + R_c$) for monolayers with nonideal triangular particle lattice and for partially-ordered monolayers. The RDF of the monolayer with a triangular lattice is calculated using the blurring function $\sigma(u) = \sigma_0 u$ at σ_0=0.01, while the filling coefficient of monolayers is η=0.5, diameter of particles is D=0.3 μm.

The plots display the influence that the spatial ordering of particles in the monolayer has on coherent transmission and reflection coefficients. At wavelengths comparable with the particle size, spectra of the regularly-packed monolayers have the sharp peaks caused by periodicity in the particle locations. For $\lambda \geqslant 0.35$ μm, the $T_c + R_c$ sum of the regularly-packed monolayers is unity (see Fig. 4c). At these wavelengths, practically all radiation transmits straight through the monolayers and reflects straight back. This means that the incoherent (diffuse) component [46] of radiation is negligible. The $T_c + R_c$ sum of the partially-ordered monolayers monotonically increases from $\lambda \approx 0.41$ μm (for monolayer of SiO_2 particles) and

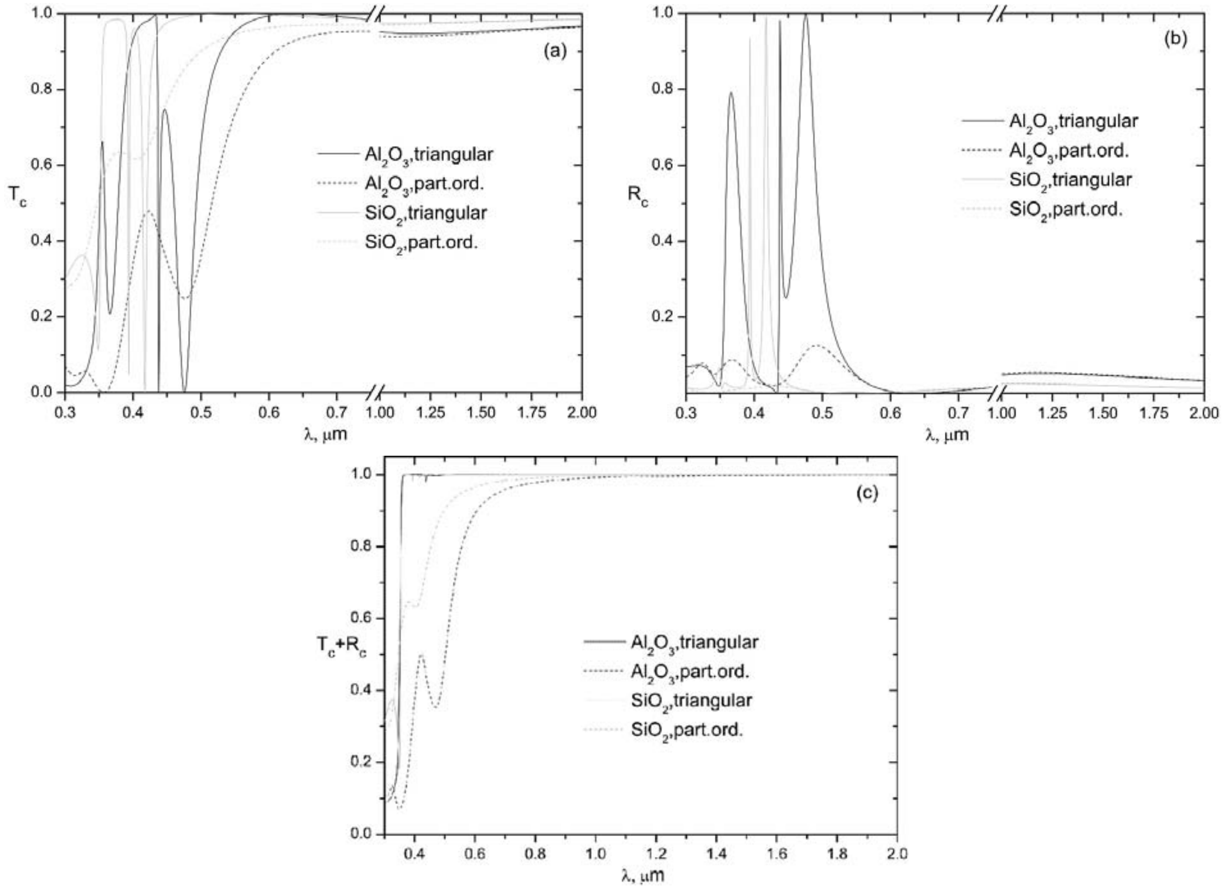

FIG. 4. Spectral dependence of the coherent transmission T_c (a) and reflection R_c (b) coefficients and their sum T_c+R_c (c) of the individual monolayers with a triangular lattice (solid lines) of monodisperse spherical Al_2O_3 (black lines) and SiO_2 (gray lines) particles and the partially-ordered monolayers (dashed lines) of the same particles. Diameter of particles is D=0.3μm. Filling coefficient of monolayers is η=0.5. $\sigma(u) = \sigma_0 u$ at σ_0=0.01

from λ $\approx$0.5 μm (for a monolayer of Al_2O_3 particles) and tends to unity with increased wavelength.

3. Transmittance and reflectance of a multilayer structure

3.1. Basic equations

The amplitude coherent transmission t_c and reflection r_c coefficients obtained in the QCA for individual monolayers [see Eqs.(1),(2)] are used to calculate coherent transmission and reflection coefficients of the multilayer under the transfer matrix method (TMM) [25-27]. We consider the monolayers as interfaces and the spaces between them as the layers. Under the TMM, the amplitude coherent transmission t and reflection r coefficients of a multilayer can be written as follows [25,27]:

$$t = \frac{1}{T_{11}}, \tag{9}$$

$$r = \frac{T_{21}}{T_{11}}, \tag{10}$$

where T_{ij} are elements of the transfer matrix $\mathbf{T}$ of the multilayer. For a system of N interfaces the transfer matrix $\mathbf{T}$ can be written as [25,27]:

$$\mathbf{T}_{0,N} = \begin{bmatrix} T_{11} & T_{12} \\ T_{21} & T_{22} \end{bmatrix} = \begin{bmatrix} \frac{1}{t_{0,N}} & \frac{-r_{N,0}}{t_{0,N}} \\ \frac{r_{0,N}}{t_{0,N}} & \frac{t_{0,N}t_{N,0}-r_{0,N}r_{N,0}}{t_{0,N}} \end{bmatrix}. \tag{11}$$

Here, $t_{0,N}$ and $r_{0,N}$ are the amplitude coherent transmission and reflection coefficients of the multilayer for the forward propagating wave, $t_{N,0}$ and $r_{N,0}$ are the amplitude coherent transmission and reflection coefficients of the multilayer for the backward propagating wave.

The transfer matrix of a multilayer is calculated by the sequential multiplication of the transfer matrices of interfaces $\mathbf{T}_j$ with the propagation matrices of the layers $\mathbf{P}_j$:

$$\mathbf{T}_{0,N} = \left(\prod_{j=1}^{N-1} \mathbf{T}_j \mathbf{P}_j \right) \mathbf{T}_N, \tag{12}$$

where

$$\mathbf{T}_j = \begin{bmatrix} \frac{1}{t_{j-1,j}} & \frac{-r_{j,j-1}}{t_{j-1,j}} \\ \frac{r_{j-1,j}}{t_{j-1,j}} & \frac{t_{j-1,j}t_{j,j-1}-r_{j-1,j}r_{j,j-1}}{t_{j-1,j}} \end{bmatrix}, \tag{13}$$

is the matrix of j-th interface,

$$\mathbf{P}_j = \begin{bmatrix} \exp(-ik_jh_j) & 0 \\ 0 & \exp(ik_jh_j) \end{bmatrix}, \tag{14}$$

is the propagation matrix of j-th layer, $t_{j-1,j}$ and $r_{j-1,j}$ are the amplitude coherent transmission and reflection coefficients of j-th interface for the forward propagating wave; $t_{j,j-1}$ and $r_{j,j-1}$ are the amplitude coherent transmission and reflection coefficients of j-th interface for the backward propagating wave (we calculate these coefficients in the QCA, see Eqs. (1),(2)); the wave number is $k_j=2\pi \mathrm{m}_j/\lambda$, m_j and h_j are the complex refractive index and thickness of j-th layer, respectively.

The energy coherent transmission T_c and reflection R_c coefficients of the multilayer are the squares of the absolute values of the amplitude coefficients:

$$T_c = |t|^2 = \left| \frac{1}{T_{11}} \right|^2, \tag{15}$$

$$R_c = |r|^2 = \left| \frac{T_{21}}{T_{11}} \right|^2. \tag{16}$$

3.2. Spectra of structures with different number of monolayers

Let us consider multilayers with different number of monolayers arranged in different sequences. Under the approach used, we study only the coherent component of radiation. That is why we restrict our consideration to the spectral range where the incoherent (diffuse) component is negligible.

Figure 5 depicts the spectra of the coherent transmission and reflection coefficients of the multilayers consisting of monolayers arranged in the regular, Fibonacci, and Thue-Morse sequences. The individual monolayers have the nonideal triangular lattice of monodisperse spherical Al_2O_3 and SiO_2 particles with a filling coefficient η=0.9. The spacing s (see Fig. 2) between the adjacent monolayers is 0.3 μm. These parameters correspond to the three-dimensional (3D) ordered disperse structure, which is similar to the structure of the colloidal crystal. The symbols A and B denote the monolayer of Al_2O_3 and SiO_2 particles, respectively.

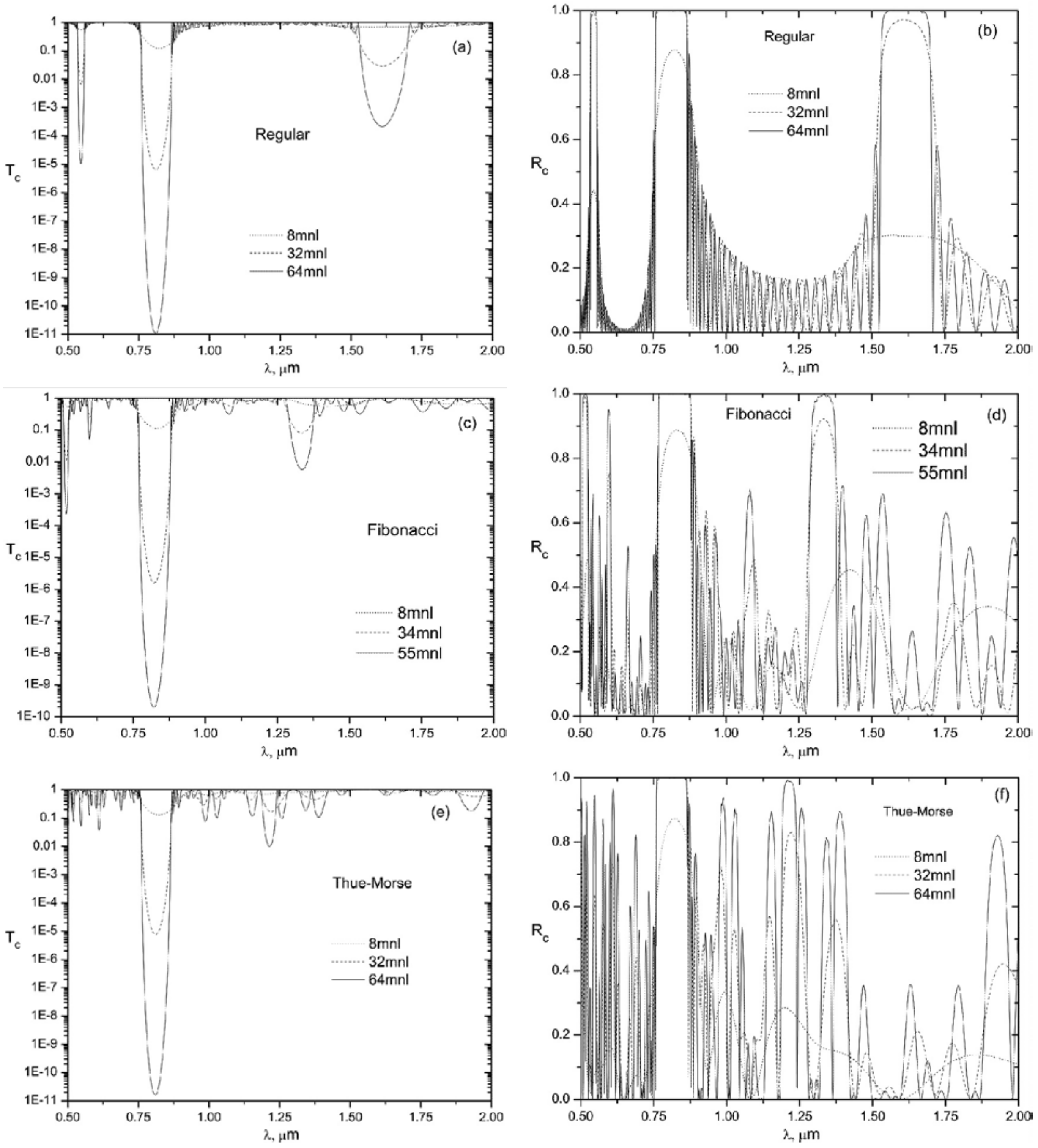

FIG. 5. Spectra of coherent transmission T_c (a),(c),(e) and reflection R_c (b),(d),(f) coefficients of the multilayer consisting of regular (a),(b), Fibonacci (c),(d), and Thue-Morse (e),(f) sequences of monolayers with a triangular lattice of monodisperse spherical Al_2O_3 (type A) and SiO_2 (type B) particles. Diameter of particles is D=0.3 μm. Filling coefficient of monolayers is η=0.9. The number of monolayers is 8, 32, 64 (a),(b),(e),(f), and 8, 34, 55 (c),(d). Blurring function is $\sigma(u) = \sigma_0 u$, σ_0=0.001. Spacing between adjacent monolayers is s=0.3 μm

As follows from the presented results, with an increased number of monolayers, photonic band gaps (PBGs) occur in the spectra of all considered sequences. In the spectrum of the regular sequence the one “main” and two “secondary” PBGs occur. They are caused by the regularity of the alternating monolayers of A and B types. The “main” PBG is observed in the wavelength range from 0.76 μm to 0.86 μm. The spectra of multilayers with Fibonacci and Thue-Morse sequences are more complicated. The “main” PBGs of their spectra occur practically in the same wavelength range as for the regular sequence. As one can see from Fig. 5(c),(e), the number of PBGs increases with an increased number of monolayers.

3.3. The PBG at different particle materials and filling coefficients of the adjacent monolayers

Let us consider the formation of the “main” PBG in more detail. Figure 6 depicts the coherent transmittance spectra of the layered structures consisting of 34 monolayers arranged in periodic, Fibonacci, and Thue-Morse sequences. This number of monolayers corresponds to the L_7 element of the Fibonacci sequence. The influence of the differences between the A- and B-type monolayers on the transmittance spectra of the multilayer is shown. Different particle materials [Fig. 6(a)] and different filling coefficients [Fig. 6(b)] are considered. The spacing s between adjacent monolayers is 0.3 μm, diameter of particles is D=0.3 μm.

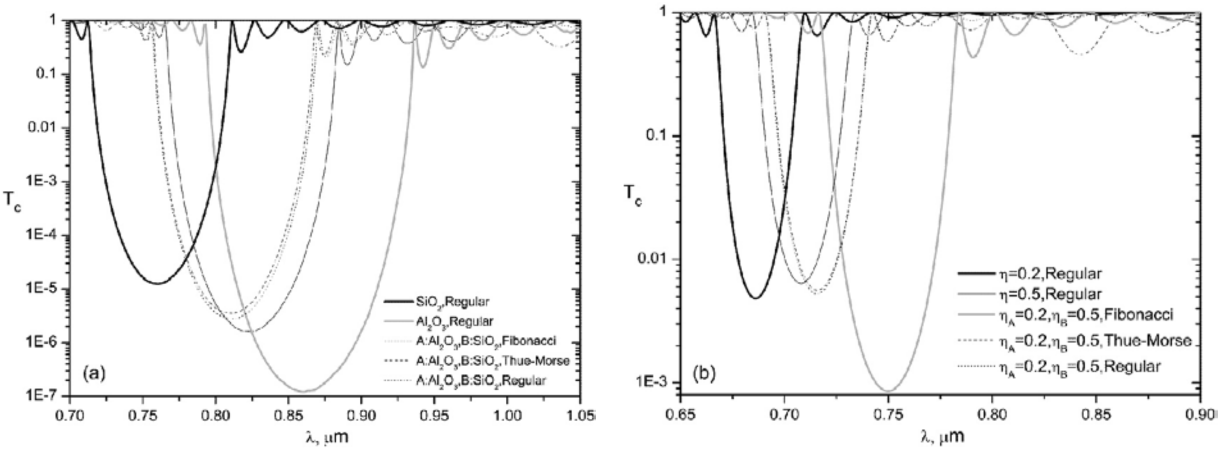

FIG. 6. Transmittance spectra of the layered structures of 34 monolayers arranged in regular, Fibonacci, and Thue-Morse sequences. D=0.3 μm, s=0.3 μm, triangular lattice. (a) sequences of monolayers of Al_2O_3 (type A) and SiO_2 (type B) particles with η=0.9; $\sigma(u) = \sigma_0 u$, σ_0=0.001. (b) sequences of monolayers of Al_2O_3 particles with η_A=0.2 (type A), η_B=0.5 (type B); $\sigma(u) = \sigma_0 u$, σ_0=0.01

The results show that the PBG for the multilayer structure consisting of both A- and B-type monolayers is located between spectral positions of the PBGs for the multilayers composed of only type A and only type B monolayers.

3.4. Spectra of particulate and homogeneous multilayers

The monolayer of particles and the homogeneous layer are different in their structure. The first one has more structural parameters (such as concentration of particles, their shape, size distribution, type of spatial arrangement, etc.), which enhance the potentialities of the layered particulate structure.

Compare the spectra of the multilayer consisting of the plane-parallel homogeneous layers (see Fig. 1) with those of the multilayer consisting of the particulate monolayers (Fig. 2). Consider the influence of particle concentration and spacing between monolayers on the spectra in two cases: (i) the individual particulate and homogeneous layers have the same material volume, (ii) the individual particulate and homogeneous layers have the same thickness.

Figure 7 depicts the coherent transmittance spectra of the multilayers of SiO_2 particles with different filling coefficients. The monolayers (type A) and spacings (type B) between them form the regular (Fig. 7a), Fibonacci (Fig. 7b), and Thue-Morse (Fig. 7c) multilayer structures.

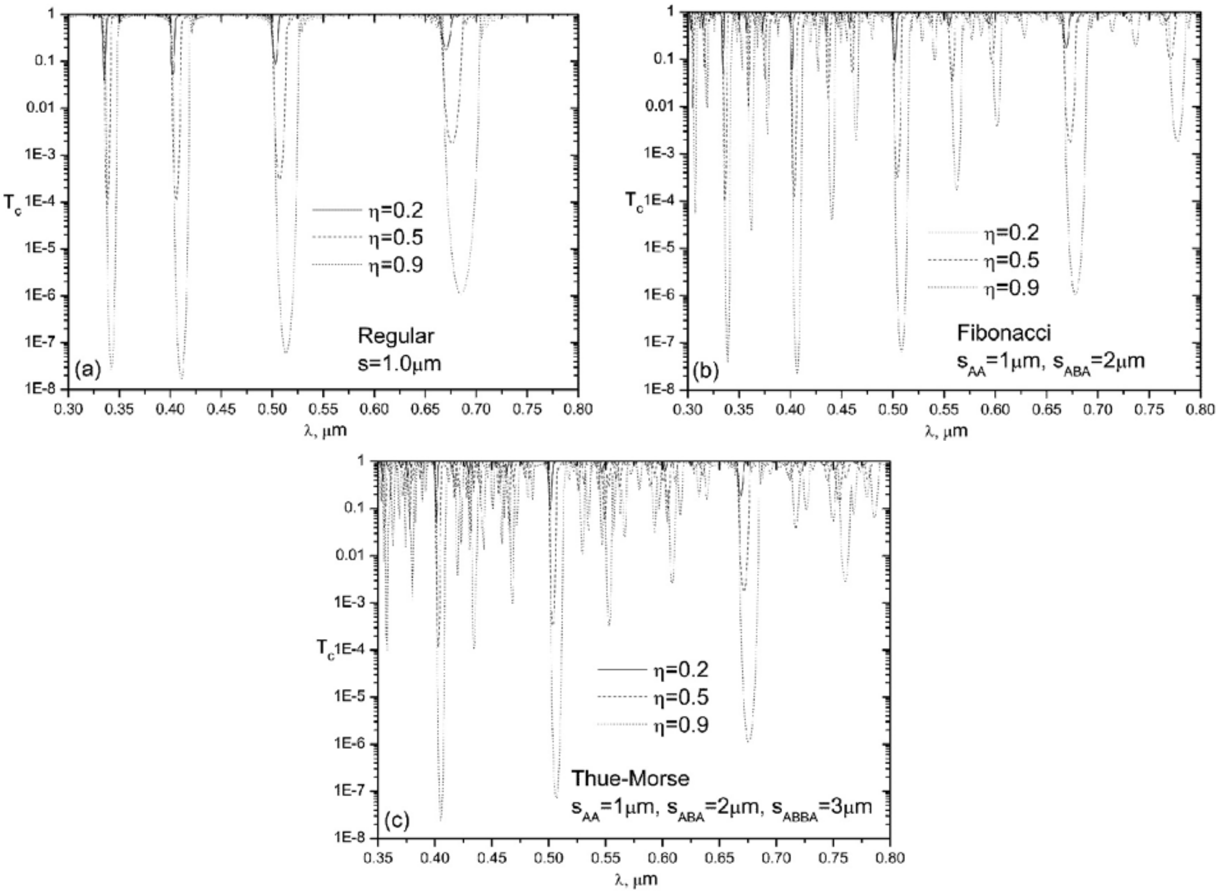

FIG. 7. The coherent transmittance spectra of the multilayers consisting of regular (a), Fibonacci (b), and Thue-Morse (c) sequences of monolayers at different filling coefficient η. The number of monolayers is 32. Individual monolayers (type A) have a triangular lattice of SiO_2 particles with diameter D=0.1 μm. $\sigma(u) = \sigma_0 u$. σ_0=0.01 for η=0.2 and η=0.5. σ_0=0.001 for η=0.9. Spacing (type B) s=1 μm in the regular sequence (a). Spacings in the Fibonacci and Thue-Morse sequences of monolayers:s_{AA}=1 μm for AA, s_{ABA}=2 μm for ABA (b),(c), and s_{ABBA}=3 μm for $ABBA$ subsequences (c)

One can see that increasing the particle concentration in the monolayers leads to an increase in the depth and width of the PBGs. The spectral positions of the PBG minima are slightly shifted as well. The results also show the influence of the spacing between monolayers on the multilayer spectra. The spacing increase leads to an increase in the number of the

PBGs and their shifting to longer wavelengths. The PBGs relating to the Fibonacci and Thue-Morse sequences are typically narrower than the PBGs of the regular sequence, and the number of PBGs is larger.

Changing the particle concentration means changing the amount of material per unit area of a layer. For the plane-parallel homogeneous layer (plate), the amount of material per unit area is proportional to the plate thickness h.

Let us consider multilayers consisting of plane-parallel homogeneous layers with volume that is equal to the volume of particles in the monolayer sequences (their spectra are shown in Fig. 7). We will name such individual homogeneous layers as the equivalent plates. The thickness h of the equivalent plate is calculated as follows:

$$h = \frac{2}{3}\eta D, \tag{17}$$

where η is the filling coefficient of the monolayer of particles with diameter of D. The spectra of sequences consisting of homogeneous SiO_2 layers (type A) and air (type B) are displayed in Fig. 8. The amount of material in homogeneous SiO_2 layers is the same as in the particulate monolayers (Fig. 7).

Comparison of results for the particulate (Fig. 7) and homogeneous (Fig. 8) layers shows that with an increased amount of material in the layers, the depth and width of the PBGs increase. The PBGs of systems with homogeneous layers are typically wider and deeper than those of the particulate systems.

Now, let us calculate the spectra of the multilayer consisting of monolayers of particles with diameters equal to the thickness of the equivalent plate (see Fig. 8), i.e. when $D = h_A$. Figure 9 depicts the transmittance spectra of such a system consisting of the periodic (a), Fibonacci (b), and Thue-Morse (c) sequences of monolayers at η=0.9, which is close to the maximum value $\eta_{\max} \approx$0.907.

The obtained results show that increasing the particle size leads to increases in the depth and width of the PBGs. The positions of PBGs in the spectra of the particulate systems are shifted to shorter wavelengths in comparison to those for homogeneous layer systems.

As follows from the results presented in Figs. 7-9, the PBGs in spectra for multilayers composed of homogeneous layers and of multilayers composed of particulate monolayers are different in their spectral positions, depths, and widths. The positions of PBGs in the spectra of the particulate structures are usually shifted to shorter wavelengths in comparison to those for homogeneous layers. Such a shift is larger for the aperiodic Thue-Morse sequence. The widths of the PBGs of the particulate systems are narrower than those for the homogeneous layer systems.

As one can see from Fig. 7 and Fig. 9, the Fibonacci and Thue-Morse sequences provide additional opportunities for spectrum manipulation in comparison with those for the regular sequence of monolayers. The layered particulate structures can be used in display applications, for creating multispectral filters, light emitting diodes, solar cells, etc.

3.5. Systems with small particles

As one can see from the results of Fig. 4c, the incoherent component of radiation of the partially-ordered monolayer is nonzero (i.e. $T_c + R_c$ <1) for the considered monolayer parameters and the wavelength range. It is well known, that scattering by an individual small (relative to the wavelength of the incident light) dielectric particle decreases with decreasing particle size [48]. As a result, the intensity of radiation scattered by a monolayer of the sufficiently small dielectric particles tends to zero as well. In this case, the T_c and

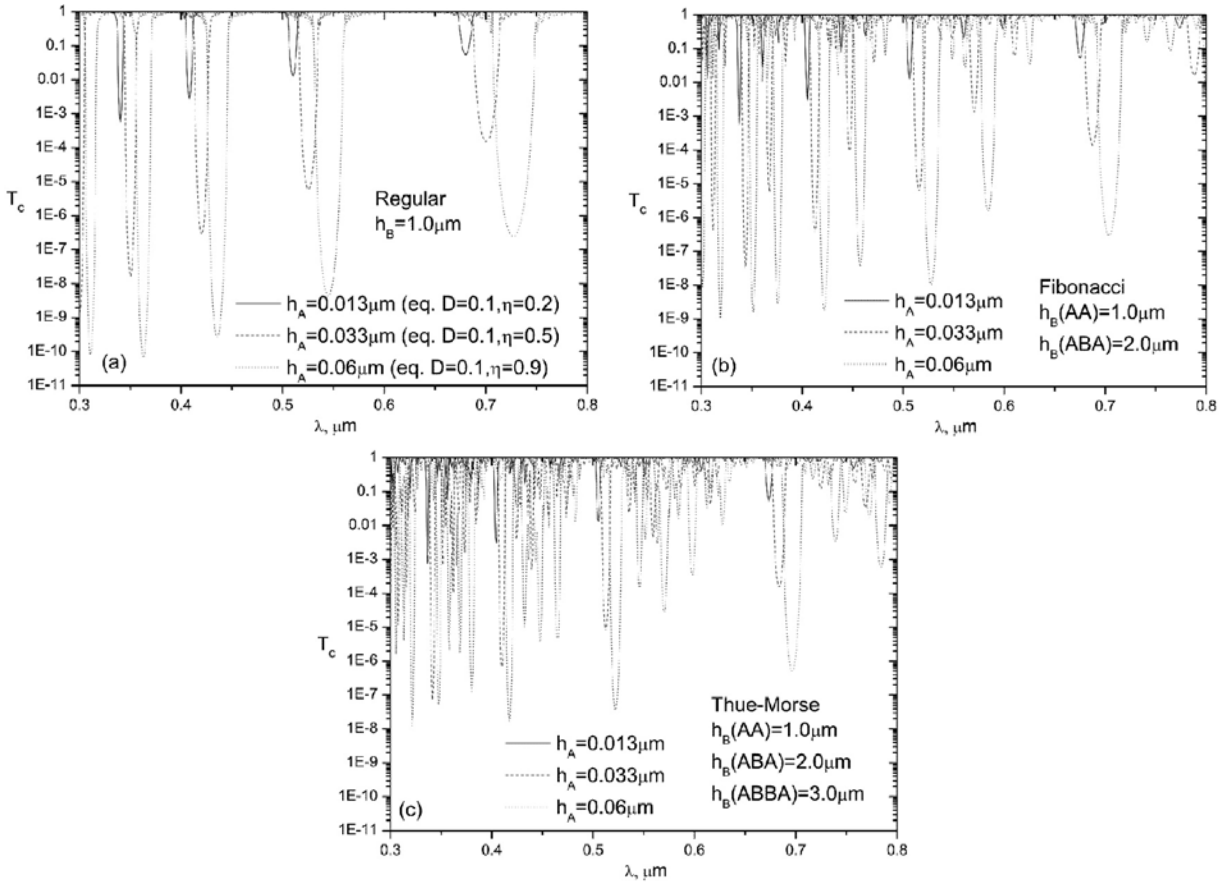

FIG. 8. Spectra of coherent transmission coefficient of the multilayer structures consisting of regular (a), Fibonacci (b), and Thue-Morse (c) sequences of homogeneous $\mathrm{SiO_2}$ layers (type A) and air (type B) at different thicknesses h_A of the layers. The number of $\mathrm{SiO_2}$ layers is 32. Spacing between the adjacent layers is h_B=1 μm for the regular sequence (a); h_B=1 μm for the AA, h_B=2 μm for ABA (b),(c), and h_B=3 μm for $ABBA$ subsequences (c) in the Fibonacci and Thue-Morse sequences of layers

R_c spectra of the individual partially-ordered and regularly-packed monolayers are nearly identical, and their $T_c + R_c$ sums are practically equal to unity.

Let us consider the coherent transmission and reflection coefficients of monolayer sequences consisting of small particles. Figure 10 depicts the T_c and R_c spectra of the multilayer composed of the partially-ordered and the regularly-packed monolayers of $\mathrm{Al_2O_3}$ (type A) and $\mathrm{SiO_2}$ (type B) particles.

One can see that spectra of the multilayers consisting of the same sequences of the partially-ordered and regularly-packed monolayers of small particles are practically identical. Thus, optical response of multilayers consisting of monolayers of such particles is “insensitive” to the ordering in the individual monolayers.

4. Conclusions

The developed technique reveals a good match with experiment [49] for the PBG position in the spectra of an artificial opal [50,51].

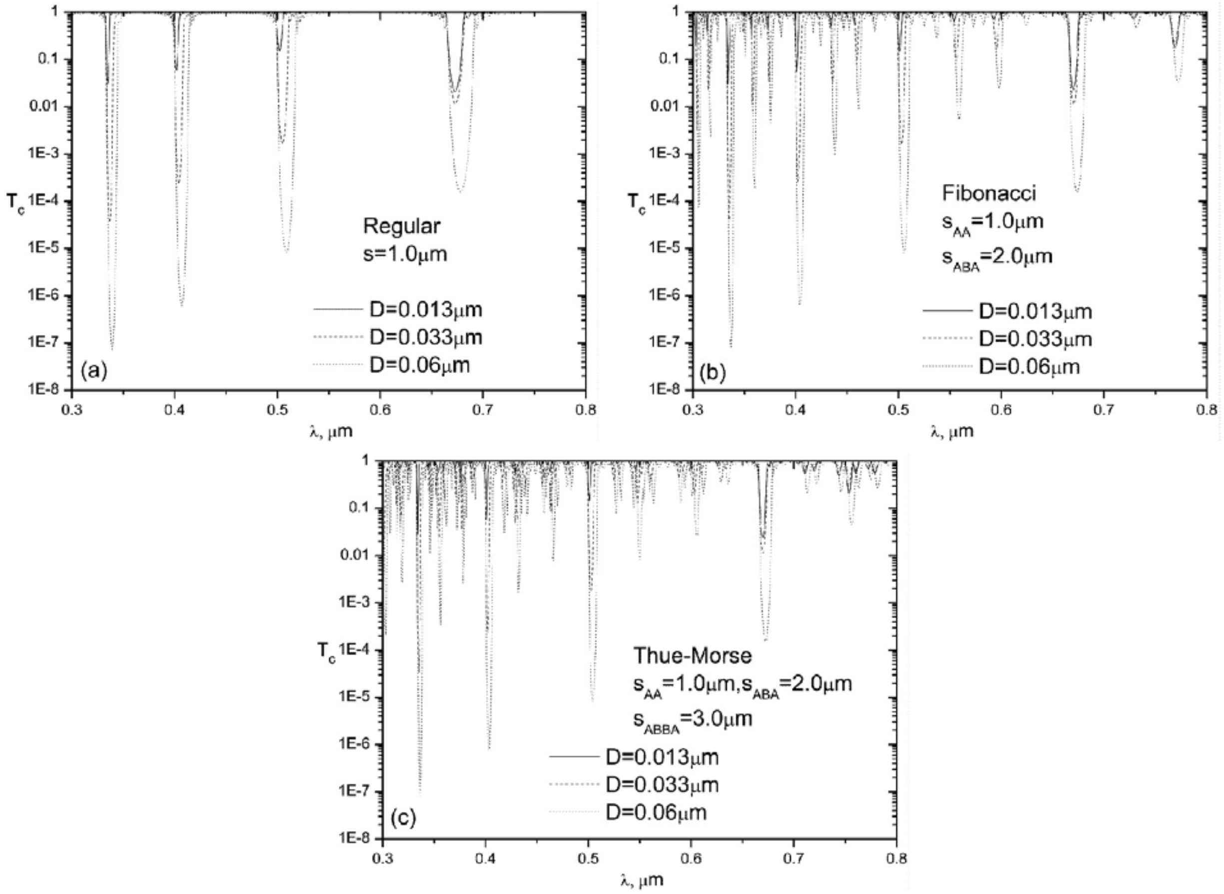

FIG. 9. Spectra of coherent transmission coefficient of the multilayer structures consisting of regular (a), Fibonacci (b), and Thue-Morse (c) sequences of 32 monolayers with triangular lattice of SiO_2 particles at different diameters D. Filling coefficient of monolayers is η=0.9. $\sigma(u)=\sigma_0 u$, σ_0=0.001. Spacing between monolayers s=1 μm in the regular sequence (a); s_{AA}=1 μm for AA, s_{ABA}=2 μm for ABA (b),(c), and s_{ABBA}=3 μm for $ABBA$ subsequences (c) in Fibonacci and Thue-Morse sequences

The spectra of the coherent transmission and reflection coefficients of the layered structures consisting of periodic (regular), Fibonacci, and Thue-Morse sequences of Al_2O_3 and SiO_2 spherical particle monolayers are calculated. The quasicrystalline approximation for the individual monolayer and the transfer matrix method for the multilayer are used.

The influence of the number of monolayers on the transmission and reflection spectra of the multilayer is considered. It is shown quantitatively that the Fibonacci and Thue-Morse structures give additional opportunities to manipulate the spectrum of the multilayer in comparison to the regular ones. Unlike the spectra of the regular structures, the number of PBGs in the spectra of the Fibonacci and Thue-Morse multilayer structures increases with an increased number of monolayers.

It is shown that the PBG in the transmittance spectrum of the system consisting of two different types (A and B) of monolayers is located in the wavelength range between the PBGs of the system consisting of only A type and of the system consisting of only B type monolayers.

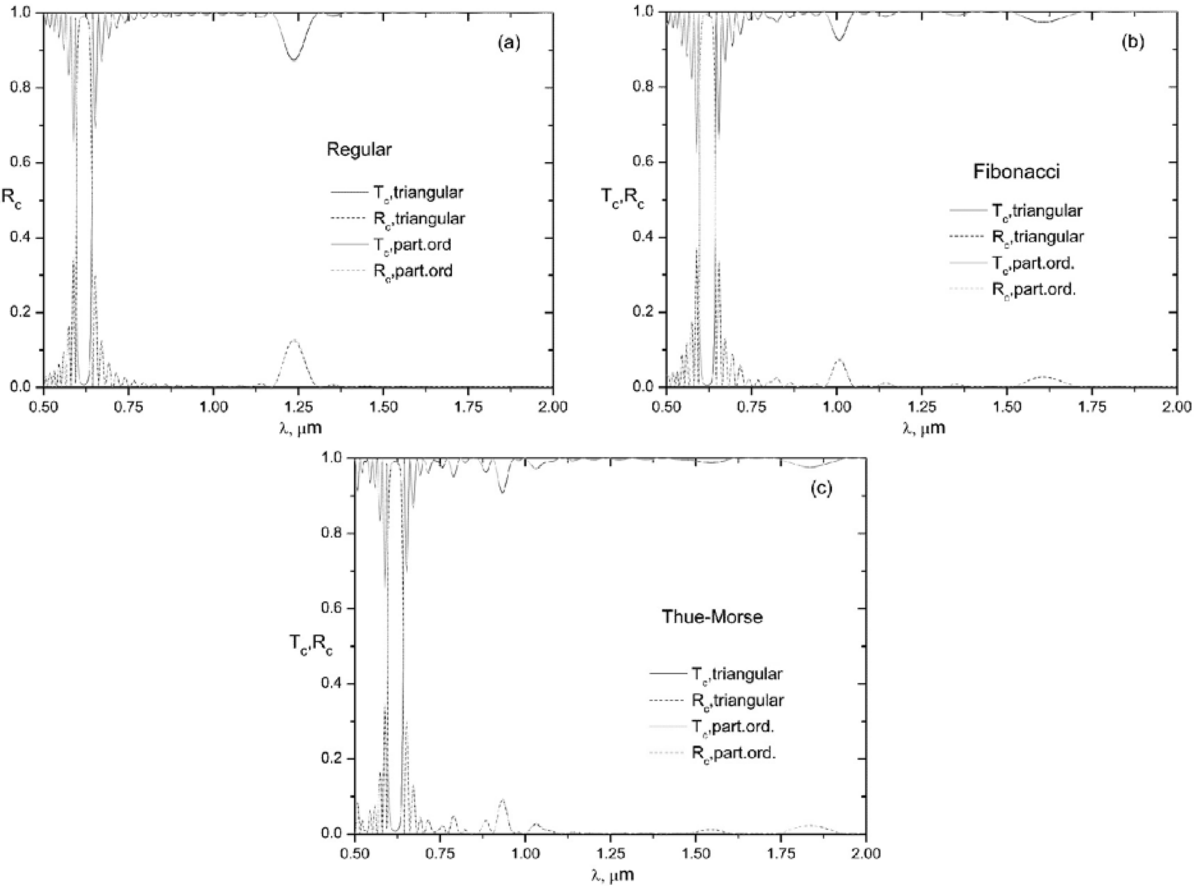

FIG. 10. Spectra of coherent transmission and reflection coefficients of a multilayer consisting of the regularly-packed (black lines) and partially-ordered (gray lines) monolayers of Al_2O_3 (type A) and SiO_2 (type B) particles. Monolayers are arranged in the regular (a), Fibonacci (b) and Thue-Morse (c) sequences. Number of monolayers is 34. Regularly-packed monolayers have a triangular lattice, $\sigma(u) = \sigma_0 u$, σ_0=0.01. D=0.05 μm, η=0.5, s=0.3 μm

The spectra for multilayers consisting of homogeneous and particulate monolayers are compared. The PBGs of particulate structures are shifted to shorter wavelengths relative to those for structures consisting of homogeneous layers. The PBGs observed in the spectra for sequences of homogeneous layers are typically wider and deeper than those observed in the spectra of particulate systems.

The influence of particle concentration and spacing between monolayers on the spectra of the multilayer is studied. Increasing the concentration leads to growth in the depth, width, and wavelength of the PBG minima. Increasing the spacing between the monolayers leads to an increase in the number of PBGs and their shifting to longer wavelengths. These results can be used for the creation of multispectral filters based on layered particulate structures.

The coherent transmittance and reflectance for multilayers of regularly-packed and partially-ordered monolayers of small particles (in comparison with the wavelength of the incident light) are calculated. It is shown that their spectra are insensitive to the monolayer's ordering.

The obtained results can be used for the development of photonic band gap devices, multispectral filters, solar cells, light emitting diodes, display applications, etc.

Acknowledgement

This work was supported in part by the state scientific and technical program of Belarus “Electronics and photonics”.

References

[1] I. A. Sukhoivanov, I. V. Guryev, *Photonic Crystals: Physics and Practical Modeling*, Springer-Verlag (2009).

[2] J. D. Joannopoulos, S. G. Johnson, J. N. Winn, R. D. Meade, *Photonic Crystals: molding the flow of light*, Princeton: Princeton University Press (2008).

[3] E. Yablonovitch, T. J. Gmitter. Photonic band structure: The face-centered-cubic case. *Phys. Rev. Let.*, **63**, P. 1950–1953 (1989).

[4] D. Levine, P. J. Steinhardt. Quasicrystals: A New Class of Ordered Structures. *Phys. Rev. Let.*, **53**, P. 2477–2480 (1984).

[5] D. Shechtman, I. Blech, D. Gratias, J. W. Cahn. Metallic Phase with Long-Range Orientational Order and No Translational Symmetry. *Phys. Rev. Let.*, **53**, P. 1951–1953 (1984).

[6] H. Huang, C. H. Lin, Z. K. Huang, K. Y. Lee, C. C. Yu, and H. C. Kuo. Double Photonic Quasi-Crystal Structure Effect on GaN-Based Vertical-Injection Light-Emitting Diodes. *Jpn. J. Appl. Phys.*, **49**, P. 022101 (2010).

[7] A. Ledermann, L. Cademartiri, M. Hermatschweiler, C. Toninelli, G. A. Ozin, D. S. Wiersma, M. Wegener, G. von Freymann. Three-dimensional silicon inverse photonic quasicrystals for infrared wavelengths. *Nat. Materials*, **5**, P. 942–945 (2006).

[8] M. Florescu, S. Torquato, and P. J. Steinhardt. Designer disordered materials with large, complete photonic band gaps. *Proc. Natl. Acad. Sci.*, **106**, P. 20658–20663 (2009).

[9] Sergei V. Zhukovsky, Andrei V. Lavrinenko, and Sergey V. Gaponenko. *Optical Filters Based on Fractal and Aperiodic Multilayers In Optics of Aperiodic Structures — Fundamentals and Device Applications.* Ed. by Luca Dal Negro, springer, 509 p. (2013). P. 109–140.

[10] A. Mouldi and M. Kanzari. Design of microwave devices exploiting Fibonacci and hybrid periodic/Fibonacci one dimensional photonic crystals. *Progress In Electromagnetics Research B*, **40**, P. 221–240 (2012).

[11] R. W. Peng, M. Wang, A. Hu, S. S. Jiang, G. J. Jin, D. Feng. Photonic localization in one-dimensional k-component Fibonacci structures. *Phys. Rev. B*, **57**, P. 1544–1551 (1998).

[12] L. Dal Negro and N.-N. Feng. Spectral gaps and mode localization in Fibonacci chains of metal nanoparticles. *Opt. Exp.*, **15**, P. 14396–14403 (2007).

[13] P. W. Mauriz, M. S. Vasconcelos, E. L. Albuquerque. Optical transmission spectra in symmetrical Fibonacci photonic multilayers. *Phys. Let. A*, **373**, P. 496–500 (2009).

[14] H. Aynaou, V. R. Velasco, A. Nougaoui, E. H. El Boudouti, B. Djafari-Rouhani, D. Bria. Application of the phase time and transmission coefficients to the study of transverse elastic waves in quasiperiodic systems with planar defects. *Surface Science*, **538**, P. 101–112 (2003).

[15] C. Sibilia, M. Bertolotti, M. Centini, G. D’Aguanno, M. Scalora, M. J. Bloemer, and Ch. M. Bowden. Linear and Nonlinear Optical Properties of Quasi-Periodic One-Dimensional Structures. in *Optical Properties of Nanostructured Random Media: Topics Appl. Phys.* ***82***, V. M. Shalaev. ed. Springer-Verlag, Berlin, Heidelberg (2002), pp. 63–92.

[16] C. Rockstuhl, F. Lederer, T. Zentgraf , H. Giessen. Enhanced transmission of periodic, quasiperiodic, and random nanoaperture arrays. *App. Phys. Let.*, **91**, P. 151109 (2007).

[17] S. V. Boriskina, A. Gopinath, L. Dal Negro. Optical gap formation and localization properties of optical modes in deterministic aperiodic photonic structures. *Opt. Exp.*, **16**, P. 18813–18826 (2008).

[18] Priya Rose T., E. Di Gennaro, G. Abbate, and A. Andreone. Isotropic properties of the photonic band gap in quasicrystals with low-index contrast. *Phys. Rev. B*, **84**, P. 125111-1 (2011).

[19] L. F. Rojas-Ochoa, J. M. Mendez-Alcaraz, P. Schurtenberger, J. J. Saenz and F. Scheffold. Photonic properties of strongly correlated colloidal liquids. *Phys. Rev. Let.*, **93**, P. 073903 (2004).

[20] M. Reufer, L. F. Rojas-Ochoa, P. Schurtenberger, J. J. Saenz and F. Scheffold. Transport of light in amorphous photonic materials. *Appl. Phys. Let.*, **91**, P. 171904 (2007).

[21] J. F. Galisteo-Lopez, M. Ibisate, R. Sapienza, L. S. Froufe-Prez, A. Blanco, C. Lopez. Self-assembled photonic structures. *Adv. Mater.*, **23**, P. 30–69 (2011).

[22] C. Pouya, D. G. Stavenga, P. Vukusic. Discovery of ordered and quasi-ordered photonic crystal structures in the scales of the beetle Eupholus magnificus. *Opt. Exp.*, **19**, P. 11355 (2011).

[23] O. Deparis, C. Vandenbem, M. Rassart, V. Welch, J. P. Vigneron. Color-selecting reflectors inspired from biological periodic multilayer structures. *Opt. Exp.*, **14**, P. 3547–3555 (2006).

[24] C. Campos-Fernández, D. E. Azofeifa, M. Hernández-Jiménez, A. Ruiz-Ruiz, W. E. Vargas. Visible light reflection spectra from cuticle layered materials. *Opt. Mater. Exp.*, **1**, P. 85–100 (2011).

[25] C. C. Katsidis, D. I. Siapkas. General transfer-matrix method for optical multilayer systems with coherent, partially coherent, and incoherent interference. *Appl. Opt.*, **41**, P. 3978–3987 (2002).

[26] E. Centurioni. Generalized matrix method for calculation of internal light energy flux in mixed coherent and incoherent multilayers. *Appl. Opt.*, **44**, P. 7532–7539 (2005).

[27] M. C. Troparevsky, A. S. Sabau, A. R. Lupini, Z. Zhang. Transfer-matrix formalism for the calculation of optical response in multilayer systems: from coherent to incoherent interference. *Opt. Exp.*, **18**, P. 24715–24721 (2010).

[28] M. Born, E. Wolf. *Principles of Optics. 7th ed.* Cambridge University Press (2002).

[29] E. D. Palik, ed. *Handbook of optical constants of solids.* Academic (1985).

[30] M. Lax. Multiple Scattering of Waves II. The effective field for dense systems. *Phys. Rev.*, **85**, P. 621–629 (1952).

[31] K. M. Hong. Multiple scattering of electromagnetic waves by a crowded monolayer of spheres: application to migration imaging films. *J. Opt. Soc. Am.*, **70**, P. 821–826 (1980).

[32] V. A. Loiko, A. A. Miskevich. Light propagation through a monolayer of discrete scatterers: analysis of coherent transmission and reflection coefficients. *Appl. Opt.*, **44**, P. 3759–3768 (2005).

[33] A. A. Miskevich, V.A. Loiko. Two-dimensional planar photonic crystals: Calculation of coherent transmittance and reflectance at normal illumination under the quasicrystalline approximation. *JQSRT*, **112**, P. 1082–1089 (2011).

[34] A. A. Miskevich, V. A. Loiko. Coherent transmission and reflection of a two-dimensional planar photonic crystal. *JETP*, **113**, P. 1–13 (2011).

[35] L. L. Foldy. The multiple scattering of waves. *Phys. Rev.*, **67**, P. 107–119 (1945).

[36] P. C. Waterman, R. Truell. Multiple scattering of waves. *J. Math. Phys.*, **2**, P. 512–537 (1961).

[37] V. A. Babenko, L. G. Astafyeva, V. N. Kuzmin, *Electromagnetic scattering in disperse media.* Praxis Publishing Ltd (2003).

[38] J. M. Ziman, *Models of Disorder.* Cambridge University (1979).

[39] Z. Fisher. *Statistical Theory of Liquids.* University of Chicago Press (1964).

[40] D. A. Varshalovich, A. N. Moskalev, V. K. Khersonskii, in *Quantum theory of angular momentum.* Singapore: World Scientific (1988). Original Russian edition: Leningrad: Nauka (1975).

[41] J. P. Mondia, Tan Hong Wee, S. Linden, H. M. van Driel, J. F. Young. Ultrafast tuning of two-dimensional planar photonic-crystal waveguides via free carrier injection and the optical Kerr effect. *J. Opt. Soc. Am. B*, **22**, P. 2480–2486 (2005).

[42] M. Devetak, J. Milavec, R. A. Rupp, B. Yao, I. Drevenšek-Olenik. Two-dimensional photonic lattices in polymer-dispersed liquid crystal composites. *J. Opt. A: Pure Appl. Opt.*, **11**, P. 024020 (2009).

[43] Y. Kurokawa, Y. Jimba, H. Miyazaki. Internal electric-field intensity distribution of a monolayer of periodically arrayed dielectric spheres. *Phys. Rev. B*, **70**, P. 155107 (2004).

[44] L. S. Ornstein, F. Zernike. Accidental deviations of density and opalescence at the critical point of a single substance. *Proc. Acad. Sci.*, **17**, P. 793–806 (1914).

[45] J. K. Percus, G. J. Yevick. Analysis of classical statistical mechanics by means of collective coordinates. *Phys. Rev.*, **110**, P. 1–13 (1958).

[46] A. P. Ivanov, V. A. Loiko, V. P. Dick. *Propagation of light in close-packed disperse media.* Minsk: Nauka i Tekhnika (1988) (in russian).

[47] V.A. Loiko, A.V. Konkolovich. Spatial Optical Noise of a Monolayer of Discrete Inhomogeneities: I. Basic Relations for the Wiener Spectrum. *Optics and spectroscopy*, **85**(4), P. 563–567 (1998).

[48] H. C. van de Hulst. *Light Scattering by Small Particles.* Dover Publications (1981).

[49] V. N. Bogomolov, S. V. Gaponenko, I. N. Germanenko, A. M. Kapitonov, E. P. Petrov, N. V. Gaponenko, et al. Photonic band gap phenomenon and optical properties of artificial opals. *Phys. Rev. E*, **55**, P. 7619–7625 (1997).

[50] V. A. Loiko, A. A. Miskevich. Coherent Transmission and Reflection Spectra of Ordered Structures from Spherical Alumina Particles. *Opt. and Spectrosc.*, **115**, P. 274–282 (2013).

[51] A. A. Miskevich, V. A. Loiko. Layered periodic disperse structures of spherical alumina particles: Coherent transmittance and reflectance spectra. *JQSRT* (2013), http://dx.doi.org/10.1016/j.jqsrt.2013.05.013.

NANOSYSTEMS: PHYSICS, CHEMISTRY, MATHEMATICS, 2013, 4 (6), P. 795–799

ON THE POSSIBILITY OF MAGNETORESISTANCE GOVERNED BY LIGHT

I. Yu. Popov
St. Petersburg National Research University of Information Technologies,
Mechanics and Optics, 49 Kronverkskiy, St. Petersburg, 197101, Russia
popov1955@gmail.com

PACS 75.47.De Giant magnetoresistance

PACS 68.65.Ac Multilayers

PACS 72.80.Le Polymers; organic compounds (including organic semiconductors)

It has been shown that it is possibility to control magnetoresistance by light. The use of light-sensitive banana-shape molecules has been suggested as an engine for varying the thickness or spacer between the magnetic layers. The spacer is filled by a conducting polymer with copper-like conductivity (with inserted bent molecules), ensuring the proper interlayer exchange coupling, which is necessary for transition from a ferromagnetic to an anti-ferromagnetic ordering (and inverse) when the thickness of the spacer changes.

Keywords: magnetoresistance, banana-shape molecule, conducting polymer.

1. Introduction

The discovery of the phenomenon of giant magnetoresistance has greatly accelerated the development of computer memory and related topics. This phenomenon is observed in layered nanostructures consisting of sequentially ordered magnetic and non-magnetic conducting layers [1], [2]. In such sandwich structures, the magnetic layers can have two different orderings: ferromagnetic, FM, (when the magnetic orientation of all layers are aligned) and anti-ferromagnetic, AFM, (when the neighbor layers have opposing magnetic orientations). Correspondingly, there is a spin-dependent electron transport in the system. While electrons with the same spin direction as the layer's magnetization cannot pass through this layer (all the corresponding energy levels are occupied), but it can pass through the magnetic layer with the opposite orientation. In this case, the transition from an anti-ferromagnetic to a ferromagnetic ordering of the layers gives rise to the growth of electric resistance. One can stimulate this transition by switching on an external magnetic field. This is, in short, the idea of giant magnetoresistance. This phenomenon is widely used today for memory elements. This method of giant magnetoresistance control has some disadvantages, e.g., the external magnetic field isn't readily focused. That is why it is interesting to find other ways to effectively control giant magnetoresistance. An interesting possibility is related to the interlayer exchange coupling. It is known that the type of the magnetic layer ordering (FM or AFM) depends on the thickness of the non-magnetic spacer [3]. One can control the type of magnetic ordering by varying this thickness. Particularly, the hydrogenation of the spacer leads to a change in the thickness [4], and, correspondingly, the type of magnetic ordering which causes a jump in the resistance. Unfortunately, hydrogenation can be a very slow process, and one can't use it for memory devices. In the present paper, another way to modify the thickness is suggested. This is based on using photosensitive banana-shape molecules and conducting polymers. The use of light to govern magnetoresistance seems to be very attractive. In this study, we analyze the possibility of its realization.

2. Magnetoresistance governing

There are different ways to change the thickness of thin (polymer) layer excluding mechanical pressure. One is based on the properties of an azobenzene molecule which preferentially absorbs light polarized along its transition dipole axis (long axis of the molecule). Repeated trans-cis-trans isomerization cycles result in a statistical depletion of trans chromophores that lie along the polarization direction, while enriching those lying perpendicular to that direction. Irradiation with unpolarized light can then reverse the process by re-establishing isotropic orientation. The reversibility of the process enables subsequent photo-reorientations.

The trans-cis photoisomerization is the transformation of molecular shape from the rod-like shape of the trans isomer to the bent cis isomer. This transition is reversible. UV light (365 nm wavelength) induced the trans-cis transition, while 465 nm wavelength UV light causes the inverse cis-trans transition. This property is widely used in liquid crystal applications [5–7]. Namely, if these molecules are inserted into a liquid crystal (LC), then the trans isomer stabilizes the phase structure of the LC. Transition to a cis isomer, which acts as an impurity, results in the destruction of ordered mesophase structures, and one observes the phase transition from a nematic to an isotropic LC [8]. Photochemical phase transitions in polymeric liquid crystals (PLCs) have also been induced using spiropyrans, spirooxazines and fulgides [9–11].

The phase-transition behavior of LC mixtures and photochromic spiropyran derivatives, induced by isomerization of the guest molecules, have been investigated. Two types of spiropyran derivatives were employed: normal spiropyrans which are stable in the closed form (spiropyran form; SPF) and open-form (merocyanine form; MCF) stabilized derivatives. These spiropyran derivatives were doped into two LC compounds: 5-cyanobiphenyl (5CB) and 4-butoxyphenyl-4'-ethylcyclohexanecarboxylate (ECH 204). SPF-Stabilized derivatives exhibited photoisomerization behavior from SPF to MCF in LC media which was accompanied by an isotropic (I) to nematic (N) phase transition of the mixtures. On the other hand, an $N \to I$ phase transition of the mixtures was observed when the MCF-stabilized spiropyran doped in both LCs was photoisomerized from MCF to SPF. The result was interpreted in terms of shape anisotropy of the guest molecule associated with each isomer of the spiropyrans.

An interesting example of light-dependent bent angle of a molecule was demonstrated in [12], [13] (see Fig. 1 from [12]). A series of linear polyimides was examined and found to exhibit a polarization-dependent photomechanical response for the wavelengths of 442 nm, 488 nm and 514 nm. The bent angle varies over a wide range (up to 70 °). Their results indicate that the isomerization process is about 10 percent efficient; that is, 10% of the incident photon energy $(4 \cdot 10^{-19} J)$ is converted into mechanical work $(\approx 4.5 \cdot 10^{-20} J)$. Photomechanical responses at the macroscopic scale, be that in cantilever or film form, are, to date, significantly less than 1% efficient. As for mechanical stress, it depends on the concentration of the corresponding molecules. The authors obtained the storage modulus (E'= 3.8-6.2 GPa), a stress up to 260 kPa. Such a stress cannot cause a variation of the thickness in the metallic layer (ionic bond is essentially greater). To get an effect, one should use another material. But there is one important feature — this material should have metal-like conductivity. This

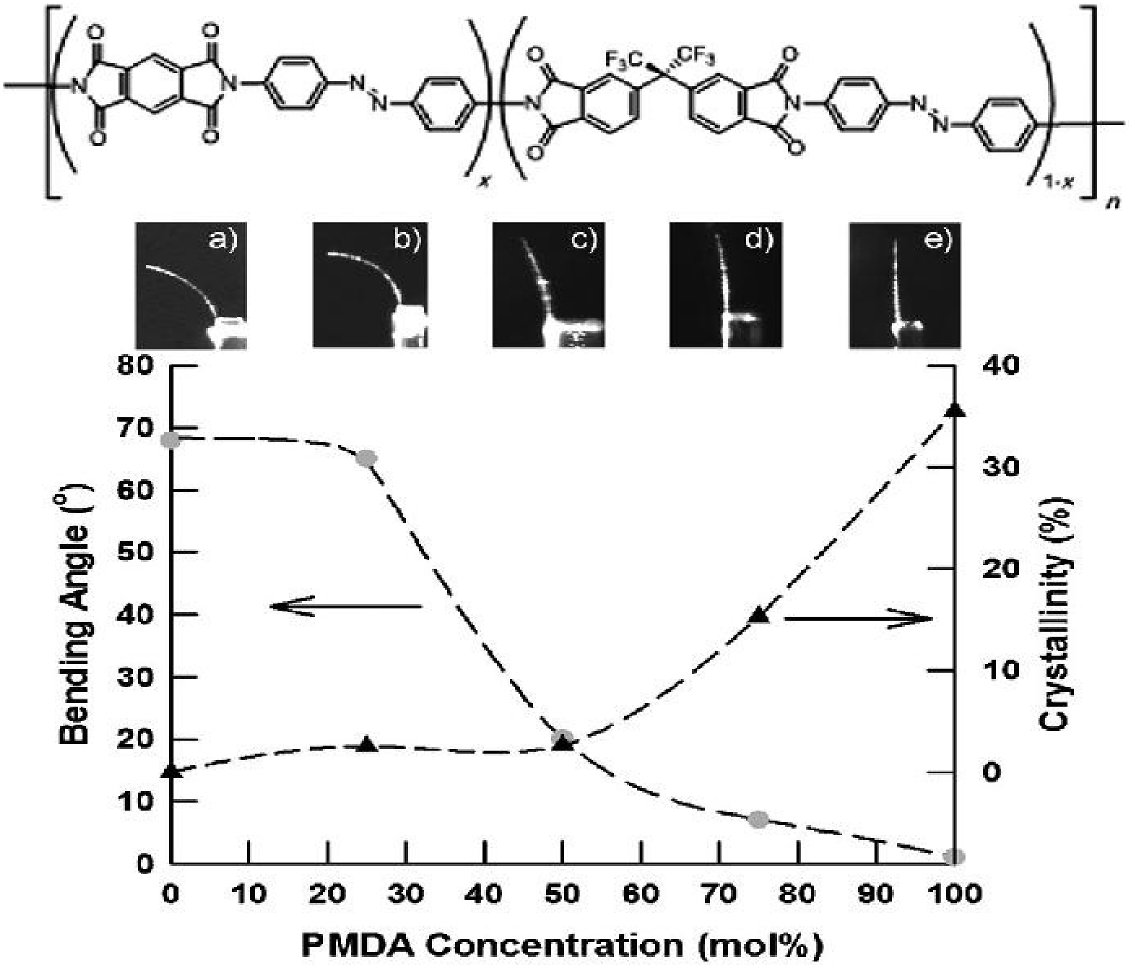

Fig. 1. Summary of photomechanical response (bending angle) and crystallinity as a function of PMDA (pyromellitic dianhydride) concentration for a series of azobenzene-functionalized linear polyimides (generic structure inset). Images of $5mm \cdot 1mm \cdot 0.02mm$ cantilevers composed of azo-PI- 6FDA (a), copolymers of 6FDA/PMDA (azo-coPI-xx) (bd), and azo-PIPMDA (e) after 1 h of irradiation with $\lambda = 442nm$ light polarized parallel to the long axis of the cantilever

is necessary to ensure interlayer exchange coupling [1]. Only under this condition, can one vary the type of magnetic ordering (ferromagnetic or anti-ferromagnetic), which depends on the thickness of the non-magnetic spacer. Fortunately, there are conducting polymers with metal-like conductivity. Particularly, polyacetylene exhibits copper-like conductivity [14]. Currently, it is the only conducting polymer with such properties. This material has environmental instability which is an obstacle for using of this polymer for wiring, but for our purpose it is not crucial. Thus, the spacer should be filled by a conducting polymer having copper-like conductivity with a great number of light sensitive bent molecules inserted. Such a spacer gives one the possibility to control magnetoresistance by light. The procedure is schematically shown on Fig. 2. Namely, light of the proper wavelength causes the variation of the bent angles of banana-shape molecules which are oriented in the appropriate manner (particularly, they can be attached by their ends to the neighboring magnetic layers). The technology (see, e.g., [15]) allowing one to arrange the bent molecules in a proper way between the layers (see Fig. 2) is known. In this situation, changing the angle of the bend leads to variation of the spacer width, and, consequently, to the type of magnetic ordering due to the interlayer exchange coupling. As a result, we get a jump in the magnetoresistance.

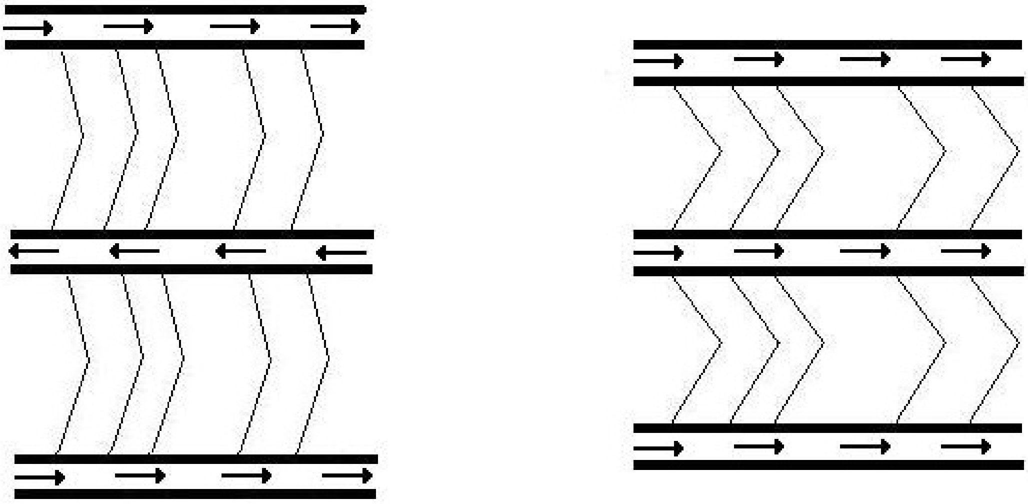

Fig. 2. Arrangement of bent molecules between the magnetic layers. Magnetic layers are strips with arrows, showing the magnetization. Molecules of the conducting polymer filling the spacer aren't shown. Mechanism of thickness governing and the corresponding change of magnetic ordering (left - AFM, right - FM) are schematically shown

Acknowledgements

The work was supported by FTP "Scientific and Educational Human Resources for Innovation-Driven Russia" (contract 16.740.11.0030, grant 2012-1.2.2-12-000-1001-047), grant 11-08-00267 of RFBR and by Program of Development of Leading Russian Universities.

References

[1] P.Grünberg. Layered magnetic structures: facts, figures, future. *J.Phys.: Condens. Matter.*, **13**, P. 7691–7706 (2001).

[2] L.V. Gortinskaya, I.Yu. Popov, E.S. Tesovskaya, V.M. Uzdin. Electronic transport in the multilayers with very thin magnetic layers. *Physica E*, **36**, P. 12–16 (2007).

[3] V.M. Uzdin, N.S. Yartseva, L. Adamowicz. Phase shift of exchange coupling oscilations in magnetic multilayers. *J. Magn. Magn. Mater.*, **203**, P.283–285 (1999).

[4] S. Ostanin, V. M. Uzdin, C. Demangeat, J.M. Wills, M. Alouani and H. Dreysse. Effect of hydrogen on the interlayer exchange coupling in FeOV superlattices. *Phys. Rev.*, **B 61**(7), P. 4870–4876 (2000).

[5] K.Ichimura. Photoalignment of Liquid-Crystal Systems. *Chem. Rev.*, **100**, P. 1847–1874 (2000).

[6] Y. L.Yu, T.Ikeda. Alignment modulation of azobenzene-containing liquid crystal systems by photochemical reactions. *J. Photochem. Photobiol*, C **5**, P. 247–265 (2004).

[7] T.Ikeda. Photomodulation of liquid crystal orientations for photonic applications. *J. Mater. Chem.*, **13**, P. 2037–2057 (2003).

[8] P. M.Hogan, A. R.Tajbakhsh, E. M.Terentjev. UV manipulation of order and macroscopic shape in nematic elastomers. *Phys. Rev. E.*, **65**, P. 041720 (2002).

[9] S.Kurihara, T.Ikeda, S.Tazuke, J. E.Seto. Isothermal phase transition of liquid crystals induced by photoisomerization of doped spiropyrans. *J. Chem. Soc., Faraday Trans.*, **87**, P. 3251–3254 (1991).

[10] I.Cabrera, V.Krongauz. Dynamic ordering of aggregated mesomorphic macromolecules. *Nature*, **326**, P. 582–585 (1987).

[11] I.Cabrera, A.Dittrich, H.Ringsdorf. Thermally Irreversible Photochromic Liquid Crystal Polymers. *Angew. Chem. Int. Ed. Engl.* **30**, P. 76–78 (1991).

[12] K. M. Lee, D. H. Wang, H. Koerner, R. A. Vaia, L.-S. Tan, T. J.White. Enhancement of Photogenerated Mechanical Force in Azobenzene-Functionalized Polyimides. *Angew. Chem.*, **124**, P. 4193–4197 (2012).

[13] D. H. Wang, K. M. Lee, Z. Yu, H. Koerner, R. A. Vaia, T. J.White, L.-S. Tan. Photomechanical Response of Glassy Azobenzene Polyimide Networks. *Macromolecules*, **44**, P. 3840–3846 (2011).

[14] M. Angelopoulos. In: *Handbook of Conducting Polymers.* eds. T.A.Skoteum, R.L.Elsenbaumer, J.R.Reynolds (Marcel Dekker, Inc. New York. 1998), p. 921.

[15] L.-Yu. Wang, H.-Yi Tsai, H.-Ch. Lin. Novel Supramolecular Side-Chain Banana-Shaped Liquid Crystalline Polymers Containing Covalent- and Hydrogen-Bonded Bent Cores. *Macromolecules*, **43**, P. 1277–1288 (2010).

NANOSYSTEMS: PHYSICS, CHEMISTRY, MATHEMATICS, 2013, 4 (6), P. 800–809

A QUANTITATIVE MODEL FOR QUANTUM TRANSPORT IN NANO-TRANSISTORS

U. Wulf[1], M. Krahlisch[1], J. Kučera[2], H. Richter[1], J. Höntschel[3]
[1] BTU Cottbus-Senftenberg, Fakultät 1, Postfach 101344, 03013 Cottbus, Germany
[2] Institute of Physics, Academy of Sciences of the Czech Republic,
Cukrovarnická 10, 162 53 Praha 6, Czech Republic
[3] GLOBALFOUNDRIES Dresden, Wilschdorfer Landstraße 101,
01109 Dresden, Germany
wulf@physik.tu-cottbus.de, TheBrute@gmx.de, kucera@fzu.cz,
richter@gfww.de, jan.hoentschel@globalfoundries.com

PACS 73.23.A,03.65.Xp,73.63.-b

In a number of recent publications, a one-dimensional effective model for quantum transport in a nano-transistor was developed yielding qualitative agreement with the trace of an experimental transistor. To make possible a quantitative comparison, we introduce three phenomenological parameters in our model, the first one describing the overlap between the wave functions in the contacts and in the transistor channel, the second one is the transistor temperature, and the third one is the maximum height of the source-drain barrier. These parameters are adjusted to the traces of three experimental transistors. An accurate fit is obtained if the three adjustable parameters are determined for each gate voltage resulting in three calibration functions. In the threshold- and subthreshold regime the calibration functions are physically interpretable and allow one to extract key data from the transistors, such as their working temperature, their body factor, a linear combination of the flat band voltage and the built-in potential between substrate and source contact, and the quality of the wave function coupling between the contacts and the electron channel.

Keywords: nano-transistor, quantum transport, quantitative transistor model, nano-FET, drain current.

1. Introduction

The continuing reduction of the channel length for state-of-the-art nano-transistors necessitates a quantum mechanical treatment of carrier transport [1–3]. Here the solution of the Schrödinger equation can be achieved using a variety of methods. We choose the R-matrix formalism [4–13] to calculate the drain current of a planar MOSFET. In this approach it is possible to reduce in a systematic way a complete three-dimensional quantum-description of transport [6] to a one-dimensional effective model [7, 10, 11]. In this reduction process the assumption is made that only the lowest transverse mode in the electron channel contributes significantly to transport (single mode approximation, SMA). In Ref. [11], the SMA was shown to provide an accurate qualitative description of the drain current of an experimental nano-transistor. In this paper, our approach is extended to allow for a quantitative comparison with three further nano-transistors. To move from a qualitative to a quantitative description three suitable calibration parameters are introduced, one for the wave function overlap between the channel and the contacts, a second for the device temperature, and a third for the height of the source-drain barrier (calibrated SMA, cSMA). It is found that the cSMA allows an accurate fit for the $I_D - V_D$-traces of the experimental transistors if the three described parameters are determined for each gate voltage, resulting in three calibration functions. Even though the cSMA is a strongly simplified transistor model, a major advantage is that in the entire threshold- and subthreshold regime, all three calibration functions can be constructed in a simple and physically interpretable way from four constants only (see dotted lines in Figs. 2 and 3). From the four fixed values of these constants, key data for the transistors can be extracted which take reasonable values.

2. Calibration of a one-dimensional effective transistor model

In the cSMA the drain current per width J is calculated according to:

$$J = CJ_0 \int_0^\infty d\epsilon \, [s(\epsilon - m) - s(\epsilon - m + v_D)] \, T(\epsilon). \tag{1}$$

In addition to the multiplicative parameter C for the wave function overlap between electron channel and contacts, Eq. (1) is equivalent to the corresponding expression in the SMA [10, 11]: The normalization constant for the current per width is given by $J_0 = 2eN_v^{ch}E_F/(h\lambda)$ where N_v^{ch} is the number of equivalent conduction band minima in the electron channel, E_F is the Fermi energy in the source contact, $\lambda = \hbar/\sqrt{2m^*E_F}$ is the scaling length, and m^* is the effective electron mass. The current transmission T in Eq. (1) is calculated from the right-moving scattering solutions of the normalized Schrödinger equation

$$\left[-\frac{1}{l^2}\frac{d^2}{dx^2} + v_{eff}(x) - \epsilon\right]\psi(x) = 0 \tag{2}$$

which is the one-dimensional effective Schrödinger equation (3) in Ref. [10] with energies normalized to E_F and lengths normalized to the channel length $L = l\lambda$ of the transistor. The normalized effective scattering potential is given by

$$v_{eff}(x) = \begin{cases} 0 & \text{for } x < 0 \\ v_0 - v_D x & \text{for } 0 \le x \le 1 \\ -v_D & \text{for } x \ge 1, \end{cases} \tag{3}$$

where $V_D = v_D E_F$ is the applied drain voltage and $V_0 = v_0 E_F$ is the maximum height of the source-drain barrier. (s. Fig. 1).

The effective potential is a Fowler-Nordheim-type field emission barrier used in the gate tunneling problem as well [15]. In the context of the transistor problem the simple trapezoidal form of the scattering potential corresponds to the neglect of image charges in the source-drain barrier associated with drain induced barrier lowering. In the effective potential v_{eff} the right-moving scattering states take the form $\psi(x < 0) = e^{ik_1x} + re^{-ik_1x}$ in the source and $\psi(x > 1) = te^{ik_2x}$ in the drain, with $k_1 = \sqrt{l^2\epsilon}$ and $k_2 = \sqrt{l^2(\epsilon + v_D)}$. The transmission coefficient t is calculated solving the discretized Eq. (2) by a recursive procedure and the current transmission is then given by $T = k_1^{-1}|t|^2k_2$. The first factor of the integrand in (1) is the difference of the supply functions in the source- and in the drain contact calculated from

$$s(\alpha) = \sqrt{\frac{u}{4\pi}} F_{-\frac{1}{2}}\left(-\frac{\alpha}{u}\right), \tag{4}$$

where F_j is the Fermi-Dirac integral of order $j = -1/2$ and $u = k_BT/E_F$ is the normalized temperature. The normalized chemical potential in the source contact is given by $m = \mu/E_F = uX_{\frac{1}{2}}[4/(3\sqrt{\pi}u^{3/2})]$, where $X_{1/2}$ is the inverse function of $F_{1/2}$. From Refs. [10] and [11] we adopt parameter values which are reasonable for a wide Si n-channel nano-FET with heavily doped contacts, $\lambda = 1$ nm, $J_0 = 5 \times 10^{-2} A/\mu m$, and $E_F = 0.35eV$.

Then, the channel lengths L =22 nm, 26 nm, and 30 nm of the three experimental transistors presented in the next section correspond to characteristic lengths of l =22, 26, and 30 and the chosen Fermi energy leads to $u \sim 0.1$ at room temperature.

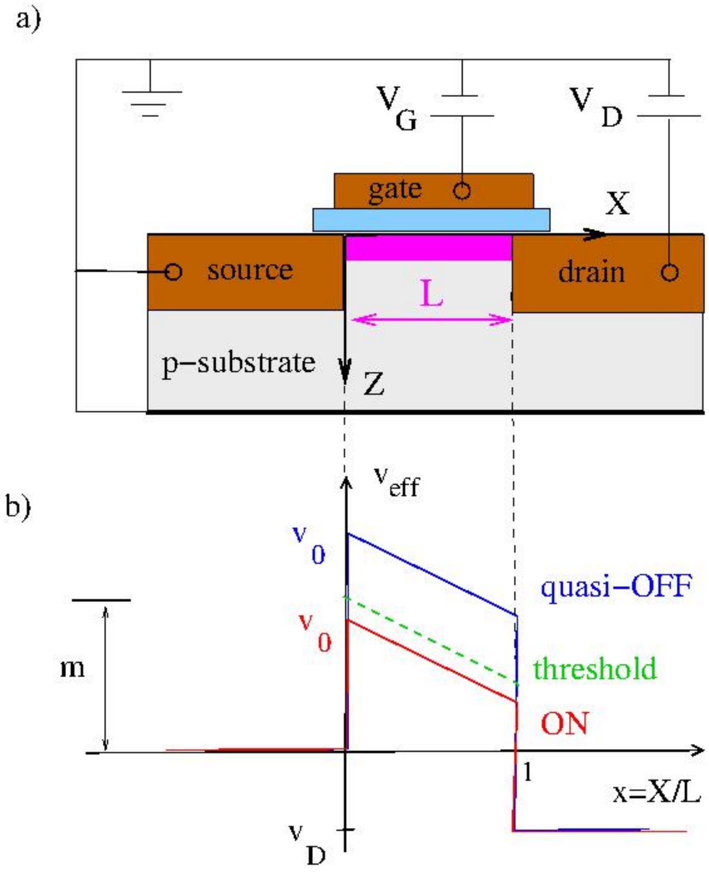

FIG. 1. a) Field effect transistor (here conventional n-FET) with external circuitry. b) Normalized effective potential v_{eff} in Eq. (3) at different applied gate voltages. Solid lines: Quasi-OFF-state, $v_0 > m$, corresponding to $I_D - V_D$ traces with positive curvature (s. filled rectangles in Fig. 2). Dashed lines: Threshold, $v_0 \sim m$, the $I_D - V_D$ trace exhibits a close-to-linear dependence on the drain voltage (s. asterisks in Fig. 2). Dotted line: ON-state corresponding to $I_D - V_D$ traces with negative curvature (s. open circles in Fig. 2). Shown here is the effective potential for gate voltages slightly above threshold. For larger gate voltages, v_0 increases above m because of device-heating (s. Fig. 3 (b)).

In the described one-dimensional effective model, neither the temperature, the barrier height nor the overlap parameter are known. To overcome this problem three calibration functions $u(V_G)$, $v_0(V_G)$, and $C(V_G)$ are introduced. These result from the minimization of the root mean square deviation

$$\Delta J_{rms}(V_G) = \sqrt{\frac{1}{N}\sum_i^N \left[\frac{J^{exp}(V_D^i, V_G) - J^{cal}(V_D^i, V_G)}{J^{exp}(V_D^i, V_G)}\right]^2} \tag{5}$$

at given V_G. Here $J^{exp}(V_D^i, V_G)$ is the experimental current measured at N equidistant drain voltages V_D^i where the calibrated theoretical current is calculated from (1) as

$$J^{cal}(V_D^i, V_G) = J(v_D = V_D^i/E_F, v_0, u, C, l = L/\lambda). \tag{6}$$

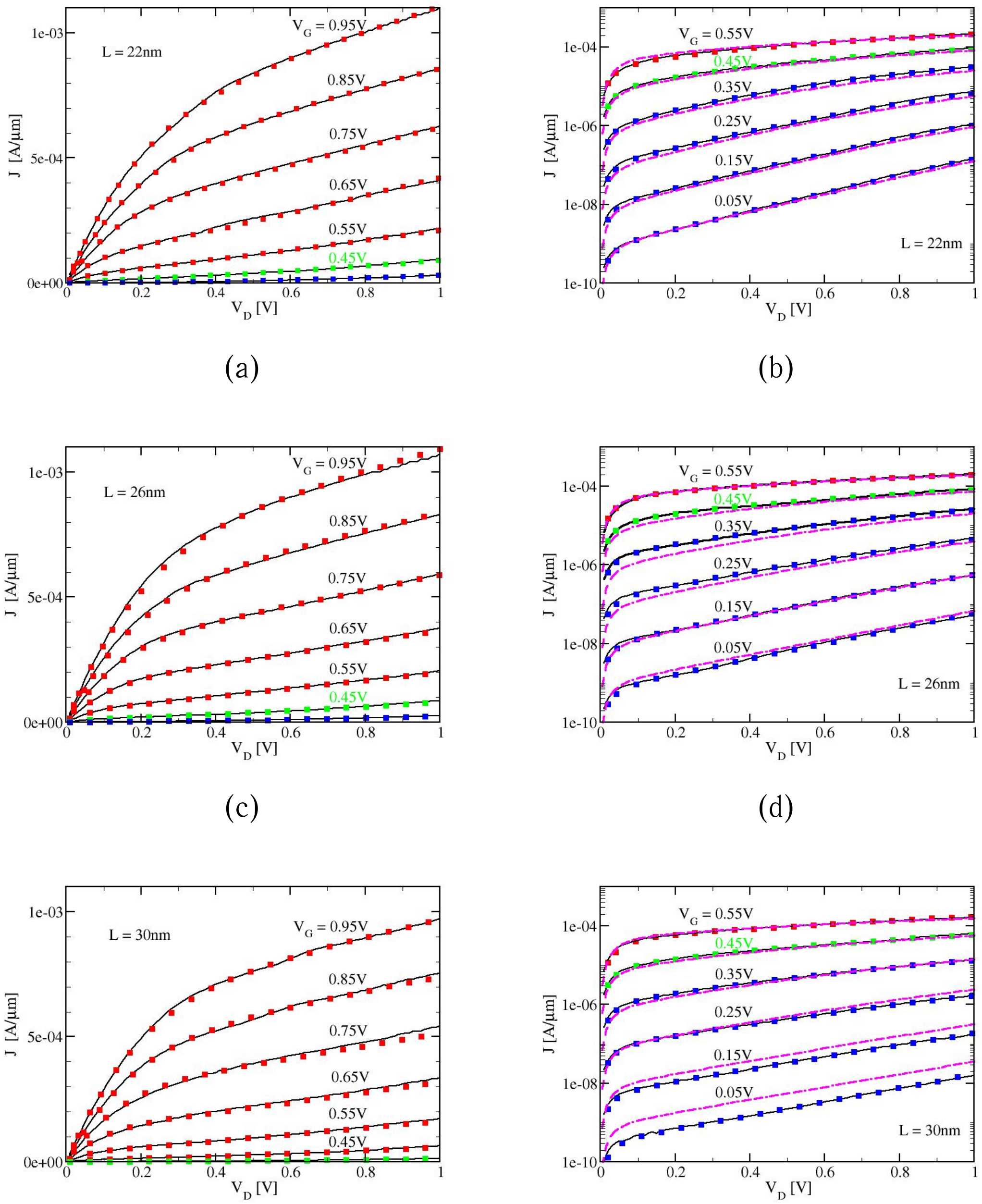

(a) (b)

(c) (d)

(e) (f)

FIG. 2. In solid lines drain-characteristics J^{exp} of a series of n-channel nano-FETs with gate lengths of 22 nm ((A) linear scale and (B) logarithmic), 26 nm ((C) linear and (D) logarithmic), and 30 nm ((E) linear and (F) logarithmic). Marked with symbols J^{cal} according to Eq. (6): ON-state (open circles), experimental trace closest to the threshold trace at V_T (asteriks), and quasi-OFF-state (solid rectangles). In (B), (D), and (F) the dotted lines represent the four-constants-fit $u = 0.09$, $C = 0.1$, $\beta = 2/V$, $v_s^0 = -1V$ corresponding to the dotted lines in Fig. 3.

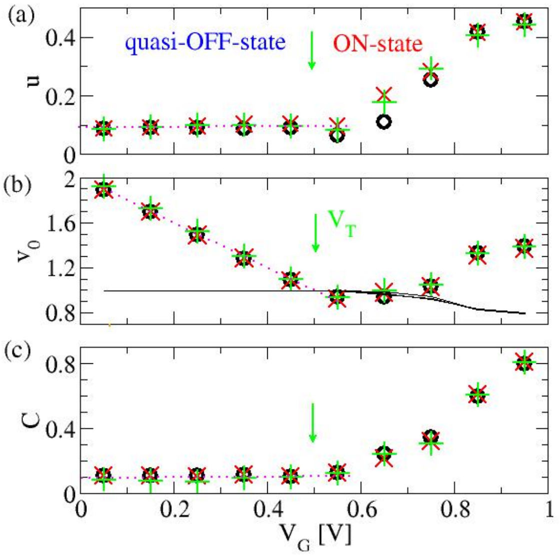

FIG. 3. Calibration functions (a) $u(V_G)$, (b) $v_0(V_G)$, and (c) $C(V_G)$, filled circles $L = 22$ nm, symbols $'x'$ $L = 26$ nm, and open rectangles $L = 30$ nm. In dotted lines the four-constants-fit $u = 0.09$, $C = 0.1$, $\beta = 2/V$, and $v_s^0 = -1V$. The solid black line in (b) marks the position of m.

The function $\Delta J_{rms}(V_G)$ is then minimized by varying in (6) the parameters C, v_0, and u. The parameter values leading to the minimum of $\Delta J_{rms}(V_G)$ constitute the calibration functions $u(V_G)$, $v_0(V_G)$, and $C(V_G)$.

3. Results

The drain characteristics, J^{exp}, of a series of three nano-FETs with different channel lengths but otherwise equal nominal device structure are shown in Fig. 2. These traces are compared to the calibrated theoretical current per width J^{cal} (s. Eq. (6)), demonstrating a good agreement between theory and experiment. The calibration functions $v_0(V_G)$, $u(V_G)$, and $C(V_G)$ obtained from the minimization procedure associated with Eq. (5) are plotted in Fig. 3. It can be determined that the calibration functions depend very little on the channel length. Furthermore, their gate-voltage-dependence shows two distinct regions separated by the threshold voltage $V_T \sim 0.5V$ (arrows in Fig. 3). Here, V_T follows from an inspection of the $I_D - V_D$-traces [11]: For gate voltages above V_T, in the ON-state, the traces show a negative curvature, while below V_T, it is positive. At $V_G = V_T$ there is a close-to-linear threshold $I_D - V_D$-trace (s. asterisks in Fig. 2).

We begin our detailed discussion of the calibration functions considering gate voltages below threshold: For $V_G < V_T$ the barrier height parameter decreases linearly with the gate voltage,

$$v_0(V_G) = -\beta V_G + v_0^0, \tag{7}$$

with $\beta = 2/V$ and $v_0^0 = 2$. To explain the linear relation in (7) we establish in the appendix the relation between the cSMA and the standard MIS capacitor model described in Refs. [16, 17]. As a result, within the depletion approximation to the standard MIS capacitor model the linear dependence can be attributed to a constant body factor n of the transistor which is defined in Eq. (12). It can be calculated from β according to

$$n = \frac{q}{E_F \beta}, \tag{8}$$

yielding the value $n = 1.4$ for our transistors. This result lies within the typical values for bulk MOSFETs ranging between 1.2 and 1.5 [14] and it is close to $n = 1.6$ found from the measured subthreshold slope (s. Fig. 5). Furthermore, one obtains from the standard MIS capacitor model the following:

$$V_{bi} + \frac{1}{n} V_{FB} = \frac{E_F}{q} v_0^0, \tag{9}$$

i. e. v_0^0 represents the material constants V_{bi} and V_{FB} where V_{bi} is the built-in potential between the n^+-doped source contact and the p-substrate and V_{FB} is the flat-band voltage of the MIS-structure [16].

From Fig. 3 (c) it can be taken that in the threshold- and subthreshold regime the overlap parameter takes the constant value of $C = 0.1$. In the appendix we argue that within the depletion approximation to the standard MIS capacitor model, the transverse confinement potential in the electron channel is given by the acceptor density in the substrate, essentially independent of the gate voltage (s. Eq. (15)). Since the confinement potentials in source- and drain contact are essentially independent of the gate voltage as well, the transversal overlap of the wave functions is seen to be approximately constant. One can show that within SMA it holds that $0 \leq C \leq 1$, so that $C = 0.1$ indicates a rather poor wave-function-coupling between contacts and transistor channels caused by back-reflections.

Finally, in the threshold- and subthreshold regime the temperature calibration function in Fig. 3 (a) stays close to the room temperature value of $u \sim 0.1$. This is in agreement with the presence of only small tunneling drain currents in this regime leading to negligible Joule heating. To summarize, the results in Figs. 2 and 3 demonstrate that in the threshold- and subthreshold regime all $I_D - V_D$ traces of the three transistors can be derived from only four constants, namely $u = 0.09$, $C = 0.1$, $\beta = 2/V$, and $v_0^0 = 2$ ('four-constants-fit' in Figs. 2 and 3).

Above threshold voltage the chemical potential in the source contact rises above the maximum height of the barrier. Then the occupation of the lowest transverse level in the channel but also that of the higher transverse levels is strongly enhanced. This population of the electron channel leads to its widening as signaled by the increase in C. Furthermore, since the current grows due to the onset of classically allowed transport enhanced Joule heating occurs and the temperature increases rapidly. The widening of the electron channel and the heating of the transistor, in turn, favor the occupation of higher transverse channels in the electron channel and the SMA becomes invalid. As a consequence, the calibration parameters of the cSMA in Fig. 3 have to be regarded as pure fit-parameters in the ON-state. Therefore, at higher V_G one has to consider as an artifact, first, the extent of the transistor heating and, second, the extent of the reentrant increase for the maximum barrier height above the chemical potential.

4. Conclusions

The combination of the recently developed SMA and a special fitting procedure with three calibration functions yields excellent quantitative agreement with experimental data. In the threshold regime and below, the calibration functions can be calculated from four constants only. Making contact to the standard MIS-model, these four constants can be physically interpreted, allowing one calibration function to extract central device parameters: The body factor, the built-in potential between source and substrate, the flat band voltage and the wave function overlap factor between electron channel and contacts.

Acknowledgement

We gratefully acknowledge funding by the 'Nachwuchsforschergruppe *Hybride Systeme* des Landes Brandenburg'.

References

[1] Lundstrom M., Guo J. Nanoscale Transistors. Springer, New York, 2006.

[2] Anantram M. P., A. Svizhenko. Multidimensional Modeling of Nanostructures. *IEEE Trans. Electron Devices*, **54**, P. 2100–2115 (2007).

[3] Vasileska D., Mamaluy D., et al. Semiconductor Device Modeling. *J. Comput. Nanosci.* , **5**, P. 999–1030 (2008).

[4] Smrčka L. R-matrix and the coherent transport in mesoscopic systems. *Superlattices and Microstructures*, **8**, P. 221–224 (1990).

[5] Wulf U., Kučera J., Racec P. N., Sigmund E. Transport through quantum systems in the R-matrix formalism. *Phys. Rev. B*, **58**, P. 16209 (1998).

[6] Nemnes G. A. , Wulf U., Racec P. N. Nano-transistors in the Landauer-Büttiker formalism. *J. Appl. Phys.*, **96**, P. 596–604 (2004).

[7] Nemnes G. A. , Wulf U., Racec P. N. Nonlinear I-V characteristics of nanotransistors in the Landauer-Büttiker formalism. *J. Appl. Phys.*, **98**, P. 843081 (2005).

[8] Nemnes G. A., Ion L., Antohe S. Self-consistent potentials and linear regime conductance of cylindrical nanowire transistors in the R-matrix formalism. *J. Appl. Phys.*, **106**, P. 113714 (2009).

[9] Descouvemont P., Baye D. The R-matrix theory, *Rep. Prog. Phys.*, **73**, P. 36301 (2010).

[10] Wulf U., Richter H. Scale-invariant drain current in nano-FETs. *Journal of Nano Research*, **10**, P. 49–62 (2010).

[11] Wulf U., Richter H. Scaling properties of ballistic nano-transistors. *Nanoscale Research Letters*, **6**, P. 365–372 (2011).

[12] Mil'nikov G., Mori N., Kamakura Y. Application of the R-matrix formalism method in quantum transport simulations. *J. Comput. Electron*, **10**, P. 51–64 (2011).

[13] Raffah B. M., Abbott P. C. Efficient computation of Wigner-Eisenbud functions. *Computer Physics Communications*, **184**, P. 1581–1591 (2013).

[14] Colinge J.-P. Fully-Depleted SOI CMOS for Analog Applications. *IEEE Trans. Electron Devices*, **45** P. 1010–1016 (1998).

[15] Jensen K. L. Improved FowlerNordheim equation for field emission from semiconductors. *J. Vac. Sci. Technol. B*, **13**, P. 516–527 (1995).

[16] Taur Y., Ning T.H. Fundamentals of modern VLSI devices. Cambridge University Press, Cambridge, 2009, Sect. 2.3.

[17] Sze S.M. Physics of Semiconductor Devices. John Wiley and Sons, New York, 1981, Sect. 7.

APPENDIX

A. Calibration functions in the standard MIS-model

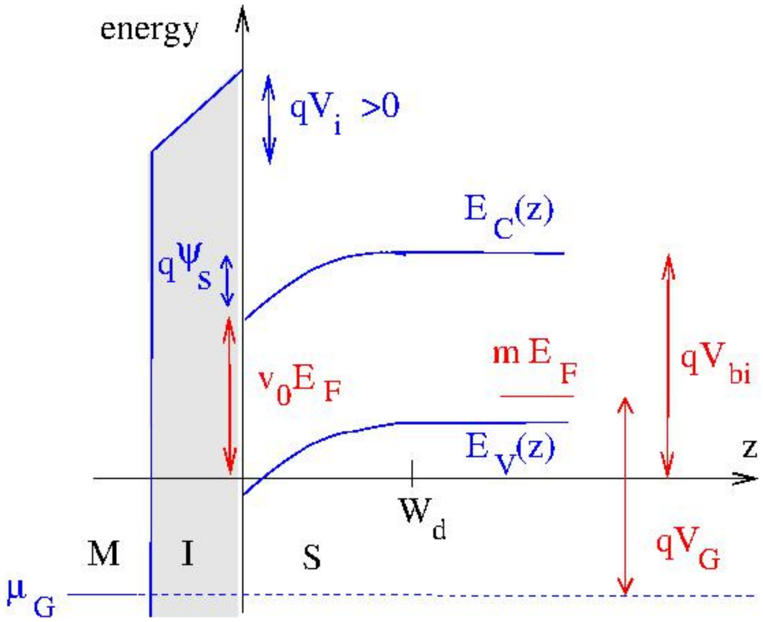

FIG. 4. Energy bands $E_{C/V}(z)$ of a standard MIS-structure (s. Fig. [2.35] in [16]) and energy levels in the cSMA (times-italic font and filled left right arrows, s. Fig. 1) in one diagram. To arrive at the basic relation Eq. (10), first, $E_C(0)$ is set equal to the height of the potential barrier, $v_0 E_F$ in Eq. (3). Second, one identifies $E_C(W_d) = qV_{bi}$ where W_d is the depletion layer width and qV_{bi} is the built-in potential between source contact and p-substrate.

In the threshold- and subthreshold regime, it can be assumed that the quantum mechanical electron charge in the transistor channel is negligible against the charge of the ionized acceptors, which can be treated in standard device theory (s. Sect. 2 of [16]). In this depletion approximation the position of the bottom of the conduction band $E_C(z)$ in the standard MIS-model can be associated with the transverse quantum-confinement potential $V(z)$ in the electron channel at zero drain voltage (s. Eq. (15)). For interpretation of the calibration functions in the cSMA we now plot in one diagram, shown in Fig. 4, the energy bands in the standard MIS-model (s. Fig. [2.35] in [16]) and the energy levels in the cSMA (filled left right arrows in Fig. 1). To construct a plot of these quantities in the common energy diagram the energy zero is set to the bottom of the conduction band in the source. Furthermore, we equate the chemical potential in the source contact, $\mu = mE_F$, with the chemical potential in the bulk of the p-substrate because, both, the source contact and the back gate are grounded. It is assumed that the host material in the substrate and in the grounded source are the same. Then, the bottom of the conduction band in the bulk p-substrate $E_C(z > W_d)$ is given by the built-in potential qV_{bi} between the isolated host materials of the source contact and in the substrate. The barrier height v_0 in Eq. (3) gives the position of the bottom of the conduction band $E_C(0)$ at the interface so that

$$v_0 E_F = E_C(0) = E_C(z > W_d) - q\Psi_s = qV_{bi} - q\Psi_s, \tag{10}$$

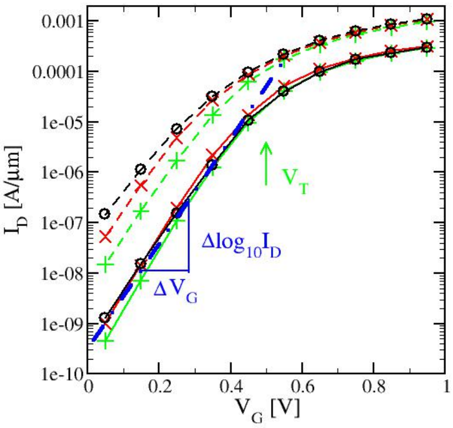

FIG. 5. Transfer characteristics of the experimental transistors in Fig. 3, dash-dotted lines for $V_D = 0.1V$ and dashed lines for $V_D = 1.0V$. Open circles $L = 22$ nm, filled triangles $L = 26$ nm, and symbols $'+'$ $L = 30$ nm. At the lower drain voltage, thermally activated behavior according to Eq. (14) is found with a slope $[d\log_{10} I_D/dV_G]^{-1} \sim 96mV/$decade, corresponding to $n = 1.6$ taken from the solid line. At the higher drain voltage thermal activation is overlayed with source-drain tunneling [11].

where Ψ_s is the potential drop across the space charge region of thickness W_d. Assuming a gate voltage controlled electron channel, one now writes in the standard MIS model the following:

$$V_G - V_{FB} = V_i + \Psi_s = -\frac{Q_s}{C_i} + \Psi_s, \tag{11}$$

where V_G is the applied gate voltage, V_i is the voltage that drops across the insulator barrier, $Q_s < 0$ is the total charge per area in the space charge region, and C_i is the constant insulator capacitance. In the depletion approximation the depletion layer capacitance can be written as $C_D = -\partial Q_s/\partial \Psi_s = \epsilon_s/W_d \sim \epsilon_s/W_{dm}$ [s. Eq. (2.201) of [16]]. Here, ϵ_s is the dielectric constant of the p-substrate, and around the threshold, we may replace W_d by its maximum value W_{dm} so that C_D is a constant. In this approximation Eq. (11) becomes $\Psi_s = (V_G - V_{FB})/n$ with a constant body factor

$$n = 1 + \frac{C_D}{C_i}. \tag{12}$$

Insertion of this result in the basic relation (10) leads to the following:

$$v_0 = -\underbrace{\frac{q}{nE_F}}_{\beta} V_G + \underbrace{\frac{q}{E_F}\left(V_{bi} + \frac{1}{n}V_{FB}\right)}_{v_0^0}. \tag{13}$$

This equation has the same form as the numerical quantum-result (7). A comparison of (13) and (7) yields Eqs. (8) and (9).

In the assumed approximation $W_d \sim W_{dm}$ one obtains from the standard model a constant inverse subthreshold slope [s. Eq. (3.41) in [16]]

$$S = \left[\frac{d\log_{10} I_D}{dV_G} \right]^{-1} = 2.3 \frac{k_B T}{q} n, \tag{14}$$

which is found in the experimental transistors (s. Fig. 5) for small drain voltages. From the slope of the traces in their transfer characteristics one deduces $S = 96mV/$decade and then from (14) it follows that $n = 1.6$.

To finally discuss the overlap calibration function, one interprets $E_C(z)$ as the transverse confinement potential $V(z)$ in the electron channel. In depletion approximation with $W_d \sim W_{dm}$ it follows that

$$V(z) \sim 2\Psi_B \left(1 - \frac{z}{W_{dm}}\right)^2 + qV_{bi} \tag{15}$$

[s. Eqs. (2.183) and (2.187) of Ref. [16]]. Here $\Psi_B = \mu_i - \mu$, where μ_i is the chemical potential of the intrinsic substrate semiconductor in the bulk. The channel confinement potential is seen to be essentially independent of the gate voltage. Therefore it is to be expected that the transversal overlap between the wave functions in the contacts and in the electron channel (and thus C) is independent of the gate voltage as well.

NANOSYSTEMS: PHYSICS, CHEMISTRY, MATHEMATICS, 2013, 4 (6), P. 810–815

EFFECT OF HYDROTHERMAL SYNTHESIS CONDITIONS ON THE MORPHOLOGY OF ZrO_2 NANOPARTICLES

A. N. Bugrov[1,2], O. V. Almjasheva[2,3]

[1]Institute of Macromolecular Compounds RAS, Saint Petersburg, Russia

[2]Saint Petersburg Electrotechnical University "LETI", Saint Petersburg, Russia

[3]Ioffe Physical-Technical Institute RAS, Saint Petersburg, Russia

bugrov.an@mail.ru, almjasheva@mail.ru

PACS 61.46.-w

Nanoparticles based on ZrO_2 in the form of spheres, cylinders and agglomerates in the form of hollow microspheres were obtained. It is shown that the main factor influencing on the formation of nanostructures based on zirconium dioxide under hydrothermal conditions is the chemical prehistory of the starting materials. The possibility of varying the synthetic parameters to obtain a zirconia-based material with high porosity and specific surface area was shown.

Keywords: nanoparticles, hydrothermal synthesis, zirconia.

1. Introduction

Analysis of the size, morphology and structural characteristics of nanoparticles shows that they are highly dependent on the method and conditions of their production [1-3]. Moreover, even within the same method changing the synthetic parameters can lead to a significant change in the characteristics of the resulting nanostructures. One such method is hydrothermal synthesis. This method, as shown in [2, 4-6], allows one to obtain weakly agglomerated nanoparticles with different chemical composition and narrow particle size distribution. Through a wide range of variable parameters (chemical prehistory of the starting materials, pressure, temperature, time, chemical composition of hydrothermal solutions) nanostructures with desired the dispersion, morphology and structure can be obtained [7-11]. However, the existing differences in the results of various researchers [2, 4-12] does not allow one to predict the possibility of obtaining nanoparticles with specified characteristics, which leads to the need for a comprehensive study and the establishment of the influence of prehistory and chemical parameters of hydrothermal treatment on the formation of nanoparticles.

In that regard, this article examines the influence of the method by which the initial zirconium hydroxide was obtained and the conditions of its subsequent hydrothermal treatment on the size, structure and shape of the formed nanostructures.

2. Experiment

The following were used as the starting materials for hydrothermal treatment:

(1) Zirconium hydroxide was obtained by precipitation from a solution of 1M $ZrOCl_2$ with 12M NH_4OH. The precipitate was then washed with distilled water until a negative reaction to Cl^-ions and neutral pH (pH ≈ 7) and dried at $100\,^\circ$C.

(2) Zirconium hydroxide was obtained by adding $ZrOCl_2$ to a 0.5 M solution of NaOH. The precipitate wasn't washed from the neutralization reaction products, however, subjected to sonication (ν = 3.5 kHz) for 30 minutes with continuous mechanical stirring.

(3) The suspension obtained by dissolving $ZrOCl_2$ in an ethanol-HCl mixture with the addition of $(NH_2)_2CO$ to adjust the pH. The ratio of C_2H_5OH:HCl in the mixture was 3:2.

Hydrothermal treatment was performed in a steel autoclave with a teflon vial from 160–240 ° C for 4–72 hours. Distilled water solutions of either NaOH or an acid-alcohol mixture were used as the hydrothermal solution.

To determine the elemental composition of the hydrothermal treatment products, we used the method of energy dispersive X-ray analysis (EDX) (electron microscope Hitachi S-570, equipped with a microprobe system Bruker Quantax 200).

In the case of ZrO_2 based nanostructures, the chemical composition of the post hydrothermal synthesis medium was determined using the Fourier AVANCE-400 NMR spectrometer (Bruker, Germany) with an operating frequency for ^{1}H: 400 MHz. ^{1}H NMR spectra of hydrothermal solution in heavy water D_2O was obtained at T = 298 K in a single-pulse method with a suppressed water signal.

The phase composition of the samples was determined by X-ray diffraction analysis on a Shimadzu XRD-7000 diffractometer (CuK_α - radiation).

The crystallite size was calculated by X-ray diffraction line broadening samples using Scherrer's formula. The particle size was determined by analysis of the results obtained by transmission electron microscopy (Tesla BS-500 U = 90 kV).

The specific surface area values for ZrO_2 nanoparticles of different composition, size and morphology were determined on the Micromeririca ASAP 2020 analyzer (USA) by removing the nitrogen adsorption isotherms at 77 K.

3. Results and discussion

According to X-ray analysis of composition 1, treated at 240 ° C for 4 hours using a distilled water hydrothermal solution leads to the formation of predominantly tetragonal ZrO_2 nanoparticles with a size of coherent scattering area (CSA), about 20 nm (Fig. 1a). Analysis of the electron microscopy data indicated that the formed nanoparticles were close to spherical with a narrow size distribution (Fig. 1.b). These results were consistent with the results of articles [12-14].

Hydrothermal treatment of composition 2 was conducted at 200 ° C for 24–72 hours. A solution of NaOH was used as the hydrothermal solution. Based on X-ray diffraction and electron microscopy data, it can be concluded that changing the feed preparation process and the chemical composition of the hydrothermal solution leads to some changes in the flow processes of dehydration and crystallization under hydrothermal conditions.

Hydrothermal treatment of composition 2 at 240 ° C for 24 h resulted in a rather broad peak in the X-ray diffraction pattern corresponding to 100% reflex of t-ZrO_2, against which, relatively narrow maxima of m-ZrO_2 were recorded (Fig. 2a).

According to results of a SEM study, the sample contains two types of particles. One can be characterized as rod shaped (Fig. 2b) particles having diameter of 50 nm and length of 100 nm and other as considerably smaller particles with close to spherical morphology.

When hydrothermal treatment was increased from 24 to 48 and 72 hours, the intensity of t-ZrO_2 peaks for composition 2 considerably decreased (Fig. 2a). Herewith, it should be

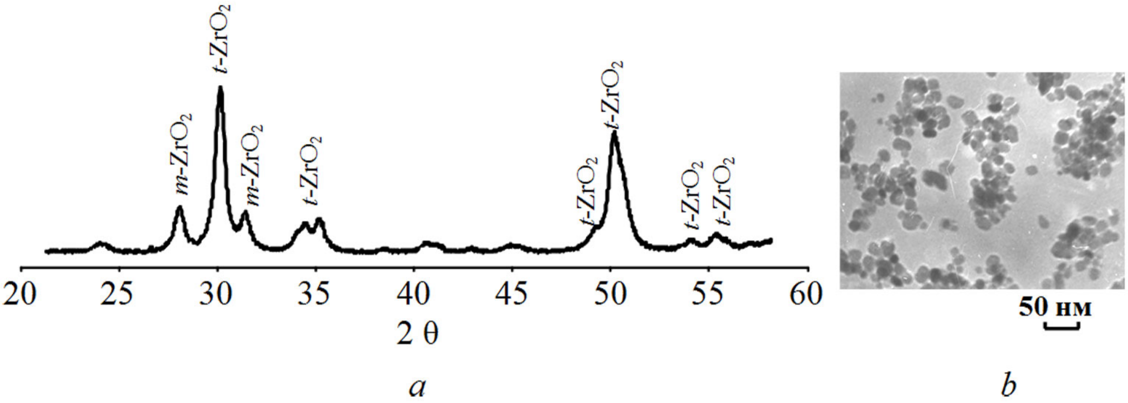

FIG. 1. X-ray diffraction pattern and photomicrograph of nanoparticles based on ZrO_2, obtained by hydrothermal treatment of composition 1

noted that the because of the lack of a discernible change in the width of peaks for monoclinic as well as cubic zirconia, one can argue that the size of the formed crystallites was constant.

However, the results of the SEM study showed not only an increase in the quantity of the ZrO_2 particles in the form of rods, apparently with monoclinic crystalline structure, but also in their length, which average 200 nm, while at the same time, the diameter of rods didn't change appreciably.

As was reported in papers [12, 15], the use of distilled water as the hydrothermal solution at the same temperature didn't lead to a noticeable change in the shape and structure of the zirconia nanoparticles, even in the case of prior ultrasonic treatment of the initial suspension and increasing the hydrothermal treatment duration to 72 hours. Additionally, it was shown [13] that the direct addition of sodium hydroxide or chloride to the hydrothermal solution also didn't drastically change the shape and size of zirconia nanoparticles in comparison with distilled water.

Results of an EDX study showed that the hydrothermal synthesis product of composition 2 contained a noticeable quantity of sodium (about 5 mol. %), but at the same time, in samples obtained from compositions 1 and 3, those impurities were not found.

Seemingly, in this case, because sodium hydroxide was used at the generating stage of the $[Zr(OH)_2{\cdot}4H_2O]_4^{2+}(OH)_8^-$ hydroxo-complex, its role in the formation of zirconia nanoparticles with one or another crystallite structure was previously noted [12, 14], sodium ions are kept in a zirconia nanoparticle structure, thus stabilizing the tetragonal phase in a manner similar to water molecules as has been shown previously [15]. Herein, analysis of obtained data showed that formation of monoclinic phase occurs not because of t-ZrO_2 →m-ZrO_2 crystalline phase transition, but because of a recrystallization process. In other words, the use of NaOH as a hydrothermal solution provides pH value, which is enough to activate dilution of t-ZrO_2 nanoparticles, stabilized by impurity ions, with size of coherent scattering region about 10 nm and subsequent crystallization of thermodynamically stable m-ZrO_2 in the form of rods.

The hydrothermal treatment of composition 3, which is a high temperature hydrolysis of $ZrOCl_2$ in an acid-alcohol medium, was carried out at 160 °C over 24 hours. According to X-ray diffraction line broadening analysis, the obtained zirconia particles have size of coherent scattering region of about 5 nm (Fig. 3a).

In this case, SEM images showed the formation of hollow spheres in the range of 300–700 nm with wall thickness of approximately 50 nm (Fig. 3b).

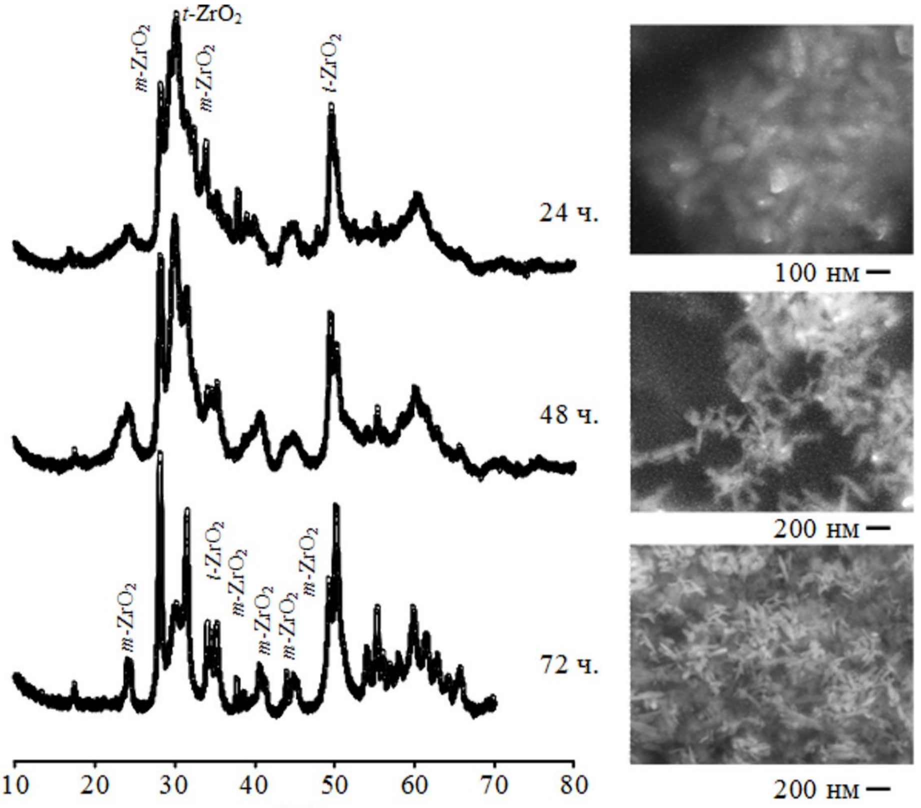

a *b*

FIG. 2. X-ray diffraction pattern and photomicrograph of nanoparticles based on ZrO_2, obtained by hydrothermal treatment of composition 2

Apparently in this case, the observed hollow microspheres are agglomerates, consisting of m-ZrO_2 crystallites with average size of about 5 nm. Analysis of the specific surface area, which amounts 140 m^2/g, confirmed this fact. At the same time, the specific surface area of zirconia nanoparticles, produced by hydrothermal treatment of composition 1, is only 85 m^2/g.

NMR spectral analysis of the hydrothermal solution after heat treatment (Fig. 4) indicated the presence of two quartets at 3.5 ppm region assigned to CH_2 groups of ethanol and diethyl ether, the signals at 4.2 ppm and 1.0 ppm assigned to HDO and CH_3 groups of ethanol and ether. Furthermore, the presence of a small amount of ammonium ions, which apparently could be formed by decomposition of urea during hydrothermal treatment was shown by the signal at 7.0 ppm

It can be assumed that in this case the formation of the observed structure occurs by a template synthesis mechanism. That is, ethanol in the presence of concentrated hydrochloric acid at elevated temperature dehydrates to form an ether, which, due to the low solubility in the mixed solution of ethanol and water, may exist in the form of oil droplets in the solution [10]. When the temperature is raised urea located in the initial mixture slowly reacts with water to form NH_4OH and CO_2, which leads to higher pH and as a consequence hydrolysis of $ZrOCl_2$ on the oil drop-aqueous solution interface.

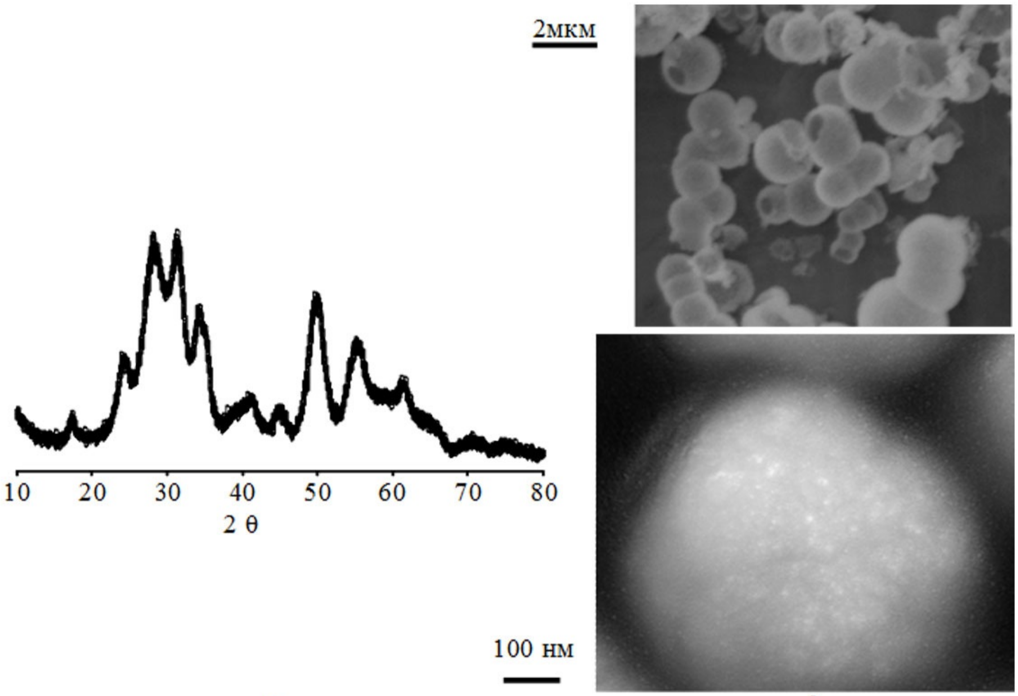

a *b*

Fig. 3. X-ray diffraction pattern and photomicrograph of nanoparticles based on ZrO_2, obtained by hydrothermal treatment of composition 3

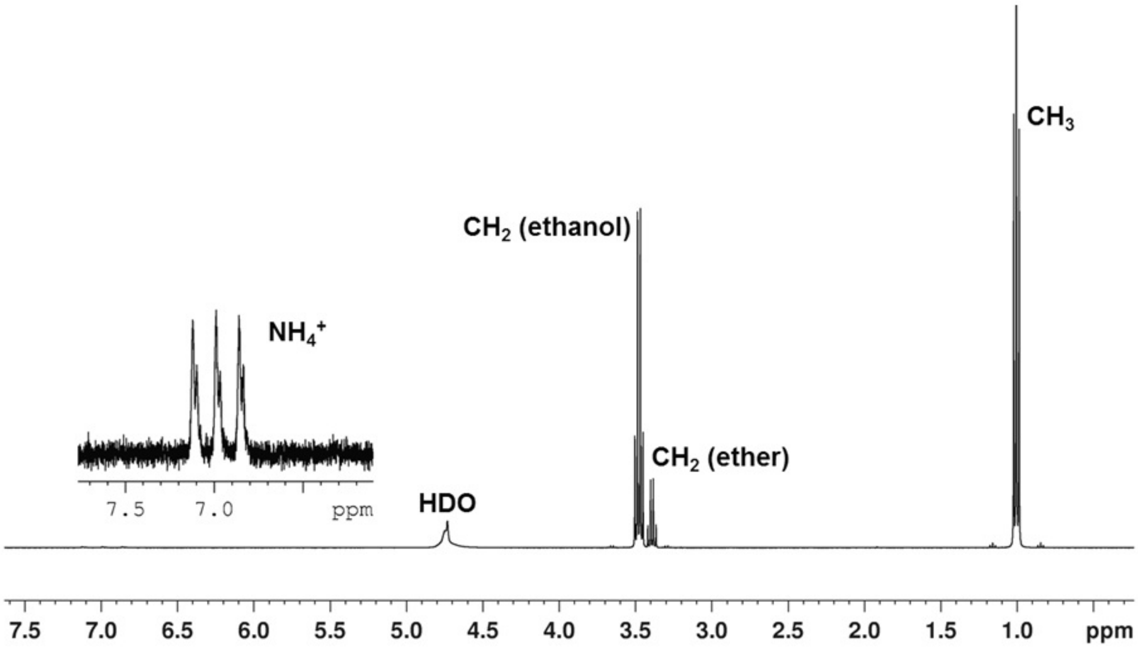

Fig. 4. NMR spectrum of hydrothermal solution after heat treatment of composition 3

4. Conclusions

Thus, on the basis of these data, it can be concluded that the main factor contributing to the formation of nanostructures based on zirconium dioxide under hydrothermal conditions is the prehistory of the starting materials.

This work has shown that it is possible to vary synthetic parameters to obtain a zirconia-based materials with high porosity and a specific surface area, which is promising for the generation of nanoparticles for use as nanoreactors, catalyst or catalyst carrier, adsorbent, etc.

Acknowledgement

We are deeply grateful to V. V. Gusarov for the attention to work. This work was supported by the Russian Foundation for Basic Research (grant 13-08-01207).

References

[1] J.P. Jolivet, S. Cassaignon, C. Chanéac, et al. Design of metal oxide nanoparticles: Control of size, shape, crystalline structure and functionalization by aqueous chemistry. *Comptes Rendus Chimie*, **13**(1–2), P. 40–51 (2010).

[2] A. Aslani. Controlling the morphology and size of CuO nanostructures with synthesis by solvo/hydrothermal method without any additives. *Physica B: Condensed Matter*, **406**(2), P. 150–154 (2011).

[3] H. Eltejaei, J. Towfighi, H.R. Bozorgzadeh, M.R. Omidkhah, A. Zamaniyan. The influence of preparation conditions on ZrO_2 nanoparticles with different PEG–PPG–PEG surfactants by statistical experimental design. *Materials Letters*, **65**(19–20), P. 2913–2916 (2011).

[4] O.V. Almjasheva, B.A. Fedorov, A.V. Smirnov, V.V. Gusarov. Size, morphology and structure of the particles of zirconia nanopowder obtained under hydrothermal conditions. *Nanosystems: physics, chemistry, mathematics*, **1**(1), P. 26–36 (2010).

[5] E. Lester, P. Blooda, J. Lia, M. Poliakoff. Advancements in the supercritical water hydrothermal synthesis (scWHS) of metal oxide nanoparticles. NSTI-Nanotech. Boston, May 7–11, 2006, 1, P. 347–350.

[6] X.Y. Shen, Y.C. Zhai, Y.H. Zhang Preparation and characterization of ultrafine zinc oxide powder by hydrothermal method. Transactions of Nonferrous Metals Society of China, **20**(1), P. 236–239 (2010).

[7] K. Byrappa, M. Yoshimura. Handbook of hydrothermal technology — A technology for crystal growth and materials processing. Norwich, N.Y.: Noyes Publications, 870 p. (2001).

[8] H. Hayashi, Y. Hakuta. Hydrothermal synthesis of metal oxide nanoparticles in supercritical water. *Materials*, **3**, P. 3794–3817 (2010).

[9] E. Lester, P. Blood, J. Denyer, et al. Reaction engineering: The supercritical water hydrothermal synthesis of nano-particles. *Journal of Supercritical Fluids*, **37**(2), P. 209–214 (2006).

[10] F.Q. Lin, W.S. Dong, C.L. Liu, et al. In situ source–template-interface reaction route to hollow ZrO_2 microspheres with mesoporous shells. *Journal of Colloid and Interface Science*, **323**, P. 365371 (2008).

[11] G. Gundiah, S. Mkhopadhyay, U.G. Tomkurkar, A. Govindaraj, U. Maitra, C.N.R. Rao. Hydrogel route to nanotubes of metal oxides and sulfates. *Journal of Materials Chemistry*, **13**, P. 2118–2122 (2003).

[12] O.V. Pozhidaeva, E.N. Korytkova, D.P. Romanov, V.V. Gusarov. Formation of ZrO_2 nanocrystals in hydrothermal media of various chemical compositions. *Russian Journal of General Chemistry*, **72**(6), P. 849–853 (2002).

[13] O.V. Pozhidaeva, E.N. Korytkova, I.A. Drozdova, V.V. Gusarov. Phase state and particle size of ultradispersed zirconium dioxide as influenced by conditions of hydrothermal synthesis. *Russian Journal of General Chemistry*, **69**(8), P. 1219–1222 (1999).

[14] A. Mondal, S. Ram Reconstructive phase formation of ZrO_2 nanoparticles in a new orthorhombic crystal structure from an energized porous $ZrO(OH)_2{\cdot}xH_2O$ precursor. *Ceramics International*, **30**(2), P. 239–249 (2004).

[15] O.V. Almyasheva. Hydrothermal synthesis, structure and properties of nanocrystals and nanocomposites based on the system ZrO_2-Al_2O_3-SiO_2 (In Russian): dissertation. St. Petersburg, ISC RAS, 239 p. (2007).

NANOSYSTEMS: PHYSICS, CHEMISTRY, MATHEMATICS, 2013, 4 (6), P. 816–822

ELECTRICAL PROPERTIES OF HOT WALL DEPOSITED PbTe–SnTe THIN FILMS

V. A. Ivanov[1], V. F. Gremenok[1], H. G. Seidi[1], S. P. Zimin[2], E. S. Gorlachev[2]

[1]State Scientific and Production Association "Scientific-Practical Materials Research Centre
of the National Academy of Sciences of Belarus, P. Brovka Street 19, 220072 Minsk, Belarus,
Tel.: +375 172 84 12 49, Fax: +375 172 84 08 88
[2]Yaroslavl State University, Sovetskaya Street 14, 150000 Yaroslavl, Russia,
Tel.: +7 4852 797774, Fax: + 7 4852 797751

vasil@physics.by, zimin@uniyar.ac.ru

PACS 73.50.-h

Polycrystalline $Pb_{1-x}Sn_xTe$ $(0.0 \leq x \leq 1.0)$ telluride alloys were synthesized by the direct fusion technique. Thin films of these materials were prepared by a hot wall deposition method on glass substrates at T_{sub} =230–330 °C and in a vacuum of about 10^{-5} Torr. The microstructure of the films was characterized by XRD, SEM, EDX and AES. The films showed a natural cubic structure. The thin films' microstructure consisted of densely packed grains with dimensions of 50–300 nm and crystallite growth direction is perpendicular to substrate plane. The as-grown $Pb_{1-x}Sn_xTe$ films showed p-type conductivity. Thermoelectric measurements of the films showed high values for the room-temperature Seebeck coefficient ranging, from 20 to 400 μV·K^{-1}, for SnTe to PbTe thin films, respectively. The conductivity of the films was in the range of $3\cdot10^1$–$1\cdot10^4$ $\Omega^{-1}\cdot$cm^{-1}.

Keywords: hot wall deposition, electrical properties, thin films.

1. Introduction

IV–VI compound semiconductors are potentially attractive materials for a variety of electronic applications: IR detectors and sources, thermoelectric converters, solar cells, memory units, spintronic devices, and others [1–4]. The fundamental characteristics of these compounds, in particular their narrow band gap, high dielectric permittivity, radiation hardness, high carrier mobility, and high bond ionicity, make them unique among compound semiconductors. The main characteristics of IV–VI compound solid solutions (band gap, spectral response, lattice parameter, thermal expansivity, and others) depend on their composition. An important issue in the synthesis and practical application of materials is a precise knowledge of the composition stability limits of solid solutions' dependence on temperature, as well as their physical characteristics' dependence on composition. The rocksalt-structure IV-VI semiconductor compounds such as PbTe and SnTe have small band gaps, high dielectric constants, and a variety of very unusual thermodynamic, vibrational, electronic, and infrared properties [4]. These narrow band-gap semiconductors have been of great interest for the last four decades for their fundamental physics and their application in infrared devices and thermoelectric materials. In fact, PbTe was one of the first materials studied by Ioffe and his colleagues in the middle of the 20th century when there was a revival of interest in thermoelectricity [1]. In addition, lead and tin containing materials in electronic devices would decrease the production costs, because they are cost effective, abundant in nature, and relatively less-toxic. Several methods have been used to deposit SnTe and PbTe films, including e-beam sputtering, spray pyrolysis, chemical and electrochemical deposition. However, most of these methods involve subsequent annealing to obtain the required quality of the films. In our continuing effort to prepare the

PbTe-SnTe semiconductor films, we have used a hot wall deposition (HWD) method. Among the various thin film deposition techniques, HWD has become a popular and reliable synthesis for film preparation [5–11]. In this method, a heated silica tube directs the evaporated source material towards the substrate. This deposition technology yields high quality thin films with smooth surfaces grown under conditions very close to a quasithermal equilibrium conditions. High quality electro-optic thin films of the different II–VI materials produced by this method didn't require the post-growth heat treatments [6, 7]. Here, we report for the first time on the preparation of $\mathrm{Pb}_{1-x}\mathrm{Sn}_x\mathrm{Te}$ thin films by the hot wall deposition of bulk materials onto glass substrates at different physical parameters. The microstructure and electrical properties of the as-deposited thin films are also described. Our work shows that HWD processing is promising for the fabrication of PbTe–SnTe ternary compounds.

2. Experimental Details

Polycrystalline $\mathrm{Pb}_{1-x}\mathrm{Sn}_x\mathrm{Te}$ ($0.0 \leq x \leq 1.0$) alloys were synthesized by the fusion method. In this method, the reaction between the sulfur vapors and molten metals were allowed to take place gradually in evacuated silica tubes. High purity (99.999%) mixtures of constituent elements (Pb, Sn, and Te) in stoichiometric proportions (with an accuracy of $5{\cdot}10^{-4}$ g) were sealed into evacuated silica tubes at 10^{-3} Torr. The evacuated tube was then placed into an electric furnace and kept at 450 °C for 7 days, and after that, at 700 °C for 10 days. In order to avoid explosions due to the telluride vapor pressure, the tube was heated slowly. The tubes were gradually cooled with a cooling rate of about 20 °C h^{-1} to room temperature in order to obtain polycrystalline $\mathrm{Pb}_{1-x}\mathrm{Sn}_x\mathrm{Te}$ compounds. The main feature of the hot wall deposition system is the heated linear quartz tube of 1.2 cm diameter, which served to enclose and direct the vapor from the source to the substrate. The quartz tube and substrates were heated independently. $\mathrm{Pb}_{1-x}\mathrm{Sn}_x\mathrm{Te}$ films were deposited by keeping the quartz tube temperatures around 600 °C. Glass plates were chemically cleaned, rinsed with distilled water and blown dried with compressed air before deposition. Substrate temperature was varied from 230 to 330 °C. The substrate was held at a distance of about 1 mm above the open end of the quartz tube acting almost as a lid closing the tube with the help of a substrate holder heater. The pressure in the chamber was about 10^{-5} Torr during evaporation. Chromel–alumel thermocouples were used to measure the temperatures of the quartz tube and the substrate. The deposition time was varied from 10 min to 50 min in order to obtain thin films in a wide range of thicknesses. The crystal structure of $\mathrm{Pb}_{1-x}\mathrm{Sn}_x\mathrm{Te}$ in both powder and thin film forms was investigated by X-ray diffraction (XRD) using a Siemens D-5000 diffractometer with CuK_α ($\lambda = 1.5405$ Å) radiation. The observed phases were determined by comparing the d-spacing with the Joint Committee on Powder Diffraction Standard (JCPDS) data files. Surface morphology and cross-section of films were investigated with scanning electron microscope (SEM) (Hitachi S-806). The elemental composition of the obtained films was determined from energy dispersive X-ray (EDX) data, using scanning electron microscope Stereoscan-360 with EDX spectrometer AN 10000 with an accuracy of about 2%. The depth profiling was done by Auger electron spectroscopy (AES) using a Perkin Elmer Physical Electronics model 590 with simultaneous sputter etching. The conductivity (σ) of the films was measured by the Van der Pouw method. The temperature range during the conductivity investigation was provided by a special cryostat from 80 to 450 K. Measurements of the conductivity temperature characteristics were carried out in vacuum of about $1{\cdot}10^{-3}$ Torr. The 'Leit-C' conductive carbon-based paste was used as electrical contacts to the films. The ohmic nature of the contacts was checked by recording the current–voltage characteristics. Thermoelectric properties (Seebeck coefficient) of the films were investigated at the room temperature. The temperature difference between the 'hot' and 'cold' ends of the probes was 25 K.

3. Results and discussion

3.1. Compositional and structural analysis

The physical properties of $Pb_{1-x}Sn_xTe$ thin films are influenced by the elemental composition and the substrate temperature. The characteristics of these layers were studied by the appropriate techniques and are discussed in the following sections. The as-deposited films were pinhole free, uniform and strongly adherent to the surface of the substrate. The evaluated thickness varied from 0.7 to 4.0 μm. The energy dispersive analysis of all as-deposited films showed that the obtained films are homogeneous and the compositions of the films are reproducible. This clearly shows that composition control can be easily achieved using HWD technique. The AES depth profile was used to study the concentration of elements present in the bulk of the as-grown $Pb_{1-x}Sn_xTe$ films. The data were obtained by sputtering an area of 10×10 μm^2 with energetic argon ions at a rate of 1000 Å/min. The AES depth profiles of the films reveal relatively uniform distribution of the components in the bulk of the films through the depth. This observation supports the XRD data, indicating uniform, single-phase thin film material. The chemical composition was determined by averaging the values from 5 different points on the surface of the same films. Elemental composition of the as-deposited $Pb_{1-x}Sn_xTe$ films has been confirmed by the AES method. The influence of the substrate temperature on the phase formation and crystalline structure of the $Pb_{1-x}Sn_xTe$ thin films was studied using XRD. The XRD spectra of the hot wall deposited layers showed that the films exhibited a polycrystalline nature (Fig. 1).

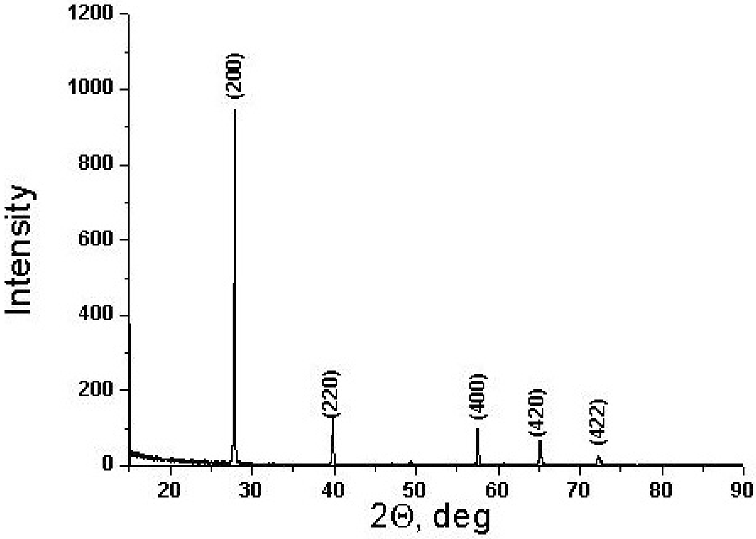

FIG. 1. Typical XRD spectrum of $Pb_{1-x}Sn_xTe$ films

The thin film powder patterns matched the powder target pattern satisfactorily and indicated the absence of binary phases. Differences in the relative intensities between the powder target and experimental patterns may be attributed to some texturing of the films. All thin films exhibited a strong (200) peak representing the preferable orientation. The spectrum also showed other peaks in addition to the (200) peak. The most intense peaks correspond to (220), (400) and (420) orientations. As-deposited $Pb_{1-x}Sn_xTe$ thin films showed a single phase cubic structure (space group $O^5{}_{h-}F_{m3m}$). The cell parameter (a) was evaluated using the standard equation for a cubic crystal structure. The change of lattice parameters with substrate temperature is marginal. SEM studies of the as-deposited layers demonstrated that the surface topology of the films is dependent on the growth temperature. SEM cross-section image of the $Pb_{0.72}Sn_{0.28}Te$ thin film on the glass substrate is shown in Fig. 2. The thin films microstructure consisted of densely packed grains with dimensions of 50–300 nm and crystallite growth direction is perpendicular to the substrate plane. A gradual change in growth of crystallites was observed with the increase of the substrate temperature. The films had a columnar structure with the lateral grain size in the range of tens of nanometers to several microns. The films grown at high temperature consisted of large crystallites. Scanning electron microscopy measurements showed that the surface roughness for all the $Pb_{1-x}Sn_xTe$ films was 10–40 nm and the surface was characterized by crystallites with distinct boundaries. SEM studies demonstrated that the thickness of the layers depends on growth conditions. The increase in substrate temperature at constant deposition time leads to an increase in the film thickness. The temperature dependence of the film thickness could be explained by the availability of the thermal energy for a nucleation at different substrate temperatures, which in turn increases with increasing substrate temperature.

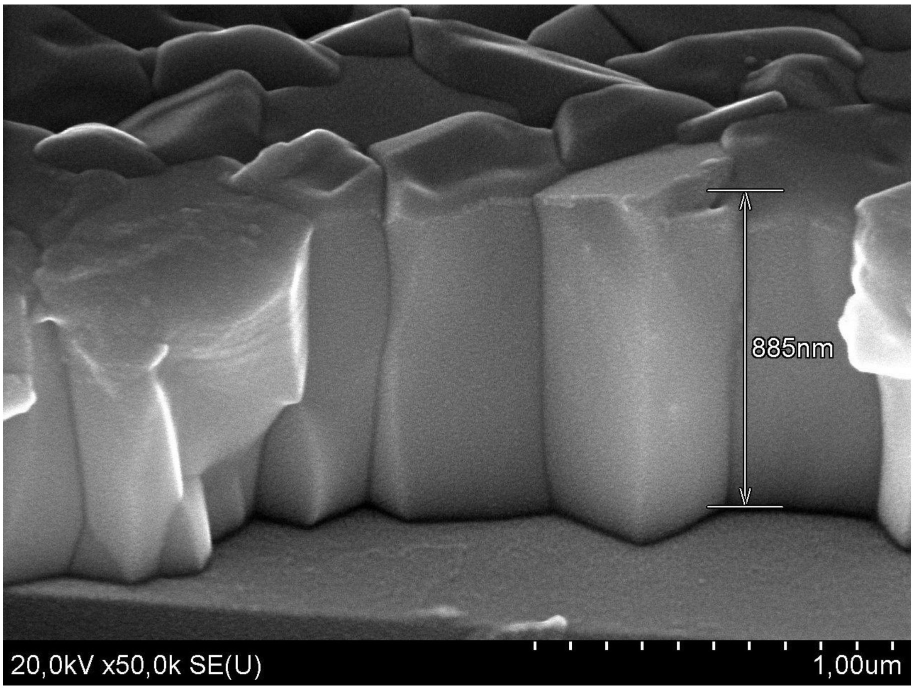

FIG. 2. SEM cross-section image of the $Pb_{0.72}Sn_{0.28}Te$ thin film on glass

SEM images of the $Pb_{1-x}Sn_xTe$ layers showed a densely packed microstructure free of pinholes. The grains are electrically well connected to each other, which is essential for the development of p-n junction. The density of the films is of critical importance, since it will prevent the diffusion of atoms during the growth of the other material layers for the production of electronic devices.

3.2. Electrical properties

The as-prepared films showed p-type electrical conductivity, which is confirmed by the thermoelectric probe measurement. The Seebeck coefficient and the conductivity of the $Pb_{1-x}Sn_xTe$ films was in the range of α =20–400 μV·K^{-1} and σ =3·10^1–1·10^4 Ω^{-1}·cm^{-1} respectively, at room temperature depending on the concentration of Pb in the films. Fig. 3 shows the dependence of the Seebeck coefficient on the concentration of the lead atoms at room temperature.

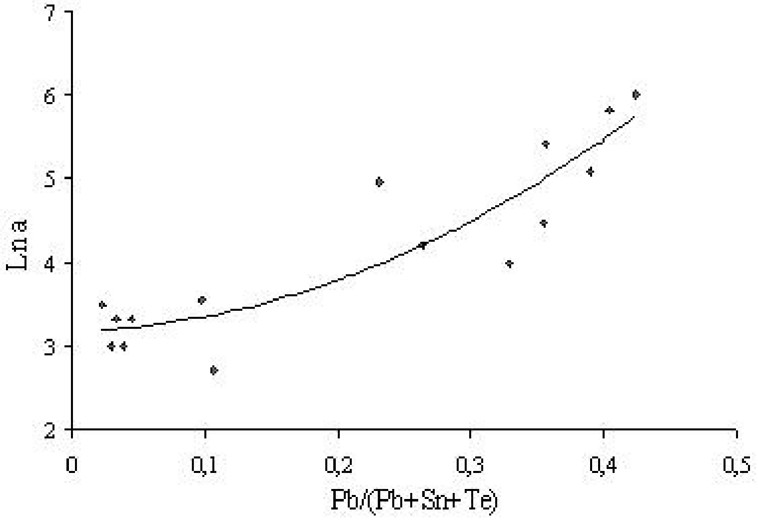

FIG. 3. Dependence of the Seebeck coefficient on lead concentration

Increasing of Pb concentration leads to an increase of the Seebeck coefficient. This coefficient is determined by various parameters of a material. In the case of a single-phase material with different kind of defects (or impurities), which produce both acceptor and donor energy levels in the band gap, the Seebeck coefficient can be written in the following form [12]:

$$\alpha = k_B\sigma^{-1}\left[\mu_n n\left(S+5/2-\ln n/N_c\right)-\mu_p p\left(S+5/2-\ln p/N_v\right)\right], \quad (1)$$

where μ_n, μ_p – mobility of carriers, σ – conductivity, S – charge carriers scattering mechanism, k_B – Boltzmann constant, n, p – charge carriers concentration, N_c, N_v – effective states density in the conduction band and in the valence band, respectively. As is seen from (1), the coefficient α is inversely proportional to the conductivity and directly proportional to the ratio between parameters determining the conductivity type. The increase of the Seebeck coefficient could be rationalized by both a decrease of the conductivity and by an increase in the holes mobility [13]. Increasing the lead concentration resulted in a decrease in the conductivity, as shown in Fig. 4.

The decrease of the conductivity could be explained by a decrease in the hole concentration in the films. The conductivity of the lead chalcogenides is independent of temperature at low temperatures [13]. The temperature dependence of the dark conductivity of the $Pb_XSn_{1-X}Te$ films is shown in Fig. 5.

As seen from Fig. 5, the conductivity does not vary appreciably from 90–190 K. Conductivity decreases by law $\sigma = T^{-n}$ with increasing temperature above 190 K. The decrease in conductivity can be explained by the decrease in the carrier mobility [13]. Conductivity begins to increase at temperatures above 300 K. It can be assumed that the thermal increase in conductivity (semiconductor conductivity) is due to the valence band-acceptor level transitions. Such

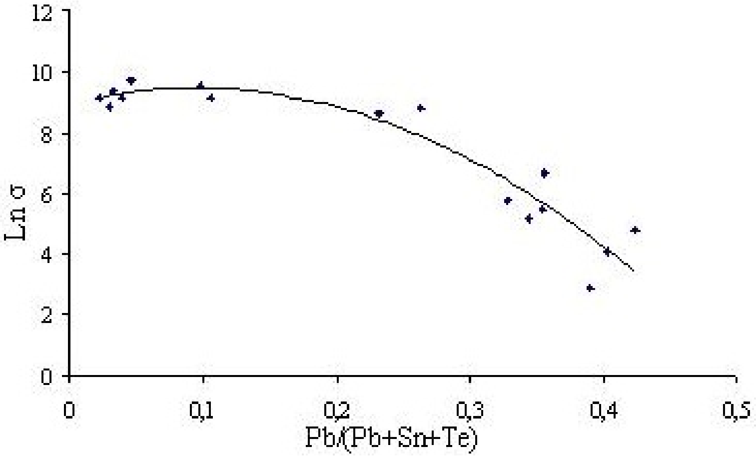

FIG. 4. Dependence of the film's electrical conductivity on lead concentration

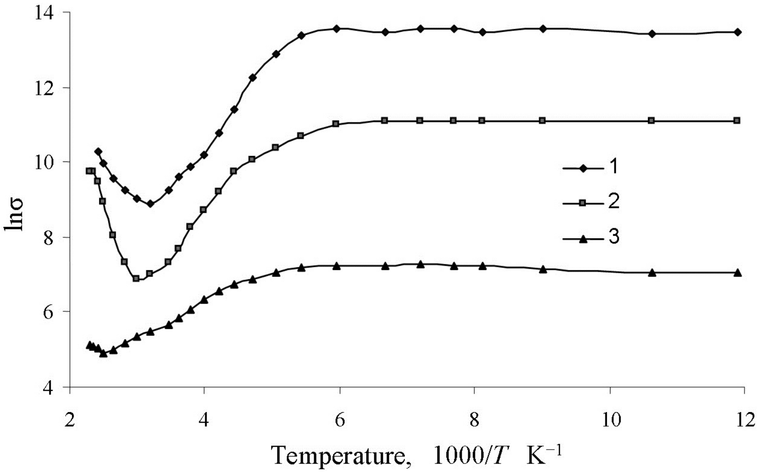

FIG. 5. Temperature dependence of the dark conductivity for films with different Pb concentration, at.%: 1 – 2.26; 2 – 23.14; 3 – 40.36

temperature dependence of conductivity is typical for all the investigated $Pb_{1-x}Sn_xTe$ films. The nature of the impurities responsible for the electrical properties requires further study.

4. Conclusions

Lead tin telluride films were deposited at different substrate temperatures from 230 °C to 330 °C by hot wall vacuum deposition of bulk material onto glass substrates. X-ray diffraction measurements showed that as-grown $Pb_{1-x}Sn_xTe$ films have a cubic crystal structure. With the increase of the substrate temperature, the crystal structure of the films remains unaffected and the change in lattice parameters is marginal. Using HWD, it is possible to produce layers of (Pb,Sn)Te mixed crystals, which are several microns thick, pinhole free conformal to the substrate, and which consist of densely packed columnar grains. The electrical measurements showed that as-grown $Pb_{1-x}Sn_xTe$ films were non-degenerate semiconductors of p-type conductivity. Increasing the lead concentration resulted in an increase of the Seebeck coefficient and in the decrease of electrical conductivity for as-grown thin films.

Acknowledgments

This work has been supported by Belarusian Republican Foundation for Fundamental Research and by Russian Foundation for Basic Research (grants 12-02-90029-Bel_a, 13-02-00381).

References

[1] Goldsmith J.H. Thermoelectric refrigeration. Plenum New York, 2000, 281 p.
[2] Nishida I.A. Grain size effect on thermoelectric properties of PbTe prepared by spark plasma sintering. *Material Japan, JIM*, **35**, P. 943–947 (1996).
[3] Dimmock J.O. Meingailis I. Band structure and laser action in $Pb_xSn_{1-x}Te$. *Phys. Rev. Lett.*, **26**, P. 1193–1197 (1966).
[4] Xing Gao, Murray S.D. Investigation of band inversion in (Pb,Sn)Te alloys using ab initio calculations. *Physical Review B*, **77**, P. 033103 (2008).
[5] Lopez O. Hot wall epitaxy. *Thin Solid Films*, **49**, P. 3–7 (1978).
[6] Schikora D., Sitter H., J. Humenberger J. High quality CdTe epilayers on GaAs grown by hot wall epitaxy. *Appl. Phys. Lett.*, **48**, P. 1276–1279 (1986).
[7] Pal A.K., Mondal A., Chaudhuri S. Preparation and characterization of ZnTe/CdSe solar cells. *Vacuum*, **41**, P. 1460–1463 (1990).
[8] Seto S., Yamada S., Suzuki K. Growth kinetics and structural characterization of polycrystalline CdTe films grown by hot-wall vacuum evaporation. *Solar Energy Materials and Solar Cells*, **50**, P. 133–137 (1998).
[9] Muthukumarasamy N., Balasundaraprabhu R., Jayakumar S., Kannan M.D. Photoconductive properties of hot wall deposited $CdSe_{0.6}Te_{0.4}$ thin films. *Materials Science and Engineering B*, **137**, P. 1–3 (2007).
[10] Bashkirov S.A., Lazenka V.V., Gremenok V.F., Bente K. Microstructure of SnS thin films obtained by hot wall vacuum deposition method. *J. Adv. Microsc. Res.*, **6**, P. 153–156 (2011).
[11] Bashkirov S.A., Gremenok V.F., et al. Tin sulfide thin films and ZnO/n-CdS/p-SnS/Mo heterojunctions for photovoltaic applications. *Thin Solid Films*, **520**, P. 5807–5810 (2012).
[12] Schaffler R., Klose M., Schock H.W. Pulsed laser deposition and characterization of CuInSe thin films for solar cell applications. *Materials Science Forum Vois.*, **173**, P. 135–138 (1995).
[13] Farinre T.O., Zemel J.N. Preparation and properties of $Pb_{1-x}Sn_xTe$ epitaxial films. *J. Vacuum Sci. Technology*, **7**, P. 121–123 (1970).

NANOSYSTEMS: PHYSICS, CHEMISTRY, MATHEMATICS, 2013, 4 (6), P. 823–833

INFLUENCE OF Sb CONTENT ON PHASE COMPOSITION CHANGE OF NANOSCALED Co-Sb FILMS DEPOSITED ON HEATED SUBSTRATE

Yu. N. Makogon, E. P. Pavlova, S. I. Sidorenko, R. A. Shkarban

National Technical University of Ukraine “KPI”,
03056, Peremogy Avenue, 37, Kiev, Ukraine
y.makogon@kpi.ua, el_pavlova@inbox.ru, sidorenko@kpi.ua, haben@ukr.net

PACS 68.37.Ps, 68.55.Nq, 68.60.Dv, 73.50.Lw, 82.80.Yc, 84.60.Rb, 85.80.Fi

The subject of this study is the formation of the phase composition and structure in nanoscaled $\mathrm{CoSb_X}$ (30 nm) ($1.82 \leqslant x \leqslant 4.16$) films deposited by molecular-beam epitaxy on substrates of oxidized monocrystalline silicon at 200 ° C and the following thermal treatment in vacuum from 300–700 ° C. It is established that after deposition, the films are polycrystalline without texture. With increased Sb content, the formation of the phase composition in the films takes place in such a sequence as is provided by the phase diagram for the bulk state of the Co–Sb system. With annealing in vacuum at temperatures above 450–500 ° C, sublimation occurs not only for the crystalline Sb phase, but for the antimonides as well. This is reflected in the phase composition change by the following chemical reactions: $\mathrm{CoSb_2} \xrightarrow{600^\circ C} \mathrm{Sb}\uparrow = \mathrm{CoSb}$, $\mathrm{CoSb_3} \xrightarrow{600^\circ C} \mathrm{Sb}\uparrow = \mathrm{CoSb_2}$, $\mathrm{CoSb_3} + \mathrm{Sb}\uparrow \xrightarrow{600^\circ C} \mathrm{CoSb_3}$ and leads to increases in the amounts of the CoSb and $\mathrm{CoSb_2}$ phases and decreases in the amounts of $\mathrm{CoSb_3}$. CoSb_x(30 nm) ($1.82 \leqslant x \leqslant 4.16$) films are found to be thermostable up to ≈350 ° C.

Keywords: skutterudite, phase, film, sublimation.

1. Introduction

Thermoelectricity, which is a priority in science and technology development, is based on the direct conversion of heat energy to electricicity and vice versa. Skutterudite $\mathrm{CoSb_3}$ has potential for use as a thermoelectric material [1-3]. Currently utilized thermoelectric materials have a maximum of efficiency ZT only in the range of 1 [4-5]. ZT is calculated by the formula $ZT = S^2\, \sigma \mathrm{T}/(k_{el} + k_L)$, where S is the Seebeck coefficient, σ is the electrical conductivity, T is the absolute temperature, k_{el} is the thermal conductivity from electrons, k_L is the thermal conductivity from lattice [2,6]. According to theoretical calculation, ZT increases with decreases in size and in nanomaterials, one can reach values $\geqslant 2$ because of decreases in thermal conductivity from the lattice [7].

The aim of this work is to investigate the influence of deposition and thermal treatment conditions on the formation of phase composition and structure in nanoscaled $\mathrm{CoSb_X}$ (30 nm) ($1.82 \leqslant x \leqslant 4.16$) films on oxidized monocrystalline silicon.

2. Experimental procedure

30 nm thick $\mathrm{CoSb_X}$($1.82 \leqslant x \leqslant 4.16$) films were produced by molecular-beam epitaxy on a substrate of thermally oxidized (100 nm thick $\mathrm{SiO_2}$) monocrystalline Si (001). Antimony was deposited at a constant rate of 0.3 Å/s by an effusor heated to 470 ° C. Simultaneously, Co was codeposited by the electron-beam method. Phase composition modification was

accomplished by varying the Co deposition rate from 0.027 – 0.049 Å/s. The pressure in the work chamber was $9.3{\cdot}10^{-11}$ Pa. Substrate temperature was 200 °C. The Co content was determined by luminous flux in the molecular beam. The Co deposition rate was measured by an EIES (Electron Induced Emission Spectroscopy) optical system and was controlled by SENTINEL III Leybold system during deposition. The deposition process was thus regulated in order to maintain a film thickness of 30 nm.

The film composition was determined by Rutherford backscattering (RBS) with an accuracy of ± 1 at.% using He^+-ions at an acceleration energy of 1.7 MeV.

The film thickness was determined by simulation of the RBS-spectra using the programm “Simnra” for the handling of RBS-data. The statistical accuracy for the measurement of film thickness was ± 1 nm. This was confirmed by X-ray reflectometry. Samples were annealed in vacuum and under nitrogen from 300–700 °C for 0.5 – 5 hours. Chemical composition of films was determined by Rutherford backscattering spectrometry. Phase composition and structure were characterizated by methods of X-ray diffraction (XRD) (Debye-Sherrer photomethod with photographic registration of x-ray beams and on diffractometer ULTIMA IV Rigaku with using Cu k_α radiation in Bragg-Brentano geometry). The XRD data were corrected by the Rachinger algorithm [8]. The films’ electroconductive properties were investigated by resistometry using the four-point method. The quantitative change of the phase composition in the films was determined metallographically by the intercept method on the photographs of the surface obtained by a scanning electron microscope. The relative error of this method is ≈ 4 %.

3. Results and discussion

Figure 1 presents the XRD patterns and photographs of the XRD patterns of the $CoSb_X(1.82 \leqslant x \leqslant 4.16)$ films after deposition. Identification of the phase composition showed that in the $CoSb_{1.82}$ (64.5 at.% Sb) film, the antimonide of $CoSb_2$ was formed with a monoclinic crystal lattice (Fig. 1a). As follows from the photographs of XRD patterns, the films under investigation were polycrystalline without texture (Fig. 1b). Increased Sb content also resulted in the formation of polycrystalline skutterudite phase of $CoSb_3$ with a cubic lattice. This two-phase state is preserved in the films with up to 74.6 at.% Sb content. In this Sb content interval, the intensity ratio of the diffraction maxima of $I(210)CoSb_2/I(310)CoSb_3$ decreased, as is evidenced by the increase in $CoSb_3$ phase amount and decrease in $CoSb_2$ with increased Sb content (Fig. 2).

Fig. 3 represents the change of the films’ phase composition with increased Sb content in the interval from 64.5 to 74.6 at.%, according to the results of quantitative metallographic analysis of SEM-images. The single-phase structure is observed in both $CoSb_{1.82}$ and $CoSb_{2.89}$ films. In the $CoSb_{1.82}$ film, the $CoSb_2$ phase is formed and in the $CoSb_{2.89}$ film, the $CoSb_3$ phase is fixed. At intermediate compositions, these phases coexist. Meanwhile, with increased Sb content in films, the skutterudite $CoSb_3$ amount increases and the $CoSb_2$ phase amount decreases. Use of these two methods showed good correlation with the change of the phase composition in as-deposited films, subject to Sb content (Fig. 1 and Fig. 3).

In the as-deposited $CoSb_X(3.19 \leqslant x \leqslant 4.16)$ films with higher Sb content, the two-phase composition was also observed. In addition to $CoSb_3$ in the films, the crystalline phase of Sb (Fig. 1) was also formed. From the change of ratio of diffraction peaks intensities of $I(012)Sb/I(310)CoSb_3$ it follows that with increased Sb content from 76.1 to 80.6 at.%, the amount of the crystalline Sb phase increases (Fig. 4).

The results of XRD structure and phase analysis of the films under investigation are presented in Table 1. It should be noted that in nanoscale films deposited at the substrate

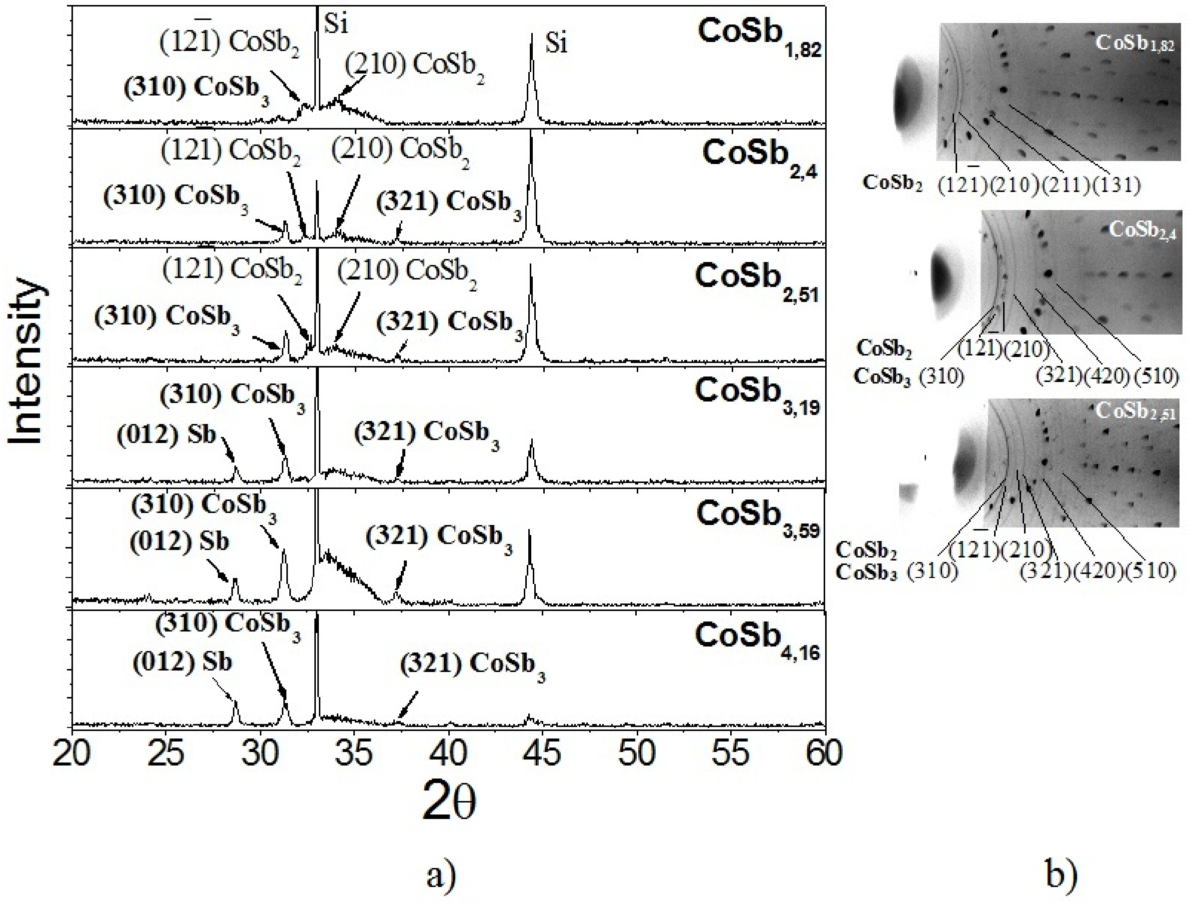

FIG. 1. XRD patterns (a) and photographs of XRD patterns (b) of the CoSb$_X$ (1.82$\leqslant$ x $\leqslant$4.16) films after deposition

temperature of 200 ° C good coincidence was observed for the phase composition with the phase diagram for bulk state.

TABLE 1. Phase composition of the as-deposited CoSb$_X$ (1.82 $\leqslant$ x $\leqslant$ 4.16) films

Substrate temperature, ° C	Sb content in the film, at.%			
	64.5	64.5–70	70–74.6	76.1–80.6
	Ratio Sb/Co in the film			
	1.82	1.82–2.3	2.3–2.89	3–4.16
200	CoSb$_2$	CoSb$_2$+ CoSb$_3$	CoSb$_3$+ (CoSb$_2$)	CoSb$_3$+ Sb

Annealing of CoSb$_X$(2.4 $\leqslant$ x $\leqslant$ 2.89) films in vacuum causes a change in their phase composition.

As follows from Figure 5, after annealing at 620 ° C, the ratio I(210)CoSb$_2$/I(310)CoSb$_3$ increases with a noted absence of texture. This indicated an increase in the CoSb$_2$ amount.

The as-deposited CoSb$_X$ (3.19 $\leqslant$ x $\leqslant$ 4.16) films had a two-phase crystalline structure from a skutterudite phase of CoSb$_3$ and a crystalline Sb phase. From the change in the ratio of the diffraction peak intensities of I(210)CoSb$_2$/I(310)CoSb$_3$ after annealing in the Sb-enriched films of CoSb$_{3.59}$ and CoSb$_{4.16}$, it follows that with annealing under 500 ° C, phase changes don't occur (Fig. 6).

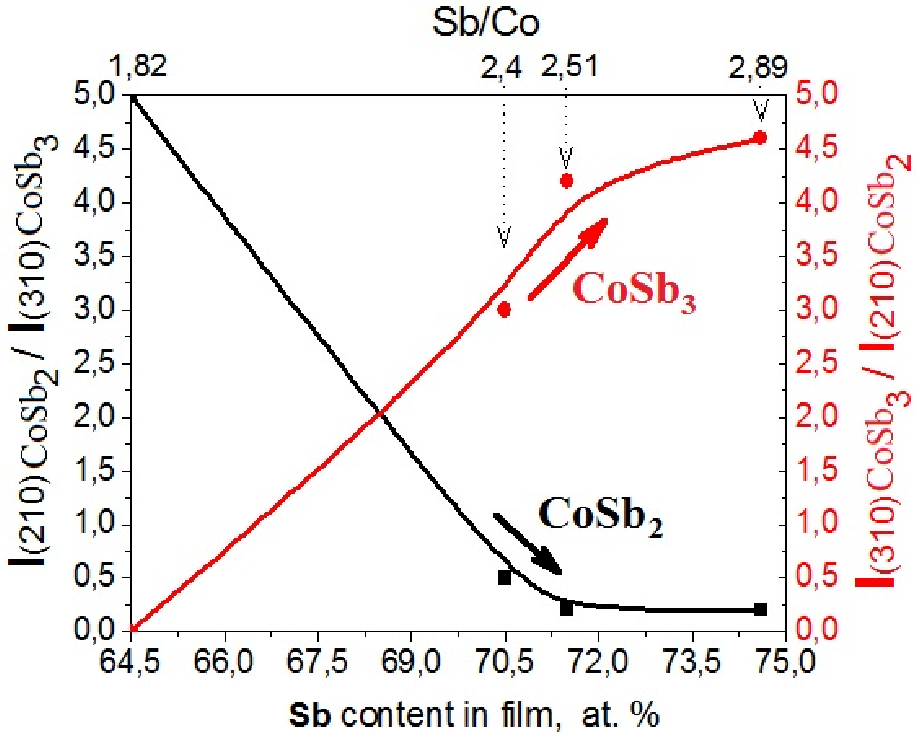

FIG. 2. XRD integral intensity ratio of I(210)$CoSb_2$/I(310)$CoSb_3$ and I(310)$CoSb_3$/I(210)$CoSb_2$ for the as-deposited $CoSb_X$ ($1.82 \leqslant x \leqslant 2.89$) films

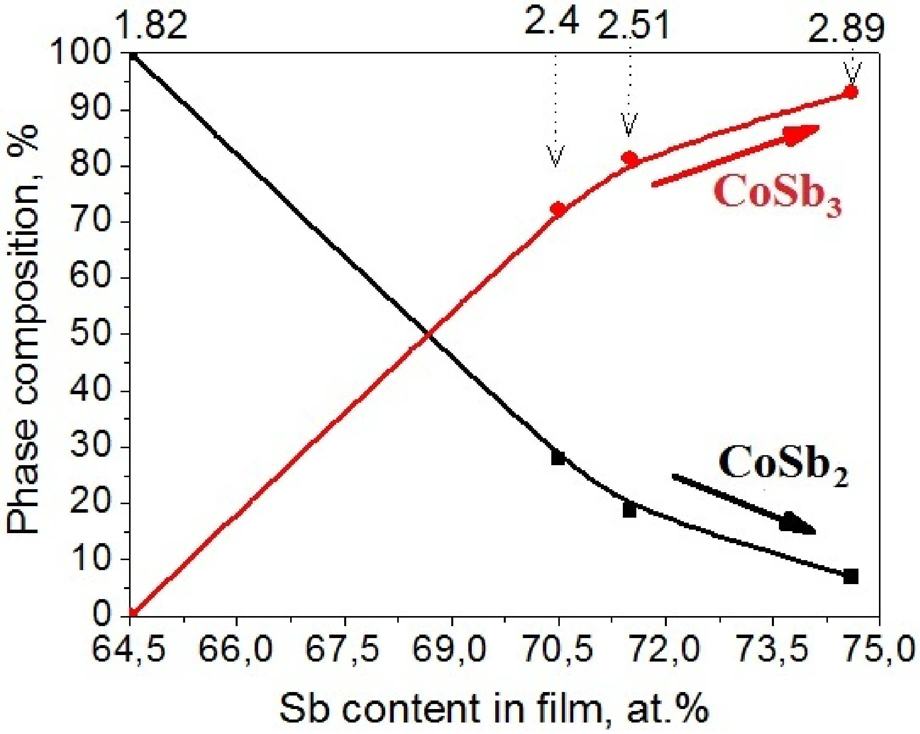

FIG. 3. Change of phase composition in the as-deposited $CoSb_x$ ($1.82 \leqslant x \leqslant 2.89$) films

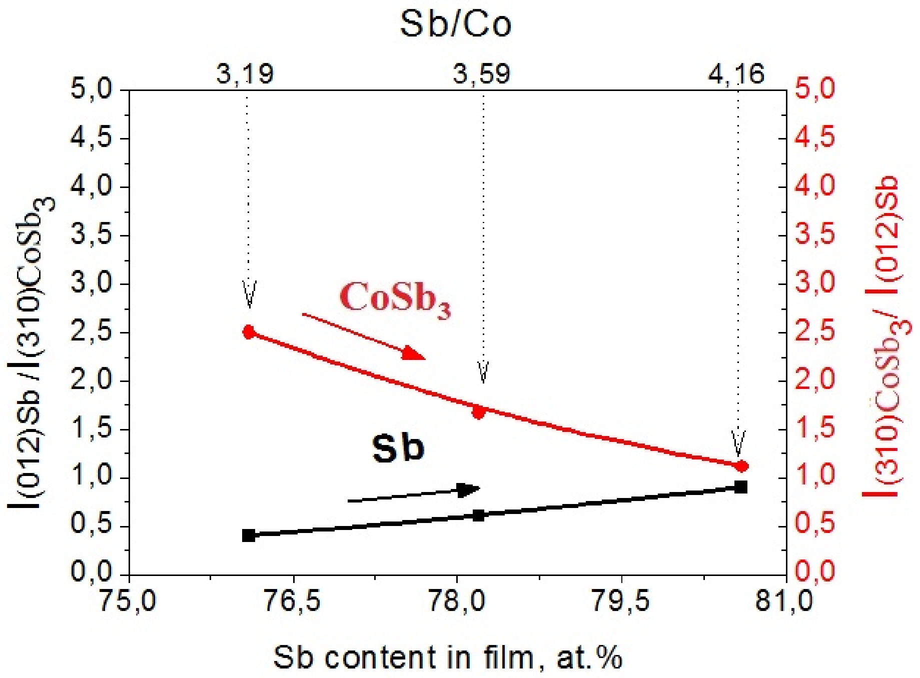

FIG. 4. XRD integral intensity ratio of I(012)Sb/I(310)CoSb$_3$ and I(310)CoSb$_3$/I(012)Sb for the as-deposited CoSb$_x$($3.19 \leqslant x \leqslant 4.16$) films

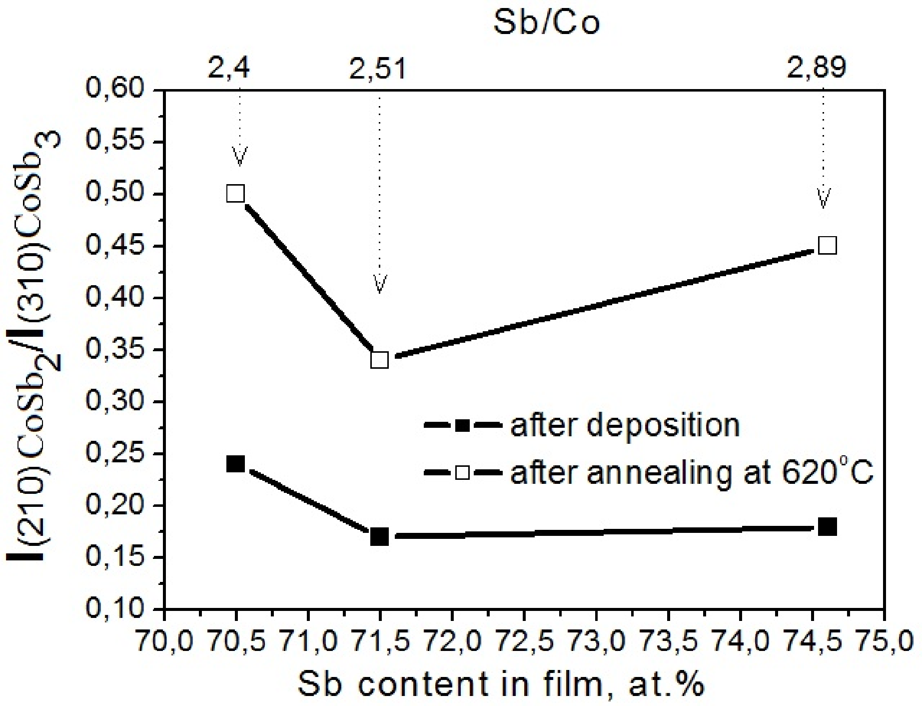

FIG. 5. XRD integral intensity ratio of I(210)CoSb$_2$/I(310)CoSb$_3$ for the CoSb$_x$ ($2.4 \leqslant x \leqslant 2.89$) films after deposition and annealing in vacuum at 620 °C for 30s

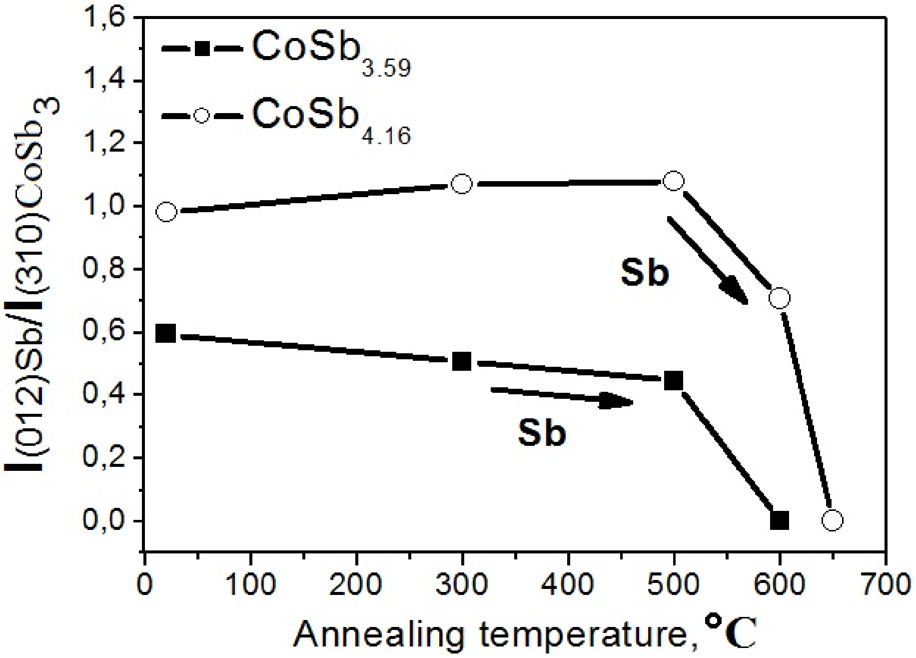

FIG. 6. XRD integral intensity ratio of I(012)Sb/I(310)$CoSb_3$ for the $CoSb_{3.59}$ and $CoSb_{4.16}$ films after annealing in vacuum at different temperatures

During annealing at higher temperatures, intense sublimation of Sb occurred. After annealing at 600 °C, the reflexes of the crystalline Sb weren't observed and only the $CoSb_3$ phase remained.

Figure 7 shows the data for the quantitative analysis of the phase composition change in films having a two-phase composition of ($CoSb_3$+ Sb) after annealing, determined using the ratio intensities of the diffraction lines for (012)Sb and (310)$CoSb_3$ according to a previously reported method [9]. The process of Sb sublimation, also from antimonides, also holds for the annealing of bulk materials [10].

The process of Sb sublimation also occurs with annealing under nitrogen. According to XRD data for the structure and phase analysis in the as-deposited $CoSb_{1.82}$ film with lowest Sb content (64.5 at.% Sb), only the $CoSb_2$ phase was observed, and after annealing at 600 °C, a two-phase state of $CoSb_2$ and Sb was formed. In the $CoSb_{2.4}$ and $CoSb_{2.51}$ films with Sb content of 70.5 and 71.5 at.% respectively, before and after such annealing, the two-phase composition was preserved for the antimonides of $CoSb_2$ and $CoSb_3$.

Figure 8 represents the data for the quantitative metallographic analysis of the SEM-images of the $CoSb_X(1.82 \leqslant x \leqslant 2.51)$ films after deposition and thermal treatment. After annealing a quantitative change of the phase composition was observed. In the film with Sb content of 64.5 at.% after annealing at 600 °C, nearly 30% of the Sb phase appeared. In films with 70.5 and 71.5 at.% Sb content, the amount of the $CoSb_2$ phase increased and amount of the $CoSb_3$ skutterudite decreased.

This can explained by the partial sublimation of Sb from the crystalline lattices of the CoSb and $CoSb_3$ antimonides with annealing both in nitrogen and in vacuum due to the following chemical reactions: $CoSb_2 \xrightarrow{600^\circ C} Sb\uparrow = CoSb_2 + CoSb$; $CoSb_3 \xrightarrow{600^\circ C} Sb\uparrow = CoSb_3 + CoSb_2$.

Thermal stability of the nanoscale skutterudite films of $CoSb_X$ $(3.19 \leqslant x \leqslant 4.16)$ was preserved up to ≈ 300–350 °C (Fig. 9).

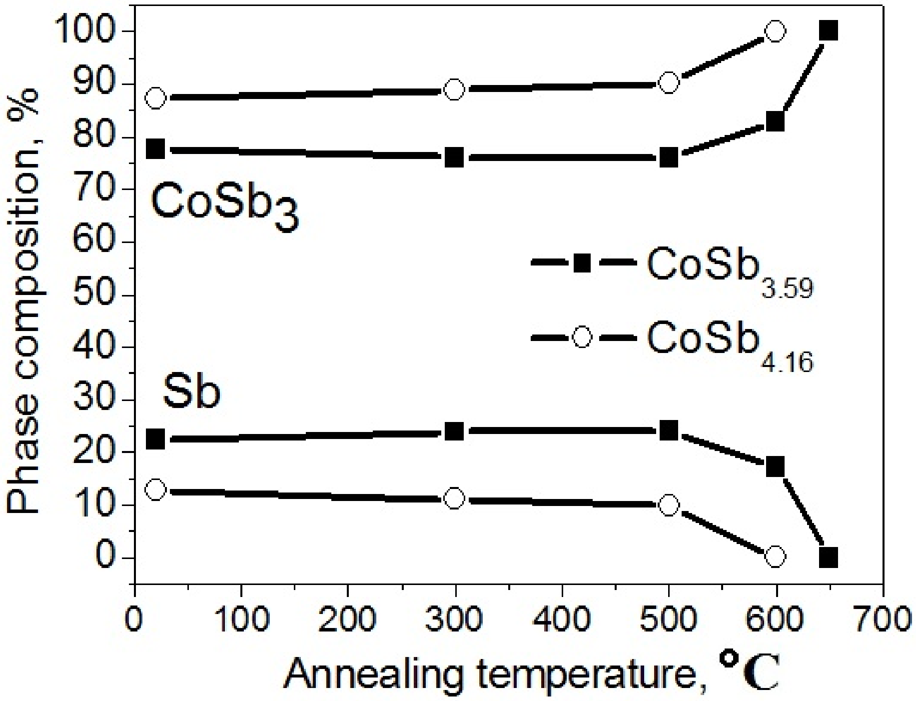

FIG. 7. Phase composition of the $CoSb_{3.59}$ and $CoSb_{4.16}$ films after annealing in vacuum at the different temperatures for 30s

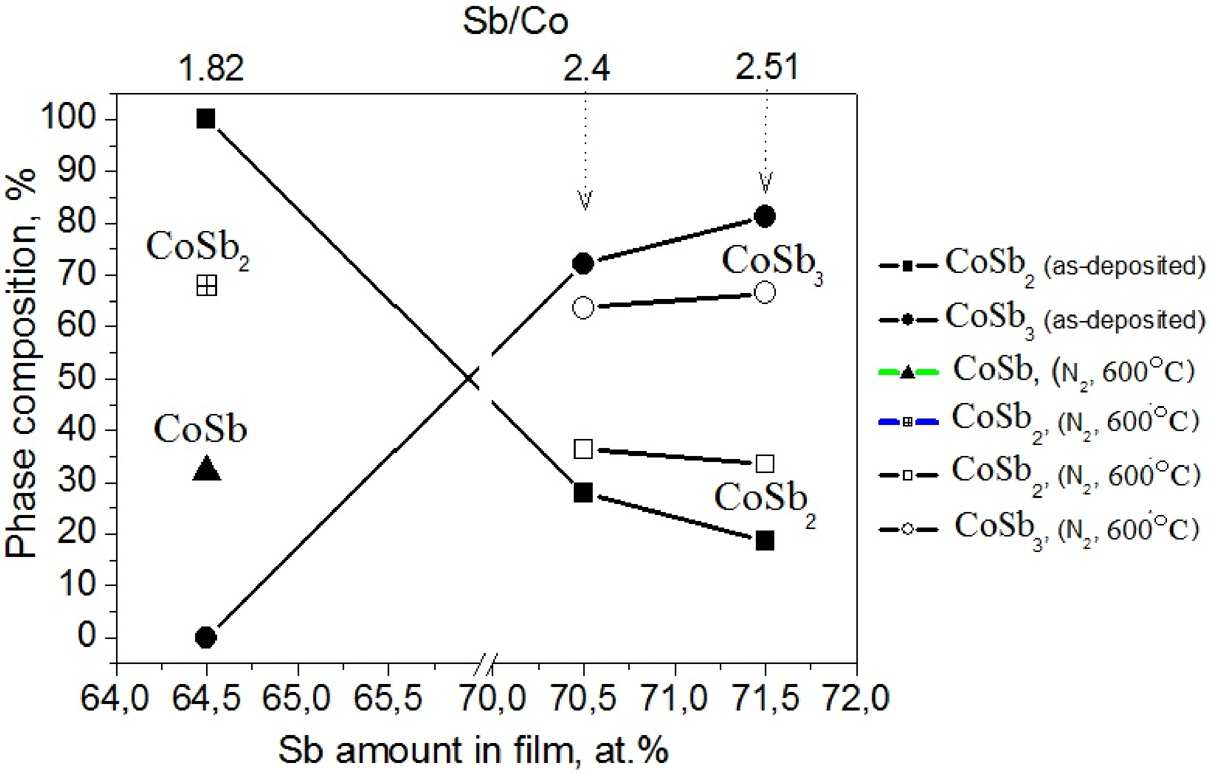

FIG. 8. Phase composition of the as-deposited films and the films post-annealed in nitrogen at 600 ° C for 30s

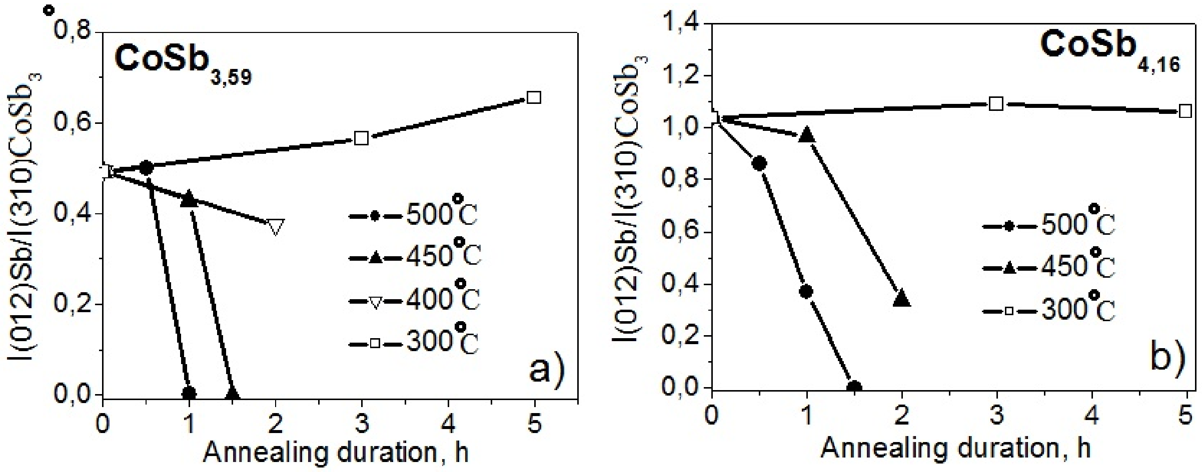

FIG. 9. Dependence of the ratio of the diffraction peaks intensities of I(012)Sb/I(310)$CoSb_3$ of the $CoSb_{3,59}$ (a) and $CoSb_{4,16}$ (b) films on annealing duration in vacuum at 300 ° C, 400 ° C, 450 ° C, 500 ° C

The activation energy for the Sb sublimation process was determined using the rate of the Sb sublimation at different annealing temperatures, according to the Arrhenius equality [10].

The sublimation process for crystalline Sb is dependent upon the chemical composition of the films (Fig. 10).

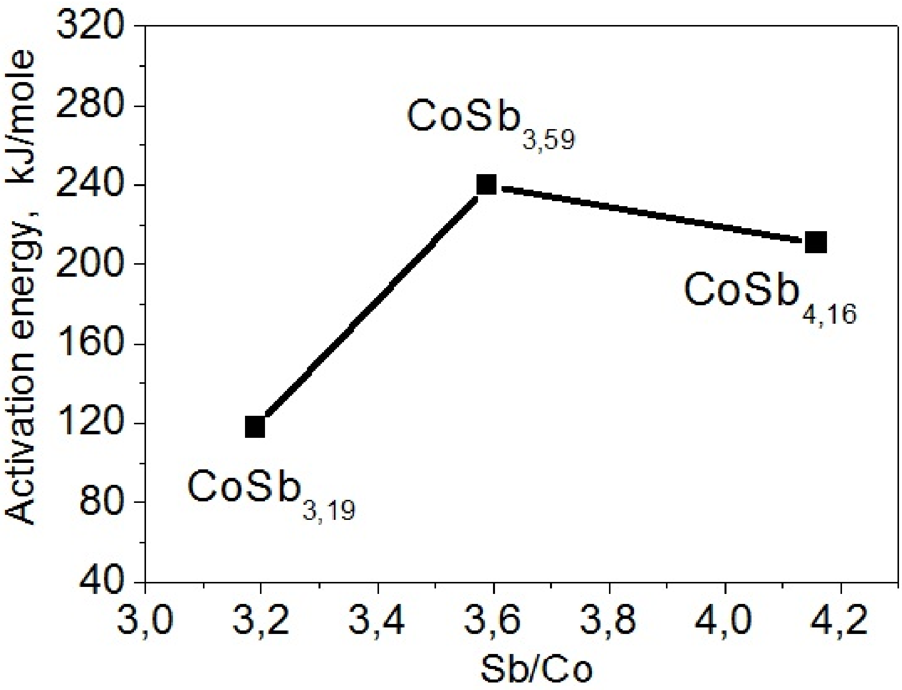

FIG. 10. Change of the activation energy of Sb sublimation in the $CoSb_X$ ($3.19 \leqslant x \leqslant 4.16$) films

The electrophysical properties of the Co-Sb films depended on their phase composition. The dependence of the resistivity of the as-deposited films on the Sb amount has a parabolic character with a maximum of 15 $\mu\Omega\cdot$ cm at the Sb concentration of 75 at.% (Fig. 11).

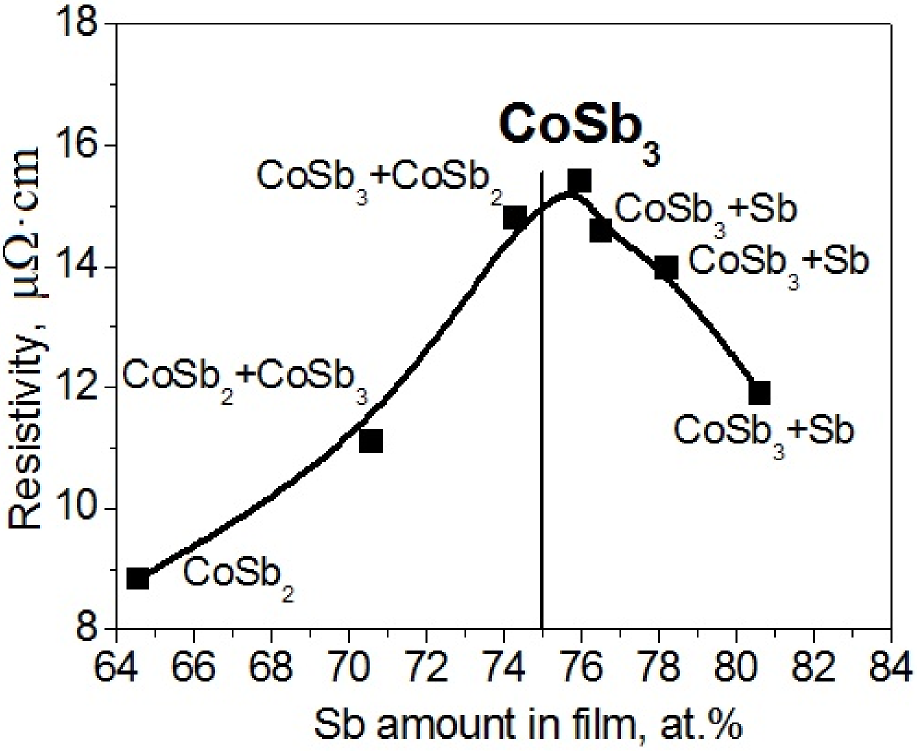

FIG. 11. Dependence of the resistivity of $CoSb_X$ ($1.82 \leqslant x \leqslant 4.16$) on Sb amount

Skutterudite $CoSb_3$ is a semiconductor and has higher resistivity in comparison with phases of $CoSb_2$ and Sb having a semiconductor and metallic type of the conductivity respectively. The difference in the phase composition has influence not only on the absolute values of the film resistivity, but also on their temperature dependence. So, for the $CoSb_{2.98}$ and $CoSb_{3.055}$ films, in which the $CoSb_3$ phase was generally present, the dependence of the resistivity on the temperature has a semiconductor character (Fig. 12).

In the films having two-phase composition from $CoSb_3$ and Sb, the temperature dependence of the resisitivity takes on a form typical for metals. According to report [8], Sb has a metallic type of conductivity.

4. Conclusion

It was established that at a substrate temperature of 200 ° C, during the deposition of $CoSb_X$ ($1.82 \leqslant x \leqslant 4.16$) films, they were formed in a crystalline state. The films were in a polycrystalline state without texture. Good correlation between the film phase composition and the phase diagram for the bulk materials was observed. With increased Sb content, the formation of the phase composition occurs in same sequence as is provided by the phase diagram for bulk materials of the Co-Sb system.

In $CoSb_X$ films, the phase formation sequence versus Sb amount is as follows:

- at 64.5 at.% Sb, the film formed is an antimonide of $CoSb_2$;
- from 64.5 to 75 at.% Sb, along with the $CoSb_2$ phase, the skutterudite of $CoSb_3$ was formed. $CoSb_3$ content increased with increased Sb;
- near 75 at.% Sb, the crystalline phase of $CoSb_3$ was formed;

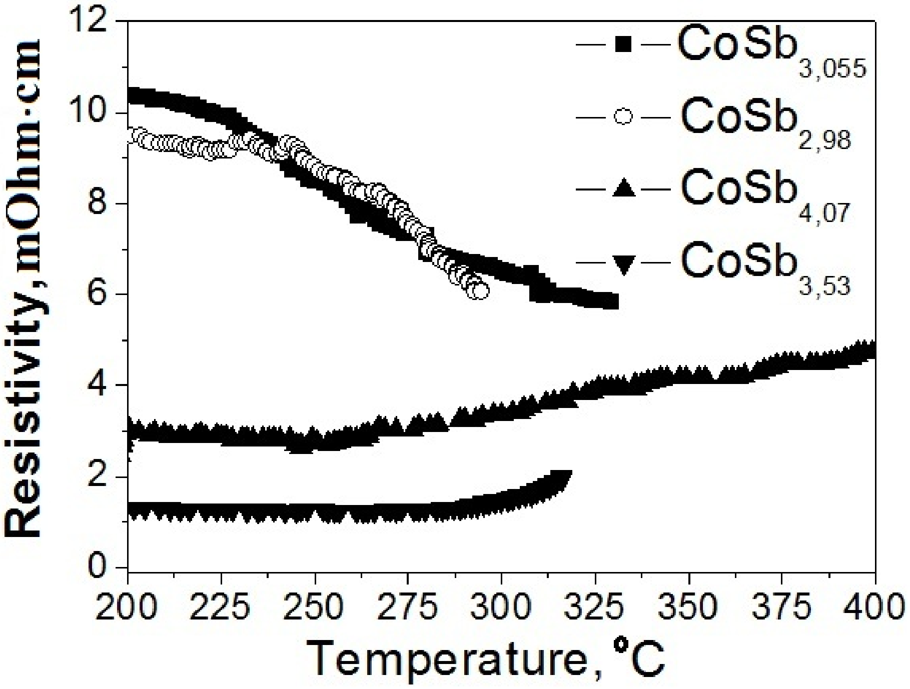

FIG. 12. Dependence of the resistivity of the $CoSb_X$($2.98 \leqslant x \leqslant 4.07$) films on temperature

- at greater than 75 at.% Sb, in addition to $CoSb_3$, the crystalline phase of Sb was formed;

With annealing in vacuum at temperatures higher than 450–500 °C, Sb sublimation occurred, which is reflected in the change of the phase composition according to the following chemical reactions: $CoSb_2 \xrightarrow{600^\circ C} Sb\uparrow = CoSb$, $CoSb_3 \xrightarrow{600^\circ C} Sb\uparrow = CoSb_2$. This resulted in an increase in the CoSb and $CoSb_2$ amount and a decrease in the $CoSb_3$ amount.

The $CoSb_x$ ($1.82 \leqslant x \leqslant 4.16$) films were thermostable up to ≈ 350 °C.

Acknowledgments

The authors would like to thank Prof. M. Albrecht and Dr. G. Beddies, PhD. M. Daniel and workers from Chemnitz University of Technology (Germany) for sample preparation, assistance in conduction of investigations and discussion of results.

This work was financially supported by the Deutsche Akademischer Austauschdienst (DAAD) in the frame of the Leonard-Euler-Program (Grant N 50744282).

References

[1] G.A. Slack, in CRC Handbook of Thermoelectrics, edited by D.M. Rowe (CRC, Boca Ration, 1995), p. 407.

[2] Peng-Xian Lu,Qiu-Hua Ma, Yuan Li, Xing Hu. A study of electronic structure and lattice dynamics of $CoSb_3$ skutterudite. *Journal of Magnetism and Magnetic Materials*, **322**, P. 3080–3083 (2010).

[3] Xu-qiu Yang, Peng-cheng Zhai, Li-sheng Liu, and Qing-jie Zhang. Thermodynamic and mechanical properties of crystalline $CoSb_3$: A molecular dynamics simulation study. *Journal of Applied Physics*, **109**, P. 123517 (2011).

[4] Ruiheng Liu, Xihong Chen, Pengfei Qiu, Jinfeng Liu, Jiong Yang, Xiangyang Huang, and Lidong Chen. Low thermal conductivity and enhanced thermoelectric performance of Gd-filled skutterudites. *Journal of Applied Physics*, **109**, P. 023719 (2011).

[5] Jian-Li Mi, Mogens Christensen, Eiji Nishibori, and Bo Brummerstedt Iversen. Multitemperature crystal structures and physical properties of the partially filled thermoelectric skutterudites $M_{0.1}Co_4Sb_{12}$(M = La,Ce,Nd,Sm,Yb, and Eu). *Physical Review B* **84**, P. 064114 (2011).

[6] Jianjun Zhang, Bo Xu, Li-Min Wang. Great thermoelectric power factor enhancement of $CoSb_3$ through the lightest metal element filling. *Applied physics letters*, **98** P. 072109 (2011).

[7] M. Wilczyski. Thermopower, figure of merit and spin-transfer torque induced by the temperature gradient in planar tunnel junctions. *J. Phys.: Condens. Matter*, **23**, P. 456001 (2011).

[8] M. Daniel, M. Friedemann, N. Jöhrmann, A. Liebig, J. Donges, M. Hietschold, G. Beddies, M. Albrecht. Influence of the substrate thermal expansion coefficient on the morphology and elastic stress of $CoSb_3$ thin films. *Phys. Status Solidi A*, **210**(1), P. 140–146 (2013).

[9] A.A. Rusakov. *Rentgenographiya metallov.* Uchebnic dlya vusov. M., Atomizdat (1977), P. 389–407.

[10] Degang Zhaoa, Changwen Tiana, Yunteng Liua. High temperature sublimation behavior of antimony in $CoSb_3$ thermoelectric material during thermal duration test. *Journal of Alloys and Compounds.* **509**, P. 3166–3171 (2011).

NANOSYSTEMS: PHYSICS, CHEMISTRY, MATHEMATICS, 2013, 4 (6), P. 834–843

THE EFFECT OF FULLERENE C_{60} ON THE MECHANICAL AND DIELECTRICAL BEHAVIOR OF EPOXY RESINS AT LOW LOADING

D. V. Pikhurov[1], V. V. Zuev[1,2]

[1]National Research University of Information Technologies, Mechanics and Optics,
49 Kronverkskiy pr., 197101 Saint Petersburg, Russian Federation
[2]Institute of Macromolecular Compounds of the Russian Academy of Sciences,
31 Bolshoi pr., 199004 Saint Petersburg, Russian Federation
firus07@rambler.ru, zuev@hq.macro.ru

PACS 81.07.Lb

Fullerene C_{60} / epoxy polymers nanocomposites with different C_{60} loadings (0.01-0.12 wt.%) have been prepared. Mechanical testing shows that compared with the neat epoxy, the mechanical and toughening properties of the composites are greatly improved. The addition of fullerene C_{60} increased the modulus of the epoxy (up to 20 %), but the glass transition temperature was unaffected. The measured impact strength was also increased, from 38 to 115 kJ/m^2 with the addition of 0.12 wt.% of fullerene C_{60}. The toughening mechanism has been discussed. Dielectric spectroscopy was used to investigate the influence of nanoparticles on the relaxation processes in the polymer matrix.

Keywords: epoxy resins, fullerene C_{60}, nanocomposites, mechanical properties; dielectric spectroscopy; relaxation processes.

1. Introduction

Epoxy resins are widely used in high performance applications, such as structural adhesives, composite materials and microelectronics encapsulants. Unfortunately, most of these resins are inherently brittle. The fracture toughness of an unmodified epoxy can be enhanced with the addition of fillers and additives. In the past decade, attention has been focused on using nanoparticles as filler to overcome the trade-off encountered in traditional composite systems [1]. Such nanoparticle modification has been shown to increase the toughness and cyclic-fatigue resistance of the epoxy polymer [2], and also, due to the very small size of these fillers, not lead to a significant increase in the viscosity of the epoxy monomer [3]. The nanoparticles not only stiffen, strengthen and toughen epoxy, but also reduce the effect of flaws on mechanical performance.

In this research, we will investigate the effect of fullerene C_{60} on the mechanical properties, fracture toughness and toughening mechanism of epoxy resins. Because of the outstanding physical properties and large specific surface area of fullerene C_{60} [4], fullerene-based composites are expected to show significantly improved mechanical performance, when compared with neat matrix materials. A number of toughening mechanisms were proposed to explain the toughening effect of nanopartices [5]. Recent molecular-dynamics studies have suggested that the mobility of the nanoparticles in the matrix might be crucial for introducing new energy-dissipating mechanisms that lead to enhanced toughness in the nanocomposite [6]. Here, we use broadband dielectric spectroscopy (BDS) to directly measure the influence of fullerene C_{60} on polymer relaxations corresponding to different lengths and time scales. BDS is one of the most efficient tools for studying molecular relaxations of polymers. It covers a broad frequency range, allowing measurement of different relaxation processes simultaneously, including secondary, and even entire chain relaxation processes under favorable circumstances [7]. In this paper, we report the synthesis of epoxy/ fullerene C_{60} nanocomposites, study their mechanical properties, and the data of BDS measurements.

2. Materials and Methods

A diglycidyl ether of bis-phenol F (Araldite GY285) supplied by Hunstman, UK was used as epoxy. The resin mixture was cured with a standard polyether-amine DEH24 (Dow Chemical). This resin and hardener were mixed to a ratio of 1:1. Fullerene C_{60} (purity 99.9%), which was supplied from ZAO ILIP (Saint Petersburg, Russia), was used as filler. The calculated amount of filler was mixed with hardener using ultrasonic method. The resins were cured at 140 °C for 2 h and then post-cured at 160 °C for 2 h.

3. Techniques

Uniaxial tensile tests were conducted on the epoxy polymers in accordance with ISO 527 [8,9]. Tests were conducted using 4 mm × 10 mm × 40 mm specimens for toughness estimation and 6 mm × 6 mm × 40 mm specimens for compression Young's modulus and yield stress estimation. Five specimens were taken for each sample to obtain an average value. Tensile properties were measured using a compression method on UTS 10 instrument (UTS test systeme, Germany). The acoustic modulus was measured ultrasonically using a UK-10 PM instrument (Volna, USSR) at a frequency of 200 kHz. The specimens for test were cylinders with a length of 50 mm and diameter of 10 mm.

The fracture surfaces of the epoxy polymers were studied using scanning electron microscopy (SEM). This was performed using a scanning electron microscope with Zeiss ULTRA-plus FEG-SEM instrument equipped with field-emission gun with magnification 20–2000.

Differential scanning calorimetry (DSC) measurements were performed using Netzsch DSC 204F1 instrument at a scan rate 10 K/min in temperature range 20–200 °C. The thermal gravimetric analysis (TGA) measurements were performed in an inert nitrogenous atmosphere and an oxigenous atmosphere on a Perkin-Elmer TGA-7 instrument with platinum pan using 5 mg of polymer as probe. The samples were heated 25–900 °C and the temperature was raised at the rate of 20 K/min.

Dielectric measurements were performed using a RCL WK 4270 Waynekerr (USA) Impendance Analyzer in the frequency range from 0.01 Hz to 40 kHz at different temperatures. The instrument was interfaced with a computer and equipped with a custom-modified heating and cooling system for sequential measurement from low to high frequency.

The epoxy monomers (epoxy plus hardener) with calculated amounts of filler for nanocomposite samples were placed in a parallel-plate capacitor with 20 mm diameter, and a pair of glass fiber spacer with 50 μm diameter was used between the electrodes. This sample capacitor was heated at 140 °C for 2 h and then at 160 °C for 2 h. The sample capacitor was mounted in the fixture and placed in the thermostat under permanent vacuum of about 1 mm Hg. Temperature stabilization was about 0.1 K throughout the measurements. The experiments were carried from 100 to 458 K by 5 K steps. At each temperature, the ten chosen frequencies (1 Hz to 40 kHz) were measured.

TABLE 1. Effect of loading on properties of nanocomposites based on epoxy matrix

Loading, wt.%	T_g, °C	Acoustic Young's modulus, GPa	Tensile strength σ, MPa	Contraction at compression ε, %
Neat epoxy	124	4.92±0.10	110± 5	7.0± 0.5
C_{60}, 0.02	124	5.11±0.10	118± 5	8.0± 0.5
0.04	123.5	5.22±0.10	122± 4	7.5± 0.5
0.06	124	5.45±0.10	138± 5	8.0± 0.5
0.08	124	5.70±0.10	145 ± 5	8.0± 0.5
0.10	124	5.83±0.10	163 ± 4	8.0± 0.5
0.12	124	5.91±0.10	166 ± 3	8.0± 0.5

4. Results and Discussion

4.1. The effect of fullerene C_{60} on basic properties

The SEM microscopy of all epoxy polymers, unmodified and modified with fullerene C_{60}, showed that these were homogeneous thermoset polymers. The primary and secondary aliphatic amines added readily and repeatedly across the C_{60} molecule, producing complex reaction mixtures composed of numerous structures and isomers [10]. Each amination reaction reportedly added the elements R(R')N and H across π-bond on the fullerene C_{60}. A number of regiochemistries are possible but hydroamination is preferred over 1,2- or 1,4- addition. Considerable evidence exists that radical ion-pairs form when fullerene C_{60} is mixed with an aliphatic amine. The molecules of fullerene C_{60} can incorporate up to 48 such amine functionalities [10]. Therefore, as a result of such reaction with polyether-amine hardener, the fullerene C_{60} was homogeneously incorporated into the epoxy polymer structure. The quality of fullerene C_{60} dispersion in the epoxy matrix is important because numerous studies have shown that the interfacial adhesion provided by the chemical reaction of the filler surface with the matrix is critical for nanoparticle dispersion, as well as mechanical , damping and thermal properties [11, 12]. The incorporation of fullerene C_{60} into the epoxy matrix structure was supported by TGA data (Fig.1).

The TGA results showed a tripartite degradation which began at ca 300 °C both in an inert nitrogenous atmosphere and an oxygenated atmosphere. There were not distinct differences between those two runs. However, the incorporation of fullerene C_{60} leads to a prolongation in the last stage of degradation over 700 °C (Fig.1b). Hereby, the fullerene C_{60} may act like carbon nanotube (CNT) in polymer nanocomposites, where interphase formation can be found through TGA analysis [13].

Furthermore, the glass transition temperatures were unchanged upon the addition of fullerene C_{60} (Table 1), within experimental uncertainty, compared to the value of the neat epoxy, and the value received here was equivalent to the value of epoxy found in literature (about 123–124 °C for first heating and about 130 °C for second). Hence, the incorporation of fullerene C_{60} did not change the phase structure and the crosslinked density of the epoxy thermosets in comparison with pristine epoxy polymer because the larger crosslinked density should lead to an increase of the Tg. Similar results, showing no change in Tg due to addition of nanoparticles (for example, silica nanoparticles or carbon nanotubes) was reported previously [11].

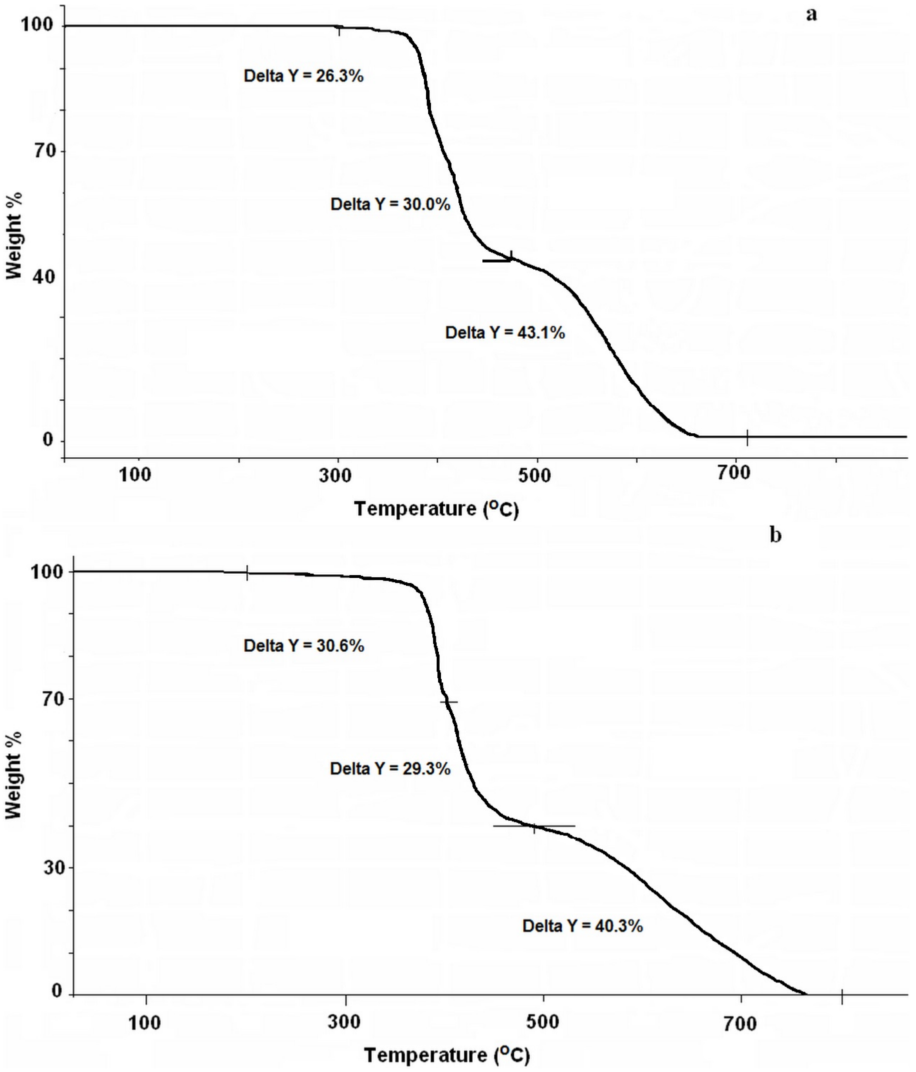

FIG. 1. TGA curve of neat epoxy (a); and with 0.1 wt.% of fullerene C_{60} (b)

4.2. Young's modulus and tensile strength

Typical stress-strain curves are portrayed in Fig.2. Although the strain-stress behaviors of fullerene modified epoxy are almost identical to those of the base epoxy, the tensile strength failure strain and the ductility are all improved. Fullerene nanoparticles are able to improve strength and elongation to break simultaneously, leading to an increase of the areas under the curve, (this implies toughness enhancement in the nanotubes) which have been reported by other authors [14,15]. The Young's modulus values, E, and tensile strength measured from the tensile tests are summarized in Table 1. In spite of small amount of fullerene addition ($<$ 0.1 wt.%), the improvement of Young's modulus and tensile strength are about 20%, which suggests that fullerene might be a modifier of the epoxy resin system. Such improvement in modulus is similar with earlier reported results [12]. The Young's modulus is related to the depth of atomic bond energy function where the polymer chain mobility is restricted by fillers, which contribute to an improved tensile modulus [16].

The fullerenes restrict the mobility and deformation of the matrix by introducing a mechanical restraint. According to this mechanism, the improved modulus for composites containing nanoparticles would be expected over composites containing larger particle sizes.

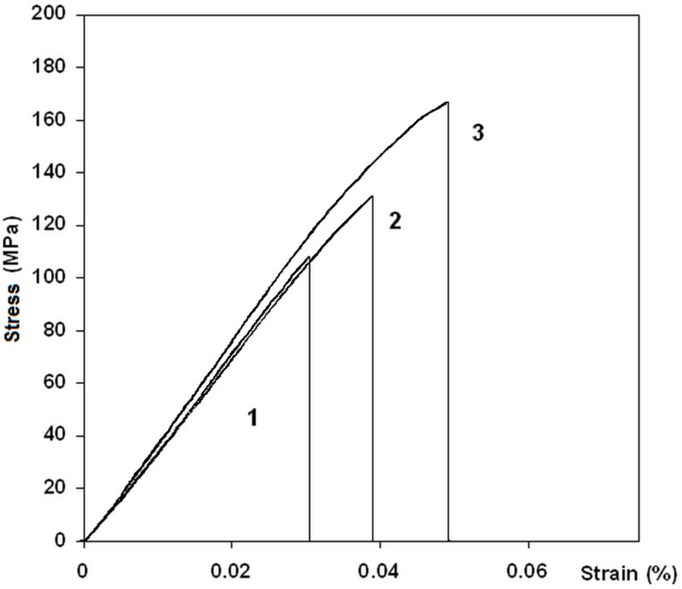

FIG. 2. Typical stress-strain curves of neat epoxy (1); with 0.04 wt.% of fullerene C_{60} (2); with 0.1 wt.% of fullerene C_{60} (3)

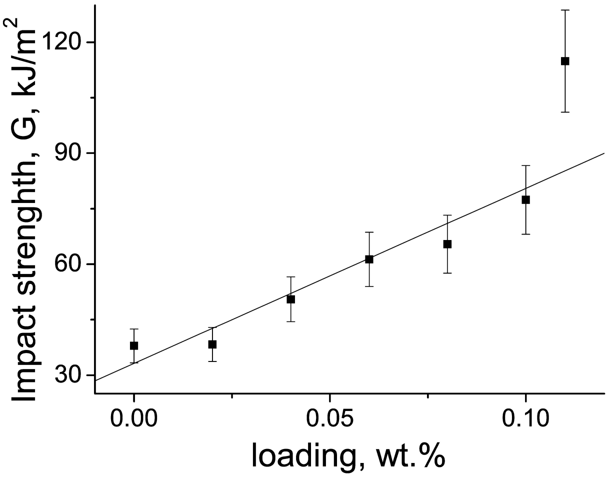

FIG. 3. The impact strength values are plotted as a function of fullerene C_{60}

The yield stress of the composites is greater than that of the polymer matrix, hence, one can conclude that bonding between the fillers and the matrix is strong enough.

4.3. Toughness testing results

Results of toughness testing for the neat epoxy and fullerene modified composites are shown in Fig. 3. The values of impact strength (G) showed significant improvement with increasing fullerene C_{60} concentration. The 0.12 wt.% fullerene C_{60} loading resulted in largest increase in G, i.e. from 38 kJ/m^2 for neat epoxy to 115 kJ/m^2 at 0.12 wt.% loading, a threefold improvement.

The SEM samples were prepared from brittle fracture surfaces of the impact tests pieces. Pictures showed the initiation position of fractures. Examination of fracture surfaces by SEM revealed the neat epoxy to have the classic fracture surface for brittle failure (Fig. 4a) observed in highly crosslinked polymer systems [17]. The fracture surface of the test piece of pure epoxy

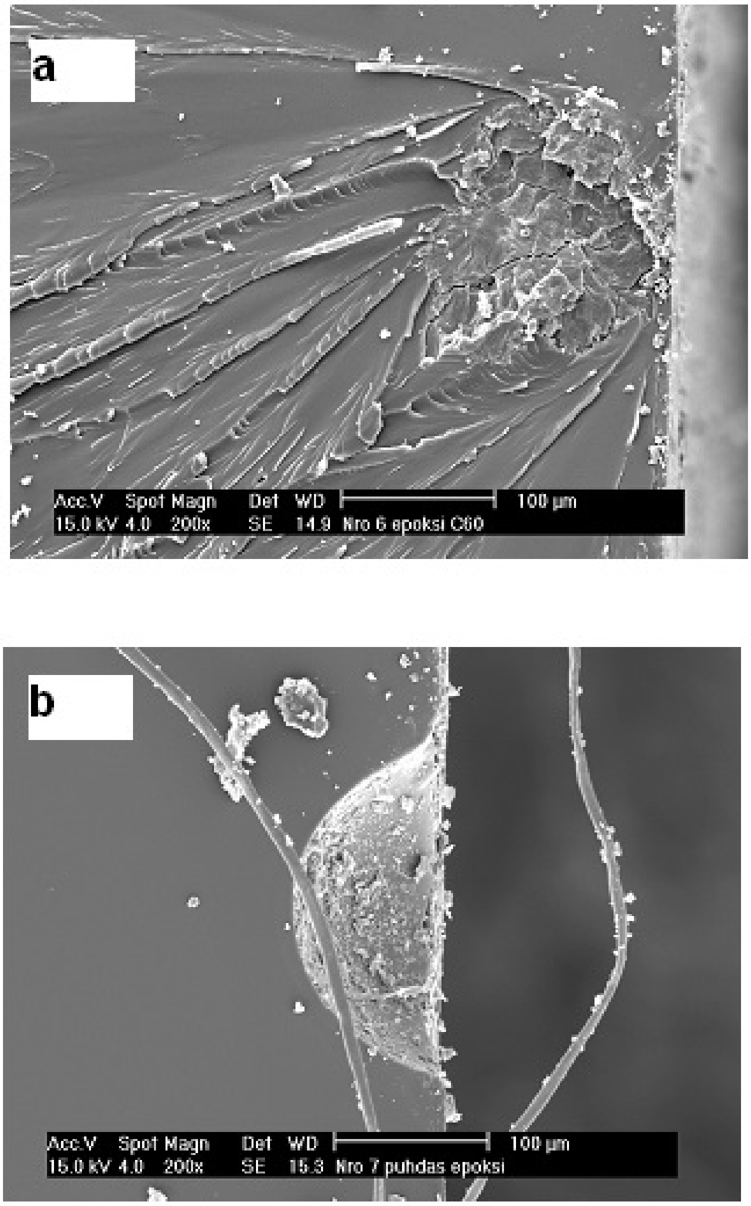

FIG. 4. SEM micrographs of the of fracture surfaces of the test piece of pure epoxy (a) and of the 0.1 wt.% fullerene C_{60} modified epoxy (b) at magnification 200

was very cracked. The fracture was initiated by a small hole at the edge of the sample. River marks leading to the initial site of crack growth were detected, but substantial indication of plastic deformation in the reference material was not noted. Quantitatively speaking, the lack of plastic deformation and a cracked fracture surface well agree with relatively low toughness of the material. Inspection of the 0.1 wt.% fullerene C_{60} modified epoxy confirmed the composite to display a much smooth fracture surface (Fig. 4b). This image clearly shows the occurrence of plastic deformation. The implication of the above results will be discussed further later, when toughening mechanisms initiated by the presence of the fullerene nanoparticles are described.

The ability of fullerenes to enhance the mechanical properties of epoxy resins is improved in relation to the published data for other nanoparticle-modified epoxy resins. Thus, the fracture toughness of epoxy with $\sim$ 0.1 wt.% of amine-functionalized double-walled CNT was increased by 18% [18]. The weight fraction of Al_2O_3, SiO_2, and TiO_2 nanoparticles required to increase the fracture toughness of the neat epoxy by $> 50\%$ is nearly fifty- to one hundred-fold higher ($\sim$ 5–20 wt.%) [19,20]. Similarly, clay nanocomposites require the same amount ($\sim$ 5–10 wt.%) of additives in various epoxy resins to achieve a 60% increase in toughness [21–23]. By contrast, for the case of the fullerene C_{60} filler, we find that toughness of epoxy composites at a nanofiller weight fraction of $\sim$ 0.1 %.

4.4. Toughening mechanisms

The previous studies [1] have considered the toughening mechanisms induced by nanoparticles in detail. These mechanisms included (a) crack pinning, (b) crack deflection, (c) immobilized polymer around the particles, and (d) the ability of nanoparticles to induce an increased extent of plastic deformation. All these mechanisms are connected with mobility of nanoparticles in polymer matrix. We use BDS to directly measure the influence of fullerene C_{60} on polymer relaxation corresponding to different lengths and time scales. Fig. 5 presents the temperature dependence of tan δ spectra for the fullerene C_{60}/composite (0.02 wt.% of fullerene C_{60}) measured at different frequencies. Similar to neat epoxy, we observed two relaxation processes: β and α. Both relaxation processes are well separated in these measurements, providing a good opportunity for analyzing their dependence on the fullerene C_{60} concentration at different temperatures. The α relaxation process corresponds to the segmental mode, which is associated with the glass transition of the system, whereas the β relaxation process is connected with secondary relaxation. For all the samples investigated, we observed no qualitative changes in the shape of the nanocomposite relaxation modes with the fullerene C_{60} additive. In order to obtain $\tau_{\max}$ values(as $\tau_{\max} = 1/2\pi f_{\max}$, where f is frequency) at the temperature of maximum on the temperature dependence of $\tan\delta$ for the fullerene C_{60}/ epoxy composite, a non-linear curve fitting procedure was applied to experimental curves of Fig. 5. The fitting was done using Microcal Origin 8.0. Futher details about the fitting procedure are given in [24].

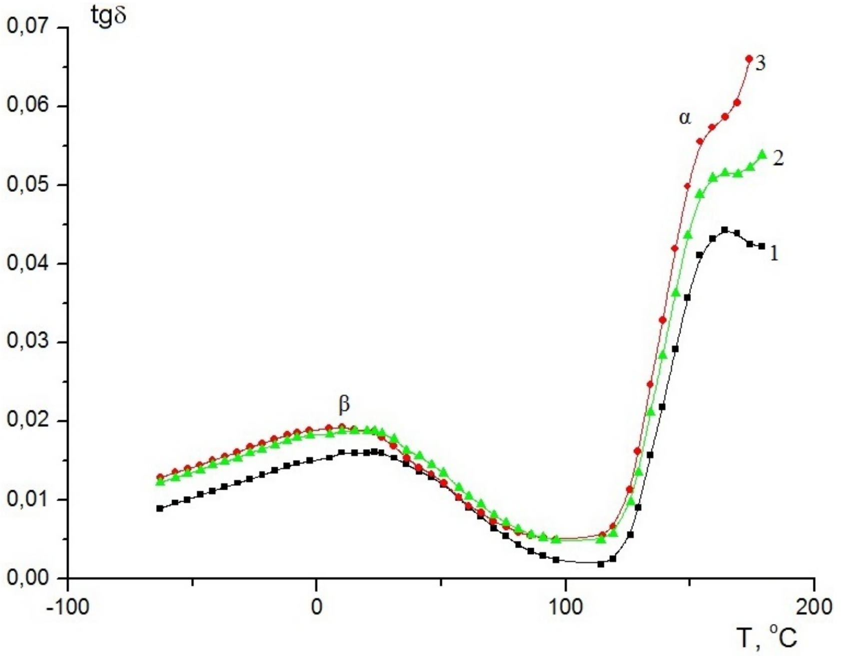

FIG. 5. Temperature dependence of $\tan\delta$ for the fullerene C_{60}/ epoxy composite (0.02 wt.% of fullerene C_{60}); frequency 40 kHz (1); 25 kHz (2); 3 kHz (3)

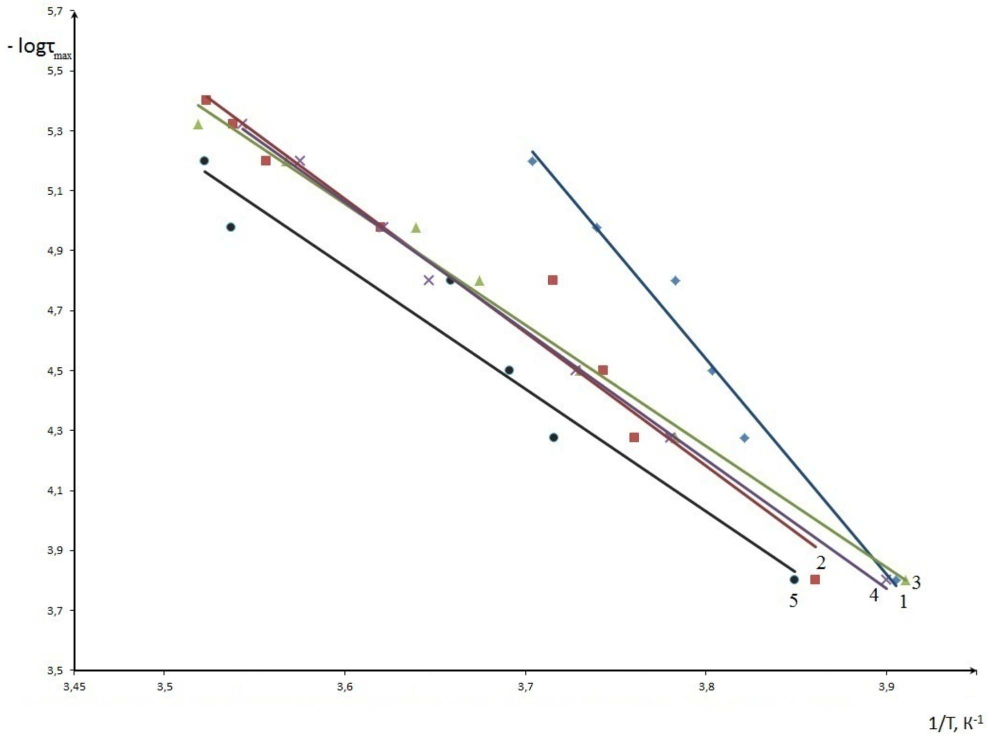

FIG. 6. Relaxation plot of $-\log\tau_{\max}$ determined from $\tan\delta$ spectra for pristine epoxy 1(♦) and for the fullerene C_{60}/ epoxy composite: 0.02 wt.% of fullerene C_{60} – 2(■); 0.04 wt.% of fullerene C_{60} – 3(▲); 0.06 wt.% of fullerene C_{60} – 4(×); 0.08 wt.% of fullerene C_{60} – 5(•)); for β process

TABLE 2. Parameters of β relaxation process of fullerene C_{60} /epoxy composites at different loading

Sample	Ea, kJ/mol	$-\log\tau_0$[s]
neat	33.03	31.8
0.02% C_{60}	20.46	21.1
0.04% C_{60}	18.62	19.6
0.06% C_{60}	18.76	20.5
0.08% C_{60}	19.72	19.5

It is well known that secondary relaxation (β process) is connected with toughness of polymer [25].

Figure 6 shows the relaxation times for the β relaxation processes as a function of temperature for nanocomposites. The secondary relaxation process for composites is shifted to higher temperatures compared to the same process for neat epoxy. Hence, the introduction of fullerene in an epoxy matrix leads to the restriction of molecular motions. Since the distance between cross-links in this study can be assumed as an epoxy molecule size (2–3 nm), these particles may be in motion within the matrix molecules at a similar time and length scale. As a result, the presence of fullerene hampers the molecular motions in epoxy composites because it leads to hardening of polymer chain and impedes secondary relaxation processes.

The activation energies for the β relaxation processes for nanocomposites were obtained from an Arrhenius plot of $-\log\tau_{\max}$ (Table 2). All epoxy composites demonstrate a 30 %

activation energy decrease with fullerene loading; this indicated that carbon nanoparticles can significantly improve energy dissipation processes in epoxy resins, probably independent of the loading level. This process can lead to domination of plastic deformation mechanism in the epoxy composite which effectively blunts the crack trip. Hence, the suggested mechanism is a major reason for the higher values of impact strength G which were observed.

5. Conclusions

The mechanical and fracture properties of epoxy nanocomposites containing 0–0.12 wt.% of fullerene C_{60} have been studied. Several major conclusions may be reached from the present work.

Firstly, considering the Young's modulus of these materials, when the loading level was increased, the modulus of epoxy polymer steadily increased.

Secondly, the presence of fullerene C_{60} always leads to an increase in the toughness of epoxy resins.

Thirdly, the two toughening mechanisms which were operative in all the epoxy polymers containing nanoparticles have been identified. Namely, (a) immobilized polymer around the particles, and (b) the ability of nanoparticles to induce an increased extent of plastic deformation.

References

[1] Leng J., Lau A.K.T. *Multifunctional polymer nanocomposites*. CNC Press,N-Y., 2011, 560 p.

[2] Wichmann M., Schulte K., Wagner H.D. On nanocomposites toughness. *Compos. Sci. Technol.*, *68*, P. 329–331 (2008).

[3] Roscher C. Tiny particles, huge effect: radiation curable silica nanocomposites for scratch and abrasion resistant coatings. *Eur. Coat. J.*, **4**, P. 131–141 (2003).

[4] Prato M. [60]Fullerene chemistry for material science applications. *J. Mat. Chem.*, **7**, P. 1097–1109 (1997).

[5] Hsich T.H., Kinloch A.J., et al. The mechanisms and mechanics of the toughening of epoxy polymer modified with silica nanoparticles. *Polymer*, **51**, P. 6284–6294 (2010).

[6] Gersappe D. Molecular mechanisms of failure in polymer nanocomposites. *Phys. Rev. Lett.*, **89**, P. 058301 (2002).

[7] Adachi K., Kotaka T. Dielectric normal mode relaxation. *Progr. Polym. Sci.*, **18**, P. 585–622 (1993).

[8] ISO-527-1. Plastics – Determination of tensile properties – Part 1: general principles. Geneva. International Standard Organisation (1993).

[9] ISO-527-2. Plastics – Determination of tensile properties – Part 2: test conditions for moulding and extrusion plastics. Geneva. International Standard Organisation (1993).

[10] Miller G.P. Reactions between aliphatic amines and [60]fullerene: a review. *Compt. Rend. Chem.*, **9**, P. 952–959 (2006).

[11] Ogasawa T., Ishida Y., Kasai T. Mechanical properties of carbon fiber/ fullerene dispersed epoxy composites. *Comp. Sci. Technol.*, **69**, P. 2002–2008 (2009).

[12] Rafiee M.A., Yavari F., Rafiee J., Koratkar N. Fullerene- epoxy nanocomposites – enhanced mechanical properties at low nanofiller loading. *J. Nanopart. Res.*, **13**, P. 721–731 (2011).

[13] Zhang W., Picu R.C., Koratkar N. Suppression of fatigue crack growth in carbon nanotube composites. *Appl. Phys. Lett.*, **91**, P. 193109 (2007).

[14] Kinloch A.J., Mohammed R., et al. The effect of silica nano particles and rubber particles on the toughness of multiphase thermosetting epoxy polymers. *J. Mat. Sci.*, **40**, P. 5083–5086 (2005).

[15] Hsich T.H., Kinloch A.J., Taylor A.C., Kinloch I.A. The effect of carbon nanotubes on the fracture toughness and fatigue performance of a thermosetting epoxy polymer. *J. Mat. Sci.*, **46**, P. 7525–7535 (2011).

[16] Dittanet P., Pearson R.A. Effect of silica nanoparticle size on toughening mechanisms of filled epoxy. *Polymer*, **53**, P. 1890–1905 (2012).

[17] Kinloch A., Taylor A. The toughening of cyanate-ester polymers: part 1. Physical modification using particles, fibers and woven-mats. *J. Mat. Sci.*, **37**, P. 433–466 (2002).

[18] Zhu J., Kim J., et al. Improving the dispersion and integration of single-walled carbon nanotubes in epoxy composites through functionalization. *Nano Lett.*, **3**, P. 1107–1113 (2003).

[19] Wetzel B., Rosso P., Haupert F., Friedrich K. Epoxy composites fracture and toughening Mechanisms. *Eng. Fract. Mech.*, **73**, P. 2375–2398 (2006).

[20] Blackman B.R.K., Kinloch A.J., et al. The fracture and fatigue behaviour of nano-modified epoxy polymers. *J. Mat. Sci.*, **42**, P. 7049–7051 (2007).

[21] Zerda A.S., Lesser A.J. Intercalated clay nanocomposites: Morphology, mechanics, and fracture behavior. *J. Polym. Sci. B: Polym. Phys.*, **39**, P. 1137–1146 (2001).

[22] Wang K., Chen L., et al. Epoxy nanocomposites with highly exfoliated clay: mechanical properties and fracture mechanisms. *Macromolecules*, **38**, P. 788–800 (2005).

[23] Liu W., Hoa S.V., Pugh M. Fracture toughness and water uptake of high-performance epoxy/ nanoclay nanocomposites. *Comp. Sci. Technol.*, **65**, P. 2364–2373 (2005).

[24] Nikonorova N.A., Diaz-Calleja R., Yakimansky A. Molecular mobility in comb-like copolymethacrylates with chalcone-containing side-chains. *Polym. Int.*, **60**, P. 1215–1221 (2011).

[25] Boyer R.F. Dependence of mechanical properties on molecular motion in polymers. *Polym. Eng. Sci.*, **8**, P. 161–185 (1968).

NANOSYSTEMS: PHYSICS, CHEMISTRY, MATHEMATICS, 2013, 4 (6), P. 844–850

EFFECT OF SINTERING TEMPERATURE ON THE STRUCTURE OF COMPOSITES BASED ON SPINEL AND PEROVSKITE

M. V. Talanov[1], L. A. Shilkina[1], V. M. Talanov[2], N. P. Shabelskaya[2], L. A. Reznichenko[1]

[1]Research Institute of Physics, Southern Federal University, 344090 Rostov-on-Don, Russia

[2]South- Russian State Polytechnic University, 346428, Novocherkassk, Russia

mvtalanov@sfedu.ru

PACS 81.05.Mh, 81.05.Ni, 81.05.Pj, 81.05.Qk

Magnetoelectric composites of $0.6(\mathrm{Ni_{0.7}Zn_{0.3}Fe_2O_4})$ / $0.4((\mathrm{Na, Li, Sr})\mathrm{NbO_3} + \mathrm{MnO_2})$ are prepared by conventional ceramic technology. The effect of composite sintering temperature on their phase composition and structure is studied. It is stated that the composites obtained are two phase systems (perovskite and spinel). It is established that modulation of spinel structure is shown more accurately at low sintering temperatures (1180 ° C), while modulation of perovskite structure is shown at high temperatures (1220 ° C). The discovered modulations of perovskite and spinel structures are assumed be connected with extended defects such as crystallographic shear planes. Increasing composite sintering temperature ($T_{\mathrm{sint.}} \geqslant 1200\,^\circ$C) was shown to lead to the disappearance of an impurity phase and the change of perovskite phase composition.

Keywords: composite, perovskite, spinel, temperature of sintering, structure modulation, crystallographic shear planes.

1. Introduction

The coexistence and interrelation of magnetic and electric subsystems in magnetoelectric materials allow us to use them to make different transducers. Towards this end, the principal possibility of controlling magnetic characteristics by variations of electric field appears and vice versa. However, at present, there are almost no materials that have magnetoelectric coefficients of the proper magnitude to make this practical.

As a result, in solid-state physics and chemistry, a new direction in scientific-research is being made — the creation and research of composites with magnetoelectric properties based on heterophase structures having ferroelectric and magnetic components (phases). The advantage of the given approach is the possibility of choosing the magnetic and ferroelectric phases separately and the method of their combination in one material (for example, layers, mixtures, etc.).

In order to create a composite with high magnetoelectric coefficients, it is necessary to satisfy a few conditions: first, magnetic and ferroelectric components of material should have high values for magnetostrictive and piezoelectric parameters; second, low conductivity values for the components and third, a developed mechanical contact between the phases. Additionally, the composite should have the optimal content of the magnetic and ferroelectric phases too.

Composites having magnetic components with spinel structures and ferroelectric components with perovskite structures satisfy these conditions. As a result, these have become widespread [1, 2], however there are poorly studied questions: mutual influence of phases which are different on structure and properties; the target optimization of compositions; and methods for producing composites with high magnetoelectric coefficients.

In this paper, the results of research aimed at finding and creating new spinel — perovskite composites with high magnetoelectric coefficients are presented. A magnetic component has been selected on the basis of a solid solution of spinel $NiFe_2O_4$ and $ZnFe_2O_4$, characterized by high resistance and magnetostrictive coefficient values. The study of composite structures $0.9BaTiO_3$-$0.1Ni_xZn_{1-x}Fe_2O_4$ and Pb(Ti, Zr)O_3-$Ni_xZn_{1-x}Fe_2O_4$ showed that the maximum magnetoelectric coefficient was observed at x = 0.2–0.3 [3,4]. Thus, to create a composite structure, the spinel $Ni_{0.7}Zn_{0.3}Fe_2O_4$ has been selected. The ferroelectric component was lead-free perovskite solid solutions based on (Na, Li)NbO_3, characterized by relatively high piezoelectric activity and Curie temperature [5].

The aim of this work is to establish the laws of formation for lead-free composites structures of $0.6(Ni_{0.7}Zn_{0.3}Fe_2O_4)$ / $0.4((Na, Li, Sr)NbO_3 + MnO_2)$ obtained using different production means.

2. Experimental

The composites studied in this work were prepared from mixtures of pre-formed spinel and perovskite. Synthesis of the spinel structure $Ni_{0.7}Zn_{0.3}Fe_2O_4$ was carried out using ceramic technology. To intensify the synthetic process for the samples, "chemically pure" potassium chloride was injected. Synthesis was performed according to [3] at 900 ° C for 5 hours. Upon completion of the synthesis, the samples were milled to grains by size less than 0.3 mm and washed with distilled water to remove KCl. Synthesis of perovskite based on (Na, Li)NbO_3 was made at $T_{sint.} = (850 - 870)^\circ$ C for 6 hours. Basic components of the composite have the following structural characteristics: $Ni_{0.7}Zn_{0.3}Fe_2O_4$ – cubic symmetry, the cell parameter a = 8.372Å, 1/8V = 73.35Å^3, (Na, Li, Sr)NbO_3 + MnO_2 – phase mixture: rhombic to monoclinic (M) reduced cell and rhombohedral (Rh) in approximately equal amounts. Parameters of M cell are: a = 3.912Å, b = 3.876Å, $\beta = 90.78^\circ$, V = 59.32 Å^3, Rh cell parameters: a = 3.907Å, $\alpha = 89.17^\circ$, V = 59.58Å^3 (at $T_{sint.} = 1200^\circ$ C).

The starting materials were weighed with an accuracy of 0.1 mg, homogenized in an agate mortar, placed in an alundum crucible and subjected to heat treatment at 900 ° C for 2 hours. In order to determine the optimal conditions, sintering temperatures of 1110, 1150, 1180, 1200 and 1220 ° C were selected and the samples were sintered with exposure for 2 hours.

X-ray diffraction studies were performed using a DRON 3.0 (CoK_α - radiation). The measured density ($\rho_{meas.}$) was defined by the method of hydrostatic weighing in octane. Calculation of X-ray density ($\rho_{X\text{-ray.}}$) was made by the formula: $\rho_{X\text{-ray.}}$=1,66·M/V, where is the weight of formula unit in grams, V is the volume of the perovskite cell in Å^3. Relative density ($\rho_{rel.}$) was calculated by the formula: $(\rho_{meas.}/\rho_{X\text{-ray.}})\cdot 100\%$.

3. Results and discussion

In Fig. 1, the dependence of $\rho_{meas.}$ on $T_{sint.}$ is given, testifying to the strong influence of $T_{sint.}$ upon $\rho_{meas.}$ Experimental data showed that $((\rho_{max} - \rho_{min})/\rho_{min.} \approx 12\%$, where ρ_{max} — maximum, and ρ_{min} — minimum values of $\rho_{meas.}$, achieved by changing the $T_{sint.}$).

The slowing in growth and the "saturation" of the dependence of $\rho_{meas.}$ ($T_{sint.}$) at $T_{sint.} = 1180^\circ$ C, may be attributed to the approach of the temperature to the melting point of the sample ($T_{sint.} = 1250^\circ$ C). The maximum value of $\rho_{rel.}$ (95.6 %) is reached at $T_{sint.} = 1200^\circ$ C.

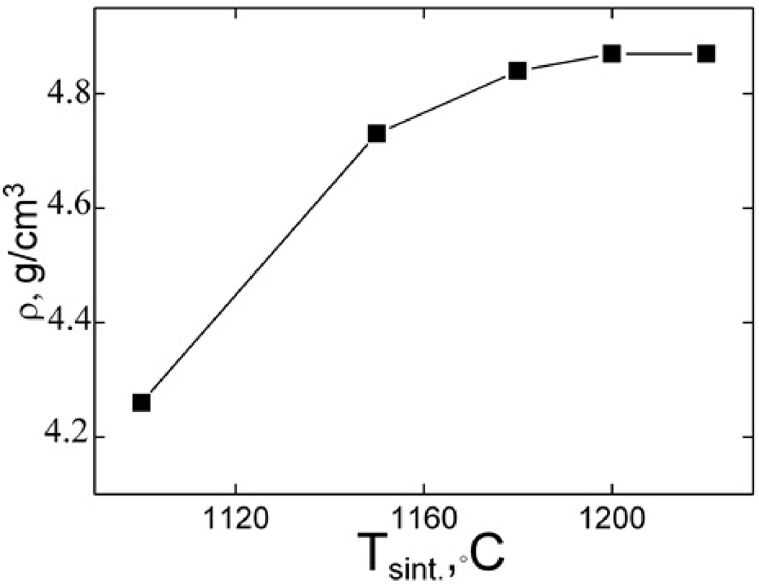

FIG. 1. The dependence of the measured density of the composite from $T_{sint.}$

Fig. 2 shows the diffraction pattern of the studied composite at $T_{sint.} = 1180$, 1200 and 1220 ° C.

In the $T_{sint.} = 1180$ ° C diffractogram, besides reflections for $Ni_{0.7}Zn_{0.3}Fe_2O_4$ and solid solutions based on the (Na, Li)NbO_3 system, few lines are present ($I/I_1 = 4$, where I — relative intensity of a strong reflex of an impurity phase, I_1 — relative intensity of the strongest line on diffractogram) for the outside phase (presumably pyrochlore). Increasing the $T_{sint.}$ to 1200 ° C and 1220 ° C leads to the disappearance of the lines for an impurity phase and an increase of the reflex intensity for the spinel phase. This is associated with the approach to the optimal $T_{sint.}$ For the spinel phase, at which more perfect crystal structure is formed. Thus, based on X-ray analysis and the results of ρ_{meas} measurement, the optimum $T_{sint.}$ of 1200 ° C was chosen.

In Fig. 3, X-ray lines $(200)_C$ and $(220)_C$ of perovskite phase of composite are shown. In Fig. 4 X-ray lines (400) and (440) of spinel phase are given.

Fig. 3 shows that the diffraction patterns for perovskite phase is characterized by a strong diffuse scattering, which distorts the line profiles, especially the $(220)_C$. It is not possible to establish unambiguously the composition of the perovskite phase in the composite. At $T_{sint.} = 1180$ ° C, the solid solution is a mixture of orthorhombic and pseudocubic (not Rh) phases. Pseudocubic phases at $T_{sint.} = 1200$ and 1220 ° C disappear, and the presence of a small amount of Rh phase is not excluded.

Table 1 shows the unit cell parameters for the phases of the composite, and the measured, x-ray and relative densities for the ceramic samples. It is seen that the volume of cells in both cases is reduced when $T_{sint.}$ is increased to 1220 ° C and the volume approaches values characteristic of the initial components.

In Fig. 3, it is seen that close to lines $(200)_C$ weak satellites are located. They testify to structure modulation (in Fig. 3, they are denoted with "c^-" and "c^+" from smaller and larger angles θ, respectively). Modulation wavelength, Λ, calculated on the position of the satellite c^- with respect to the main peak-(200), is equal to 127Å. This value equals 32.5 of the cell parameter. The calculation was performed using the formula $\Lambda = (1/d_{200}\text{-}1/d_c^-)^{-1}$ [6].

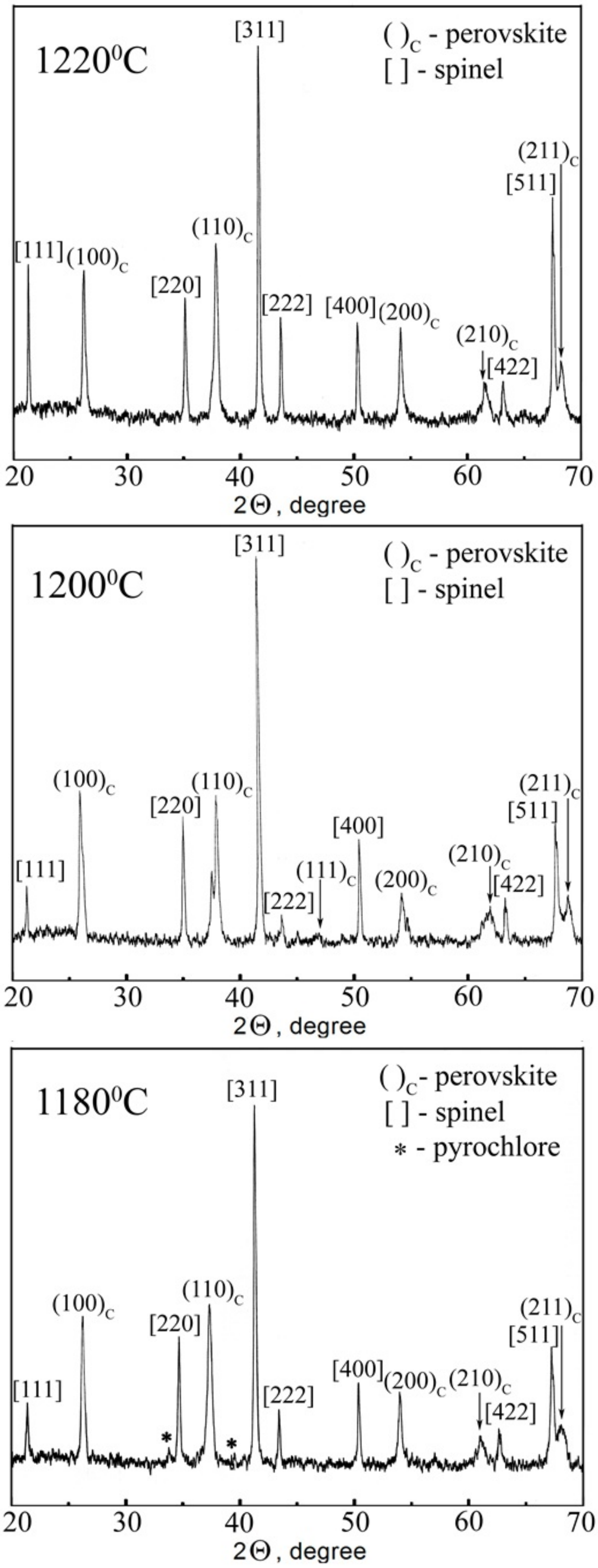

FIG. 2. The XRD pattern of the composite ($T_{\mathrm{sint.}} = 1200\,^{\circ}\mathrm{C}$) in the angular range $2\theta = 20$–$70\,^{\circ}$. In square brackets denote spinel lines, while parentheses denote perovskite lines

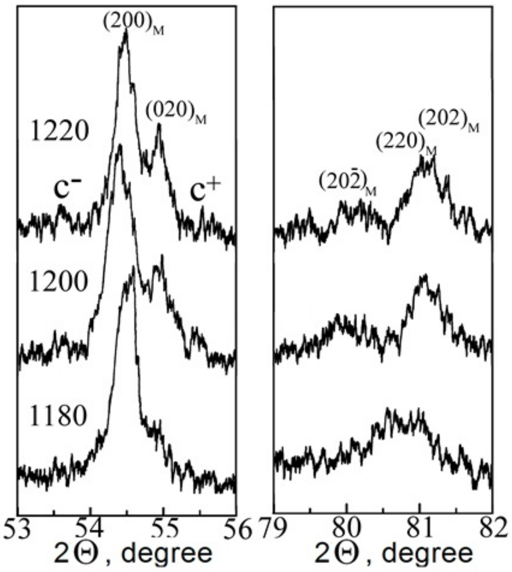

FIG. 3. Diffraction reflections $(200)_C$ and $(220)_C$ of the perovskite phase of the composite at different $T_{sint.}$

TABLE 1. Structural characterization of the composite phases, and the density of the ceramic samples: measured, x-ray and relative

T_{sint} °C	Composition, I/I_1 relative units	Symmetry	Monoclinic cell parameters of the perovskite				$\rho_{x\text{-ray}}$ of the M phase, g/cm^3	Cubic cell parameters of the spinel		$\rho_{x\text{-ray}}$ cubic phase, g/cm^3	$\rho_{x\text{-ray}}$ composite, g/cm^3	ρ_{meas} composite, g/cm^3	ρ_{rel} %
			a,Å	b,Å	β, angle degree	V,Å^3		a,Å	1/8V, Å^3,				
1180	100-spinel 38-perovskite 4-pyrochlore	Cubic+ Monoclinic+ Pseudocubic	- 3.913 3.915	3.883	90.67	59.45 60.01	4.521	8.380	73.55	5.367	5.085	4.84	95.18
1200	100-spinel 38-perovskite	Cubic+ Monoclinic	3.914	3.880	90.76	59.44 60.01	4.543	8.379	73.53	5.369	5.094	4.87	95.60
1220	100-spinel 47-perovskite	Cubic + Monoclinic	3.912	3.878	90.70	59.34	4.551	8.375	73.44	5.376	5.101	4.87	95.48

Half of the cells having wavelength modulation values for the perovskite structure means that the cause of the modulation can be ordered extended defects, such as crystallographic shear planes. In [7,8], for samples with Ti- and Nb- containing compounds, it is shown that the presence of variable valency ions in the material structure may contribute to point defects — anionic vacancies. The latter can be eliminated by shifting one part of the structure relative to the other along a particular crystallographic direction, forming extended defects — plane crystallographic shear. They can be regarded as a translational modulation of the initial structure [9].

Fig. 4 shows that the diffraction of the spinel, unlike perovskite, is characterized by sharp, narrow lines, which indicates well-formed structure.

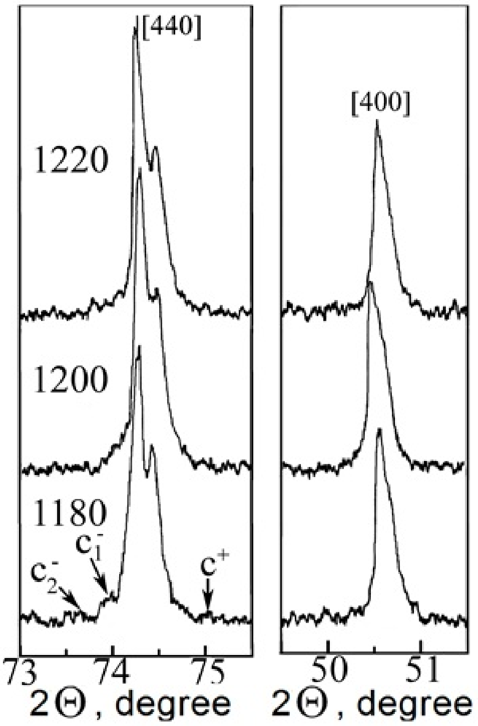

FIG. 4. Diffraction reflexes [400] and [440] of the spinel phase of the composite at different $T_{sint.}$ At $T_{sint.}$=1180 ° C diffusion maxima (satellites c_1^- and c_2^-) are accurately seen based on the [440] line from the side of smaller angles

On the pattern diffraction, obtained for $T_{sint.} = 1180$ ° C, side satellites close to the [440] line from the smaller angles θ are clearly visible. They are indicated in Fig. 4 as c_1^- and c_2^-, corresponding to the wavelength modulation $\Lambda_1 = 421$Å (35.5 cells), $\Lambda_2 = 210$Å, $\Lambda_2 = 1/2\ \Lambda_1$. Note that modulation of the spinel structure is more apparent at low sintering temperatures, while modulation of the perovskite structure – at higher $T_{sint.}$. This can be explained by the following fact; ions with more stable valency states (Ni^{2+} and Zn^{2+}) are in the spinel composition. The iron ion is supposed to be in the trivalent state. The disappearance of modulation in the spinel phase structure for increased $T_{sint.}$ may be connected with the formation of a more perfect crystal structure when approaching the optimal $T_{sint.}$

A perovskite phase contains an ion with a variable valency — Nb^{5+}. This ion is restored at increased temperatures with the formation of oxygen vacancies. These oxygen vacancies in process of their accumulation are ordered and excluded by a crystallographic shift. In [10] it was shown that in stable high-temperature modification of α-Nb_2O_5, which is the main structure-forming reagent of a perovskite phase, the density of extended defects (the planes of the crystallographic shift) increased with increased temperature.

4. Conclusion

Thus, in this paper the following results were obtained:

— the technology for the production of uncontaminated composites $0.6(Ni_{0.7}Zn_{0.3}Fe_2O_4)$ / $0.4((Na, Li, Sr)NbO_3 + MnO_2)$ is developed;

— the dependence of phase composition and structure upon $T_{sint.}$ was stated; it was shown that the optimal $T_{sint.}$ for the composite was $1200\,^\circ$C;

— it was found that by varying the $T_{sint.}$, the phase composition of perovskite changes; the disappearance of an impurity phase at increased $T_{sint.}$ ($\geqslant 1200\,^\circ$C) was observed; modulation of perovskite structure appeared at higher sintering temperatures ($T_{sint.} = 1220\,^\circ$C) and modulation of spinel structure — at lower $T_{sint.}$ ($T_{sint.} = 1180\,^\circ$C);

— it was supposed that the detected modulation of the structure of perovskite and spinel may be associated with ordered extended defects such as crystallographic shear planes, which condense and strengthen the composite structure.

References

[1] H. Zheng, J. Wang, S.E. Lofland, et al. Multiferroic $BaTiO_3$-$CoFe_2O_4$ Nanostructures. *Science*, **303**, P. 661–663 (2004).

[2] W. Eerenstein, N.D. Mathur, J.F. Scott. Multiferroic and magnetoelectric materials. *Nature*, **442**, P. 759–765 (2006).

[3] S.K. Upadhyay, V.R. Reddy. Study of $0.9BaTiO_3$-$0.1Ni_xZn_{1-x}Fe_2O_4$ magneto-electric composite ceramics. *J. Appl. Phys.*, **113**, P. 114107(1–5) (2013).

[4] G. Srinivasan, E.T. Rasmussen, R. Hayes. Magnetoelectric effects in ferrite-lead zirconate titanate layered composites: The influence of zinc substitution in ferrites. *Physical Review B*, **67**, P. 014418(1–10) (2003).

[5] A method for producing iron-chromium-nickel spinel, Patent 1 2257953 Russia: B 01 J 23/86, 37/04. V.M. Talanov, N.P. Shabelskaya. South-Russian State Tech. Univ. (NPI); statement 29.01.2004; Publ. 10.08.2005, Bull. N 22.

[6] A. Guinier. *Radiocristallographie.* Moscow, 604 p. (1961).

[7] L.A. Reznichenko, L.A. Shilkina, S.V. Titov, O.N. Razumovskaya. Magnéli phases in Ti-containing oxides and their solid solutions. *Crystallography Reports*, **48**(3), P. 377–383 (2003).

[8] L.A. Reznichenko, L.A. Shilkina, E.S. Gagarina, Yu.I. Yuzyuk, O.N. Razumovskaya, A.V. Kozinkin. Crystallographic shear in niobium oxides of different compositions. *Crystallography Reports*, **49**(5), P. 820–827 (2004).

[9] C.N.R. Rao, J. Gopalakrishnan. *New directions in solid state chemistry.* Cambridge University Press, Cambridge, 568 p. (1997).

[10] L.A. Reznichenko, V.V. Akhnazarova, L.A. Shilkina, O.N. Razumovskaya, S.I. Dudkina. Invar effect in n-Nb_2O_5, αht-Nb_2O_5, and L-Nb_2O_5. *Crystallography Reports*, **54**(3), P. 483–491 (2009).

NANOSYSTEMS: PHYSICS, CHEMISTRY, MATHEMATICS, 2013, 4 (6), P. 851–856

FORMATION MECHANISM OF $GdFeO_3$ NANOPARTICLES UNDER THE HYDROTHERMAL CONDITIONS

E. A. Tugova[1,2], I. A. Zvereva[3]

[1]Ioffe Physical Technical Institute of RAS, Saint Petersburg, Russia

[2]Saint Petersburg Electrotechnical University “LETI”, Saint Petersburg, Russia

[3]Saint Petersburg State University, Saint Petersburg, Russia

katugova@inbox.ru; irinazvereva@yandex.ru

PACS 61.46.+w

The formation mechanism of $GdFeO_3$ nanoparticles by varying of the hydrothermal conditions has been investigated. The mean size of coherent scattering regions of $GdFeO_3$ was determined to be equal to 53, 68 and 73 nm. The observed regularities allowed us to assume the oriented attachment of nanocrystals.

Keywords: nanoparticles, hydrothermal synthesis, nucleation, phase formation.

1. Introduction

Perovskite-type compounds possess unique electrical, magnetic, thermal properties [1-6]. The potential exists for materials production based on the application of perovskite-like oxide nanoparticles. However, in the literature there is little data concerning investigations into the chemical pre-history and synthetic technique's influence on size, morphology and properties of obtained $LnFeO_3$ (Ln = rare earth element) [7, 8]. The sonochemical method is suggested [9] for the synthesis of nanoparticles of the rare earth series of orthoferrites, using iron pentacarbonyl and rare earth carbonates as precursors. In this manner, $GdFeO_3$, $TbFeO_3$ nanoparticles of 60 nm and $EuFeO_3$, $ErFeO_3$ of 40 nm were obtained. According to the presented data [10] $LaFeO_3$ was synthesized by three different preparation methods, i.e., by the calcination of both mixtures of La_2O_3 and Fe_2O_3 (I), co-precipitated $La(OH)_3$ and $Fe(OH)_3$ hydroxides (II) and $La[Fe(CN)_6]\cdot 5H_2O$ heteronuclear complex (III). The formation of $LaFeO_3$ is recognized for I, II and III cases at calcining temperatures above 1000, 800 and 600 °C, respectively. The mean particle diameter of $LaFeO_3$ after heat treatment of $La[Fe(CN)_6]\cdot 5H_2O$ at 600 °C for 2 hours was 30 nm [10].

It was also shown [11, 12] that the mean size of coherent scattering regions, morphology and magnetic characteristics of $YFeO_3$ target product were strongly dependent upon the synthetic techniques. Besides, it is well known [13, 14], that hydrothermal synthesis allows the production of highly crystallized and well dispersed powders at relatively low temperatures. There is little literature concerning the hydrothermal synthesis of $LnFeO_3$ (Ln = rare earth element), particularly, $GdFeO_3$.

These reasons demonstrate the importance of systematic investigations of the peculiarities of nanocrystalline $GdFeO_3$ formation under hydrothermal conditions.

2. Experimental

2.1. Synthesis procedure

The initial mixture, corresponding to the stoichiometry of $GdFeO_3$ was prepared by precipitation method from aqueous solutions of stoichiometric amounts of 1M $Gd(NO_3)_3{\cdot}5H_2O$ and $Fe(NO_3)_3{\cdot}9H_2O$ by a previously published procedure [15]. The obtained powders were then transferred to autoclaves and heated at 300–480 ° C for 1–3 h under 60–90 MPa pressure in distilled aqueous media. The required pressure was determined by temperature and water filling content and produced on Kennedy table data [16]. After cooling, the product was unloaded and then dried at the ambient temperature.

2.2. Characterization of prepared nanocrystals

Purity and crystallization of $GdFeO_3$ samples were characterized by powder X-ray diffraction (XRD) using a Shimadzu XRD-7000 with monochromatic CuK_α radiation (λ= 154.178 pm). Crystallite sizes of the obtained powders were calculated by the X-ray line broadening technique based on Scherer's formula.

The microstructure of the specimen, elemental composition and the composition of separate phases were analyzed by means of scanning electron microscopy (SEM) using Quanta 200, coupled with EDAX microprobe analyzer. The error in determining the elements content by this method varies with the atomic number and equals to ±0.3 mass% on average.

3. Results and discussion

The performed X-Ray and SEM/EDAX analysis of co-precipitated initial mixture corresponding to the stoichiometry of $GdFeO_3$ shows the amorphous state and heterogeneity of the produced powders. But, it should be noted, that X-Ray diffraction pattern related to the initial mixture demonstrates the weak affect which can be attributed to hexagonal modification of $Gd(OH)_3$ (Fig. 1(1)).

TABLE 1. Electron probe microanalysis data for the regions indicated in Fig. 1($b-d$)

Sample	Sintering temperature ° C	Examined region	Components content, mol%		Phases
			$GdO_{1.5}$	$FeO_{1.5}$	
b	300	SQ1	36.58	63.42	$Gd_3Fe_5O_{12}$
		P1	38.67	61.33	$Gd_3Fe_5O_{12}$
		P2	17.92	82.08	Fe_2O_3
		P3	37.44	62.56	$Gd_3Fe_5O_{12}$
c	400	SQ2	43.97	56.03	$GdFeO_3$ + $Gd_3Fe_5O_{12}$
		P4	50.30	49.70	$GdFeO_3$
		P5	41.02	58.98	$GdFeO_3$ + $Gd_3Fe_5O_{12}$
		P6	46.71	53.29	$GdFeO_3$
d	480	SQ3	48.85	51.15	$GdFeO_3$

Based on X-ray and SEM/EDX data (Fig. 1(2,3), Table 1), samples treated at 300 ° C and 400 ° C under 70 MPa pressure for 1 hour contain $Gd(OH)_3$, FeOOH and small amounts of $Gd_3Fe_5O_{12}$ and $GdFeO_3$. At the same time, the presence of Gd_2O_3 and Fe_2O_3 are observed

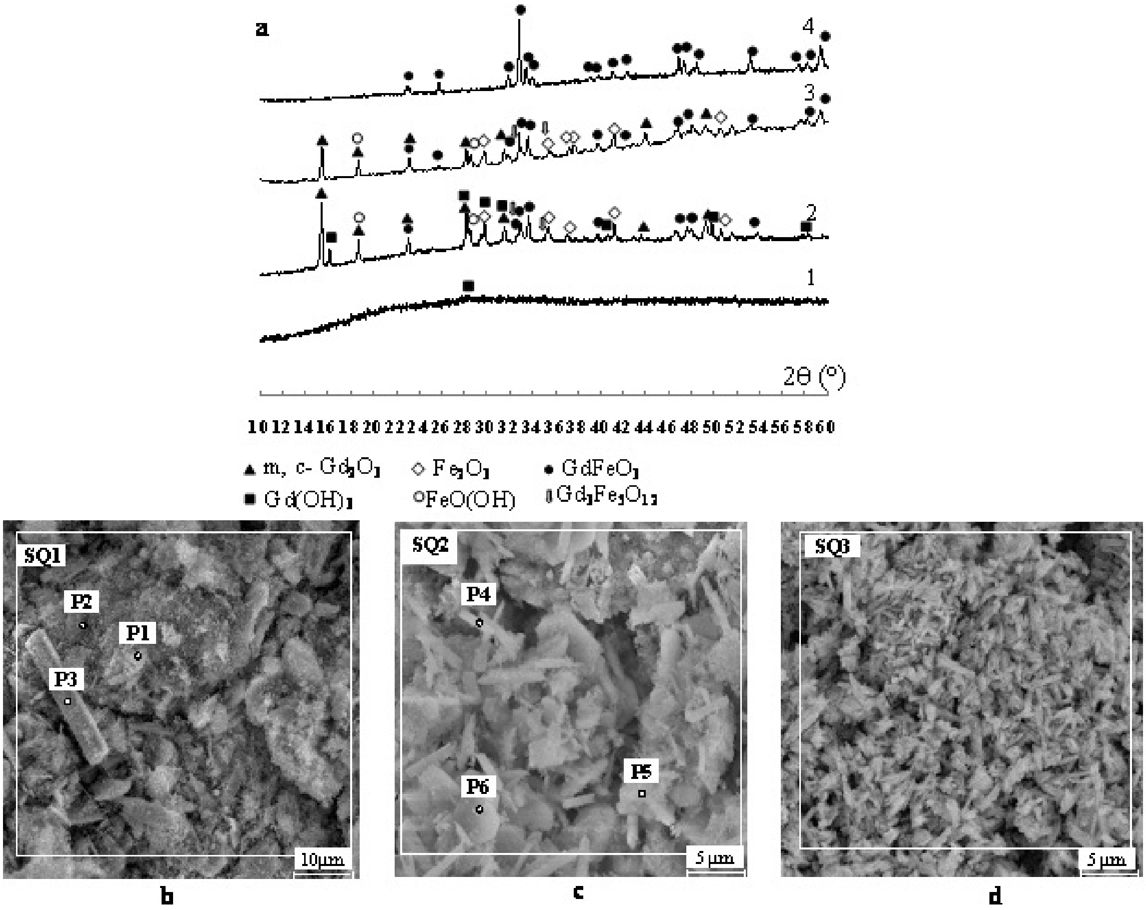

Fig. 1. **a)** X-Ray diffraction patterns and **b-d)** SEM photographs of: **1)** initial mixture, **2-4)**, **b-d)** initial mixtures after hydrothermal treatment at 300, 400, 480 ° C under 70 MPa for 1 h

Table 2. Electron probe microanalysis data for the regions indicated in Fig. 2(*b*,*c*)

Sample	Hydrothermal conditions	Examined region	Components content, mol%		Phases
			$GdO_{1.5}$	$FeO_{1.5}$	
b	600	SQ	46.71	53.29	$GdFeO_3$
		SQ1	46.79	53.21	
		1	47.64	52.36	
c	900	SQ	48.18	51.82	
		1	41.60	58.40	
		2	41.08	58.92	
		3	48.58	51.42	
		4	45.76	54.24	
		5	47.63	52.37	

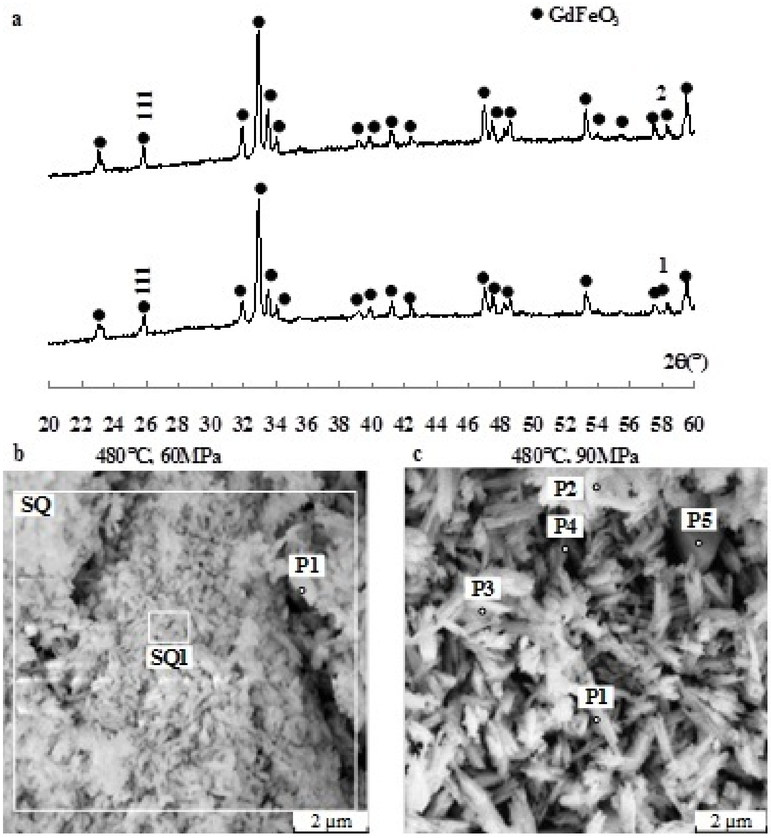

FIG. 2. **a)** X-Ray diffraction patterns and **b,c)** SEM photographs of initial mixtures after hydrothermal treatment at 480 °C under 60 MPa (1,b) and 90 MPa (2,c) for 1 h

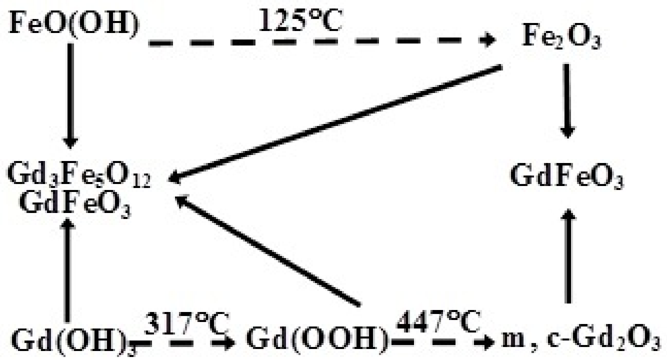

FIG. 3. Phase formation scheme, describing processes which are taken place under initial mixture hydrothermal treatment to yield $GdFeO_3$

(Fig. 1(2,3); Table 1). Raising the temperature rising to 480 ° C leads to homogeneous $GdFeO_3$ formation (Fig. 1(4), Table 1).

The formation of $GdFeO_3$ nanoparticles was investigated by varying pressure from 60 to 90 MPa and was carried out at the same temperature, 480 ° C. Fig. 2 and Table 2 present results for X-ray and SEM/EDX data of the initial mixture samples treated under 60 and 90 MPa at 480 ° C for 1 hour. According to the presented data (Fig. 2,*a* and Table 2), all characteristic reflects corresponded to the target product. The mean size of coherent scattering regions (D_{111}) was determined from X-ray data for peak with (111) index for samples of $GdFeO_3$ produced after initial mixture treatment under 60, 70, 90 MPa at 480 ° C. The D_{111} values were equal to 53, 68 and 73 nm, respectively. Figure 2(*b*,*c*) shows that the product was entirely composed of crystals with a relatively uniform, rod-like morphology.

Thus, according to presented and literature data [17, 18], the formation mechanism for $GdFeO_3$ nanoparticles under the hydrothermal conditions can be illustrated as the shown scheme (Fig. 3).

The large values of mean size of coherent scattering regions of $GdFeO_3$ nanoparticles can be explained by oriented attachment of nanocrystals proceeding via the described mechanism [19, 20].

4. Conclusion

These results showed that the mechanism by which $GdFeO_3$ nanoparticles were formed proceeded through the dehydration stages of $Gd(OH)_3$ and FeOOH. The target product was entirely composed of crystals with a relatively uniform, rod-like morphology. The large values of mean size of coherent scattering regions of $GdFeO_3$ nanoparticles ranging from 53–73 nm size were obviously attributed to oriented attachment of nanocrystals.

Acknowledgments

The authors would like to thank Prof. V. V. Gusarov for useful discussions.

This work was financially supported by the Russian Foundation for Basic Research, project N 13-03-12470 ofi_m2.

References

[1] I.A. Leonidov, M.V. Patrakeev , J.A. Bahteeva, K.V. Poholok, D.S. Filimonov, K.R. Poeppelmeier, V.L. Kozhevnikov. Oxygen-ion and electron conductivity in $Sr_2(Fe_{1-x}Ga_x)_2O_5$. *Journal of Solid State Chemistry*, **179**, P. 3045–3051 (2006).

[2] A.G. Petrosyan, V.F. Popova, V.L. Ugolkov, D.P. Romanov, K.L. Ovanesyan. A study of phase stability in the Lu_2O_3–Al_2O_3 system. *Journal of Crystal Growth*, **377**, P. 178–183 (2013).

[3] J.F. Scott. Magnetic phases of bismuth ferrite. *Journal of Magnetism and Magnetic Materials*, **321**, P. 1689–1691 (2009).

[4] T. Goto, T. Kimura, G. Lawes, A.P. Ramirez, Y. Tokura. Ferroelectricity and giant magnetocapacitance in perovskite rare-earth manganites. *Physical review letters*, **92**, P. 257201 (2004).

[5] T.I. Chupakhina, G.V. Bazuev. Synthesis, structure, and magnetic properties of $Sr_{0.8}Ce_{0.2}Mn_{1-y}Co_yO_{3-\delta}$ (y = 0.3, 0.4). *Inorganic Materials*, **47**(12), P. 1361–1366 (2011).

[6] J. Á Prado-Gonjal, M. Arévalo-López, E. Morán. Microwave-assisted synthesis: A fast and efficient route to produce $LaMO_3$ (M = Al, Cr, Mn, Fe, Co) perovskite materials. *Materials Research Bulletin*, **46**, P. 222–230 (2011).

[7] H. Shen, J. Xu, A. Wu. Preparation and characterization of perovskite $REFeO_3$ nanocrystalline powders. *Journal of Rare earths*, **28**(3), P.416–419 (2010).

[8] S. Goswami, D. Bhattacharya, P. Choudhury. Particle size dependence of magnetization and noncentrosymmetry in nanoscale $BiFeO_3$. *Journal of applied physics D*, **109**(7), P. 737–739 (2011).

[9] M. Sivakumar, A. Gedanken, D. Bhattacharya, I. Brukental, Y. Yeshurun, W. Zhong, Y.W. Du, I. Felner, I. Nowik. Sonochemical synthesis of nanocrystalline rare earth orthoferrites using $Fe(CO)_5$ precursor. *Chem. Mater*, **16**, P. 3623–3632 (2004).

[10] S. Nakayama. $LaFeO_3$ perovskite-type oxide prepared by oxide-mixing, co-precipitation and complex synthesis methods. *Journal of Materials Science*, **36**, P. 5643–5648 (2001).

[11] A.T. Nguyen, O.V. Almjasheva, I.Ya. Mittova, O.V. Stognei, S.A. Soldatenko. Synthesis and magnetic properties of $YFeO_3$ nanocrystals. *Inorganic Materials*, **45**(11), P. 1304–1308 (2009).

[12] I.Ya. Mittova, A.T. Nguyen, O.V. Almjasheva. Influence of the synthesis conditions on the particle size and morphology of yttrium orthoferrite obtained from aqueous solutions. *Russian Journal of Applied Chemistry*, **82**(11), P. 1915–1918 (2009).

[13] R. Lu, J. Yuan, H. Shi, Bin Li, W. Wang, D. Wang, M. Cao. Morphology-controlled synthesis and growth mechanism of lead-free bismuth sodium titanate nanostructures via the hydrothermal route. *CrystEngComm*, **15**, P. 3984–3991 (2013).

[14] M.V. Tomkovich, E.R. Andrievskaya, V.V. Gusarov. Formation under hydrothermal conditions and structural features of nanoparticles based on the system ZrO_2–Gd_2O_3. *Nanosystems: physics, chemistry, mathematics*, **2**(2), P. 6–14 (2011).

[15] E.A. Tugova, V.V. Gusarov. Structure peculiarities of nanocrystalline solid solutions in $GdAlO_3$ – $GdFeO_3$ system. *Nanosystems: physics, chemistry, mathematics*, **4**(3), P. 352–356 (2013).

[16] G.C. Kennedy. Pressure-volume-temperature relations in water at elevated temperatures and pressures. *American Journal of Science*, **248**, P. 540-564 (1950).

[17] M.W. Shafer, R. Roy. Rare-earth polymorphism and phase equilibria in rare-earth oxide-water systems. *Journal of the American Ceramic Society*, **42**(4), P. 563–570 (1959).

[18] Ch. Chang , Zhang Q.-an, Ma D. The hydrothermal preparation, crystal structure and photoluminescent properties of GdOOH nanorods. *Nanotechnology*, **17**, P. 1981–1985 (2006).

[19] R.L. Penn, J.F. Banfield. Imperfect oriented attachment: dislocation generation in defect-free nanocrystals. *Science* ,**281**, P. 969–971 (1998).

[20] R.L. Penn, J.F. Banfield. Oriented attachment and growth, twinning, polytypism, and formation of metastable phases: Insights from nanocrystalline TiO_2. *American Mineralogist*, **83**, P. 1077–1082 (1998).

NANOSYSTEMS:

PHYSICS, CHEMISTRY, MATHEMATICS

INFORMATION FOR AUTHORS

The journal publishes research articles and reviews, and also short scientific papers (letters) which are unpublished and have not been accepted for publication in other magazines. Articles should be submitted in English. All articles are reviewed, then if necessary come back to the author to completion.

The journal is indexed in Chemical Abstract Service of the American Chemical Society and in Russian Scientific Citation Index.

Author should submit the following materials:

1. Article file in English, containing article title, the initials and the surname of the authors, Institute (University), postal address, the electronic address, the summary, keywords, MSC or PACS index, article text, the list of references.
2. Files with illustrations, files with tables.
3. The covering letter in English containing the article information (article name, MSC or PACS index, keywords, the summary, the literature) and about all authors (the surname, names, the full name of places of work, the mailing address with the postal code, contact phone number with a city code, the electronic address).
4. The expert judgement on possibility of publication of the article in open press (for authors from Russia).

Authors can submit a paper and the corresponding files to the following addresses: nanojournal.ifmo@gmail.com, popov1955@gmail.com.

Text requirements

Articles should be prepared with using of text editors MS Word or LaTEX (preferable). It is necessary to submit a pdf copy. In the name of files the English alphabet is used. The recommended size of short communications (letters) is 4-6 pages, research articles – 6-15 pages, reviews – 30 pages.

Recommendations for text in MS Word:

Formulas should be written using Math Type. Figures and tables with captions should be inserted in the text. Additionally, authors present separate files for all figures and Word files of tables.

Recommendations for text in LaTex:

Please, use standard LaTex without macros and additional style files. The list of references should be included in the main LaTex file. Single LaTex file of the paper with the corresponding pdf file should be submitted.

References in the article text are given in square brackets. The list of references should be prepared in accordance with the following samples:

[1] N. Surname. *Book Title*. Nauka Publishing House, Saint Petersburg, 281 pp. (2000).
[2] N. Surname, N. Surname. Paper title. *Journal Name*, **1**(5), P. 17-23 (2000).
[3] N. Surname, N. Surname. Lecture title. In: Abstracts/Proceedings of the Conference, Place and Date, P. 17-23 (2000).
[4] N. Surname, N. Surname. Paper title (2010). URL: http://books.ifmo.ru/ntv.
[5] N. Surname, N. Surname. Patent Name. Patent No. 11111, Bul. No. 33, 5 pp. (2010).
[6] N. Surname, N. Surname. Thesis Title. Thesis for full doctor degree in math. and physics, Saint Petersburg, 105 pp. (2000).

Requirements to illustrations

Illustrations should be submitted as separate black-and-white files. Formats of files – jpeg, eps, tiff.

Mathematical Challenge of Quantum Transport in Nanosystems, “Pierre Duclos Workshop”, NRU ITMO, Saint Petersburg, Russia

(September 23-26, 2014)

September 23, 2014 *Young Researchers Symposium (YRS)*
September 24-26, 2014 *Pierre Duclos Workshop*

Invited Speakers

- Pavel Exner (Prague, Czech Republic)
- Horia Cornean (Aalborg, Denmark)
- Hagen Neidhardt (Berlin, Germany)
- Valentin Zagrebnov (Marseille, France)
- Konstantin Pankrashkin (Paris, France)
- Mikhail Belishev (St. Petersburg, Russia)

The **main topics** of the conference:

- Spectral theory
- Scattering
- Quantum transport
- Quantum communications and computations

Conference language: English.

Location
The workshop will take place at Saint Petersburg National Research University of Information Technologies, Mechanics, and Optics: Kronverkskii, 49, 197101 Saint Petersburg, Russia.

Registration fee (paid the equivalent sum in roubles on arrival)
For Pierre Duclos Workshop: 100 euro (book of abstracts, conference bag, coffee breaks, conference dinner).
For YRS: 20 euro (book of abstracts, conference bag, coffee breaks). Students and postgraduate students who attend YRS can attend "Pierre Duclos Workshop" sessions as well.

The **Proceedings** will be published in the journal "Nanosystems: Physics, Chemistry, Mathematics".

Deadlines
Visa Application and Registration (for Shengen zone residents who need a Russian visa): July 1, 2014.
Visa Application and Registration (for other countries residents who need a Russian visa): June 15, 2014.
Registration (for participants who do not need a Russian visa): September 8, 2014.

Contact
Prof. Igor Yu. Popov
tel: +7-812-232-67-65, e-mail: popov1955@gmail.com; conference site: http://mathdep.ifmo.ru/mcqtn2014/

NANOSYSTEMS:

PHYSICS, CHEMISTRY, MATHEMATICS

Журнал зарегистрирован
Федеральной службой по надзору в сфере связи, информационных технологий и массовых коммуникаций
(свидетельство ПИ № ФС 77 - 49048 от 22.03.2012 г.)
ISSN 2220-8054

Учредитель: федеральное государственное бюджетное образовательное учреждение высшего профессионального образования
«Санкт-Петербургский национальный исследовательский университет информационных технологий, механики и оптики»

Издатель: федеральное государственное бюджетное образовательное учреждение высшего профессионального образования
«Санкт-Петербургский национальный исследовательский университет информационных технологий, механики и оптики»

Отпечатано в учреждении «Университетские телекоммуникации»
Адрес: 197101, Санкт-Петербург, Кронверкский пр., 49

Подписка на журнал НФХМ
На 2014 год подписка осуществляется через ОАО Агентство «Роспечать»
Подписной индекс 57385 в каталоге «Издания органов научно-технической информации»